Intense laser-plasma interactions with gaseous targets for energy transfer and particle acceleration

Inaugural-Dissertation

zur Erlangung des Doktorgrades
der Mathematisch-Naturwissenschaftlichen Fakultät
der Heinrich-Heine-Universität Düsseldorf

vorgelegt von

Thomas Gangolf
aus Stade

Düsseldorf, November 2017

aus dem Institut für Laser- und Plasmaphysik
der Heinrich-Heine-Universität Düsseldorf

Gedruckt mit der Genehmigung der
Mathematisch-Naturwissenschaftlichen Fakultät der
Heinrich-Heine-Universität Düsseldorf

Referent: Prof. Dr. Oswald Willi

1. Korreferent: Prof. Dr. Alexander Pukhov

2. Korreferent: Prof. Dr. Dr. Carsten Müller

Tag der mündlichen Prüfung: 20. Dezember 2017

Abstract

In the field of laser-matter interaction, plasma densities ranging from extremely low values (such as in laboratory astrophysics) to extremely high values (such as for laser-driven nuclear fusion) are experimentally realized. For a given laser wavelength, they are specified in terms of the critical density n_c. Shortest and most intense pulses are currently generated with lasers in the near infrared for which $n_c \approx 10^{21}\,\mathrm{cm}^{-3}$. Low-density targets ($n_e < 5\,\% n_c \approx 5 \ldots 9 \times 10^{19}\,\mathrm{cm}^{-3}$) are commonly created from gas jets or gas cells, whereas high-density targets ($n_e > 100 n_c \approx 10^{23}\,\mathrm{cm}^{-3}$) are created from solids.

This thesis is about laser interaction with targets in the intermediate density range ($0.05\,n_c$ to $2.5\,n_c$), which are more challenging to create. Using novel high-density Hydrogen gas jet targets, the plasmas are either created by prepulses or directly by the interaction pulses. The laser-plasma interaction of both the generating pulses and the subsequently transmitted pulses are investigated with regard to two applications: First, the creation of a collisionless shock by a laser in a near-critical target $n_e \gtrapprox n_c$ can contribute to proton acceleration. Second, undercritical plasmas are used to transfer energy from one laser pulse to another. As a long-term objective, laser pulses are to be amplified using this scheme to reach intensities beyond the damage thresholds of conventional optical components.

Collisionless Shock Acceleration For many applications, directional monoenergetic ion beams are desirable. Ion beams accelerated by target normal sheath acceleration (TNSA) are directional but have a broad spectrum. One of the processes that might overcome this limitation is collisionless shock acceleration (CSA).

In this thesis, ion acceleration by CSA is studied experimentally. In an experiment at the TITAN Nd:glass laser, a 210 J, 5 ps pulse is focused into a $0.9 \ldots 2.5\,n_c$ gas jet target. It is demonstrated experimentally that for an overcritical target, a collimated proton beam is generated in forward direction. The proton spectrum shows a monoenergetic peak at $0.2 \ldots 1$ MeV over a broadband spectrum. Numerical simulations indicate the formation of a collisionless shock and acceleration of protons both by the shock and TNSA on the rear surface of the target under these conditions. Therefore, the experimental proton spectrum can be ascribed to the coexistence of both processes. The dependence of the proton spectrum on the laser intensity and the plasma density is comparable to theoretical estimates.

Laser pulse amplification by stimulated Brillouin backscattering The other part of the thesis is about an experimental study on amplification of laser pulses by Stimulated Brillouin Backscattering in the strongly-coupled regime (sc-SBS). In these experiments,

the amplification of an ultrashort seed beam by a picosecond pump beam in a $5\,\% \, n_c < n_e < 15\,\% \, n_c$ plasma is studied.

In a first experiment at the ELFIE Nd:glass laser, a plasma created by a 30 J, 600 ps uncompressed prepulse, and subpicosecond seed pulses are amplified in it. The 6 J, 4 ps pump and the 4 mJ, 700 fs seed are counterpropagating, and overlap in space and time in the preformed plasma. For optimal conditions, the seed pulse is amplified, shorter in time, the spectrum broader and shifted compared to an unamplified pulse. This demonstrates amplification in the self-similar regime, where the pump is effectively attenuated. Tens of millijoules of energy are transferred from the pump to the seed.

For shorter pulses, amplification by sc-SBS is studied at the ARCTURUS Ti:sapphire laser. The role of the preionization is studied by either using a preformed plasma, generated and heated by a 400 mJ, 780 fs prepulse, or relying on the pump pulse to ionize the gas. In both cases, the 700 mJ, 800 fs pump and counterpropagating 1 . . . 12 mJ, 30 . . . 160 fs seed interact with the target. Without preionziation, a considerable amount of pump energy is lost for amplification due to collisions and Raman scattering. This transmission is greatly increased in the case of the preformed plasma. Furthermore, it can be seen that amplification is reduced due to the influence of the chirp on the pump beam, as expected from theory.

Zusammenfassung

Im Gebiet der Laser-Materie-Wechselwirkungen werden Plasmadichten in einem großen Bereich von sehr niedrigen Werten (z. B. Laborastrophysik) bis hin zu extrem hohen Werten (z. B. Kernfusion) experimentell realisiert. Für eine bestimmte Laserwellenlänge werden sie in Einheiten der kritischen Dichte n_c angegeben. Die kürzesten und intensivsten Pulse werden aktuell mit Lasern im nahen Infrarot erreicht, für die $n_c \approx 10^{21}\,\mathrm{cm}^{-3}$ ist. Targets niedriger Dichte ($n_e < 5\,\% \, n_c \approx 5 \ldots 9 \times 10^{19}\,\mathrm{cm}^{-3}$) werden typischerweise mit Gasjets oder Gaszellen hergestellt, während Targets hoher Dichte ($n_e > 100 n_c \approx 10^{23}\,\mathrm{cm}^{-3}$) mit festen Targets erreicht werden. In dieser Dissertation geht es um Wechselwirkungen von Laserpulsen mit den schwieriger herzustellenden Targets mittlerer Dichte ($0.05\,n_c$ to $2.5\,n_c$). Mit neuen Hochdruck-Wasserstoffjets werden die Plasmen entweder durch Vorpulse oder direkt durch die Hauptpulse hergestellt. Die Wechselwirkungen der Pulse mit dem Plasma werden hinsichtlich zweier Anwendungen untersucht: Erstens trägt die Erzeugung eines kollisionslosen Schocks durch den Laser in einem Target nahe der kritischen Dichte $n_e \gtrapprox n_c$ zur Protonenbeschleunigung bei. Zweitens werden unterkritische Plasmen genutzt, um Energie von einem Laserpuls auf einen anderen zu übertragen. Als langfristige Anwendung sollen damit Laserpulse verstärkt werden, bis hin zu Intensitäten jenseits der Zerstörschwellen konventioneller Optiken.

Schockbeschleunigung Für viele Anwendungen sind gerichtete monoenergetische Ionenstrahlen wünschenswert. Durch target normal sheath acceleration (TNSA) beschleunigte Ionenstrahlen sind gerichtet, haben aber ein breites Spektrum. Einer der Prozesse, die diese Begrenzung überwinden könnten, ist die Schockbeschleunigung (collisionless shock acceleration, CSA). In dieser Dissertation wird CSA experimentell untersucht. Am Nd:Glas-Laser TITAN wird ein 210 J, 5 ps Puls in ein $0.9 \ldots 2.5\,n_c$ Gasjet-Target fokussiert. Das Experiment zeigt, dass sich für ein überkritisches Target ein kollimierter Protonenstrahl in Vorwärtsrichtung bildet. Das Protonenspektrum zeigt einen monoenergetischen Peak (bei $0.2 \ldots 1\,\mathrm{MeV}$) über einem Breitband-Spektrum. Numerische Simulationen zeigen, dass sich unter diesen Bedingungen ein kollisionsloser Schock bildet, und dass Protonen durch den Schock und durch TNSA an der Targetrückseite beschleunigt werden. Daher kann das gemessene Spektrum durch die Koexistenz beider Prozesse erklärt werden. Die Abhängigkeit des Protonenspektrums von Laserintensität und Plasmadichte ist vergleichbar mit theoretischen Vorhersagen.

Laserverstärkung Im anderen Teil der Arbeit geht es um Experimente zur Verstärkung von Laserpulsen durch stimulierte Brillouin-Rückstreuung im Regime der starken Kopplung (stimulated Brillouin Backscattering in the strongly-coupled regime, sc-SBS). In

Experimenten wird die Verstärkung eines ultrakurzen Seed durch einen Pikosekunden-Pump in einem $5 \ldots 21\,\% \, n_c$ Plasma untersucht. In einem ersten Experiment am Nd:Glas-Laser ELFIE wird ein Plasma mit einem 30 J, 600 ps Vorpuls erzeugt, und es werden darin Subpikosekundenpulse verstärkt: Der 6 J, 4 ps Pump und der 4 mJ, 700 fs Seed sind gegenläufig und in Raum und Zeit im Plasma überlappt. Unter optimalen Bedingungen ist der Seed energiereicher und kürzer und hat ein breiteres und verschobenes Spektrum im Vergleich zum unverstärkten Seed. Dies ist typisch für Verstärkung im selbstähnlichen Regime, das erreicht wird, wenn der Pump durch den Prozess abgeschwächt wird. Es werden einige 10 Millijoule vom Pump auf den Seed übertragen. Für kürzere Pulse wird Verstärkung durch sc-SBS am Ti:Saphir-Laser ARCTURUS untersucht. Die Rolle der Vorionisation wird untersucht, indem das Plasma zum einen durch einen 400 mJ, 780 fs Vorpuls, zum anderen direkt durch den Pump erzeugt wird. In beiden Fällen wechselwirken ein 700 mJ, 800 fs Pump und ein gegenläufiger $1 \ldots 12$ mJ, $30 \ldots 160$ fs Seed mit dem Target. Ohne Vorionisation ist die Transmission gering, da ein erheblicher Anteil der Pumpenergie durch Kollisionen und Ramanstreuung für sc-SBS verloren geht. Im Falle eines vorgeformten Plasmas ist die Transmission deutlich höher. Darüber ist die Verstärkung wegen des deutlich höheren Chirp des Pumppulses hier geringer, wie auch von der Theorie her zu erwarten war.

Contents

1. Introduction

The ever growing field of interaction of laser pulses with matter is important to both fundamental and applied research. Applications range from nuclear fusion [1] and laboratory astrophysics [2] to particle acceleration [3, 4], laser amplification [5, 6], pulsed radiation sources [7], and generation of attosecond pulses [8].

Plasma densities realized for these experiments range from extremely low values in laboratory astrophysics and electron acceleration to extremely high values for laser-driven nuclear fusion. Because electrons have a lower mass than ions, the electric field of a laser pulse at a given wavelength λ (with the wavenumber $k = 2\pi/\lambda$) couples mostly to the electrons as it interacts with a plasma. The non-relativistic dispersion relation of an electromagnetic wave in a plasma is [9]

$$\omega^2 = \omega_{pe}^2 + c^2 k^2 \,, \tag{1.1}$$

with the light angular frequency ω, the speed of light in vacuum c, and the eigenfrequency of an electron oscillation in the plasma

$$\omega_{pe} = \sqrt{\frac{e^2 n_e}{\epsilon_0 m_e}} \,, \tag{1.2}$$

where e is the elementary charge, n_e is the electron density, ϵ_0 is the vacuum permittivity ϵ_0, and m_e is the electron mass. Equation (1.1) does not allow for a real k, i. e. a wave-like solution, if $\omega < \omega_{pe}$, or a density n_e higher than the critical density

$$n_c = \frac{\epsilon_0 m_e}{e^2} \left(\frac{2\pi c}{\lambda} \right)^2 \,. \tag{1.3}$$

If the laser fields are strong enough, relativistic effects in the motion of the charged particles, especially the electrons, arise. In the single-electron picture, the relativistic gamma factor is

$$\gamma := \frac{1}{\sqrt{1 - v^2/c^2}} = \sqrt{1 + \frac{p^2}{m_e^2 c^2}} \,, \tag{1.4}$$

so that the relativistic electron mass γm_e rather than its rest mass m_e is relevant for a system. The relevant density for laser-plasma interaction, the critical density of the plasma, is then $\gamma n_c > n_c$.

Therefore, the ratio $n_e/(\gamma n_c)$, the plasma electron density in terms of the critical density, determines which laser-plasma interaction effects are possible and sizable.

For an overdense (overcritical) plasma where $n_e/(\gamma n_c) > 1$, the laser cannot propagate in the medium. The pulse is in part reflected, in part absorbed at the surface where

$n_e/(\gamma n_c) = 1$. The absorption leads to electron heating (Sec. 2.2.2), which in turn can result in the formation of an electron sheath at the target surface whose electric field can accelerate ions on the target surface [10] (Sec. 2.4.1). The reflection leads to a momentum transfer to the target electrons. Once they are moved, the accompanying electrostatic field moves the target critical surface inwards by dragging the ions behind. It can accelerate them to sizable energies (hole boring acceleration, Sec. 2.4.2). If the critical surface moves faster than the speed of sound in the plasma, it can also create a shock wave. As it propagates forward, this shock wave can also reflect ions of the target material, which are initially at rest (collisionless shock acceleration, Sec. 2.4.3). These properties allow using a plasma as a particle accelerator (Sec. 1.1).

In contrast, a laser pulse is, in part, transmitted through an underdense (undercritical) plasma with $n_e/(\gamma n_c) < 1$. It is also, in part, absorbed (Sec. 2.2.1) and it can trigger parametric processes: Moving electrons, it acts on the plasma density (and refractive index) profile, which modifies the laser transmission, which in turn modifies the density profile, and so on. Therefore, these processes can be instable. Notable instabilities are Brillouin backscattering (the decay of an electromagnetic wave into another electromagnetic wave and an ion acoustic wave, Sec. 2.1.1), Raman backscattering (the decay of an electromagnetic wave into another electromagnetic wave and an electron plasma wave, Sec. 2.1.2), and filamentation (the creation of zero-frequency transverse density fluctuations, Sec. 2.1.3). Their growth can be analytically predicted for the non-relativistic (low-intensity) case, whereas for higher intensities relativistic effects can inhibit their growth. Therefore the relevant parameters are non-relativistic. Filamentation and Brillouin backscattering happen at any plasma density $n_e < n_c$, Raman backscattering only for $n_e < n_c/4$ [9]. These processes permit to use the plasma to transfer energy from one laser beam to another, thereby using it as a plasma amplifier (Sec. 2.3).

1.1. Plasma accelerators

Due to the strong electrostatic forces in a plasma, it is possible to use a laser system as a table-top accelerator for proton and ion beams [11–13]. In medicine, this technology could make hadron therapy available to a much broader population [14, 15]. This application would benefit from the much lower cost and the short pulse duration compared to a conventional particle accelerator [16]. Another, already largely exploited, application is the use of protons to probe the electric and magnetic field in a plasma. It provides a novel way to diagnose laser-generated plasmas [17–19], compared to optical and x-ray probing, as it can retrieve complementary information. Laser-generated proton beams can also be used to generate warm dense matter by isochoric heating [20]. Finally, in the context of inertial confinement fusion, the use of ion beams is discussed to make fast ignition possible [21].

The most commonly used regimes of laser-driven proton and ion acceleration are the Coulomb explosion regime [22] (at typically $5\,\%n_c$) and the target-normal sheath acceleration (TNSA) regime [23] (attained at overcritical densities, typically solid density). A major challenge for laser-based ion acceleration, however, is the high energy spread in

the accelerated particle bunches, which is difficult to mitigate in both regimes.

Novel particle acceleration schemes, such as radiation-pressure acceleration (RPA) and collisionless shock acceleration (CSA), can provide proton beams with a high repetition rate, a controllable energy spectrum, and low divergence [12]. The generation of a monoenergetic proton bunch through CSA has been first demonstrated with a carbon dioxide (CO_2) laser with a laser wavelength of 10.6 μm [24]. In this thesis, the results of an experiment are discussed that demonstrates CSA with an Nd:glass laser at a wavelength of 1054 nm (Chap. 4). Gas jet targets allow to create a plasma at a density of $n_e = 10^{21} \ldots 10^{22}\,\mathrm{cm}^{-3}$, slightly higher than the critical density for this wavelength, $10^{21}\,\mathrm{cm}^{-3}$. It is thus so high that laser pulse is stopped at the critical surface and transfers momentum to the bulk of the plasma. It is, however, still so low that the given laser momentum is sufficient for this surface to move at supersonic velocity, rather than at much lower speed as would be the case for a denser (hence, higher inertia) target. That is why this density is particularly favorable for acceleration in the CSA scheme (Sec. 2.4).

1.2. Plasma optics

For particle acceleration applications, a laser system serves as the workhorse to generate laser pulses that are used in an experiment. In contrast to this, the development of plasma optics provides a way to use laser-plasma interactions to create optics that can be used as components of a laser system [25, 26]. Such a scheme benefits from the fact that a plasma can sustain much higher intensities than a solid state amplifier[27]. The most well-known example is the plasma mirror: If a high-power pulse train is focused onto an anti-reflection coated glass slab, low-power prepulses are transmitted, but the sufficiently powerful main pulse's leading edge creates an overcritical plasma on the glass surface which reflects the remainder of the pulse. The plasma's critical surface is so flat and smooth that the reflected pulse can be collimated again. This setup is widely used as a fast optical switch [28]: Other concepts have been proposed, including photonic crystals made from a plasma to reflect high-intensity pulses on a density grating [29], laser amplification by parametric processes [30, 31], and the use of plasma mirrors as focusing devices [25]. Especially amplification by a laser is of interest because a plasma amplifier can amplify ultrashort high-intensity pulses in a scheme in which the pulse does not need to be compressed again after amplification.

Using a plasma to amplify a laser pulse has been proposed as early as in 1979 [32], but was quickly disregarded and neglected as a research topic for almost 20 years. Solid-state laser amplifiers, being much easier to implement and control, became the main technology for short-pulse laser amplification. Due to their reliability and technological simplicity, they have been the dominant laser amplification technique ever since the inception of the laser (Fig. 1.1). This did not even change when intensities approached the damage thresholds of the optics. As a workaround – in order to continue using solid-state amplifiers – the energy density is reduced by using large optics and beam diameters, and by using long chirped pulses in chirped pulse amplification (CPA) [33]

systems. As an improvement, optical parametric chirped pulse amplifiers (OPCPA)[34] have been built. Rather than generating a population inversion on certain energy transitions in the material, they use nonlinear dispersion to transfer energy from the pump to the signal (seed) pulse. They offer higher contrast and higher bandwidth, but they are still plagued by low damage thresholds as they involve solid-state optics. The weakest

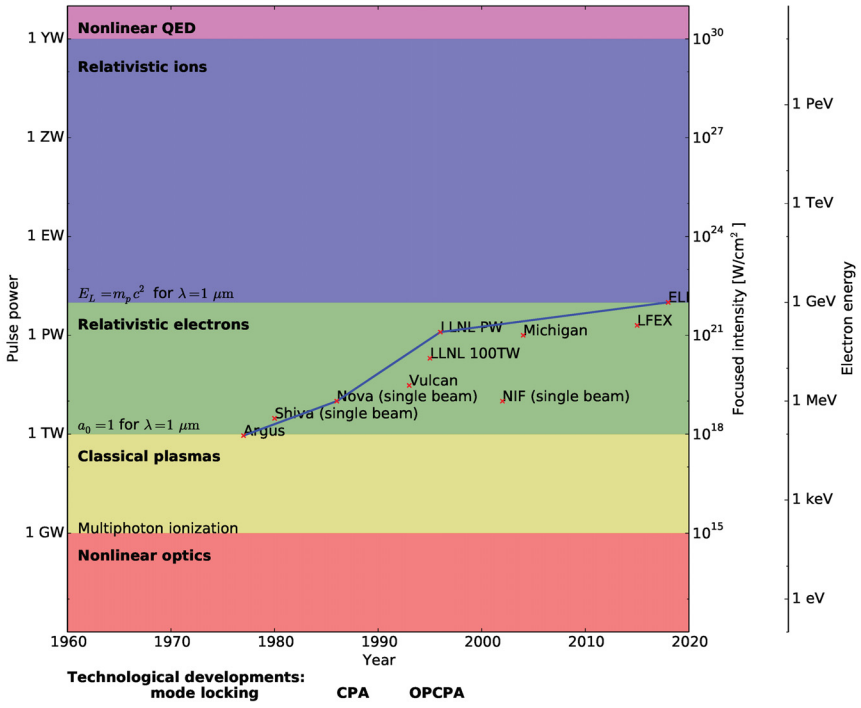

FIG. 1.1.: Evolution of high-power laser systems [35].

part in the laser chain (which is, basically, composed of oscillator, pulse picker, stretcher, amplifier, compressor) is the last grating of the compressor for the amplified pulse. Here, not only the fluence is high but also the intensity. For example, to keep the fluence below the grating damage threshold of 200 mJ/cm^2 at 30 fs [36] (corresponding to a breakdown intensity of 6×10^{12} W/cm^2) for 300 J pulses, the beam diameter has to be larger than 43 cm. This makes optics prohibitively expensive.

Therefore, a plasma's ability to amplify and compress ultrashort high-intensity pulses has come to attention again in the late 1990s [37, 38]. In the envisioned scheme [39], the plasma amplifier would be added as a last amplification stage to a CPA or OPCPA laser. It would amplify and compress pulses that are already intense and ultrashort. These amplified pulses would then be focused using a plasma mirror [25].

Even if a plasma amplifier can generate a centimeter-sized beam at an intensity of not more than 10^{18} W/cm^2, focusing it to a micrometer-sized focal spot allows to reach

an intensity of $10^{26}\,\mathrm{W/cm^2}$. This is considerably more than possible with state-of-the-art lasers, such as the APOLLON laser facility, currently under construction at LULI (Palaiseau, France), which is designed to deliver intensities of up to $2\times10^{22}\,\mathrm{W/cm^2}$ [40].

In a plasma, energy can be transferred from a moderate-intensity not too short laser pulse (pump) to a low energy ultrashort pulse (seed), which is consequently amplified [27] (Fig. 1.2). Like in a solid-state OPCPA, amplification is achieved due to a parametric process, but in a plasma as the amplifying medium. Energy is exchanged either via a plasma electron wave (stimulated Raman backscattering, SRS) [38] or via an ion acoustic wave (stimulated Brillouin backscattering, SBS) [41].

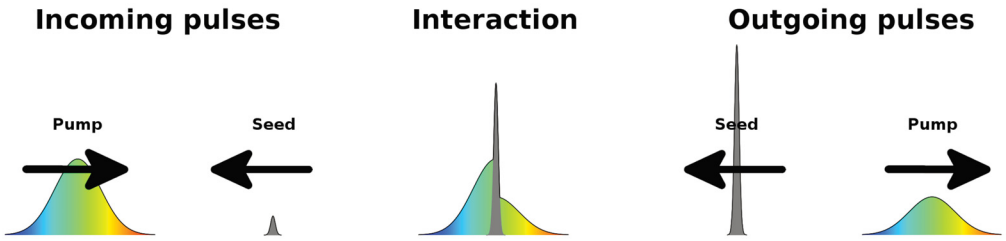

FIG. 1.2.: Concept of a plasma amplifier.

Both processes offer different growth rates for the signal under different conditions: Amplification by SRS can amplify ultrashort seed pulses down to typically 10 fs and requires plasma densities of some percent of n_c. Amplification by SBS is efficient for longer pulses (typically $>$ 100 fs), uses plasma densities around $10\,\%n_c$ and generates higher growth rates. Since this thesis deals with lasers interacting with plasmas at high but subcritical densities ($10\,\%\ldots100\,\%$ of the critical density), amplification by stimulated Brillouin backscattering is studied. A comparison of SBS and SRS amplification is given in Sec. 2.1.

Laser amplification by SRS has been studied by several workgroups in theory [37, 38, 42–45] and experiment [5, 30, 46–48]. Laser amplification by SBS has been less investigated. It was studied by the workgroups at LULI and ILPP in theory [49, 50] and was demonstrated at LULI, using an Nd:glass laser in a proof-of-principle-experiment [51].

In this thesis, it is demonstrated that SBS amplification of a subpicosecond pulse can be efficient enough to deplete the pump (Chap. 6), and that SBS amplification is possible for pulses in the range of tens of femtoseconds (Chap. 5).

1.3. Targets

Experimentally, plasmas at a given density are made by ionizing a solid, liquid, or gaseous target. Upon ionization, the plasma keeps the density profile of the target during a time window accessible for laser-plasma interaction experiments. Therefore, the density of the plasma can be chosen by ionizing a specifically designed target. In order to generate

highly underdense plasmas ($< 5\,\%n_c$), gas cell and pulsed supersonic gas jet targets are routinely used [52]. To reach high densities ($> 10\,n_c$), solid targets [13] are frequently used. Plasmas at the density range in between are less obvious to generate: Targets such as capillary ablation targets [53], foam targets [54], exploded foils [55], clustered gases [56], and liquid targets [57], are more cumbersome to use and less flexible in the design of the density profile than a gas jet. Compared to these techniques, high-pressure gas jets (see, e. g., Refs. [58–60]), as in the present work, allow for a high reproducibility and good control of the plasma density profile. Unlike for foam and ablation targets, there is no need for careful realignment after each shot. Compared to tape targets, there is a higher flexibility concerning the density profile, and the required temporal contrast is much lower. Compared to gas cells, gas jets are easily accessible for beams from all sides. Compared to cryogenic targets (clustered gases and liquids), no complicated cooling technology is needed. As for cryogenic targets, the use of high density gas jets requires a considerable vacuum pump throughput, which can be provided by differential pumping techniques [61]. As opposed to cryogenic targets, in the case of gas jets the requirement can be alleviated by reducing the repetition rate if suitable pumping is unavailable. Using high backing pressures, it is possible to create overdense targets even for near-infrared lasers, as will be shown in this thesis. They can also be used at high repetition rates, making them perfectly suitable as damageless optics: The plasma target is destroyed on each shot but a new plasma is formed in less than 100 ms using a gas jet.

1.4. Role of the author

The experiments described in the thesis at hand have done by two laser-plasma laboratories: LULI (Palaiseau, France) and ILPP (Düsseldorf, Germany). The author of the present thesis formed part of both.

Methods The experiments have been carried out at three existing laser facilities: ELFIE (Palaiseau), ARCTURUS (Düsseldorf), and TITAN (JLF, Livermore/CA, USA). The facilities (Sec. 3.1) have been developed and maintained by the scientific and technical teams in the respective institutes.

The author set up the off-line gas jet characterization described in Sec. 3.2. Using this setup, he characterized the gas targets (Sec. 3.3), except for the target for the TITAN experiment, the second target for the first ARCTURUS experiment, and the target for the ELFIE EXPERIMENT (characterized by R. Riquier using a setup at LULI).

The diagnostics (Sec. 3.4) were developed at LULI and ILPP, except for the water switch contrast measurement, which was set up and done by the JLF technical team. The magnetic field measurement of the magnetic spectrometer was done by H.-P. Schlenvoigt.

Proton acceleration experiment The experiment on proton acceleration (Chap. 4) was done by the authors of the article (CHEN et al. [62], No. 4 on the list in appendix A). The author fielded and calibrated the magnetic proton spectrometers. He measured the proton spectra.

SBS experiments at ARCTURUS The author conceived and prepared, in part, the setup of the experiments (Chap. 5), especially the configuration of the targets and diagnostics used in these experiments. The beam setup was conceived by M. Blecher. Shots and data acquisition were done by an experimental workgroup including B. Aurand, M. Blecher, S. Bolaños, M. Cerchez, J. Fuchs, L. Lancia, J.-R. Marquès, R. Prasad, and the author. The latter evaluated all the data of the experiment I and most of experiment II. A part of the data analysis and calibration of the spectrometers was done by M. Blecher and S. Bolanos. The data interpretation was done by M. Blecher, S. Bolanos, J. Fuchs, and the author. The plasma temperature calculation was done by the author for experiment I. The plasma temperature simulation for the second experiment was done by P. Loiseau. The calculation on the chirp influence in Sec. 5.5 was done by J.-R. Marquès with the envelope code written by M. Chiaramello [63].

SBS experiment at ELFIE This experiment (Chap. 6) was conceived, carried out, and evaluated by the authors of the article (Lancia et al. [6], No. 2 on the list in appendix A). The author participated in the data analysis of this experiment (transverse interferometry).

2. Laser-plasma interaction with gaseous targets

As mentioned in Sec. 1.3, gaseous targets can be both overdense or underdense for lasers in the near infrared (e. g., 800 nm or 1053 nm).

The laser field amplitude can be specified by the amplitude of the normalized vector potential (also called laser field strength parameter)

$$a_0 = \frac{\lambda e \mathcal{E}}{2\pi m_e c^2}\,, \tag{2.1}$$

where e is the electron charge, $\mathcal{E}$ is the electric field, m_e is the electron mass, λ is the angular frequency of the laser field, and c is the speed of light in vacuum. In practical units, it is

$$a_0 = 8.5 \times 10^{-5} \sqrt{\frac{I}{10^{16}\,\mathrm{W/cm^2}}}\,\frac{\lambda}{1\,\mathrm{nm}}\,. \tag{2.2}$$

Due to the low electron inertia, the laser field couples mostly to the electrons. In an overdense plasma, this happens only at the critical surface where the pulse is in part reflected, in part absorbed. In an underdense plasma, it happens in the target as the laser traverses it. Generally, this motion is relativistic. In the single-electron picture, the relativistic gamma factor is

$$\gamma := \frac{1}{\sqrt{1 - v^2/c^2}} = \sqrt{1 + \frac{p^2}{m_e^2 c^2}}\,, \tag{2.3}$$

and can be averaged over a laser cycle [64]

$$\bar{\gamma} = \sqrt{1 + \frac{a_0^2}{2}}\,. \tag{2.4}$$

The average energy of the electron in this quiver motion is referred to as the ponderomotive potential [64]:

$$E_{pond} = m_e c^2 \left(\bar{\gamma} - 1\right) = m_e c^2 \left(\sqrt{1 + \frac{a_0^2}{2}} - 1\right)\,. \tag{2.5}$$

This potential gives rise to the ponderomotive force

$$F_{pond} := -\nabla E_{pond}\,. \tag{2.6}$$

If $a_0 \ll 1$, or $m_e c^2 \ll \lambda e \mathcal{E}$, the electron motion is nonrelativistic. Then, the ponderomotive potential is

$$E_{pond,NR} = a_0^2 m_e c^2/4 = \frac{1}{2cn_c} I \,, \tag{2.7}$$

where $I := c\epsilon_0 \mathcal{E}^2/2$ is the laser intensity, and ϵ_0 is the vacuum permittivity. Therefore, the ponderomotive force in the nonrelativistic limit is proportional to the light intensity: Electrons are pushed away from zones of high intensity. This can be understood as a light pressure (or radiation pressure) acting on the plasma, i. e. the gradient of the electromagnetic energy density [65]. It leads to a secular movement mostly of the electrons, due to their lower inertia [66].

This can lead to the excitation of plasma waves, which in turn can transfer energy into scattered light. Thus in an underdense plasma, a laser beam undergoes parametric instabilities, which do not involve absorption by themselves (Sec. 2.1). They both affect the laser beam and the plasma density profile, and they can generate radiation at other wavelengths than the laser wavelength. They include spontaneous and stimulated Brillouin (Sec. 2.1.1) and Raman (Sec. 2.1.2) backscattering, which both can be used for laser amplification in a plasma (Sec. 2.3).

Additionally, energy is converted to heat upon interaction with the target. This increases the plasma electron and ion temperatures (Sec. 2.2). Absorption processes differ in whether the pulse can enter the plasma: If so, the pulse moves electrons the bulk of the target is heated, mainly via electron-ion collisions (Sec. 2.2.2). Otherwise, it is reflected at the critical surface and absorption happens only there (Sec. 2.2.2).

Both heating and light pressure can lead to ion acceleration. Depending on laser and target parameters, sufficiently strong fields can be generated by hot electrons at a plasma surface (Target Normal Sheath Acceleration, [TNSA] Sec. 2.4.1), by the charge displacement caused by the radiation pressure (Radiation Pressure Acceleration [RPA] and Hole Boring Acceleration [HBA], Sec. 2.4.2), by a collisionless shock (Collisionless Shock Acceleration [CSA], Sec. 2.4.3), or by an expanding magnetic field close to the laser axis when the pulse leaves an underdense target (Magnetic Vortex Acceleration [MVA], Sec. 2.4.4).

The parameter regimes for both sc-SBS amplification (Sec. 2.3) and CSA acceleration (Sec. 2.4.3) are discussed. Prior results are reviewed.

2.1. Parametric instabilities

When neglecting kinetic effects, a cold plasma can be described with the fluid equations, i. e. continuity equations for each species,

$$\frac{\partial}{\partial t} n_a + \nabla \cdot (n_a \mathbf{u}_a) = 0 \,, \tag{2.8}$$

where the index a refers to the species. Also, the momentum is conserved:

$$m_a n_a \left(\frac{\partial}{\partial t} \mathbf{u}_a + \mathbf{u}_a \cdot \nabla \mathbf{u}_a \right) = q_a n_a \left(\boldsymbol{\mathcal{E}} + \mathbf{u}_a \times \frac{\mathbf{B}}{c} \right) - \nabla p_a \,. \tag{2.9}$$

To obtain a closed system of equations, an equation for the pressure dependence on density and temperature (equation of state) is necessary. For processes whose phase velocity is low compared to the particles' thermal velocity, an isothermal equation of state holds:

$$p_a = n_a T_a \,, \tag{2.10}$$

whereas for fast processes (that spread much faster than the thermal velocity), the adiabatic equation of state holds

$$\frac{p_a}{n_a^\kappa} = \text{constant} \,, \tag{2.11}$$

with $\kappa = (2+N)/N$ as the adiabatic index, defined via the number of degrees of freedom N. For waves in plasmas, usually the isothermal ($\kappa = 1$) or adiabatic equation of state has to be used. If not otherwise stated, the adiabatic equation of state is used below. The electromagnetic wave is described by Maxwell's equations. Especially, the electrostatic potential Φ is given by the Poisson equation

$$\Delta\Phi = -4\pi e(n_i - n_e) \,. \tag{2.12}$$

A laser pulse propagating in an underdense plasma interacts with it also by other processes than heating. These processes – referred to as parametric processes – do not involve absorption, i. e. they leave the plasma temperatures unchanged. Rather, they act on the density. A globally homogeneous plasma's density profile is modified by the ponderomotive force, which pushes electrons away from high density zones. This can induce an ion acoustic wave or a Langmuir wave in the plasma, on which energy is then scattered into another plasma wave or electromagnetic wave. The scattered waves then affect the plasma density. Therefore, parametric instabilities can be described by a feedback loop model that includes the waves' electric fields and the density perturbation [9]). The processes relevant for this thesis are Stimulated Brillouin Scattering (Sec. 2.1.1), Stimulated Raman Scattering (Sec. 2.1.2), and filamentation (Sec. 2.1.3).

2.1.1. Stimulated Brillouin Backscattering (SBS)

Stimulated Brillouin Backscattering is the parametric decay of an incoming electromagnetic wave into an ion acoustic wave and a counterpropagating scattered electromagnetic wave. The energy and momentum conservation equations are

$$\omega_0 = \omega_1 + \omega_2 \,, \tag{2.13}$$

and

$$\mathbf{k}_0 = \mathbf{k}_1 + \mathbf{k}_2 \,, \tag{2.14}$$

where ω are angular frequencies, $\mathbf{k}$ are wavenumber vectors, indices 0, 1, 2, refer to pump, seed, and plasma wave, respectively.

It should be noted that the Brillouin instability can both grow from noise (spontaneous Brillouin scattering) and from an injected seed pulse (stimulated Brillouin scattering).

The mechanism of both is principally the same. In the amplifier concept (Sec. 1.2), the seed pulse is the signal (laser pulse) that is to be amplified. Similar to this process, there are also Brillouin forward and side scattering. Their growth rates are lower than for backscattering [9]. Therefore, they are not as suitable for amplification and disregarded here.

Three-wave model

In the context of SBS amplification, laser intensities are typically kept low to avoid relativistic effects, i. e. the amplitudes of the normalized vector potential of both beams are $a_0 < 0.1$. This prevents the plasma wave from being destroyed by relativistic wave breaking [64]. Kinetic effects are not strongly influencing the process. In this case, an analytical three-wave model can be used to gain insight into the amplification process.

The following definitions are used: Normalized vector potentials are named $\mathbf{A}$, electric fields $\mathcal{E}$, cgs units are used.

The dispersion relation for SBS in one dimension (plane-wave solution) can be derived [9] analytically under the following assumptions:

- The pump laser interacts with a plasma of initially uniform density and temperature.
- Electrons and ions are treated as warm fluids. Collisions, kinetic effects, and relativistic effects are neglected.
- The electron response is much faster than the ion response. The ion acoustic wave frequency is low compared to the laser.
- The electric fields are treated with a slowly varying envelope approximation. The lasers have linear parallel polarization, and the geometry is 1D (plane waves).

By convention, we choose the pump to move in positive z direction, and the seed is counterpropagating. The amplitudes and phases for pump, seed, and plasma wave are defined by $\mathcal{E}_0 = 1/2\{\hat{\mathcal{E}}_0 \exp[-i(-k_{0,vac}z+\omega_0 t)] + \text{c.c.}\}$, $\mathcal{E}_1 = 1/2\{\hat{\mathcal{E}}_1 \exp[-i(k_{1,vac}z+\omega_1 t)] + \text{c.c.}\}$, and $n = 1/2\{\hat{n} \exp[i(k_2 z - \omega_2 t)] + c.c.\}$. Here, *c.c.* is the complex conjugate, $k_{0|1,vac}$ are the vacuum wave vectors, and $k_{0|1}$ are the wave vectors in plasma for pump and seed, respectively. The plasma wave amplitude can be normalized to the background density n_0 by defining $N := \hat{n}/n_0$.

The three-wave equations for Brillouin backscattering are then:

$$\left(\frac{\partial}{\partial t} + v_0^g \frac{\partial}{\partial z}\right) \hat{\mathcal{E}}_0 = -i\frac{\omega_{pe}^2}{4\omega_0} N \hat{\mathcal{E}}_1 e^{i[(k_1-k_0)z-(\omega_1-\omega_0)t]} \tag{2.15}$$

$$\left(\frac{\partial}{\partial t} - v_1^g \frac{\partial}{\partial z}\right) \hat{\mathcal{E}}_1 = -i\frac{\omega_{pe}^2}{4\omega_1} N^* \hat{\mathcal{E}}_0 e^{i[(k_0-k_1)z-(\omega_0-\omega_1)t]} \tag{2.16}$$

$$\left(\frac{\partial^2}{\partial t^2} - c_s^2 \frac{\partial^2}{\partial z^2}\right) N = -\frac{Ze^2(k_0+k_1)^2}{2\omega_0\omega_1 m_e m_i} \hat{\mathcal{E}}_0 \hat{\mathcal{E}}_1^* e^{i[(k_0+k_1)z-(\omega_0-\omega_1)t]} \tag{2.17}$$

Pump and seed (envelopes $\hat{\mathcal{E}}_0$ and $\hat{\mathcal{E}}_1$, respectively) travel with group velocities $v_{0,1}^g = k_{0,1}c^2/\omega_{0,1}$. The speed of light in vacuum is denoted by c. The IAW propagates with the ion sound velocity $c_s = \sqrt{ZT_e/m_i}$. $\omega_{pe} = \sqrt{4\pi n_e e^2/m_e}$ is the plasma electron frequency. Z is the charge state. T_e is the electron temperature. m_e and m_i are electron and ion masses, respectively [67].

A dispersion relation for backscattering is derived by inserting the wave ansatz mentioned above into Eqs. (2.16) and (2.17) and carrying out the derivatives. Then the dispersion relation follows [9]:

$$\left(\omega_2^2 - k_2^2 c_s^2\right)\left(\omega_2^2 - 2\omega_2\omega_0 + 2k_0k_2c^2 - k_2^2c^2\right) = \frac{k_2^2 a_0^2 c^2}{4}\omega_{pi}^2\,. \tag{2.18}$$

Here $\omega_{pi} := \sqrt{4\pi n_i Z^2 e^2/m_i} = \omega_{pe}\sqrt{Zm_e/m_i}$ is the plasma ion frequency.

Weak coupling (wc) regime

For low pump intensities (albeit sufficiently high to overcome collisional and Landau damping), the pump wave does not greatly change the dispersion relation of the plasma wave, i. e. the ion acoustic wave is resonant,

$$\omega_2^{wc} = \pm k_2 c_s + i\gamma_2^{wc}\,, \tag{2.19}$$

where $c_s := \sqrt{(ZT_e + 3T_i)/m_i}$ is the ion sound velocity. Assuming an undepleted pump ($\hat{\mathcal{E}}_0$ is constant), the growth of both ion wave and seed is exponential (i. e. $\propto e^{\gamma_2^{wc}t}$ and the growth rate $\gamma_2^{wc} \ll kc_s$ is given by [9]

$$\gamma_2^{wc} = \frac{1}{2\sqrt{2}}\frac{k_{0,vac}a_0 c\omega_{pi}}{\sqrt{\omega_0 k_{0,vac}c_s}}\,. \tag{2.20}$$

This regime is referred to as weakly coupled SBS (wc-SBS) [9]. The plasma response timescale is determined by the ion acoustic wave frequency. For Hydrogen with $n_e/n_c = 0.1$ and a laser wavelength of 800 nm, for example, it is $1/\gamma_2^{wc} \approx 5$ ps. Therefore, the regime of weak coupling is not suitable for the amplification of subpicosecond pulses. In contrast, wc-SBS is an important topic in the context of inertial confinement fusion (ICF). Due to the lower intensities in the beams of the driver, energy is transferred by wc-SBS there [68]. Recently, energy transfer from a nanosecond pulse to a picosecond pulse by wc-SBS was observed [69]. Also, energy transfer from several nanosecond pump pulses to a nanosecond seed pulse was observed [70].

Strong coupling (sc) regime

The regime of strong coupling is reached when the pump pulse intensity is so high that it determines the plasma response. The threshold condition for strong coupling is [71]

$$\left(\frac{a_0 c}{v_e}\right)^2 > 4k_{0,vac}c_s\frac{\omega_0}{\omega_{pe}^2}\,, \tag{2.21}$$

with the electron thermal velocity $v_e = \sqrt{T_e/m_e}$. In practical units, this is

$$I_{14}\lambda_{\mu m}^2 > 1.1 \times 10^{-1} T_{keV}^{\frac{3}{2}} \left(\frac{Z}{A}\right)^{\frac{1}{2}} \frac{n_c}{n_e} \left(1 - \frac{n_e}{n_c}\right)^{\frac{1}{2}} \tag{2.22}$$

where I_{14} is the pump intensity in $10^{14}\,\mathrm{W/cm^2}$, $\lambda_{\mu m}$ is the vacuum pump wavelength in micrometers, T_{keV} is the plasma electron temperature in keV, Z is the charge state, and $A = m_i/m_p$ is the mass number (the ion mass in units of the proton mass m_p). The plasma wave is thus more strongly coupled to the pump laser for high pump intensity, high wavelength, low plasma electron temperature, and high density. For example, for a Hydrogen plasma with $T_e = 300\,\mathrm{eV}$ and $n_e = 10\,\%n_c$, the minimum pump intensity would be $2\times10^{13}\,\mathrm{W/cm^2}$ for an Nd:glass laser such as the ELFIE laser facility (Sec. 3.1.3) where $\lambda = 1057\,\mathrm{nm}$.

Concerning the temperature, there is a trade-off between the limit for strong coupling [Eq. (2.22)] and collisional absorption in the plasma. If the plasma is too cold, pump and seed are too much attenuated. For example, for a Hydrogen ($Z = A = 1$) plasma at $n_e/n_c = 10\,\%$, the electron temperature should be around or higher than $T_e = 300\,\mathrm{eV}$, to avoid too much absorption of the laser pulse (see Sec. 2.2.1 below). For these plasma parameters, the minimum intensity for strong coupling [Eq. (2.22)] is $I = 2\times10^{13}\,\mathrm{W/cm^2}$ at a wavelength of 1057 nm. This can be easily reached, thus the temperature is not per se a concern for sc-SBS.

During the interaction, it is both possible that the pump pulse transfers energy into the seed pulse, and that the opposite happens. The increase or decrease of the pump and seed electric field amplitudes $\hat{\mathcal{E}}_0$ and $\hat{\mathcal{E}}_1$ can be determined from the three-wave equations Eqs. (2.15) to (2.17). It is assumed that pump, seed, and plasma wave are in resonance, and that initially the pump phase ϕ_0 and seed phase ϕ_1 are equal to zero. Furthermore, the plasma density is unperturbed in the beginning ($N = 0$), and the plasma wave phase ϕ_2 is equal to π. Then, one obtains

$$\left(\frac{\partial}{\partial t} + v_0^g \frac{\partial}{\partial z}\right) \hat{\mathcal{E}}_0 = -\mu N \hat{\mathcal{E}}_1 \sin\theta \tag{2.23}$$

$$\left(\frac{\partial}{\partial t} + v_0^g \frac{\partial}{\partial z}\right) \phi_0 = -\mu N \frac{\hat{\mathcal{E}}_1}{\hat{\mathcal{E}}_0} \cos\theta \tag{2.24}$$

$$\left(\frac{\partial}{\partial t} - v_1^g \frac{\partial}{\partial z}\right) \hat{\mathcal{E}}_1 = \mu N \hat{\mathcal{E}}_0 \sin\theta \tag{2.25}$$

$$\left(\frac{\partial}{\partial t} - v_1^g \frac{\partial}{\partial z}\right) \phi_1 = -\mu N \frac{\hat{\mathcal{E}}_0}{\hat{\mathcal{E}}_1} \cos\theta \tag{2.26}$$

$$\frac{\partial^2 N}{\partial t^2} - N\left(\frac{\partial}{\partial t}\phi_2^2\right) - c_s^2\left(\frac{\partial^2 N}{\partial z^2} - N\left(\frac{\partial}{\partial z}\phi_2^2\right)\right) = -\Lambda \hat{\mathcal{E}}_0 \hat{\mathcal{E}}_1 \cos\theta \tag{2.27}$$

$$N\frac{\partial^2\phi_2}{\partial t^2} - c_s^2 N\frac{\partial^2\phi_2}{\partial z^2} + 2\frac{\partial}{\partial t}N\frac{\partial}{\partial t}\phi_2 - 2c_s^2\frac{\partial}{\partial t}N\frac{\partial}{\partial t}\phi_2 = -\Lambda \hat{\mathcal{E}}_0 \hat{\mathcal{E}}_1 \sin\theta \tag{2.28}$$

where one defined the coupling factor for the fields

$$\mu := \frac{\omega_{pe}^2}{2\omega_0}\,, \tag{2.29}$$

the coupling factor for the density perturbation,

$$\Lambda := \frac{2Ze^2}{m_e m_i c^2}\,, \tag{2.30}$$

and the total phase,

$$\theta := \phi_0 - \phi_1 - \phi_2 + \phi_{ch}\,. \tag{2.31}$$

Here, the phase ϕ_{ch} refers to the phase induced by the fact that in general, the pump pulse is chirped. This means that starting from best compression (bandwidth-limited pulse duration), the compressor grating spacing is changed so that the pulse is longer, with either the higher frequencies (down-chirp / blue first) or lower (up-chirp / red first) frequencies coming first. This adds a term $\phi(z,t) = \alpha(k_0(z-z_0) - \omega_0(t-t_0))^2$ to the pump phase, where z_0 and t_0 are constants defining the point where the pump frequency is equal to the nominal frequency ω_0. The time-dependent frequency is then $\omega(z,t) = \omega_0 - \partial\phi(z,t)/\partial t = \omega_0 + 2\alpha(k_0(z-z_0) - \omega_0(t-t_0))$. The chirp factor is related to the bandwidth-limited duration τ_0 and the stretched pulse duration τ_{ch} by

$$\alpha = \frac{1}{2\tau_{ch}\tau_0\omega_0^2}\sqrt{1-\frac{\tau_0^2}{\tau_{ch}^2}} \approx \frac{1}{2\omega^2\tau_0\tau_{ch}}\,, \tag{2.32}$$

where the approximation holds for $\tau_{ch} \gg \tau$ [72].

Growth regimes of strongly coupled SBS

Amplification can be described as a three-stage process [63]: First, only the seed amplitude and phase vary but not that of the pump (startup stage). Secondly, the pump phase varies, and the seed is further amplified without depleting the pump yet. Its electric field grows exponentially (linear phase). Then, once the pump amplitude reduces significantly, amplification changes qualitatively, yielding to a power-law growth (self-similar stage).

1. Startup stage Energy is transferred from the pump to the seed. The pump is not significantly depleted. The total phase grows proportional to $\gamma_{sc}^3 t^3$ [63].

2. Linear stage: Exponential growth For an undepleted pump, the seed phase grows linearly ($\propto t$) [63], and its intensity increases exponentially (small-signal-amplification) [41]:

$$I_1(t) = I_{1,0}\exp\left(2\gamma_2^{sc}t^{\frac{2}{3}}\left(\frac{L}{v_0^g}\right)^{\frac{1}{3}}\right)\,, \tag{2.33}$$

with the initial intensity $I_{1,0}$, the plasma length L, and the group velocity v_0^g. The typical time involved is $t = L/v_0^g$.

Under these conditions, the complex frequency of the ion acoustic wave [71] is

$$\omega_2^{sc} = \frac{1+i\sqrt{3}}{2}\left(k_{0,vac}^2 v_0^2 \frac{\omega_{pi}^2}{\omega_0}\right)^{\frac{1}{3}} . \tag{2.34}$$

In practical units, it is

$$\frac{\omega_{sc}}{\omega_0} = 3.68 \times 10^{-3}(1+i\sqrt{3})\left[\frac{Z}{A}\frac{n_e}{n_c}\left(1-\frac{n_e}{n_c}\right) I_{15}\lambda_{\mu m}^2\right]^{1/3} \tag{2.35}$$

Thus, sc-SBS has a growth rate of

$$\gamma_2^{sc} = \Im(\omega_2^{sc}) . \tag{2.36}$$

For example, for a $10^{15}\,\mathrm{W/cm^2}$ pulse from a Ti:sapphire laser propagating in a $10\,\%\,n_c$ Hydrogen target, the real part is $\Re(\omega_{sc}/\omega_0) = 0.003$, comparable to the plasma ion frequency $\omega_{pi}/\omega_0 = 0.007$ under the same conditions. Under these conditions, the characteristic growth time is $1/\gamma_2^{sc} = 173\,\mathrm{fs}$, and the growth occurs on a characteristic length of $c/\gamma_2^{sc} = 52\,\mu\mathrm{m}$.

According to Eq. (2.13), the frequency of the backscattered wave is downshifted with respect to the pump. This corresponds to an upshift of the vacuum wavelength of the seed, as could be measured on a spectrometer, which is

$$\lambda_{1,vac} - \lambda_{0,vac} = \lambda_{0,vac}\frac{\omega_{sc}}{\omega_0} . \tag{2.37}$$

For example, the parameters above ($10^{15}\,\mathrm{W/cm^2}$ Ti:sapphire pulse, $10\,\%\,n_c$ Hydrogen plasma), the shift would be 1.1 nm, which is small compared to the spectral width of the laser, which is typically in the range of tens of nanometers.

For backscattering in both the weak and the strong coupling regime, the plasma wavevector is

$$k_2 = 2k_0 - \frac{2\omega_0}{c}\frac{c_s}{c} . \tag{2.38}$$

The frequency red-shift of the seed $\Re(\omega_2^{sc})$ has the same amplitude as the growth: Whenever the growth rate is high, the seed is also more red-shifted. This is the case for a high pump intensity, a high pump wavelength, and a density close to $0.5\,n_c$. High growth rates are also obtained with a high Z/A, i. e. for full ionization. The growth rate is independent from the temperature, which adds to the robustness of the process.

3. Pump depletion stage: Self-similar growth Once the seed growth leads to saturation of the pump, the above analytic theory does not fully explain amplification because it was developed using the undepleted pump approximation. However, it is possible to demonstrate some properties of the solution analytically. In a comoving frame of reference (coordinates $\zeta := x + t$ and $\tau := -x$), its electric field has the form

$E_{\text{seed}}(\zeta, \tau) = \tau^{3/4} A(\zeta\sqrt{\tau})$. Thus, the seed electric field amplitude grows as a power law, and the duration of the seed diminishes because the pulse form A depends on $\zeta\sqrt{\tau}$, rather than on ζ or τ separately. Functions with this kind of scaling are called self-similar. Compression in time leads forcibly to spectral broadening [41, 67].

Vlasov simulations [67] show that the exponent of 3/4 only holds for very short seed pulses (pulse duration typically $\tau_s < 0.25\gamma_{sc}^{-1}$). For longer seed pulses, growth is still self-similar but the exponent is lower: For $\tau_s = \gamma_{sc}^{-1}$, for example, the exponent is 1/2 [67]. The spectral broadening is asymmetric [73, 74] and cannot be predicted analytically.

Since efficient amplification, by definition, is characterized by a high fraction of the pump energy transferred into the seed, the self-similar regime has to be reached for amplification to be efficient.

2.1.2. Stimulated Raman Backscattering (SRS)

Stimulated Raman backscattering (SRS) is a quite similar process compared to SBS: Again, an electromagnetic wave decays into a plasma wave and a backscattered electromagnetic wave. Therefore, it is also extensively under investigation as an amplification technique. The difference to SBS is that for SRS, the plasma wave is a Langmuir wave. As for Brillouin backscattering, the basic mechanism is the same for seeded (SRS) and spontaneous (RBS) scattering.

The resonance conditions are

$$\omega_0 = \omega_1 + \omega_2 \,, \tag{2.39}$$

and

$$\mathbf{k}_0 = \mathbf{k}_1 + \mathbf{k}_2 \,, \tag{2.40}$$

where the plasma wave (ω_2, k_2) is a plasma electron wave. For SRS, the plasma wave frequency, referred to as the Gross-Bohm frequency, is given by the plasma electron frequency plus a small thermal correction [9],

$$\omega_2^2 = \omega_{pe}^2 + 3k_2^2 v_e^2 \approx \omega_{pe}^2 \,, \tag{2.41}$$

with the thermal electron velocity $v_e = \sqrt{T_e/m_e}$ [75].

In addition to the relevance of SRS as an amplification technique, spontaneous Raman Backscattering of the pump (growing from noise) is relevant to both SRS and SBS amplification as a concurrent process (see also Sec. 2.3.1). In all of these experiments, Raman backscattering happens only in the weak coupling regime as its strong coupling regime is only attained for very low densities [71], i. e.

$$a_0 > 3\left(\frac{n_e}{n_c}\right)^{1/4} \,, \tag{2.42}$$

corresponding, e. g., for a laser with an intensity of $1 \times 10^{16}\,\mathrm{W/cm^2}$ at a wavelength of 800 nm, to $n_e/n_c = 1 \times 10^{-7}$, thus happening only in the outermost parts of the gas jet target on a negligibly small length. Even if one were to focus the pump pulse to relativistic intensities (e. g. $a_0 = 1$), strongly coupled SRS would just happen at

$n_e < 1\,\% n_c$. At that intensity, relativistic wave breaking would make the energy transfer from pump to seed much more difficult anyway. Therefore, for the parameters relevant in the amplification context, SRS is always weakly coupled. In this property, it is quite different to SBS.

As, of course, the plasma has to be undercritical for both electromagnetic waves, it follows from Eq. (2.39) that $\omega_1 > \omega_2 \approx \omega_{pe}$, so that $\omega_0 > 2\omega_{pe}$ or $n_e < 0.25 n_c$: SRS happens only in less than quarter-critical plasmas.

For a linearly polarized incoming pulse, some analytical relations can be derived under some simplifying assumptions [9]: One considers a small amplitude fluctuation on a homogeneous density, caused by a nonrelativistic electromagnetic wave. The ions are treated as a fixed neutralizing background and the electrons as a warm fluid, characterized by the absence of collisions and kinetic effects as well as an adiabatic equation of state. For backscattering or sidescattering, it then follows (Kruer 1988 [9], p. 78) that:

$$(\omega_{ek} - \omega_0)^2 - (\mathbf{k_2} - \mathbf{k_0})^2 c^2 - \omega_{pe}^2 = 0 \tag{2.43}$$

Since for the seed wavevector, ${\mathbf{k_1}}^2 = (\mathbf{k_2} - \mathbf{k_0})^2$, and using $\omega_{ek} \approx \omega_{pe}$ and $\omega_0^2 = k_0^2 c^2 + \omega_{pe}^2$, one can derive an expression for the wavelength of the scattered electromagnetic wave,

$$\frac{\lambda_1}{\lambda_0} = \frac{k_0}{k_1} = \sqrt{\frac{1 - n_e/n_c}{1 - 2\sqrt{n_e/n_c}}}\,, \tag{2.44}$$

which is valid for both sidescattering and backscattering.

More specifically, for pure backscattering $\mathbf{k_0} \parallel \mathbf{k_2}$, and from Eq. (2.43) the rate for the growth at the Stokes frequency is:

$$\gamma = \frac{k_2\, v_o}{4} \sqrt{\frac{\omega_{pe}^2}{\omega_2(\omega_0 - \omega_2)}}\,, \tag{2.45}$$

where v_o is the electron quiver velocity in the electric field of the pump.

Approximating, as above, $\omega_2 \approx \omega_{pe}$ and $\omega_2 \ll \omega_0$:

$$\gamma = \frac{k_2\, v_o}{4} \sqrt{\frac{\omega_{pe}}{\omega_0}}\,. \tag{2.46}$$

In practical units, then

$$\frac{\gamma}{\omega_0} = 4.3 \times 10^{-3} \sqrt{I_{14} \lambda_{\mu m}^2} \left(\frac{n_e}{n_c}\right)^{1/4} \tag{2.47}$$

In experiments that aim at amplifying seed pulses by SRS [76], typical parameters are, for example, Ti:sapphire laser pulses focused to intensities on the order of $10^{19}\,\mathrm{W/cm^2}$ propagating in a plasma with a density $n_e = 2\,\% n_c$. Then, $\gamma/\omega_0 = 0.4$, corresponding to a characteristic time for SRS growth of 1 fs, and a characteristic length of 300 nm. In the parameter range optimal for SBS amplification experiments, i. e. $10^{15}\,\mathrm{W/cm^2}$ and a

density of $n_e = 2\,\%\,n_c$, the growth rate is $\gamma/\omega_0 = 0.006$, corresponding to a characteristic time for SRS growth of 70 fs, and a characteristic length of 20 μm.

The wave number of the plasma electron wave is then

$$k_2 = k_0 + \frac{\omega_0}{c}\left(1 - \frac{2\omega_{pe}}{\omega_0}\right)^{1/2}, \tag{2.48}$$

between $k_3 = 2k_0$ for low density, which is typical for SRS amplification experiments, and $k_2 = k_0$ for $n_e = 0.25 n_c$.

In the context of plasma amplification, both by sc-SBS and SRS, spontaneous Raman backscattering can be detrimental because the pump is depleted before transferring energy into the seed. For an SBS experiment, the pump beam (for example with an intensity of $1 \times 10^{16}\,\mathrm{W/cm^2}$ at a wavelength of 800 nm) would exhibit Raman backscattering with a characteristic timescale of $1/\gamma = 20$ fs corresponding to a characteristic length of 6 μm. Therefore, the pump exhibits a strong Raman backscattering. Since the only parameters that influence this growth rate are intensity and plasma electron density, which both have to be sufficiently high for SBS to be in the strong coupling regime, the concurrent Raman backscattering has to be accepted. For the seed, however, due to its lower intensity ($1 \times 10^{13}\,\mathrm{W/cm^2}$), Raman backscattering is much lower: The timescale $1/\gamma = 700$ fs is higher than the pulse duration. To avoid this, two solutions have been proposed: taking advantage of the chirp of the laser [43, 74] and using a ramp-like plasma electron density profile [42, 49].

2.1.3. Filamentation

Filamentation is the development of zero-frequency transverse density fluctuations. It has the same dispersion relation as SBS [9]. Starting from a small inhomogeneity in density or intensity, the laser is refracted into the density depression, lowers the density there more, and is further refracted. This can lead to either self-focusing of the whole beam or to the breakup into filaments. Both refer to the same physical process.

The laser pulse can lower the plasma density by either a thermal, ponderomotive, or relativistic mechanism. Ponderomotive effects dominate over thermal effects if the laser intensity follows the condition,

$$I_{14}\lambda_{\mu m}^2 > 2 \times 10^{-4}\left(1 + \frac{3T_i}{ZT_e}\right)^2 \frac{n_e}{n_c}\frac{Z}{\lambda_{\mu m}^2 T_e^3}\left(\ln \Lambda_{ei}\right)^2 \tag{2.49}$$

where T_e is given in kiloelectronvolts and the laser wavelength in micrometers, and the intensity is the local intensity taking into account absorption by inverse bremsstrahlung and refraction in the plasma [77].

For Hydrogen with $T_i \ll T_e = 300$ eV and $n_e = 0.2\,n_c$, the Coulomb logarithm is $ln\Lambda \approx 6$. For $\lambda = 800$ nm, filamentation is thus dominated by ponderomotive effects if the intensity is above $I \approx 10^{13}\,\mathrm{W/cm^2}$.

Relativistic self-focusing effects become sizable when relativistic self-focusing dominates over diffraction [64], i. e. when the laser power

$$P_L > 17.5\,\mathrm{GW}\,\frac{n_c}{n_e}\,, \tag{2.50}$$

which is the case for a pulse energy $E_L > 300\,\mathrm{mJ}$ at 3 ps duration. Since the laser pulse is also attenuated by inverse bremsstrahlung, filamentation is more due to ponderomotive effects than relativistic effects for energies in the range of hundreds of millijoules.

The ponderomotive filamentation growth rate for this regime (short, weakly relativistic pulses) is given by

$$\frac{\gamma_{fil}}{\omega_0} = \frac{1}{8}a_0^2\frac{n_e}{n_c}\,, \tag{2.51}$$

where a_0 and ω_0 are the amplitude of the normalized vector potential and frequency of the incoming beam, respectively [78]. In practical units, it is

$$\frac{\gamma_{fil}}{\omega_0} = 10^{-5} I_{14}\lambda_{\mu m}^2\frac{n_e}{n_c} \tag{2.52}$$

For filamentation to happen, the transmitted pulse must be longer than the timescale $\tau_{fil} = 1/\gamma_{fil}$. For instance, a pulse with an intensity of $10^{16}\,\mathrm{W/cm^2}$ at a wavelength of 800 nm begins to filament in a $n_e = 0.1\,n_c$ plasma after $\tau_{fil} = 7\,\mathrm{ps}$.

2.2. Absorption of a laser pulse in a plasma

As will be detailed below, the electron motion is dissipative, so that the laser pulse is damped. This phenomenon is also known as absorption and happens in the bulk (for underdense plasmas) or at the critical surface (for overdense plasmas). The mean velocity of the oscillating electron is $v_o = a_0 c/\sqrt{2}$. This holds for circular polarization. For a linearly polarized laser field, $v_o = a_0 c$. In the ultra-relativistic limit ($a_0 \gg 1$), however, $E_{pond,rel} = a_0 m_e c^2/\sqrt{2}$.

2.2.1. Absorption of laser pulses in underdense plasmas

If $n_e < n_c$ for the laser wavelength, the electron quiver motion creates a comoving plasma wave. This plasma wave can dissipate energy either by collisions, mostly electron-ion collisions, or by Landau damping.

Collisional absorption

The collisional absorption damping rate of a light wave in a plasma can be calculated [9]. At low laser intensity, i. e. $Zv_o^2/v_e^2 \ll 1$, where Z is the charge number and v_e is the electron thermal velocity, the electron distribution function stays Maxwellian. Then, the electron-ion collision rate is

$$\nu_{ei} = \frac{1}{3(2\pi)^{3/2}}\frac{Z\omega_{pe}^4}{n_e v_e^3}\ln\Lambda\,. \tag{2.53}$$

Here $\omega_{pe} = \sqrt{e^2 n_e/(\epsilon_0 m_e)}$ is the plasma electron oscillation frequency, where e is the elementary charge. In practical units, it is

$$\nu_{ei}\,[1/\mathrm{s}] = 2.91 \times 10^{-6}\,\frac{Z n_e\,[\mathrm{cm}^{-3}]}{(T_e\,[\mathrm{eV}])^{3/2}}\,\ln\Lambda\,. \tag{2.54}$$

As usual, $\ln\Lambda$ in Eq. (2.54) is the Coulomb logarithm, i. e. the ratio of highest and lowest possible impact factor for this kind of collision. As electrons moving in the laser electric field are colliding with ions at rest, the maximum impact parameter is the distance a thermal electron moves during a laser cycle: v_e/ω, where ω is the angular frequency of the laser electric field. This is in contrast to the usual definition of the Coulomb logarithm for purely thermal collisions, where the Debye length is used,

$$\lambda_D := \sqrt{\frac{\epsilon_0 k_B T_e}{e^2 n_e}}\,, \tag{2.55}$$

where k_B is Boltzmann's constant and T_e is the electron temperature. For a uniform density n_e and a fixed neutralizing ion background, the damping rate is

$$\nu_{coll} = \nu_{ei}\frac{\omega_{pe}^2}{\omega^2}\,, \tag{2.56}$$

so that over a distance L, the energy in the laser decreases as $\exp(-\nu_{coll}L/c\eta)$. Here, the refractive index of the plasma is $\eta = \sqrt{1 - n_e/n_c}$. The rate at which laser energy is converted into heat is the damping rate ν_{coll} multiplied by the energy $E_{field} = I/(n_e c)$ of an electron in the electric field corresponding to an intensity I. This energy can be expressed as $E_{field} = 2E_{pond}n_c/n_e$ (with the ponderomotive potential E_{pond}) so that

$$R_{coll} = 2\nu_{ei}E_{pond} \tag{2.57}$$

For example, for a Ti:sapphire laser pulse (wavelength 800 nm) at an intensity $10^{15}\,\mathrm{W/cm^2}$ propagating in a $10\,\%n_c$, 200 eV Hydrogen plasma, the damping rate is $R = 10\,\mathrm{eV/ps}$.

The parameter $\alpha := Zv_o^2/v_e^2$, as introduced by Langdon [79], characterizes the relative rates of heating by electron-ion collisions and equilibration by electron-electron collisions. In the strong field / high-Z case $\alpha \gg 1$, the electron distribution function does not stay Maxwellian. This is because electron-electron collisions are not fast enough to bring it back to equilibrium [79, 80]. In this case, the absorption is reduced by a factor down to 2. This can be calculated by multiplying ν_{coll} with a correction factor [79]

$$C_{\mathrm{Langdon}} = 1 - \frac{0.533}{1 + (0.27/\alpha)^{0.75}}\,. \tag{2.58}$$

At high (but still non-relativistic) intensities, the quiver velocity is larger than the electron thermal velocity: $v_o > v_e$ and can become the dominating velocity for the collision process. In this case, it is not justified to assume the electron velocity to be the thermal velocity v_e in Eq. (2.54) but both velocities have to be taken into account. Since a

higher electron velocity leads to a shorter collision time, this means that the absorption by inverse bremsstrahlung saturates. The absorption rate has to be multiplied by a correction factor [81]

$$C_{\text{Faehl}} = \left(1 + \frac{v_o^2}{3v_e^2}\right)^{-3/2} \tag{2.59}$$

For the parameters mentioned above (Ti:sapphire laser pulse, intensity $10^{15}\,\text{W/cm}^2$, 200 eV plasma) this correction factor is $C_{\text{Faehl}} = 0.6$. Therefore at much higher intensity, especially relativistic intensity, collisional absorption is inefficient.

Landau damping

The plasma electron wave can also dissipate energy in the absence of collisions. This is possible because electrons at a thermal velocity close to the phase velocity of the wave are exposed to a nearly constant field, so that they are accelerated or decelerated. From a non-relativistic 1D treatment, it can be shown [9] that for a Maxwellian distribution with thermal velocity v_e, the growth rate is

$$\frac{\gamma_{Landau}}{\omega} = -\sqrt{\frac{\pi}{8}}\frac{\omega_{pe}^2\omega}{|k^3|v_e^3}\, e^{-\frac{\omega^2}{2k^2v_e^2}}\,, \tag{2.60}$$

where ω_{pe} is the plasma electron frequency, and ω and k are the angular frequency and the wave vector of the plasma wave. The electron plasma wave's dispersion relation is the Gross-Bohm relation

$$\omega^2 = \omega_{pe}^2 + 3k^2v_e^2\,. \tag{2.61}$$

The exponential term in Eq. (2.60) is of the order of minus one or higher if $\omega/k < 3v_e$. In this case, Landau damping is sizable. For the case of a near-infrared laser interacting with a plasma, the phase velocity can be approximated by the laser group velocity $\omega/k \approx c\eta$ (where η is the refractive index of the plasma). For example, for a 800 nm wavelength laser propagating in a $n_e = 10^{20}\,\text{cm}^{-3}$, $T_e = 100\,\text{eV}$ plasma, $\omega/k/v_e \approx 70 \gg 3$ so that Landau damping of an electron plasma wave does not attenuate the laser intensity by much.

Direct laser acceleration

At high intensities, hot electrons can be generated by direct laser acceleration [82]. This mechanism is important at intensities $> 10^{20}\,\text{W/cm}^2$ where the laser pulse is channeled by ponderomotive and/or relativistic self-focusing (Sec. 2.1.3). Under these conditions, the electrons are expelled from the laser axis, creating a positively-charged channel. Afterwards, also a part of the ions is expelled. The electric field of the channel focuses electrons that are initially comoving with the laser. The negative charge of the accelerated electrons also expels background electrons, especially further away from the focus where the intensity and hence the ponderomotive force is lower. The electron beam also creates a magnetic field whose pinching force has a focusing effect. This focusing force

and the laser field accelerate the electrons. The forward momentum is provided by the relativistic $\mathbf{v} \times \mathbf{B}$ force [83].

The electron energies generated at high intensity, in the range of megaelectronvolts, are quite suitable for TNSA acceleration of ions, as described below. They differ from laser wakefield accelerated electrons [65] in that they are less energetic and have a higher charge. The acceleration take place on a longer time scale, and amplification is efficient at higher densities than LWFA ($12\,\%n_c$ as observed by Gahn et al. [84]).

2.2.2. Absorption of laser pulses in overdense plasmas

If an ultrashort laser pulse interacts with a solid target, the surface is ionized by field ionization. This plasma is then heated by the laser. The critical surface being close to the original solid surface, only the undercritical coronal plasma is heated by collisional absorption.

The critical surface, where several processes lead to heating, is smeared out a bit because the finite contrast of real laser systems leads to ionization either by a prepulse or by an amplified spontaneous emission (ASE) pedestal. As the plasma then expands isothermally, it forms an exponential density profile with $n_e/n_c \propto \exp(z/L_G)$, with a gradient $L_G = c_s \tau_{pedestal}$ [64].

Resonance absorption An obliquely incident, p-polarized laser pulse has an electric field component parallel to the density gradient. At the target, this component can tunnel through the critical surface and excite a plasma electron wave that dissipates energy through collisional absorption, particle trapping, or wave breaking. This happens only when the density gradient is long compared to the laser wavelength ($L_G \gg \lambda$) [9].

Brunel mechanism An obliquely incident, p-polarized laser pulse can also heat a target when the density gradient is shorter than the laser wavelength. In this case, electrons at the surface can be moved away from the target beyond the Debye sheath thickness and sent back once the laser field changes sign. They subsequently penetrate further into the target than the evanescent laser electric field. Ultimately, they dissipate energy through collisions [64].

Skin effect Laser pulses at normal incidence or s-polarization can also heat electrons. This is because the laser field can penetrate the plasma to a final skin depth (scale length of the evanescent laser electric field). In this zone, electrons are made to oscillate and dissipate energy by collisions. If the electron mean free path v_e/ν_{ei} is smaller than the skin depth c/ω_{pe}, this is referred to as the normal skin effect. Once the temperature increases, v_e can reach values so that $v_e/\nu_{ei} > c/\omega_{pe}$ and even $v_e/\omega > c/\omega_{pe}$. Then, heating occurs deeper in the target [64].

Relativistic $\mathbf{j} \times \mathbf{B}$ heating At relativistic intensities (as discussed above for the ponderomotive potential), the laser electric field has a sizable relativistic $\mathbf{j} \times \mathbf{B}$ term. For a

linearly polarized laser pulse, there is a longitudinal force (along the propagation axis x) of [64]

$$F_{\mathbf{j}\times\mathbf{B}} = -\frac{m_e}{4}\frac{\partial v_o}{\partial x}(1-\cos 2\omega t)\,. \tag{2.62}$$

Here, the first (constant) term in the parenthesis is the nonrelativistic ponderomotive force (directed away from high intensity zones) and the $\cos 2\omega t$ term is the relativistic term, leading to electrons oscillating in propagation direction. Heating is caused by the oscillating electrons according to the Brunel mechanism. This is most efficient for normal incidence. It appears for all laser polarizations except circular polarization.

All of these mechanisms contribute to the generation of a population of suprathermal electrons, i. e. electrons that have a much higher temperature than the bulk electrons. Since the electron acceleration by the laser electric field and its thermalization is highly random, the hot electron distribution function is Maxwell-Boltzmann distribution with the electrostatic potential Φ and the temperature T_e:

$$n_e = n_{e0}\, e^{-\frac{e\Phi}{k_B T_e}}\,. \tag{2.63}$$

Suprathermal electrons are also referred to as hot electrons or fast electrons.

Due to the coexistence of several heating mechanisms, the scaling of the hot electron temperature with the laser intensity is nontrivial. Apart from PIC simulations [85], several models have been proposed, including:

Brunel scaling This scaling is based on the Brunel heating mechanism. It is assumed that after its movement in vacuum, it penetrates the target at a velocity $v = 2a_0 c\sin\theta$, where θ is the laser angle of incidence, and that its kinetic energy is fully converted into heat, i. e. $T_h^{\text{Brunel}} = mv^2/2$. This model is obviously nonrelativistic, and therefore cannot be expected to hold for high intensities [86].

Wilks scaling According to the relativistic $\mathbf{j}\times\mathbf{B}$ mechanism, the hot electron temperature can be considered equal to the ponderomotive potential including the relativistic terms: $T_h^{\text{Wilks}} = m_e c^2(\sqrt{1+a_0^2}-1)$ [66]. This is equivalent to equating the laser energy density to the energy density of critically dense hot electrons.

Beg scaling This scaling is not based on a theoretical model but an empirical formula which reproduces the results of hot electron measurements at the Vulcan Laser (CLF/RAL, Didcot, UK) [87]. It is similar to the Haines scaling: $T_h^{\text{Beg}}\,[\text{keV}] = 215\,(I\,[10^{18}\,\text{W/cm}^2](\lambda\,[1\,\mu\text{m}])^2)^{1/3}$.

Haines scaling This scaling, proposed by Haines et al., is based on the assumption the laser energy transferred to the electrons during the interaction time is equal to the energy of the critically dense hot electrons. The electron temperature is then calculated from the relativistic laser energy in the electron bunch rest frame [88].

The resulting scaling leads to energies lower than the Wilks scaling and similar to the Beg scaling:

$$T_h^{\text{Haines}} = m_e c^2 \left(\sqrt{1 + \sqrt{2} a_0} - 1 \right) . \tag{2.64}$$

The hot electron temperature can be determined experimentally using different methods: For one, it is possible to measure the energy spectrum of electrons emanating from the target [89]. Furthermore, one can also take advantage of the fact that the electrons eject electrons from the inner shell of the cold target material beyond the heating zone. The free energy levels are then filled by outer shell electrons, and x-rays are emitted (K_α method). Using a stacked target, K_α radiation is emitted from different material targets, chosen independently from the laser target material. In every layer, the electrons loose a part of their energy, and the spectrum can be concluded [90]. Finally, is also possible to measure the bremsstrahlung emitted by the hot electrons when they interact with the cold target [91–93].

Hot electron temperature measurements using electron spectrometers [94] and bremsstrahlung x-ray measurements [88] indicate that the hot electron temperature is well depicted by the HAINES model [95]. For example, an Nd:glass laser focused to $10^{20}\,\mathrm{W/cm^2}$ heats electrons to 1.3 MeV.

2.3. Laser amplification by strongly coupled SBS

The parameter regime at which sc-SBS can be investigated and used for amplification of laser pulses is limited by the properties of the process itself (which will be detailed in Sec. 2.3.3) and by concurrent processes (which will be detailed in Sec. 2.3.1).

Experiments

One might be tempted to use a high-Z gas to obtain a high electron density, but it is hard to fully ionize these gases with a laser. This leads to a lower charge-to-mass ratio Z/A for high Z gases. Therefore, it is better to use Hydrogen as a target gas. To reach these parameters in an experiment, one can use a preformed underdense plasma generated by ionizing a Hydrogen gas jet with an auxiliary laser pulse (ionization prepulse) that interacts with the gas before pump and seed pulses arrive.

The density is limited to $10\,\%\,n_c$ since at higher densities, pump and seed pulses would loose too much energy by refraction on small density gradients and collisional absorption in the plasma (Sec. 2.2.1). A higher temperature would also mitigate collisional absorption in the plasma, but the temperature cannot be arbitrarily high. This is because plasma heating by the prepulse is limited by the collisional heating cross-section. Therefore, a plasma electron temperature of 200 eV is a typical value. Experimentally, pump and seed pulses are be made to cross in the plasma under an angle of 180° (fully counter-propagating along the z axis). The pump intensity is chosen high enough to assure that the strong coupling regime is reached. For fully ionized Hydrogen at a density of $10\,\%\,n_c$ and an electron temperature of 200 eV, the pump intensity must be $> 5 \times 10^{12}\,\mathrm{W/cm^2}$

[Eq. (2.22)]. The growth rate [Eq. (2.35)] for this intensity corresponds to a characteristic time scale of $1/\gamma_{sc} = 170\,\mathrm{fs}$. The backscattered wave is frequency downshifted [Eq. (2.37)] by 1.1 nm.

The characteristic timescale corresponds to the spectral width of the process. It imposes a lower limit on the pulse duration: Shorter pulses will first be stretched and then amplified. Since the amplifier length is limited by the length of the plasma, this results in less efficient amplification. Longer pulses can also be amplified, but the objective is in general to have the shortest possible seed pulses.

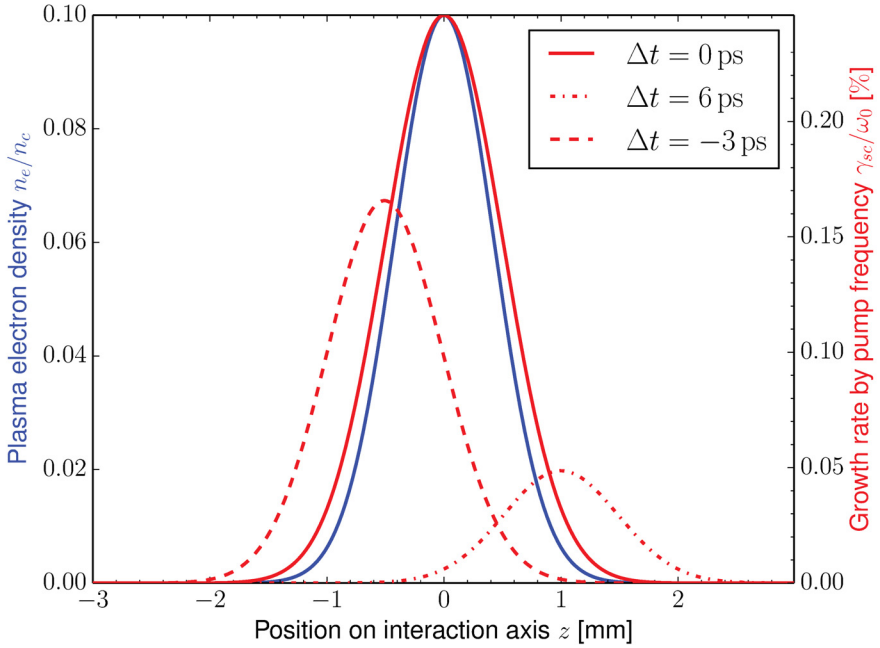

FIG. 2.1.: Growth rate seen by the seed for different delays.

The seed pulse is sent into the plasma at the right time to cross with the pump in the center of the target. Adding a small delay $\Delta t := t_p - t_s$ moves the crossing point of pump and seed in the plasma along the propagation axis z. Since the plasma density is not homogeneous but depends on z, hence the amplification occurs at different densities for different delays. Therefore, changing the delay in an experiment allows to change the density upon interaction and therefore to modify the growth rate. This way of modifying the plasma density is preferable to changing the gas backing pressure because competing processes (that typically do not depend on the delay) are not modified.

Figure 2.1 shows the growth rates for three different delays for the parameters given above. Growth is maximal if the beams meet in the center of the jet. For different delays, the growth is lower and happening elsewhere in the plasma.

2.3.1. Concurrent laser-plasma instabilities

Concurrent processes can convert energy to other forms (heat, a Raman signal, scattered radiation) or prevent the seed from growing by changing the properties of the ion acoustic wave. They are often detrimental, but in some cases, if correctly taken into account, they can be beneficial.

Filamentation Filamentation is a major concern for amplification in a plasma, both in the sc-SBS and in the SRS scheme [50]. This is even more the case since proposed experiments are designed to ramp up the energy at constant intensity by increasing the pump and seed beam diameters in the plasma amplifier, making a homogeneous transverse profile of the beams more challenging to obtain. To avoid filamentation, pump and seed pulses must be [49] shorter than the filamentation timescale $\tau_{fil} = 1/\gamma_{fil}$ (Sec. 2.1.3). For instance, a pump pulse with an intensity of $10^{16}\,\mathrm{W/cm^2}$ at a wavelength of 800 nm begins to filament in a $n_e = 0.1\,n_c$ plasma after $\tau_{fil} = 7\,\mathrm{ps}$. This upper limit for the pump duration also limits the amplifier length to $L < c\,\tau_{fil}/2 = 1\,\mathrm{mm}$. This is not a major concern since efficient amplification can produce a sizable gain on this length. The limitation on the seed intensity is more restrictive. If, for example, the seed pulse has a duration of 170 fs (to match the characteristic time scale of sc-SBS for the plasma parameters detailed in Sec. 2.1.1), filamentation can occur at an intensity of $4 \times 10^{17}\,\mathrm{W/cm^2}$ or above.

Collisional absorption A laser pulse is absorbed by inverse bremsstrahlung in the underdense plasma (see Sec. 2.2.1). This process can reduce the observed gain in an amplification process. For a very weak seed, SBS can even be suppressed if the losses due to collisions are stronger than the gain by SBS. The minimum seed intensity can be calculated from the condition $\gamma_{sc} > \nu_{ei} n_e/n_c$, i. e.

$$a_0 > \sqrt{2}\left(\frac{\nu_{ei}}{\omega_0}\right)^{1.5} \frac{n_e}{n_c}\left(\frac{m_i}{m_e}\right)^{0.5} . \tag{2.65}$$

For Hydrogen with an electron density $n_e = 9\,\%\,n_c$ and temperature $T_e = 200\,\mathrm{eV}$, and a pump with an intensity of $10^{16}\,\mathrm{W/cm^2}$ at $1\,\mu\mathrm{m}$ wavelength, the threshold intensity of the seed is $8 \times 10^8\,\mathrm{W/cm^2}$. If the initial seed is less intense, it is not amplified. Therefore, spontaneous Brillouin backscattering, growing from noise, is much weaker than stimulated Brillouin backscattering.

For the same plasma and pump parameters, the pump is attenuated over a length of 10 mm by about 80 %. Therefore, a higher plasma temperature would be desirable. In principle, a laser prepulse can ionize and heat the plasma to higher temperatures, but at these densities, much energy is needed. Also, the laser parameters must be chosen so that the ionization pulse is maximally absorbed and converted into heat by the same plasma that must be maximally transmissive for the subsequent pump and seed pulses. An optimum would be an intensity of $10^{15}\,\mathrm{W/cm^2}$ in the pre-pulse where absorption is maximal. The direct disadvantage of this is that this reduces the density by ponderomotive expulsion.

Raman Backscattering of pump and seed For typical experimental parameters, for the SBS pump beam (for example with an intensity of $1 \times 10^{16}\,\mathrm{W/cm^2}$ at a wavelength of 800 nm), a characteristic timescale for Raman backscatter is $1/\gamma = 20\,\mathrm{fs}$ corresponding to a characteristic length of $6\,\mu\mathrm{m}$. Therefore, the pump exhibits a strong Raman backscattering. For the seed, however, due to its lower intensity ($1 \times 10^{13}\,\mathrm{W/cm^2}$), Raman backscattering is much lower: The timescale $1/\gamma = 700\,\mathrm{fs}$ is longer than the pulse duration.

In the context of plasma amplification, both by sc-SBS and SRS, spontaneous Raman backscattering can be detrimental because the pump is depleted before transferring energy into the seed. To avoid this, two solutions have been proposed: taking advantage of the chirp of the laser [43, 74] and using a ramp-like plasma electron density profile [42, 49]. This drives the SRS process out of resonance while leaving SBS amplification unharmed.

SRS amplification allows to amplify very short pulses down to the characteristic timescale given by the inverse of the plasma electron frequency ($1/\omega_{pe} = 18\,\mathrm{fs}$ for a typical density of $10^{18}\,\mathrm{cm^{-3}}$). The major drawback, however, is that the resonance is very narrow. This means that even minor inhomogeneities in the plasma density drive the process out of the resonance.

Amplification by SRS can be efficient in two cases. When the seed growth is so strong that it depletes the pump, the seed breaks up into a chain of pulses that become strongly amplified and compressed. This self-similar π pulse regime has been found in theory by Malkin in 1999 [38], and reached in an experiment by Cheng in 2005 [30]. The other case is superradiant amplification. As first pointed out by Shvets in 1998 [37], it can be reached if the pump and seed are strong enough for their combined ponderomotive force to determine electron motion. It was demonstrated experimentally by Dreher in 2004 [46]. As pointed out by Ersfeld in 2005 [43], it can also be reached if the pump pulse is chirped, or the plasma density has a ramp profile. With a chirped pulse, superradiant amplification could be shown by Vieux in 2011 [96].

The arguably most successful SRS amplification experiment has been carried out by Ren et al., in 2007 [5]. A $16\,\mu\mathrm{J}$ seed was amplified to a final energy of 5.6 mJ by a 87 mJ pump, i. e. the absolute gain was 360, the transferred energy almost 5.5 mJ and the conversion efficiency 4 %.

If the strong coupling regime is reached, SBS amplification has the following advantages with respect to SRS:

1. Since the frequency downshift is $\omega_{sc} \ll \omega_0$, close to 100 % of the pump energy are converted into the seed (Manley-Rowe relations) by sc-SBS, as opposed to 90 % for SRS [41]. This defines the maximum efficiency as derived from linear theory. As a realistic pump is depleted, however, the transfer is reduced. Additionally, concurrent processes further reduce the efficiency.

2. The downshift is on the order of the nanometer, less than the spectra of pump and seed, so that the frequency mismatch is not an important issue. The difference induced by small plasma density fluctuations is low, so sc-SBS is not sensitive to

plasma inhomogeneities.

3. sc-SBS is efficient at moderate pump intensities. This allows to avoid particle trapping and wave-breaking [41].

4. Pump and seed can be of the same frequency. This makes the experimental realization easier as no frequency conversion for the seed is needed.

5. Coupling is set by a forced nonlinear oscillation rather than by a natural resonance. The energy transfer is fast and the interaction length is short ($< 1\,\mathrm{mm}$) [49].

2.3.2. Concurrent ion wave-plasma instabilities

Wavebreaking For high gains, the ion acoustic wave in the plasma can be subject to wavebreaking. Its growth rate is given by

$$\frac{\gamma_{wb}}{\omega_0} = \sqrt{\frac{2}{A}} a_0 \,, \tag{2.66}$$

or in practical units, the timescale for wavebreaking is given by [41]

$$\tau_{wb}\,[\mathrm{fs}] = 5.7 \times 10^3 \sqrt{\frac{A}{I_{14}}} \tag{2.67}$$

where I_{14} is the intensity in $10^{14}\,\mathrm{W/cm^2}$, and A, as usual, is the mass number. Therefore, a seed pulse of a duration of 170 fs (the shortest amplified duration as mentioned in Sec. 2.1.1), must not be more intense than $1 \times 10^{17}\,\mathrm{W/cm^2}$.

Landau damping of the ion acoustic wave Attenuation of the ion acoustic wave by Landau damping occurs when the ion thermal velocity reaches the phase velocity of the ion acoustic wave, i. e. when the ion temperature T_i is higher than half of the electron temperature, i. e. $T_e < 2T_i$. Since in a laser-driven plasma, typically $T_e > 50T_i$, Landau damping can be excluded.

2.3.3. Identification of the gain regimes

Strong coupling regime

To amplify a laser pulse by sc-SBS, it is necessary to reach the parameters indicated in Sec. 2.1.1.

In general, a high $I\lambda^2$ is desirable. For example, a carbon dioxide (CO_2) laser, emitting at a wavelength of $\lambda = 10.6\,\mu\mathrm{m}$) would be a good candidate. However, the spectral gain overlaps several rotational levels of the CO_2 molecule, so that the spectrum of the outgoing pulse is modulated accordingly. The corresponding temporal profile is a pulse train. Recently, however, single 5 ps, 1 TW pulses could be generated with a specifically smoothed spectrum [97]. These pulses can also be amplified using the

CPA technique [98]. Since this technology is still comparably new [99], and multi-beam facilities are not available in this range, pump and seed pulse have to be generated with an optical laser in the near infrared, which has shown (in particular due to the admissible bandwidth of Ti:sapphire systems) to be able to deliver pulses as short as 25 fs. By widening the spectral bandwidth, even durations down to 3 . . . 4 fs can be achieved [100]. Multi-beam user facilities in this range exist (Sec. 3.1).

An optimal pump intensity is around $10^{15}\,\mathrm{W/cm^2}$, which is the highest possible intensity at which one avoids filamentation of the pump.

Concerning the plasma, high densities are beneficial as they lead to a high growth rate [Eq. (2.35)]. Especially it would be useful to have a density higher than quarter-critical as in this case, Raman backscattering is fully suppressed. However in practice, high densities are much more challenging to generate, and they also lead to strong refraction in the plasma. Therefore, densities around $10\%n_c$ are preferable as a compromise. To obtain a high Z/A ratio and a most homogeneous plasma, Hydrogen is the preferred species. Since the amplification does not depend on the plasma temperature, it is less important that the plasma is homogeneous in temperature. However, the plasma temperature should be high enough to limit damping of the beams by collisional absorption, but not too high as to make sure strong coupling is safely attained. For instance, according to Eq. (2.56), a $\lambda = 800$ laser beam is attenuated in an $n_e/n_c = 0.1$, $T_e = 100\,\mathrm{eV}$, plasma by 52 %.

To assure that the interaction between pump and seed takes place over the whole amplifying medium, the plasma length L_p and the pump pulse duration τ_0 should be related as $L_p \leq \frac{1}{2} v_g \tau_0$. [41]. For amplification to be efficient, $\tau_s > \tau_{sc}$, i. e.

$$\frac{1}{\omega_0 \tau_{sc}} = \frac{\gamma_{sc}}{\omega_0} = 3.6 \times 10^{-2} \left(Z\frac{m_e}{m_i}\right)^{1/3} \left(\frac{n_e}{n_c}\right)^{1/3} \left(I_{14}\lambda_{\mu m}^2\right)^{1/3} \tag{2.68}$$

Self-similar regime

In order to investigate the transition from the linear to the self-similar regime of sc-SBS, it is necessary to optimize the parameters to obtain a high gain. In an experiment, this can be done by scanning either the pump intensity or the plasma density.

It can be detected by observing the amplification (calorimetry), spectral broadening (using a grating spectrometer), pulse compression (using, e. g., an autocorrelator), and by systematically changing the interaction length to verify the dependence of the output signal on the growth length scale.

2.3.4. Quantifying amplification

Since the growth rate γ_{sc} is not directly accessible to measurement, it is not trivial to quantify the gain obtained from SBS. Obviously, the absolute gain can be defined as

$$g_{\mathrm{abs}} = \frac{E_{\text{seed out}}}{E_{\text{seed in}}}\,, \tag{2.69}$$

where E_{out} is the energy of the amplified pulse and E_{in} is the energy of the incoming beam, as measured on a camera when shooting only the seed without pulsing the gas jet. Since it includes all detrimental effects, it can be considered as the net gain that is important in view of the practical application.

One can define a relative gain by replacing the energy of the incoming pulse by the energy $E_{\text{transmitted}}$ of the pulse transmitted in the plasma in the absence of the pump:

$$g_{\text{rel}} = \frac{E_{\text{seed out}}}{E_{\text{seed transmitted}}} \tag{2.70}$$

This compares the seed attenuated by other processes to the amplified seed.

Quite often, even the pump alone triggers some spontaneous Brillouin backscattering $E_{\text{spontaneous}}$, visible on the calorimetry in the absence of the seed:

$$g'_{\text{rel}} = \frac{E_{\text{seed out}} - E_{\text{spontaneous}}}{E_{\text{seed transmitted}}} \tag{2.71}$$

Since in the experiments outlined in Chap. 5 and 6, the spontaneous backscattering measured on the diagnostics is negligible, and we are interested in the absolute gain, g_{abs} is used as gain definition if not stated otherwise.

Another important value to quantify the process is the efficiency, obtained by dividing the energy transferred to the seed by the energy in the pump pulse before interaction:

$$\eta_{\text{amp}} = \frac{E_{\text{seed out}} - E_{\text{seed in}}}{E_{\text{pump in}}} \tag{2.72}$$

In the literature, one finds quite often definitions for certain spectral components. These are more specific to the process and less useful for the technological objective.

To assess the quality of an amplification scheme in view of the technological application, one can compare the seed energy at the output, the gain (as defined in one of the ways above) or the conversion efficiency.

Although a high output energy is one of the technological goals, it cannot be the only criterion, especially not for the experiments described here. The experiments are done on small laser facilities to explore the amplification scheme and supposed to be ramped up to higher energies by using bigger focal spots once beamtime is available on bigger systems. Since these facilities are limited in energy, it is important to have a high gain rather than a high output energy. The total output energy can obviously be high with a high energy input seed. Therefore, this it is perhaps not the best measure to gauge whether the amplification was successful. Specifying the gain is more helpful, as it shows if there has been relative or absolute amplification. Since the amplification process can create an energetic output even from low energy input seeds (in principle, it can grow as well from noise), however, the reported amplification value has to be looked at carefully: Reporting a high gain starting from a very weak input seed is not in every case a progress in view of plasma amplification. Low energy seed signals can as well be amplified with conventional solid-state amplifier technology. Therefore, the efficiency is perhaps the most useful way to specify amplification since it shows how big a fraction of pump energy the process can convert into the seed.

2.3.5. Prior experimental studies

It has been first pointed out by ANDREEV et al.[41] in 2006 that Stimulated Brillouin backscattering in the strong coupling regime can be used to amplify subpicosecond pulses. Since then, the process has been studied in theory [25, 49, 67, 73, 74, 101–105]). Experimental results, however, are not so abundant. They will be discussed below.

ELFIE 2007

In this proof-of-principle experiment [51] conducted at the ELFIE Nd:glass laser (see Sec. 3.1.3), sub-picosecond pulses were amplified by sc-SBS for the first time. Pump (3.5 ps, 3 mJ, 6.5×10^{16} W/cm^2) and seed (400 fs, 15 mJ, 5×10^{15} W/cm^2) were crossing in a preformed plasma under an angle of 20°. The interaction length was limited due to the nearly-counterpropagating setup. Argon was chosen as a target gas. As mentioned in Sec. 2.1.1, this allows to reach higher electron densities. However, full ionization was not achieved everywhere in the plasma. This created small-scale density gradients in the plasma at which the laser beams were refracted. Since both processes limited the effective amplifier length, only the linear regime of sc-SBS was attained. In a reproducible way, only relative gains of $g'_{rel} = 32$ could be attained, i. e. they partly compensated the losses in the plasma. Only on one shot, an absolute gain of 4 was attained, i. e. the outgoing seed was more energetic than the incoming seed.

VULCAN 2014

In an experiment [106] conducted at the VULCAN Nd:glass (Central Laser Facility, United Kingdom), seed pulses (1 ps, $E = 477$ mJ, focused to 2×10^{14} W/cm^2) were amplified by pump pulses (15 ps, $E = 860$ mJ), focused to 3×10^{14} W/cm^2 in a nearly-counterpropagating (10° angle) setup. Using a 17 % n_c density gas jet target of 5 mm diameter, a much higher interaction length than in the LULI experiment could be realized. Due to the low pump intensity and low plasma density, however, only the onset of strong coupling was observed in this experiment. The total gain was not determined since no calorimetry of the beams was done, but a conversion efficiency of 2.5 % of the relevant spectral component was obtained.

2.3.6. Parameter regime

Therefore, in this thesis, amplification of subpicosecond pulses by sc-SBS under optimized conditions will be studied (Chap. 6). Additionally, the amplification by sc-SBS of pulses shorter than 300 fs will be studied (Chap. 5). This enlarges the parameter regime to the shortest pulses in the optical regime that can be generated by a high-power laser systems.

2.4. Laser-based ion acceleration

Isotropic ion acceleration as a byproduct of laser-plasma interaction has been observed by time-of-flight mass spectrometry as early as in the 1970s [107–109].

Ion beam energies above some MeV, however, could be reached only with CPA systems creating laser pulses at intensities $> 10^{19}\,\mathrm{W/cm^2}$. These pulses can induce a strong charge separation that leads to electrostatic fields in the plasma, via several mechanisms: First, a pulse can heat the target electrons to high temperatures, which pass over the target surface and form an electron sheath with an accompanying strong electric field there (TNSA, Sec. 2.4.1). Second, the laser pulse can push electrons forward ponderomotively, which are followed by the more massive ions; thereby creating a charge separation (hole boring in a bulk target and RPA of thin foils, Sec. 2.4.2). Third, if these ponderomotively moved ions are faster than the plasma speed of sound, then a shock can form in the plasma, which is also accompanied by an electrostatic field (CSA, Sec. 2.4.3). All of these mechanisms have been observed first for overcritical targets and are easier (i. e. at lower laser intensity) to realize in an overdense target. In the case of TNSA, this is because hot electrons with energies in the kiloelectronvolt range can be generated most efficiently at the front surface of an overdense target (Sec. 2.2.2), as opposed to an underdense target, where collisional absorption saturates for high intensities (Sec. 2.2.1). For the radiation pressure based acceleration mechanisms, the light pressure generates a sufficiently strong longitudinal electric field only when the laser pulse interacts with the plasma at the critical surface.

It should be noted that ions can also be accelerated by the mechanism of a Coulomb explosion: If the laser field can ponderomotively expel electrons from a given target volume (either in an underdense target or an ultrathin foil), the positive charge of the remaining ions drives them away. In a thin foil target, this has been reported to have increased heavy ion acceleration from thin foils [110]. It has also been proposed as an alternate mechanism to generate directed beams of high energy protons from double layer targets [111, 112], but has not been demonstrated experimentally. This mechanism can also lead to acceleration when a high-intensity laser pulse interacts with an underdense target, such as a gas (in a jet or a gas cell). Propagating in such a target, a sufficiently strong laser pulse ionizes it at the leading flank, expels the electrons ponderomotively, and creates a zone with a strong positive charge. The repulsive electric field then accelerates ions mostly in transverse direction. This mechanism was observed by Krushelnick et al. in 1999 [22]. It is a well-tested way to accelerate protons transversely, but cannot generate a collimated proton beam. Therefore, these mechanisms are disregarded here.

Laser pulses propagating in an underdense target can, however, generate a collimated ion beam in the forward direction via another mechanism: The laser can accelerate electrons into the forward direction, so that an electron bunch moves through the underdense plasma behind the laser pulse. This electron bunch generates a vortex-shaped magnetic field, which in turn generates an electrostatic field when it emanates into vacuum. The particles are accelerated into the laser direction (MVA, Sec. 2.4.4) [113].

The TNSA, RPA, CSA, and MVA mechanisms are relevant to this thesis as they can

generate a collimated proton beam. Table 2.1 summarizes the scaling of the ion energy with the experimental parameters. The mechanisms are detailed below.

TABLE 2.1.: Electron density range in which TNSA, thin foil RPA, HBA, CSA, and MVA can happen. Scaling of the ion energy with the laser field strength parameter a_0 and the ion density n_i. For MVA, n_{max} is the maximum and n_{min} is the minimum density of the down-ramp (Sec. 2.4.4) [114, 115].

Mechanism	Density	$E(a_0)$	$E(n_i)$
TNSA	$n_e > \gamma n_c$	$E_{max} \propto a_0$	no dependence
RPA	$n_e > \gamma n_c$	$E_{peak} \propto \begin{cases} a_0^4 & (a_0^2/n_i \approx 1) \\ a_0^2 & (a_0^2/n_i \gg 1) \end{cases}$	$E_{peak} \propto \begin{cases} 1/n_i^2 & (a_0^2/n_i \approx 1) \\ 1/n_i & (a_0^2/n_i \gg 1) \end{cases}$
HBA	$n_e \geq \gamma n_c$	$E_{peak} \propto a_0^2$	$E_{peak} \propto 1/n_i$
CSA	$n_e \geq \gamma n_c$	$E_{peak} \propto a_0^2$	$E_{peak} \propto 1/n_i$
MVA	$n_e < \gamma n_c$	$E_{max} \propto a_0$	$E_{max} \propto n_{max}/n_{min}$

The electron motion discussed in this section is relativistic. Therefore, one has to consider the relativistic mass γm_e rather than its rest mass m_e. The critical density of the plasma is then γn_c, so that the refractive index is $\sqrt{1 - n_e/(\gamma n_c)}$. As always in this section, the relevant criterion is the relativistic critical density $\gamma n_c = \sqrt{1 + a_0^2} n_c$ whereas the classic critical density is $n_c = \omega_0^2 m_e \epsilon_0 / e^2$ where ω_0 is the laser angular frequency.

2.4.1. Target-normal sheath acceleration (TNSA)

TNSA is by far the most extensively characterized acceleration mechanism [12, 13, 16, 23, 88, 94, 116–140]. The first protons accelerated by TNSA were observed by Snavely et al. in experiments at the Nova laser (LLNL, Livermore/CA, USA) [23, 119], in experiments at the Vulcan laser (RAL, Chilton, UK) [116], and by the Michigan work group (Ann Arbor/MI, USA) [118]. In these experiments, the spectrum was broadband [23, 117, 118].

Mechanism

The laser heats a solid density target upon incidence, the hot electrons propagate through the target and form an electric sheath field at its surfaces. This fields then accelerates ions.

Hot electron generation and transport A typically overdense target with well-defined boundaries, (e. g. a metal foil) is irradiated with a high-intensity ultrashort pulse. The laser pulse heats a fraction of the electrons at its front surface to temperatures in the keV . . . MeV range (Sec. 2.2.2). The fraction of these hot electrons, compared to the bulk material's number of electrons, is typically below 1 % [141]. For example, an Nd:glass

laser pulse, focused to an intensity of $10^{20}\,\mathrm{W/cm^2}$ on a gold foil, generates a hot electron population with a temperature of 1.3 MeV [Eq. (2.64)].

The hot electrons propagate through the target to its rear. The resulting charge separation is balanced by a return current consisting of electrons at a much lower temperature. They stem either from collisional ionization driven by the hot electrons or, in the case of a metallic target, are in a conduction band [123]. In an insulator, the hot electron transport is disrupted, resulting eventually in a rippled proton beam. The electron beam in the target has a divergence of tens of degrees: Half-angles θ between 8° [126] and 25° [142] have been given in the literature.

At the target rear, the electrons emerge into vacuum, but only a small portion escapes because the target becomes positively charged. Most hot electrons are held back by a restoring electric field. This field ionizes the atoms on the surface. The electrons form a sheath whose thickness is on the order of the Debye length λ_D [Eq. (2.55)], typically around 1000 nm [13]. Since the sheath field drags the ions outward, a quite basic physical problem has to be modeled: The expansion of a plasma into vacuum. Quite obviously, the ion density n_i decreases from a rarefaction wave traveling inwards and the expanding ion front traveling outwards. This can be described in detail in one dimension, which allows to predict the form of the sheath and the accelerated ion spectrum.

Isothermal model This model (Mora 2003 [124]) is based on the following assumptions:

- The target, consisting of only one ion species, is semi-infinite (constant ion density n_{i0} for spatial coordinate $x < 0$, vacuum for $x > 0$).
- The laser is not modeled. Rather, an initial hot electron temperature T_{h0} is set, typically 1 MeV.
- The electrons are initially Boltzmann-distributed, $n_e = n_{e0} \exp[e\Phi_e/(k_B T_e)]$, where Φ_e is the electrostatic potential corresponding to the charge separation with the ions and n_{e0} is the density in the unperturbed plasma. The hot electron temperature T_e is assumed to be constant.
- The electrostatic potential fulfills the Poisson equation:

$$\epsilon_0 \frac{\partial^2 \Phi_e}{\partial x^2} = e(n_e - Z n_i)\,. \tag{2.73}$$

- The plasma is neutral in the bulk: $n_{e0} = Z n_{i0}$ with the charge number Z.

Under these conditions, the sheath extent and electric field and the accelerated ion spectrum can be predicted. Using the additional assumption that the plasma is quasineutral when it expands, a self-similar solution can be calculated valid for $x > c_s t$, with the density

$$n_e(x,t) = Z n_i = n_{e0} e^{\frac{-x}{c_s t} - 1}\,, \tag{2.74}$$

the ion velocity

$$v_i(x,t) = c_s + \frac{x}{t} \tag{2.75}$$

and the electric field,

$$\mathcal{E}_{ss} = \frac{\mathcal{E}_0}{\omega_{pi} t}\,, \tag{2.76}$$

where c_s is the speed of sound in the plasma, ω_{pi} is the ion plasma frequency. This corresponds to a positive charge $\sigma = \epsilon_0 \mathcal{E}_{ss}$ at $x = -c_s t$ and a negative charge on the plasma surface.

This self-similar solution has no meaning for $\omega_{pi} t < 1$ because there the scale length $c_s t$ is smaller than the Debye length $\lambda_{D0} = \sqrt{\epsilon_0 k_B T_e / (n_{e0} e^2)}$. At very late times, $\omega_{pi} t \gg 1$, the ion velocity goes to infinity. This is also obviously non-physical. In fact, the ion velocity is finite, and the ions that were on the surface in the beginning, form a localized ion front. It is situated at the place where the local Debye length is equal to the density scale length, i. e. where the model becomes valid. This is at $1 + x/c_s t = 2\ln(\omega_{pi} t)$. There, the velocity is $v_{i,\mathrm{front}} = 2c_s \ln(\omega_{pi} t)$. The electric field is $\mathcal{E}_{\mathrm{front}} = 2\mathcal{E}_{ss} = 2\mathcal{E}_0/(\omega_{pi} t)$, twice the field from the self-similar solution.

Using a 1D hydrodynamic code [124], a more precise expression for the electric field at the front has been found,

$$\mathcal{E}_{\mathrm{front}} = 2\frac{\mathcal{E}_0}{\sqrt{2e^1 + \omega_{pi}^2 t^2}}\,, \tag{2.77}$$

where $e^1 \approx 2.718$ is Euler's number. The charge density profile $Zn_i - n_e$ causing this field is characterized by a strongly negatively charged zone beyond the ion front, which is balanced by two positively charged zones: One right before the ion front and another one at the rarefaction wave front traveling into the target. The simulation also allows to derive an expression for the ion spectrum, which is quite broadband. The number of ions per unit energy and unit surface is

$$\frac{dN}{dE_i} = \frac{n_{i0} c_s t}{\sqrt{2EE_0}} e^{-\sqrt{2E/E_0}}\,, \tag{2.78}$$

where $E_0 := Zk_B T_e$. This expression for the spectrum does not reproduce the cutoff, which can, however, be determined (again from the simulation) to

$$E_{\mathrm{max}}^{\mathrm{TNSA}} = 2E_0 \left(\ln\left(t_p + \sqrt{t_p^2 + 1}\right)\right)^2\,, \tag{2.79}$$

where $t_p := \omega_{pi} \frac{t}{\sqrt{2 \times e^1}}$ is the normalized acceleration time. This is obviously unphysical for late times because the cutoff $E_{max} \to \infty$ for $t \to \infty$. This divergent behavior is caused by the assumption of a constant electron temperature. Realistically however, the electrons are cooled as they transfer energy to the ions, and the electron heating by the laser occurs only as long as the laser pulse is present at the target front surface. One can thus expect the acceleration to be over after a pulse duration τ_L plus some electron cooling time. Both are taken into account by the empirical expression by Fuchs et al. [130], $2.5\,(\tau_L + 60\,\mathrm{fs})$. The cooling down time can also be obtained from a transient model (see below).

Transient model A slightly more precise model (Mora 2005 [141]) yields a more realistic picture of the expansion, including the acceleration duration and the final ion energy cutoff. Its basic assumptions differ from the isothermal model as follows:

- The target is now a foil with thickness L (typically $20\,\mu$m). Initially, the ions have a step-like density profile (density $n_{i0} = n_{e0}/Z$ in the target at $|x| < L/2$, zero outside).
- The expansion of the heated target is symmetrical with respect to $x = 0$.
- Again, the electrons stay in equilibrium with the electric potential, but their temperature T_e is now given by energy conservation:

$$\frac{dU_e}{dt} = -\frac{dU_{ions}}{dt} - \frac{dU_{field}}{dt} \tag{2.80}$$

  where U_{ions}, U_{field}, and $U_e = g(\theta)N_e k_B T_e$ are the kinetic energies of the ions, the electric field, and the electrons, respectively. $N_e := n_{e0}L$ is the total number of electrons, and g depends on the ratio $k_B T_e/m_e c^2$, with $g = 1/2$ in the classical limit ($k_B T_e \ll m_e c^2$) and $g = 1$ in the ultrarelativistic limit ($k_B T_e \ll m_e c^2$).

The electric field can be determined by solving the Poisson equation. In the beginning ($t = 0$, the ions have not moved yet), it is at the surface

$$\mathcal{E}_{initial} = \sqrt{\frac{2}{e^1}}\sqrt{\frac{n_{e0}k_B T_e}{\epsilon_0}} \quad =: \sqrt{\frac{2}{e^1}}\mathcal{E}_0\,. \tag{2.81}$$

The subsequent expansion of the ions means that the surface (ion front) moves outwards and a rarefaction wave inwards. If the hot electron temperature were constant, this rarefaction wave would reach the target center at a time $t_L = L/(2c_{s0})$, where c_{s0} is the initial ion acoustic velocity. Thus, t_L is a characteristic timescale for the expansion process. It practice, the rarefaction wave arrives much later at the target center for two reasons: The hot electron temperature decreases, which slows down the expansion. Also, the cold electron population limits the expansion. The expanding plasma density profile is shown in Fig. 2.2.

Limitations of the 1D models These models do not take into account the presence of several different ion species. On realistic targets, however, there is always a hydrocarbon contaminant layer. It has a thickness on the order of the nanometer and is present on all solids handled in a standard room atmosphere [143]. It remains even when the sample has been put under vacuum. Mostly the light ions (protons, carbons) from the surface contaminants are accelerated because they have a much higher charge-to-mass ratio than the bulk target ions [143]. One can choose to observe exclusively the, e. g., proton spectrum using a Thomson parabola spectrometer, which distinguishes different ion species by their charge-to-mass ratio. Although the protons come from a rather

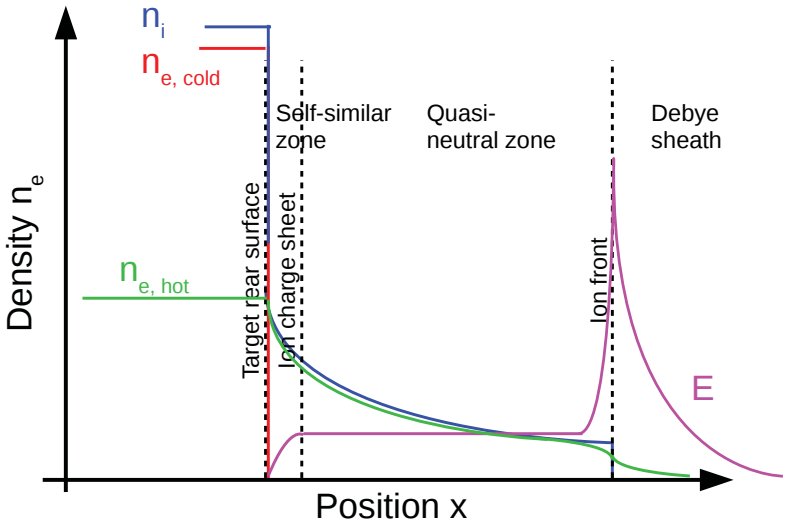

FIG. 2.2.: Schematic representation of the density profile and the electrostatic field of the expanding ion sheath.

confined place in the phase-space (the back surface), this spectrum is also broadband. This is because the electric field has a peak at this point, i. e. the initial electric field differs considerably even for protons close to each other (Fig. 2.2).

The lateral extension of the sheath, obviously not modeled in 1D, has been found experimentally to be a circle with a radius $r_s = r_0 + l \tan\theta$, where r_0 is the laser spot radius. The sheath lateral diameter r_s can be determined by imaging the target onto a camera. Repeating this measurement for several foil thicknesses, the linear relation between r_s and l with the offset r_0 could be shown experimentally, with a hot-electron beam half-angle of $\theta = 17°$ [144].

The limited lateral sheath size also reflects on the ion energies: The field can be considered sizable only up to a distance of about twice the sheath diameter. This is important for long pulses: Increasing the pulse duration (at constant intensity) above a certain optimum value does not increase the ion energy any more. Since in an experiment, the maximum energy available at a laser facility is used, stretching the pulse decreases the intensity. Therefore, for the given energy and a given spot size, there is an optimal duration that allows to reach highest ion energies. It turns out to be on the order of some hundreds of femtoseconds [12]. An analytical description is given in Schreiber et al. [133].

Experimental determination on the electric field

The prediction about the shape of the sheath electrostatic field has been validated in an experiment using TNSA accelerated protons as a diagnostic for transversal probing [128]: The sheath created by a 1.5 ps, $3.5 \times 10^{18}\,\mathrm{W/cm^2}$ laser pulse at the rear surface of a metallic target (thickness $10 \ldots 40\,\mu\mathrm{m}$) has been probed with a transversal proton beam (from a second solid target illuminated by a second laser pulse). The protons were recorded with a stack of radiochromic films (RCF) [145]. The delay of the probing was chosen by changing the timing between both laser pulses. This confirmed that the electric field is strongest at the beginning of the interaction, and that at later times there is an ion front to which corresponds a strong peak in the electric field, followed by a constant and lower electric field.

Laterally, the sheath density profile has a bell-shaped (Gaussian-type) density iso-contour. Ions are accelerated normally to that contour. A Gaussian contour has an inflection point at a certain radius where slope is highest, i. e. the normal vector to the contour is most turned outwards. Therefore, the ions accelerated there have the highest divergence angle. Therefore, the proton beam impinging on a detector leaves a signal that resembles a filled circle with a sharp periphery. Since the ion energy decreases from the center, this means that ions accelerated from the center (highest energies) are at the center of the beam, ions accelerated further outward around the inflection point (medium energies) are most divergent, and ions from the outermost areas (low energy) are more collimated again. This also contributes to the energy spread in the ion spectrum [138].

Ion beam properties

The ion energy is typically

$$E_{\mathrm{ions}}^{\mathrm{TNSA}} = Ze\mathcal{E}\lambda_D \approx Zk_BT_e \approx Zm_ic^2\left(\sqrt{1+\frac{a_0^2}{2}}-1\right). \tag{2.82}$$

The cutoff energy [Eq. (2.79)] can be approximated for $t \gg \omega_{pi}^{-1}$ to

$$E_{\mathrm{max}}^{\mathrm{TNSA}} \approx 2Zk_BT_e\left[\ln\left(2\frac{\omega_{pi}t_{acc}}{\sqrt{2e^1}}\right)\right]^2, \tag{2.83}$$

and the acceleration time can be taken as $t_{acc} \approx 2.5\,(\tau_L + 60\,\mathrm{fs})$ with the laser pulse duration τ_L. This means $E_{\mathrm{ions}}^{\mathrm{TNSA}} \approx Zm_ic^2a_0^2/2$ for $a_0 \gtrapprox 1$, but more interestingly for high intensities, we have $E_{\mathrm{ions}}^{\mathrm{TNSA}} \approx Zm_ic^2a_0$ and therefore the energy scales linearly with the square root of the laser intensity: $E_{\mathrm{ions}}^{\mathrm{TNSA}} \propto a_0 \propto \sqrt{I}$. In order to increase the laser intensity, either the laser energy has to be increased or the focal spot size has to be decreased. Simply compressing the pulse to shortest durations reduces the cutoff [Eq. (2.83)]. Therefore, highest ion energies are observed with Nd:glass lasers, rather than Ti:sapphire system [11].

The ion energy does not depend on the target density [114]. Therefore, broadband TNSA spectra can be observed at densities ranging from solid density (hundreds of n_c) [116] to some percent of n_c [146].

The ions are quite directional because the accelerating field is oriented normally to the (typically flat) target surface. The angular divergence ranges from some degrees to 60° and depends on the energy: The most energetic ions, which are accelerated in the center of the target, have the smallest divergence (envelope angle) and the lowest energy ions have the largest divergence angle. The accelerated protons are quite laminar, i. e. they spread during propagation through vacuum as if they originated from a point source in front of the target. As they are deflected by electric and magnetic fields, they can be easily used as a diagnostic to probe an object, such as the TNSA plasma's electric field itself (see below) [147].

For high-contrast, p-polarized laser pulses at oblique incidence, TNSA acceleration has also been observed at the target front side. This is possible because when laser is absorbed on the front side by the Brunel mechanism (Sec. 2.2.2), the electrons are dragged out of the target before being pushed back. Therefore, there is a negative charge with an accompanying electrostatic field on the front side that accelerates ions. The spectra are broadband. With low contrast pulses, no acceleration is observed because the density gradient is too smooth to permit the emergence of a strong electric field [135].

Optimization

The most obvious advantage of TNSA is the technological simplicity: It is simple to realize at a $< 10\,\mathrm{Hz}$ repetition rate with a table-top high-intensity laser and a solid target, in contrast to RPA of thin foils, which needs a high contrast, and CSA, which needs a near-critical target. Ironically, the use of solid targets makes TNSA much less desirable once it comes to technical applications: The debris contaminates the target chamber and can damage the optics.

Since basically, hydrocarbon impurities are accelerated, it is difficult to generate a pure beam of one ion species only, e. g., a pure proton beam. It is, however, possible to steer the process into accelerating rather heavy ion species. This can be achieved by resistively heating the target to around 1300 K using electric heating prior to irradiation [148, 149]. This can reduce the proton flux by two orders of magnitude [150], so that heavier ion acceleration dominates over proton acceleration. However, even with this techniques, TNSA accelerates several ion species.

It should be noted that the energy spread can be reduced by evaporating most of the contaminants, down to a narrow layer, off the target rear surface by heating the target before irradiation. In this case, the lighter ions are all accelerated by the same field, giving rise to a monoenergetic spectrum. Due to the sharp peak of the electric field on the target rear, however, this works only if the contaminant layer is evaporated down to an atomic monolayer. This reduces the number of accelerated ions significantly [151]. Similarly, the use of a target with a proton-rich microdot allows to confine the acceleration laterally, so that the electric field is more or less constant. This also reduces the accelerated ions' bandwidth, again at the expense of the particle flux [134].

In order to obtain a pure proton beam albeit with a broadband spectrum, an overdense Hydrogen target can be created using a cryogenic jet [152].

However, the main drawback of TNSA from foils is arguably the high energy spread,

making, e. g., medical applications difficult: Targeted deposition of energy at the Bragg peak is possible only if the ions are sufficiently monoenergetic. In addition, the scaling of the cutoff energy with the laser intensity being $E_{ions}^{TNSA} \propto \sqrt{I}$ does not give rise to the prospect of increasing the energy by much with future laser facilities.

2.4.2. Radiation pressure based mechanisms

A laser pulse with an intensity I impinging on an overcritical target does not only heat the electrons on the target surface, as described in Sec. 2.2.2, but the ponderomotive force also induces a secular motion on the particles, due to the first term in Eq. (2.62). This force's density is also – analogously to the high energy density physics literature's terminology, e. g. Drake [153] – referred to as radiation pressure

$$P_{rad} = (1 + R - T)\frac{I}{c}\,. \tag{2.84}$$

Here R is the reflection coefficient, and T is the transmission coefficient, which depend on the refractive index and the vacuum wavelength of the beam. More precisely, the radiation pressure is the energy density that corresponds to the oscillation of critically dense electrons in the laser field with the ponderomotive potential $I/(2cn_c)$. It is, therefore, proportional to a_0^2.

Since the ion inertia is much higher than that of the electrons (1836 times in the case of Hydrogen), mostly the electrons move [13]. The electrons are displaced by around a Debye length [Eq. (2.55)], which is the electron thermal velocity v_e divided by the plasma electron frequency ω_{pe},

$$\lambda_D = \frac{v_e}{\omega_{pe}} \approx \frac{c}{\omega_0}\sqrt{\gamma\frac{n_c}{n_e}} \approx \lambda \tag{2.85}$$

where the thermal electrons are approximated as relativistic $v_e \approx c$. Therefore, the Debye length is on the order of the laser wavelength λ. The electrostatic potential induced by this charge separation is balanced by the ponderomotive potential. This determines the number of displaced electrons. The electric field drags the ions behind the electrons. Therefore, the critical surface of the plasma is moved in the direction of the ponderomotive force at the piston (or hole-boring) velocity v_{HB}. [125]. Considering the radiation pressure acting on the critical surface of the plasma (in a relativistically comoving reference frame), one can equate the light pressure in this reference frame to the ion pressure,

$$(1 + \eta_R)\frac{2I}{c}\frac{1 - v_{HB}}{1 + v_{HB}} = n_i m_i v_{HB}^2 \gamma_{HB}^2 \tag{2.86}$$

where $\gamma_{HB} := (1 - v_{HB^2}/c^2)^{-1/2}$. One can conclude [13] that the hole boring velocity is

$$\frac{v_{HB}}{c} = \frac{u}{1 + u} \tag{2.87}$$

with

$$u = \sqrt{\frac{1}{2c^2}\frac{m_e}{m_i}\frac{n_c}{n_i}}\sqrt{\frac{I}{1.4 \times 10^{14}\,\mathrm{W/cm^2}}\left(\frac{\lambda}{1\,\mu\mathrm{m}}\right)^2} \tag{2.88}$$

where m_e and m_i are electron and ion mass, respectively, n_i is the ion density, n_c is the critical density at the laser wavelength. The non-relativistic ($v_{HB} \ll c$) limit of Eq. (2.87) is that already obtained by KRUER [154] and WILKS [66]:

$$\frac{v_{HB}^{nonrelativ.}}{c} = \sqrt{1+\eta_R}\sqrt{\frac{m_e n_c}{2 m_i n_i}} a_0 \tag{2.89}$$

For example, shooting with an Nd:glass laser onto a near-critical ($n_i = 1\, n_c$) Hydrogen plasma target at an intensity of $10^{20}\,\mathrm{W/cm^2}$, the hole boring velocity would be 12 % of the speed of light in vacuum.

Since this velocity is high for high a_0 and low plasma density, these acceleration mechanisms are favored by a slightly overcritical target and high laser intensity. These mechanisms dominate if electron heating is suppressed, i. e. for a circularly polarized laser beam at normal incidence.

Hole boring acceleration (HBA)

Due to the charge separation (ions being dragged by the electrons), there is a strong electric field at the moving critical surface. Ions, which are initially at rest behind the moving critical surface are reflected and have a velocity of $v_{\mathrm{ions}}^{\mathrm{HBA}} = 2v_{HB}$. This mechanism is also referred to as sweeping acceleration [155], the hole boring regime of radiation pressure acceleration, laser piston acceleration [156], or simply front side acceleration [129]. The energy is then

$$E_{\mathrm{ions}}^{\mathrm{HBA}} = 2 m_p c^2 \frac{u}{1+2\sqrt{u}}\,. \tag{2.90}$$

Since $E_{\mathrm{ions}}^{\mathrm{HBA}} \propto (v_{\mathrm{ions}}^{\mathrm{HBA}})^2 \propto I/n_i$, the scaling with the laser intensity is more favorable than in the case of TNSA. Since the energy is higher for low densities and the process works only for overcritical targets, near-critical targets are needed for HBA to dominate [114]. The laser intensity should be higher than $10^{19}\,\mathrm{W/cm^2}$ for the process to dominate over TNSA [157].

Radiation pressure acceleration (RPA) of thin foils

If laser intensity, target thickness, and density are chosen so that the force exerted by the radiation pressure is identical to the restoring force given by the charge separation field, then the whole target under the focus propagates ballistically. It gains energy continuously from the laser field, and all particle species are accelerated to the same final energy [158]. This mechanism is also referred to as light sail regime of RPA [159, 160], and, unfortunately, also the laser piston regime [161], which adds to the risk of confusion with HBA. However, it differs qualitatively from HBA, where the light pressure acts only on the surface.

The energy of the accelerated ions scales with the laser intensity as

$$E_{\mathrm{ions}}^{\mathrm{RPA}} = m_i c^2 \frac{F_L^2}{2(F_L+1)}\,, \tag{2.91}$$

where $F_L := 2\int I(t)dt/(n_i l c^2)$ is proportional to the laser fluence, which depends, for constant pulse duration, linearly on the intensity so that $E_{\text{ions}}^{\text{RPA}} \propto a_0^4$ for low a_0, and $E_{\text{ions}}^{\text{RPA}} \propto a_0^2$ for the ultra-relativistic case ($a_0 \gg 1$) [162].

These conditions are experimentally challenging. In order for the target density to remain thin, a high contrast is necessary. Heating of the electrons at the target surface (Sec. 2.2.2) must be avoided since this would lead to a high contribution of TNSA. In experiments [158, 163, 164], the laser pulse is chosen to be at circular polarization (thus, $\mathbf{j} \times \mathbf{B}$ heating is quenched) and at normal incidence (this avoids resonance absorption and Brunel heating). This is, however, difficult to realize practically because the laser finite laser spot size, leads to the target being bent inwards. Therefore, the pulse is not perfectly perpendicular on the target surface everywhere, and the Brunel mechanism still heats electrons [163]. Therefore, TNSA was always present in the experiments, causing a small monoenergetic feature on a mostly broadband ion spectrum. Mass-limited targets have been studied in theory and could limit target deformation, but the part of the laser pulse that overtakes the target also accelerates electrons [165].

Although a high laser intensity is desirable, the onset of relativistic transparency makes RPA inefficient for

$$a_0 > \pi \frac{n_e}{n_c} \frac{l}{\lambda} \tag{2.92}$$

with the foil thickness l. Once the target is relativistically transparent, the laser field removes electrons from the foil. The repulsive electrostatic force between the ions would then lead to a Couloumb explosion. Therefore, both high target density and high laser intensity are desirable for the light sail regime [13]. With current CPA systems, a plasma mirror is needed to achieve a high contrast and avoid backreflection of the laser pulse into the laser chain. A target with thickness on the order of the micrometer or below cannot be readily created with a gas or liquid jet, but typically requires the use of solid targets. Both limits the achievable repetition rate.

2.4.3. Collisionless shock acceleration (CSA)

Another way to generate a strong electrostatic field in a plasma, suitable for ion acceleration, is by producing an electrostatic shock wave in a plasma. Below, first the properties of these shocks are discussed. Then, two ways of generating these shocks are pointed out: Shock generation in a near-critical plasma at the front surface, and shock generation in a density downramp at the rear of a low-density plasma. Finally, prior experimental results are discussed.

Shock properties

Collisional shock waves are a well-known phenomenon in neutral and charged fluids. They are usually defined as a traveling discontinuity of the flow variables in the fluid equations, which are valid if the flow features are larger than the mean free path: $L \gg \lambda_{MF} = \frac{v}{\nu}$ where v is the velocity of a given species and ν is the relevant collision

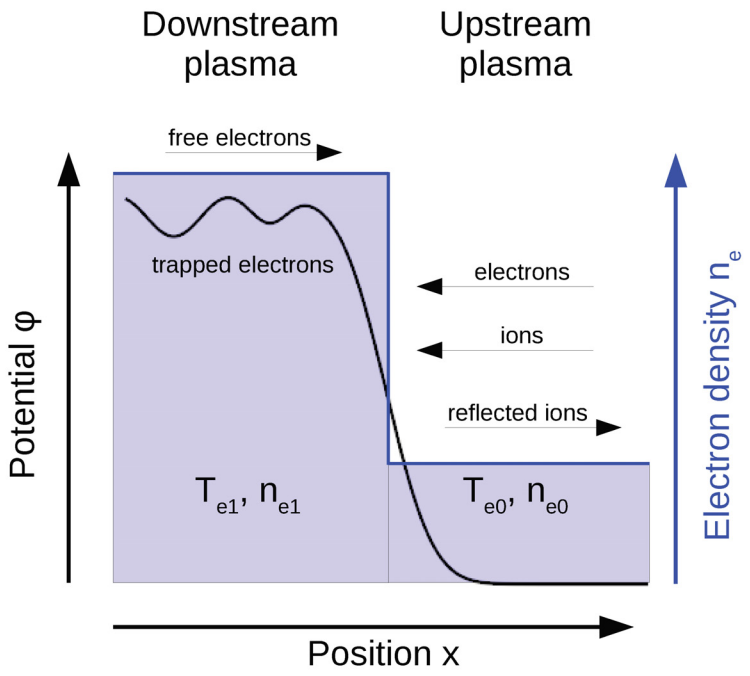

FIG. 2.3.: Schematic representation of a shock between upstream low-density (0) and downstream high-density (1) region.

frequency. In this case, the interaction between particles is provided by collisions. In a plasma, an ion shock wave is accompanied by an electric field with a potential ϕ because the thermal electrons from the high-density region form a sheath beyond the shock, resulting in a charge separation.

In the following, the plasma is modeled as a fluid. It is assumed that the electrons are Boltzmann-distributed,

$$n_e = n_{e0} e^{-e\Phi/T_e} , \tag{2.93}$$

that there is no magnetic field ($\mathbf{B} = 0$), and the ion pressure is negligible $p_i = 0$. Furthermore, we consider, in 1D, the stationary state that establishes if the ions move at constant velocity (here referred to as piston velocity v_p) in a part of the domain (downstream, $x < v_{sh}t$) towards the other domain, where they are at rest in the laboratory frame (upstream, $x > v_{sh}t$). In this situation, one expects a shock-like behavior at a boundary moving (in the laboratory frame) with a velocity $v_{sh} > v_p$, i. e. the discontinuity travels through the medium as a shock wave. The following considerations are done in the frame boosted with v_{sh} (the shock frame), in which all waves are assumed stationary. Therefore

$$\frac{\partial}{\partial t} n_i = 0 \tag{2.94}$$

and

$$\frac{\partial}{\partial t} u_i = 0\,. \tag{2.95}$$

As will be shown, two types of solutions are to be found: In the absence of dissipative effects (a strongly idealized case), the wave will be a soliton, i. e. at a point in the plasma, the ion density will rise once and come back to the previous level just once, whereas the soliton wave will not loose energy. In the presence of dissipation, the wave will be a shock, i. e. the ion density will rise suddenly and then oscillate around a value that is globally higher than the initial value. Especially, the reflection, i. e. acceleration of ions on the shock is a dissipative effect that can turn a soliton into a shock. Therefore ion acceleration is the reason for the shock formation as well as the shock is, in turn, the reason for the ion acceleration.

Solitons Under the conditions mentioned above, Eq. (2.8) becomes $\partial/\partial x(n_i u_i) = 0$. Since in the shock frame, ions are coming at the velocity $-v_{sh}$ from upstream ($x \to \infty$), one can use this boundary value:

$$n_i u_i = \frac{-n_0}{Z} v_{sh}\,. \tag{2.96}$$

Similarly, Eq. (2.9) becomes $u_i \partial/\partial x u_i = -Ze/(m_i)\partial/\partial x \Phi$, and gauging the electrostatic potential to $\Phi = 0$ for $x \to \infty$, one obtains

$$\frac{m_i}{2} u_i^2 + Ze\Phi = \frac{m_i}{2} v_{sh}^2\,. \tag{2.97}$$

Inserting Eq. (2.97) into Eq. (2.96) yields

$$n_i = \frac{n_0}{Z} v_{sh} \left(v_{sh}^2 - 2\frac{Ze\Phi}{m_i} \right)^{-1/2}\,, \tag{2.98}$$

which, quite obviously, gives a real value only if the radicand is non-negative, $m_i v_{sh}^2 > Ze\Phi$. This means that the incoming background ions must be fast enough to overcome the electrostatic field, i. e. they are not reflected.

One can introduce new units by expressing the position in terms of the Debye length ($\xi := x/\lambda_D$), the potential in terms of the thermal energy ($\phi := i\Phi/T_e$), and the shock velocity using its Mach number ($M_{sh} := v_s h/c_s$). Using Eq. (2.98), the Poisson equation [Eq. (2.12)] becomes

$$\frac{d^2\phi}{d\xi^2} = e^{\phi} - \frac{M_{sh}}{\sqrt{M_{sh}^2 - 2\phi}}\,. \tag{2.99}$$

Multiplying with $d\phi/d\xi$ and integrating,

$$0 = \frac{1}{2} \left(\frac{d\phi}{d\xi} \right)^2 + U_{soliton}(\phi) \tag{2.100}$$

where the definition

$$U_{soliton}(\phi) := -\left(e^{\phi} + M_{sh}\sqrt{M_{sh}^2 - 2\phi} + 1 + M_{sh}^2\right) \tag{2.101}$$

was used for clarity. The reason why this is called $U_{soliton}$ will be given below. Before, a useful analogy should be pointed out. Although the physical meaning is very much different, Eq. (2.99) is formally identical to the equation of motion for a point mass in a potential, as can be clearly seen from Eq. (2.100). In this analogy, $\Phi(\xi)$ is the particle trajectory (i. e. pseudo-position), ξ the pseudo-time, and $U(\phi)$ the pseudo-potential, also referred to in the literature as SAGDEEV potential.

With the initial conditions as pointed out before, the shock Mach number M_{sh} remains to be determined. However, the general shape of the curve and a range of possible Mach numbers can be given. The criterion for a non-negative radicand in Eq. (2.98), as mentioned above, fixes a maximum electrostatic potential $\phi < M_{sh}^2/2 =: \phi_{cr}$ (critical electrostatic potential) for a given incoming ion velocity. Since

$$\frac{d}{d\phi}U_{soliton}(\phi = 0) = 0\,, \tag{2.102}$$

and, as chosen, $U_{soliton}(0) = 0$, the Sagdeev potential must have a well-like shape $U_{soliton}(\phi \gtrapprox 0) < 0$ and $U_{soliton}(\phi_{cr}) > 0$. Therefore, there must be a potential ϕ_m for which $U_{soliton}(\phi_c r) = 0$.

A lower limit for the Mach number is given by

$$U_{soliton}(\phi \geq 0) \approx \frac{-\phi^2}{2}\left(1 - \frac{1}{M_{sh}^2}\right) < 0\,, \tag{2.103}$$

so that the shock must be supersonic ($M_{sh} > 1$). An upper limit is given by

$$U_{soliton}(\phi = \phi_{cr} = M_{sh}^2/2) = e^{M_{sh}^2/2} - M_{sh}^2 - 1 > 0 \tag{2.104}$$

so that $M_{sh} < 1.58\cdots \approx 1.6$.

One can consider three possible cases for a solution, i. e. a potential (pseudo-trajectory) that starts at $\phi = 0$:

Soliton: In the absence of dissipative effects, it rises until ϕ_m and then bounces back until it is at $\phi = 0$ again. This is a soliton as there is only a single oscillation.

Shock from dissipation: The potential ϕ rises until ϕ_m and bounces back. In the case of dissipative effects, it will not reach $\phi = 0$ with a Sagdeev potential $U(\phi) = 0$, but will oscillate in the Sagdeev potential well, further dissipate until the oscillation amplitude reaches zero. This scenario is to be ruled out as there are no collisions.

Shock from other processes: The ϕ rises until ϕ_m. By the time it is there, the Sagdeev potential has been risen by some other process, which, again prevents the pseudo-trajectory / electrostatic potential ϕ from coming back to zero. It will keep oscillating until there is no further dissipation. A process that can change the potential is ion reflection on the shock.

Shocks If one changes slightly the boundary conditions by assuming that a small fraction of the ions is reflected on the shock, this induces the minor change in the potential necessary to obtain a shock rather than a soliton. Assuming the background ions have a velocity distribution

$$f_i = f_0 e^{\frac{v+v_{sh}}{u_i}} \tag{2.105}$$

then the function

$$F(\Phi) := \int_{(v+v_{sh})^2<2Ze\Phi/m_i} f_i(v)dv \tag{2.106}$$

is the number of ions that are reflected at a place where the potential has the value Φ. For $x \to \infty$, $\Phi = 0$, and $F(\Phi = 0)$ is the total number of ions that are reflected anywhere up to the shock as for them $(v + v_{sh})^2 < 2Ze\Phi/m_i$.

The boundary conditions change as follows: Since there are more ions upstream, $n_0 \to n_0(1+F(0))$ and $n_i u_i = -n_0 v_{sh}/Z \to -n_0 v_{sh}/Z n_0(1+F(0))$ for $x \to \infty$. As there are less ions downstream, $n_0 \to n_0(1 - F(0))$ for $x \to -\infty$.

The Poisson equation then reads:

$$\frac{d^2\phi}{d\xi^2} = \begin{cases} \left[(1 - F(0))e^{\phi} - \frac{M_{sh}(1-F(0))}{\sqrt{M^2-2\phi}}\right] & \text{for} \quad \xi < 0 \quad \text{(downstream)} \\ \left[(1 + F(0))e^{\phi} - \frac{M_{sh}(1-F(0))}{\sqrt{M^2-2\phi}} - 2F(\phi)\right] & \text{for} \quad \xi > 0 \quad \text{(upstream)} \end{cases} \tag{2.107}$$

where the right hand side is the relevant Sagdeev potential and the extra term $-2F(0)$ represents the reflected ions. In a plasma, reflection of ions dominates over collisions as a dissipation mechanism as the shock thickness is much smaller than the mean free path [166].

In contrast to this analytic result, PIC simulations have shown that Mach numbers between 1 and 6.5 can exist in this regime, and that the shock forms typically in $(2 \ldots 10) \times 2\pi/\omega_{pi}$ [167, 168], where $\omega_{pi} = \sqrt{Zm_e/m_i}\omega_{pe}$ is the ion oscillation frequency in the unperturbed plasma.

Shock generation on the front side of a near-critical target

So far, it was assumed that in one zone of the plasma (the downstream zone), ions are moving with the piston velocity $v_p > c_s$, whereas they are at rest beyond the shock. This condition, necessary for a shock to form, can be achieved if the incident light pressure on an overdense bulk target is high enough. This means that the hole boring velocity is above the ion sound speed $c_s = \sqrt{Zk_BT_e/m_i}$, i. e. the piston Mach number $M_{HB} = v_{HB}/c_s > 1$.

The Mach number $M = v_{sh}/c_s$ of the shock, can be estimated [166]: Since the shock velocity is higher than the hole boring (piston) velocity but on the same order, one can approximate the shock velocity with the hole boring velocity: $v_{sh} \approx v_{HB}$. Using the non-relativistic expression in Eq. (2.89), this means

$$M\sqrt{\frac{k_BT_h}{m_i}} = a_0\sqrt{1+\eta_{abs}}\sqrt{\frac{1}{2}\frac{m_e}{m_i}\frac{n_c}{n_i}}\,. \tag{2.108}$$

The hot electron temperature can be estimated at $k_B T_e = 0.8 a_0 m_e c^2$ (Wilks scaling with $a_0 \gg 1$), so that

$$M = \sqrt{\frac{1}{0.4}\frac{n_c}{n_i} a_0}\,, \tag{2.109}$$

a $M \propto I^{1/4}\lambda^{1/2} n_i^{-1/2}$ scaling which shows that high laser intensities and low densities are desirable.

Still in a 1D slab geometry (semi-infinite plasmas) approximation, the accelerated ions gain a velocity, according to Fiuza et al. [169],

$$v_{\text{ions}}^{\text{CSA}} = \frac{v'_{sh} + v_0}{1 + \frac{v'_{sh} v_0}{c^2}} \tag{2.110}$$

where

$$v'_{sh} = \frac{1 M c_s}{1 + M^2 \frac{c_s^2}{c^2}} \tag{2.111}$$

More realistically, a shock can be modeled in 3D [170], also given in Stockem-Novo et al. [114] from the theory for three-dimensional shocks [171]. Here, κ is the adiabatic exponent (e. g. 5/3 for a monoatomic gas in 3D) and γ_{HB} is the relativistic gamma factor for the hole boring velocity. The jump condition for the density ratio behind / before the shock is

$$\frac{n_2}{n_1} = \frac{\kappa\gamma_{HB} + 1}{\kappa - 1} \approx \frac{\kappa + 1}{\kappa - 1} \tag{2.112}$$

where the approximation holds for non-relativistic piston velocity, and a shock velocity

$$\frac{v_{sh}}{c} = \frac{(\kappa\gamma_{HB} + 1)\sqrt{\gamma_{HB}^2 - 1}}{1 + \gamma_{HB} + \kappa(\gamma_{HB}^2 - 1)} \approx \frac{a_0}{2}\sqrt{\frac{n_c}{2n_p}\frac{Z m_e}{m_i}}(1 + \kappa)\,, \tag{2.113}$$

where, again, the approximation holds for the nonrelativistic limit $\gamma_{HB} \approx 1$ and the piston velocity is calculated with Eq. (2.89).

Shock generation in an undercritical downramp profile

A shock can also form in an undercritical plasma in a density downramp, i. e. usually at the rear side of a gas jet or exploded foil target. This regime is also referred to as low-density CSA (LDCSA). It is a two-step process [172]: First, an ion wave is started in a zone where strong magnetic fields are present [131]. When the bunch of expanding ions enters a low-density zone with strongly decreased magnetic field, the ions overtake slower ions from that zone, and an electrostatic shock forms. This scenario has been investigated in PIC simulations for initially near-critical but relativistically underdense plasmas where no shock forms at the surface [173]. PIC simulations with $8\,\% n_c$ plasmas [174] have explained peaked spectra from exploded foils [55]. Since both sheath-acceleration and shock acceleration occurred at the target rear side, the spectrum was broadband with a peak [55].

Prior experiments

Since the standard CSA regime can happen in a bulk target (opposed to a thin foil), pulsed gas jet targets can be used, eliminating the disadvantages of solid targets mentioned above. Therefore, CSA has first been observed [4, 24, 175] with carbon dioxide (CO_2) lasers [176] with a wavelength of 10 000 nm, for which the critical density is $1.1 \times 10^{19}\,\mathrm{cm}^{-3}$. These jets can be generated by applying a backing pressure of some tens of bars to a supersonic Laval type nozzle with a Mach number around 4 [60]. This can be done with a standard pressure regulator, reducing the pressure of up to 200 bar that is typical of commercial gas cylinders.

For instance, from an experiment with the ATF laser (Brookhaven National Laboratory, USA), Palmer et al. [24] report a highest flux of 3×10^{12} particles/MeV/sr at 0.6 MeV peak energy for a target with a density of $n_e/n_c = 6$ and a length of 800 μm and a laser field strength $a_0 \approx 0.5$. They report the highest peak ion energy of 1.1 MeV on a shot with a slightly higher intensity but the same gas density. In this experiment, the CO_2 system produced a pulse train (6 ps duration pulses, separated by 25 ps delays), so it is not clear if the first pulse, interacting with the unperturbed target, or subsequent pulses are responsible for acceleration.

A follow-up experiment was done with the same facility (Tresca et al. [175]), but then with a single pulse, preceded by a prepulse whose energy and delay were controlled. The prepulse created a blast wave with a localized zone of a gas density of $6n_c$ in the Helium jet, and the main pulse accelerated 1×10^9 particles/MeV/sr Helium ions to a peak energy of 1.4 MeV.

In an experiment at the Neptune CO_2 laser (UCLA, Los Angeles, USA), Haberberger et al. report proton acceleration from a Hydrogen gas jet at $2n_c$ density, with a laser intensity of $a_0 = 2.1$. Quasi-monoenergetic protons were observed in the forward direction, with a peak energy at 18 MeV, but at a remarkably low flux of 10^7 particles/MeV/sr.

These experiments show that with the facilities available with an a_0 up to 3, it is possible to accelerate ions from near-critical targets to energies in excess of 10 MeV, but realizing only a very low particle flux. Increasing the density allows to accelerate more particles but limits the energy. In order to further increase the energy, a higher laser field strength parameter is necessary, as shown in PIC simulations [4].

Lasers in the near infrared, such as Neodymium-doped glass (Nd:glass) lasers and Titanium-doped sapphire (Ti:sapphire) lasers, can reach higher intensities by up to four orders of magnitude with current facilities. As the vector potential scales with $\sqrt{I\lambda^2}$, even with a ten times smaller wavelength, this corresponds to a ten times higher a_0. Future facilities currently under construction will allow an $a_0 > 200$. The critical densities of these lasers are much higher ($1.7 \times 10^{21}\,\mathrm{cm}^{-3}$ for Ti:sapphire and $1.1 \times 10^{21}\,\mathrm{cm}^{-3}$ for Nd:glass) than that for a CO_2 laser ($7 \times 10^{19}\,\mathrm{cm}^{-3}$). One the one hand, this is arguably beneficial for the particle flux as it increases the number of particles in the focal spot volume, but on the other hand, these densities are more difficult to produce experimentally. A possibility is to increase the backing pressure on a supersonic nozzle using a compressor. Neither compressors nor fast (millisecond response time) valves that can

operate at high pressures are standard laboratory equipment, and the high gas load in the chamber reduces the repetition rate. However, engineered solutions exist as even continuous gas jet operation in vacuum chambers is possible [61].

2.4.4. Magnetic vortex acceleration (MVA)

If the target is relativistically transparent for the laser pulse, i. e. $n_e < \gamma n_c$, the pulse can propagate in the target and form a channel of lower electron density. For a target longer ($L > c\tau$) than the laser pulse duration τ, electrons are both expelled ponderomotively into transversal direction and accelerated into the laser direction. Meanwhile, the laser pulse is depleted, i. e. the energy is reduced, the frequency decreases and the amplitude of the vector potential a_0 increases [177]. The comoving electrons then generate a circular magnetic field (magnetic vortex) in the target, around the channel. Defining the electron canonical momentum $\mathbf{P} := \mathbf{p} - e\mathbf{A}$ (with the classical momentum $\mathbf{p}$ and the vector potential $\mathbf{A}$), the vorticity is then $\mathbf{\Omega} = \nabla \times \mathbf{P}$. This vortex follows the laser pulse [113]. The magnetic field strength can be calculated [178] as $B_1 = -\mu_0 e n_1 c^2 \sqrt{\gamma}/\omega_{pe1}$, where $\gamma = \sqrt{1 + a_0^2/2}$, and $\omega_{pe1} = \sqrt{n_1 e^2/m\varepsilon_0}$ is the plasma electron frequency to the maximum electron density n_1 in the target. It is of some hundreds of megaGauss, or tens of kiloTeslas [115]. This corresponds to a magnetic pressure of $p_B = \mathbf{B}^2/(2/\mu_0)$ of some hundreds of megabars. The lateral size of the vortex is approximately equal to the collisionless skin depth $l_s \approx c\sqrt{\gamma}/\omega_{pe1}$.

At the rear side of the target, where the density decreases from n_1 to n_2, the vortex moves downramp. It expands both in forward direction, where the density decreases, and in lateral direction, where the $\nabla \times \Omega$ force acts on the vortex [179], and the magnetic field is reduced because $\mathbf{\Omega}/n$ is conserved (Ertel's theorem). Therefore, the magnetic field can be estimated as $B_2 = B_1(n_1 + n_2)/2n_1$ [113]. Upon the increase in size of the vortex, an ion filament forms that reaches into the vortex, and a sharp peak of the ion density occurs in the vortex. The volume in front of this peak does not contain any ions, but a considerable number of electrons moved forward by the magnetic vortex. These electrons generate a strong electrostatic field that accelerates ions.

The ion velocity is given by the velocity of the moving vortex, which is in turn given by the Alfven velocity $v_A = B_2/\sqrt{\mu_0 A m_p n_2/Z}$, with the ion charge Z, ion mass number A, proton mass m_p, and vacuum permeability μ_0. Including a relativistic correction, the final ion energy per nucleon (in the laboratory frame) can be approximated (for $n_1 \gg n_2$ and $a_0 \gg 1$) as [115]

$$\frac{E_{ions,MVA}}{A} \approx \left(\frac{Z}{A}\right) \frac{m_c^2 a_0}{2\sqrt{2}} \frac{n_1}{n_2} \,. \tag{2.114}$$

It should be noted that the scaling of the ion energy with the laser field strength parameter is not more favorable than that of TNSA (which is also $E_{ions} \propto a_0$). The dependence on the density is a bit more subtle: The density must decrease fast enough at the target rear for the vortex to increase in size significantly. However, with too steep a gradient the vortex has not enough time to grow fast enough. From simulations, a decrease by a factor of eight over a length equal to the pulse length has been found to be a sensible

choice. This means that the gradient layer size should be in the range of tens of microns [115]. This is the case rather for clustered gas and foam targets rather than for gas jets.

This mechanism looks similar to laser wakefield electron acceleration (LWFA) in the bubble regime [180, 181], which is observed at densities of typically $n_e < 1\% n_c$. There, electrons are also accelerated in the laser direction, leading as well to magnetic vortex formation [182]. However, in that LWFA regime only the electrons are expelled by the ponderomotive force, but the magnetic vortex does neither expel the ions nor generate an ion filament in the target. In MVA, however, the vortex is generated behind the laser pulse and acts on both electrons and ions.

3. Experimental methods

This chapter reviews the techniques needed to investigate plasma-based laser amplification and particle acceleration with intermediate density targets:

First, one or more laser pulses have to be generated by a high-power laser facility (Sec. 3.1).

Second, these pulses then have to interact with a plasma, generated from initially neutral matter. As pointed out in Sec. 1.3, gas jets have been chosen to do this as their densities are in the desired range, and because they are easily accessible for beams and diagnostics. Section 3.2 reviews both the basic properties and the characterization of these gas jet targets. A simple model is given to predict the gas density in the jet for a given nozzle geometry and backing pressure.

Third, the neutral gas has to be ionized, and – in the case of the SBS amplification experiments – the thus created plasma has to be preheated to have both the density and the temperature needed to allow for parametric processes to happen without being hampered by collisional absorption. Pre-ionization and preheating are achieved by prepulses.

For the experiments discussed in Chap. 4 to 6, all the gas jet targets have been characterized. The results of these measurements are summarized in Sec. 3.3. An estimation of the temperature is also given.

Finally, Sec. 3.4 describes the diagnostics used to investigate the properties of the emitted radiation and particles.

3.1. High-power laser facilities

The experiments have been carried out at three different laser facilities, according to the parameters needed: Due to the need for high energy for the CSA experiment (Chap. 4), this was done at the TITAN Nd:glass laser (Sec. 3.1.1). The investigation of Brillouin backscattering with ultrashort pulses (Chap. 5) needed a three-beam Ti:sapphire facility, therefore the ARCTURUS laser (Sec. 3.1.2) was used. As it turned out, the optimal laser conditions (spectrum, duration, chirp) were closer to those available from an Nd:glass system. Therefore, efficient SBS amplification (Chap. 6) was investigated at the ELFIE laser facility (Sec. 3.1.3).

3.1.1. The TITAN laser facility

The TITAN laser at the Jupiter Laser facility (JLF) of the Lawrence Livermore National Laboratory (LLNL) in Livermore/CA (USA) is a flash lamp pumped Nd:glass laser. This user facility provides two main beam lines and a probe beam line:

- a short pulse (700 fs, 150 J) at low repetition rate (1 shot every 30 minutes),
- a long pulse (350 ps, 800 J) at low repetition rate (1 shot every 20 minutes), and
- a probe pulse, generated from a leakage of the short pulse (same duration), with energies in the millijoule range.

3.1.2. The ARCTURUS laser facility

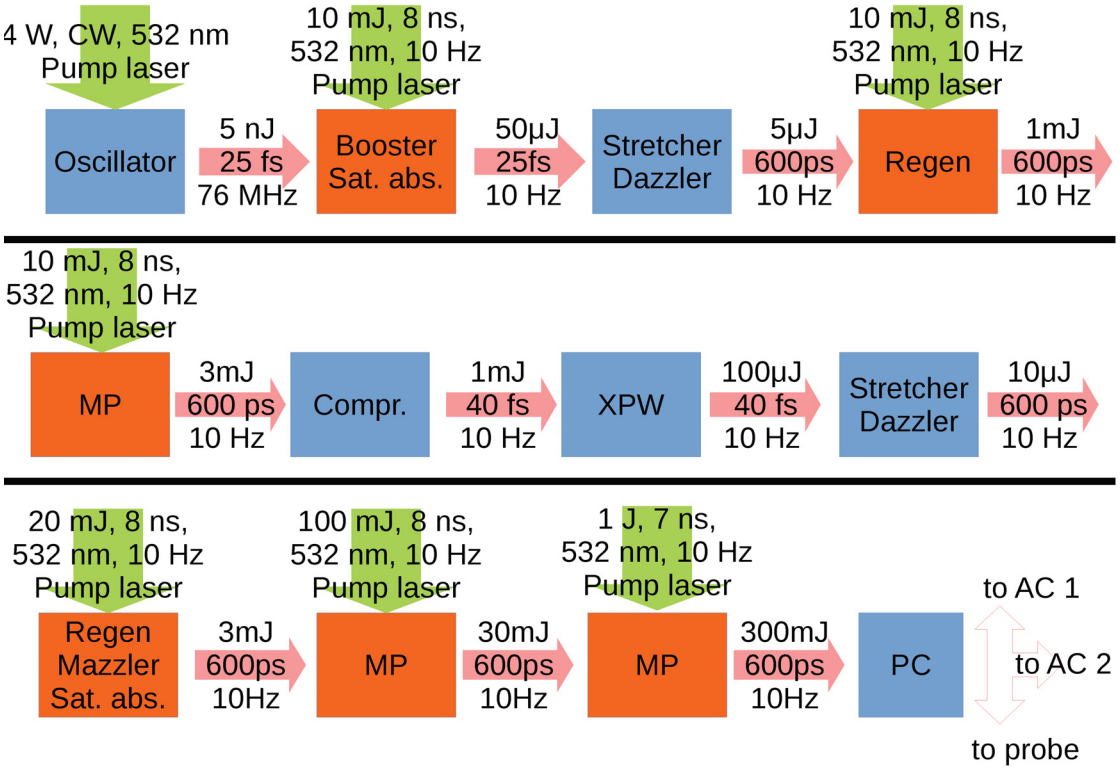

FIG. 3.1.: ARCTURUS laser facility. Front-end and first amplifier section. MP: Multi-pass amplifier. XPW: Cross-polarized wave generation. PC: Pockels cell. AC: Amplifier chain.

The ARCTURUS (the brightest star in the northern hemisphere) laser facility is a multi-beam laser facility at ILPP (Düsseldorf, Germany) [183]. It is designed to deliver pulses with energies of 2 J compressed of 30 fs, as well as uncompressed pulses with energies up to 3 J and durations in 600 ps. It is an upgraded version of a commercial Pulsar laser system (Amplitude, Evry, France)

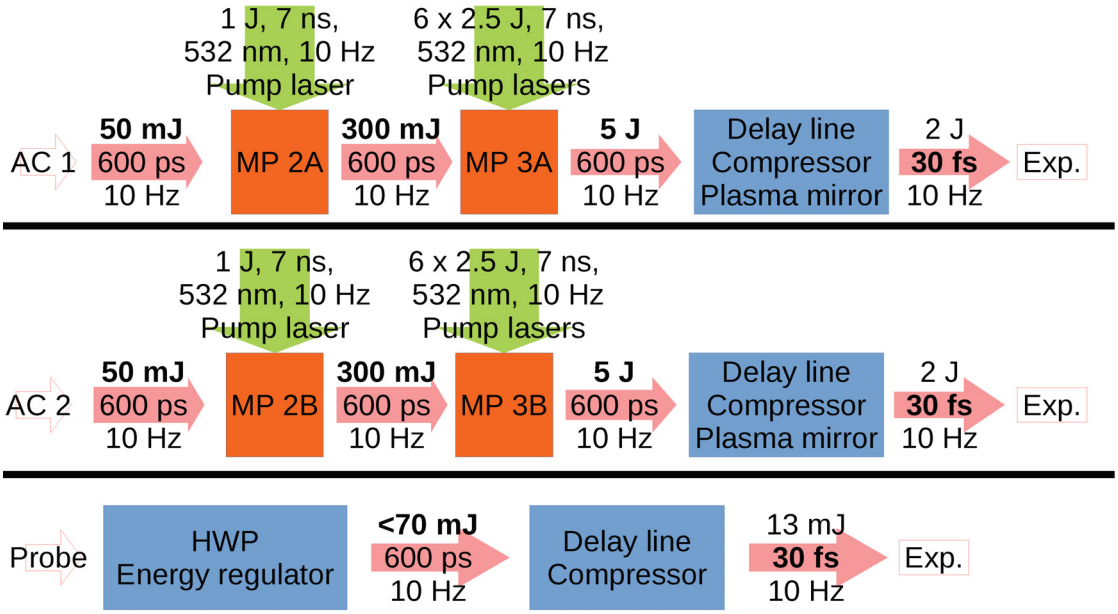

FIG. 3.2.: ARCTURUS laser facility. Main amplifiers. MP: Multipass amplifier. HWP: Half-wave plate. Exp.: Experiment.

Laser chain

The laser chain starts with a commercial oscillator (Synergy, Femtosource, Vienna, Austria), pumped by a 4 W, 532 nm diode-pumped solid state continuous-wave (CW) laser. The oscillator delivers pulses with an energy of 5 nJ and a bandwidth of 60 nm, centered at 800 nm.

The femtosecond pulse is then pre-amplified to the microjoule level by a 14-pass ring amplifier (booster), followed by a saturable absorber to obtain a high contrast. The pulse is then stretched to 600 ps by an Offner type stretcher and amplified to the millijoule level by a regenerative amplifier (Regen) and a multipass amplifier (MP). This design, using a preamplifier, allows for a low amplification ratio in the Regen, which reduces the amplified spontaneous emission (ASE), i. e. improves the pulse contrast.

The contrast is then further optimized by taking advantage of cross-polarized wave generation (XPW), a parametric process: The beam is compressed and focused onto the entrance of a hollow-core fiber which serves as a spatial filter. The outgoing beam is divergent and almost perfectly Gaussian. It is sent into a nonlinear crystal, where its energy is converted into a wave at the same frequency, in forward direction, at orthogonal polarization, whose intensity is proportional to the cube of the incoming intensity. Subsequently, a polarizer removes the residual beam at the original polarization. The XPW process increases the contrast and broadens the pulse spectrum [184].

Afterwards, the output pulse is stretched again. After a second regenerative amplifier and two more multipass amplifiers, three replica of the beam (B1, B2, probe) are

generated using beam splitters (Fig. 3.1). The probe is compressed using a grating compressor and can be used for an experiment. The main pulses (B1 and B2) are sent into two identical main amplifier chains. Each chain contains two multipass amplifiers, which amplify the beam to up to 5 J and a grating compressor, where a duration of 30 fs can be reached (Fig. 3.2). Due to the short pulse duration and therefore the high intensity already in the near field, all the beams, even the probe, have to be kept under vacuum after compression.

Each of the main beamlines is equipped with a plasma mirror. The plasma mirror is a plasma-based fast optical switch: An off-axis parabola (OAP) focuses the pulse onto an anti-reflection coated glass slab that transmits (i. e. discards) the prepulses at low power. Only the main pulse's leading edge creates an overcritical plasma on the glass surface which reflects the remainder of the pulse. The plasma's critical surface is flat and smooth enough for the reflected pulse to be collimated again by another OAP. In practice, the glass slab is not situated at the actual focus but defocused to reduce the intensity enough to create the plasma only with the leading edge of the main pulse [28].

The laser basically consists of two CPA systems, pumped with frequency doubled lamp-pumped Nd:YAG lasers at 532 nm. At first glance, it is a highly complex system: The ultrashort pulse, which is at the microjoule level before stretching, goes through the first CPA amplifier chain and the XPW and is still at the microjoule level afterwards. Only the second CPA system amplifies the pulse to the energy needed in the experiment. The purpose of the front-end section up to the XPW, however, is to inject a low-energy pulse at very high contrast and optimal spectral phase into the amplifier chain.

Pulse shaping

Directly after both stretchers, the chirped pulse goes through an acousto-optic programmable dispersive filter (AOPDF), also referred to by its commercial name as a Dazzler [185]: The pulse propagates through a uniaxial birefringent crystal onto which an acoustic wave is applied externally. This external acoustic wave is made to propagate into the same direction as the laser and its frequency changes with time (basically, it is chirped itself). The incoming pulse's propagation and polarization direction are perpendicular to the crystal's optic axis, i. e. the incoming pulse is an ordinary wave. Due to the presence of the acoustic wave, the laser pulse is diffracted into an extraordinary wave. For each laser frequency component, this happens only when the laser encounters a phase-matched spatial frequency from the acoustic wave. The point along the propagation direction where this happens is controlled by shaping the acoustic wave. As the propagation velocities in a birefringent crystal are different for the ordinary and the extraordinary beam, the Dazzler induces a different delay for each spectral component (spectral phase shaping). As the diffraction efficiency depends on the acoustic signal amplitude, the relative intensity of each spectral component can be individually modified (spectral amplitude shaping). This only works because the pulse is chirped. This procedure allows to shape the spectral phase and amplitude to minimize gain narrowing afterwards.

The second regenerative amplifier is equipped with an acousto-optic programmable

gain filter (AOPGF), also referred to by its commercial name as a Mazzler. It is basically a Dazzler put into the Regen's cavity. Here, it shapes the spectral amplitude and phase of the cavity losses.

Output

The system can shoot at a repetition rate of 10 Hz at full energy. One can obtain two short pulses (≥ 30 fs, ≤ 2 J on target) and a probe pulse (≥ 30 fs, ≤ 13 mJ on target).

If necessary, the energies of the main beams can be reduced by switching off some of the pump lasers. For the probe beam, there is an energy regulation setup: In the beamline, before the compressor, the linarly polarized beam is split into two by a polarizing beam splitter. One of these beams continues its path into the compressor. A half-wave plate (HWP, Fig. 3.2) directly before the polarizing beam splitter allows to turn the incoming polarization and therefore to control the energy fraction that goes into the compressor. The rejected beam is sent onto a calorimeter. This allows to measure the pulse energy shot-to-shot fluctuations of the laser facility. Since the additional losses after this setup (in compressor and beamline) are the same for all shots, this value is proportional to the pulse energy on target. Calibrating this instrument with an energy measurement of the focused beam in the chamber allows to determine the pulse energy impinging on the target on every shot, despite the laser fluctuations.

As a facility, ARCTURUS is a small university-scale laser, allowing for the shortest possible pulses at the Joule level in the near infrared. In terms of energy, however, the facility is limited. Unlike at most other Ti:sapphire systems, it features two beamlines, and therefore, provides two high-energy pulses and a probe that can be optically timed as they come from the same oscillator. This property, necessary for amplification experiments, is a unique capability that determined the choice of this facility.

3.1.3. The ELFIE laser facility

The ELFIE (Equipement Laser de Forte Intensité et Energie) laser facility is a multi-beam laser facility at LULI (Palaiseau, France). It is a Neodymium-doped glass laser. Using a combination of silicate and phosphate glass amplifiers, pulses with a comparably large bandwidth (6 nm) around the center wavelength of 1057 nm are amplified. It is designed to deliver pulses with energies of 12 J compressed down to 450 fs, as well as uncompressed pulses with energies up to 60 J and durations in 450 ps.

As usual for a large CPA system, initially weak pulses with a wide spectrum are generated by an oscillator, stretched to long duration and then amplified by several stages. Upon amplification, they forcibly lose a bit of their bandwidth by gain narrowing, so that the final duration of the amplified pulses is higher than their initial duration when they leave the oscillator. In order to retain a 6 nm spectral width, all of the Nd:glass amplifiers are a combination of flash-lamp pumped phosphate and silicate glass amplifiers.

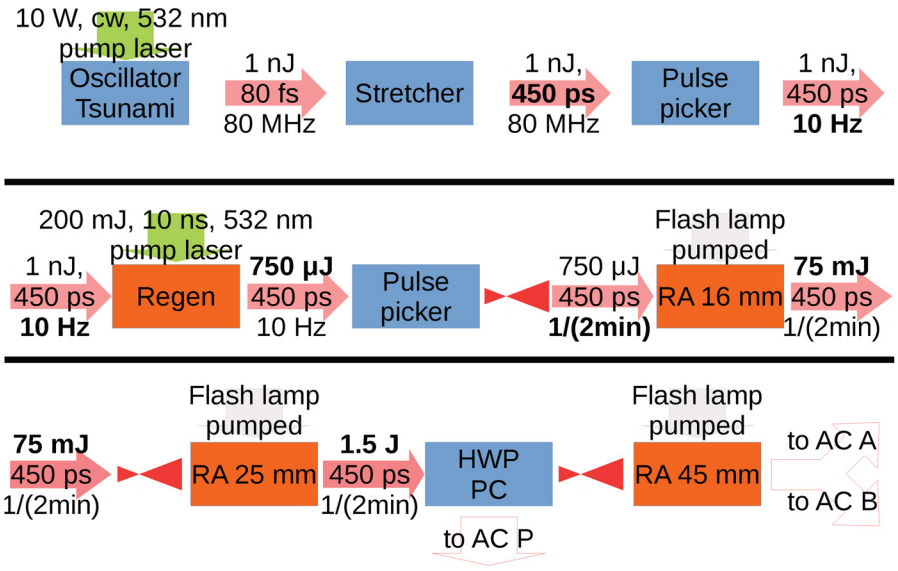

FIG. 3.3.: ELFIE laser facility: Front end and first amplifier stages. Regen: Regenerative amplifier. RA: Rod amplifier. HWP: Half-wave plate. PC: Pockels cell. AC: Amplifier chain.

The front end and the first amplifier stages are shown in Fig. 3.3. The laser chain starts with a commercial oscillator (Tsunami, Spectra-Physics, Santa Clara/CA, USA), pumped by a 10 W, 532 nm diode-pumped solid state CW laser (Millennia V, Spectra-Physics, Santa Clara/CA, USA). The oscillator delivers pulses with an energy of 1 nJ and a bandwidth of 12 nm, centered at 1057 nm. These pulses are stretched to 450 ps and pre-amplified to 1.5 J by a chain of a laser-pumped regenerative amplifier (Regen) and two flash lamp pumped rod amplifiers (RA).

At this point, a variable part of the beam is coupled out with a half-wave plate. It is recompressed using a small grating compressor and can be used as a probe for an experiment.

The other part is then split into two separate pulses. They are sent into the main amplifier chains (AC A and AC B), each containing a rod amplifier and a subsequent disk amplifier, which provides a more homogeneous spatial gain profile. The pulses are amplified up to 60 J. On each chain, a deformable mirror (DM) allows to correct the phase front of the beam, to have a decent far field profile (Fig. 3.4).

The output of chain A is split again and these two pulses are sent into the two vacuum compressors and then available to the experiment as short pulses (SP1, SP2). Optionally, they can be modified after compression (frequency-doubling, change of polarization). The output of chain B can be used at high energy, without compression (LP).

Between the amplification stages, the beam (near field) diameter is increased in steps from 2.5 mm to 16 mm, then 25 mm, 45 mm, 108 mm, to finally 120 mm between the last amplifier and the compressor. To this end, lens telescopes are used. Pinholes in the

intermediary foci control the far field of the beam. Flash lamps are used to pump all the amplifiers after the regenerative amplifier. As their repetition rate is limited by their cooling down time, amplified shots can only be done in single shot mode. The shot is triggered by a mechanical shutter after the regenerative amplifier. Shots with the first two rod amplifiers can be done once every two minutes, shots at full energy only once every twenty minutes.

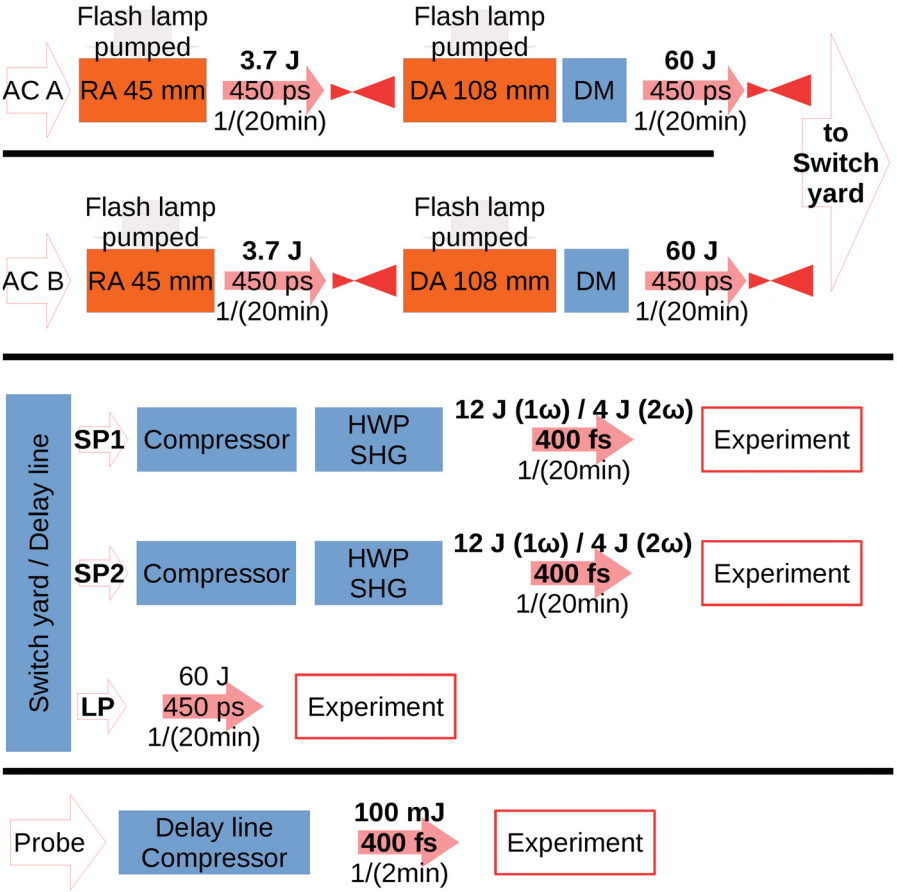

FIG. 3.4.: ELFIE laser facility: Amplifiers and compressors. AC: Amplifier chain. RA: Rod amplifier. DA: Disk amplifier. DM: Deformable mirror. FR: Faraday rotator. HWP: Half-wave plate. SHG: Second-harmonic generation crystal.

As a facility, ELFIE thus provides an intermediate range of energies, situated between low rep-rate systems (such as LULI2000, TITAN, PHELIX, VULCAN) providing more energy at a comparable pulse duration, on the one hand, and high rep-rate systems (such as ARCTURUS, JETI) providing shorter pulses of 30 fs albeit with less energy (in the Joule range). Unlike at most other systems, it provides three energetic pulses that can be optically timed as they come from the same oscillator.

Since there are Faraday rotators (FR) as optical isolators after the last amplifiers,

neither backreflection of the beams on the target nor transmission in a fully counter-propagating setup is a risk to the amplifiers. The spatial filters after the last amplifiers, and the length of the propagation distance between amplifiers add to the safety of the amplifiers.

3.2. Supersonic gas jet targets

The inherent technological problem about having a laser beam interact with a gas is the need for a spatially confined gas with a suitable density profile. In the experiments described in the thesis at hand, this was solved by generating a gas jet using a supersonic nozzle. The use of nozzles to generate gas targets is quite common for laser-plasma experiments [7, 52, 181, 182, 186–201, 201–235]. Gas cells are also frequently used [234, 236–242], but they have the disadvantage that the access to the target with laser beams (for preionization, interaction, and probing) is limited. Therefore, gas jet targets were preferred here because they allow to freely access the target with laser beams from most directions. The relevant jet properties are reviewed in Sec. 3.2.1. The method for the 3D ex-situ characterization of the gas jet targets is described in Sec. 3.2.2.

In the gas jet, the plasma was then created either by sending an ionization prepulse into the gas or from the interaction of the main pulses with the gas.

3.2.1. Gas flow created by a Laval nozzle

A jet is a gas flow emanating from an orifice into a vacuum chamber. For the target to be confined to a small space at this position, the jet divergence has to be low. This is best achieved with a supersonic jet because a gas expanded to a supersonic flow has a low temperature and a low pressure, both giving rise to a slow transversal expansion of the jet [60].

Core flow in a nozzle A supersonic jet is created using a nozzle, i. e. a duct that accelerates the flow [243]. A convergent-divergent nozzle (i. e. whose cross-section decreases up to a throat and then increases again along the mean flow direction) is referred to as a Laval nozzle (Fig. 3.5) [60]. The precise form of the cross-section can be designed according to the experimental needs. Axisymmetric and rectangular shapes are the most common forms as they can be created using turning or milling machines [59, 244]. Arbitrary forms can be created using electroerosion [245] or 3D printing. To use a nozzle in an experiment, a high pressure is applied in the gas reservoir and leads to a flow into the vacuum chamber. The form of the gas jet depends on the form of the nozzle, mostly its divergent part. Typical dimensions are throat diameters of $0.1 \ldots 1\,\mathrm{mm}$, and exit diameters of $0.1 \ldots 10\,\mathrm{mm}$. The pressure in the gas reservoir, referred to as backing pressure, is typically $1 \ldots 1000\,\mathrm{bar}$, and the background pressure in the vacuum chamber is usually around $10^{-4}\,\mathrm{mbar}$.

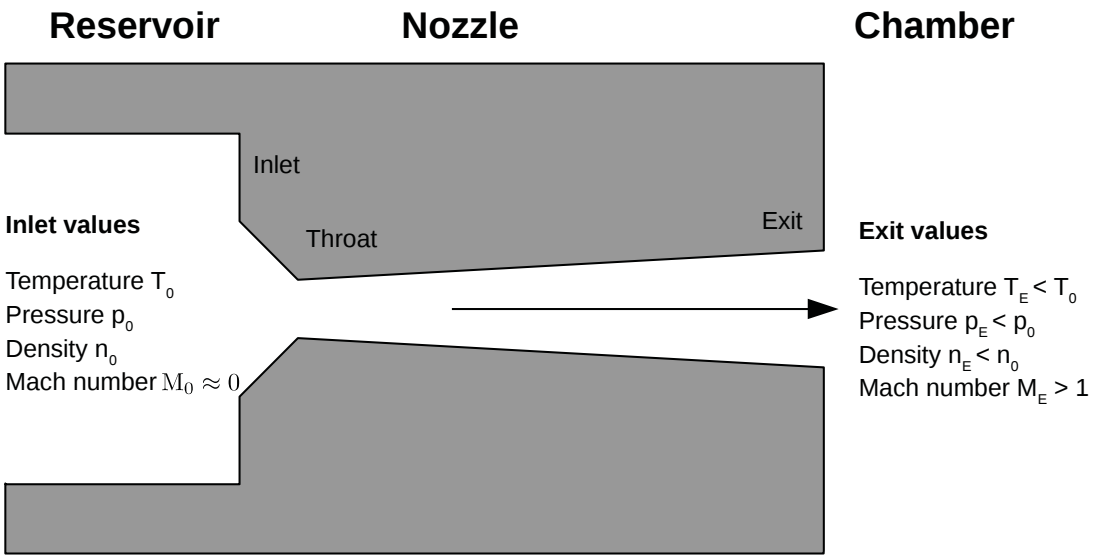

FIG. 3.5.: Sketch of a Laval nozzle.

The flow velocity in the Laval nozzle reaches the speed of sound $c_s = \sqrt{\kappa k_B T/m_m}$ at the throat. Here, m_m is a gas molecule's mass and k_B is Boltzmann's constant. The specific heat ratio (or adiabatic exponent) $\kappa := \frac{C_p}{C_V}$ is the ratio of the heat capacity at constant pressure C_p and the heat capacity at constant volume C_V. It is $\kappa = 5/3$ for a monoatomic gas and $\kappa = 7/5$ for a diatomic gas. By the exit of the nozzle, the gas velocity v is supersonic with a Mach number $M := v/c_s$ of typically $M = 4 \ldots 6$ [243]. The gas flow can be treated purely hydrodynamically (the space completely filled with particles) if the characteristic length L of the smallest flow features is large compared to the gas molecules' mean free path $\lambda_{MF} = 1/(\sqrt{2}\pi r_W^2 n)$, where r_W is the van der Waals radius and n is the molecular density (continuum approximation) [246]. This is the case if $L > 10^3 \lambda_{MF}$ [247]. For a Laval nozzle and backing pressures of tens of bars, the density in the nozzle is on the order of $n = 10^{21}\,\mathrm{cm}^{-3}$. For Hydrogen ($r_W = 120\,\mathrm{pm}$), then $\lambda_{MF} = 16\,\mathrm{nm}$, so that the continuum approximation holds for characteristic geometry sizes down to tens of micrometers. Typically, the throat diameter of a nozzle is $> 100\,\mu\mathrm{m}$, so hydrodynamics is a realistic description.

From 1-dimensional (1D) flow theory, it can be shown that the flow inside the nozzle (except for the boundary flow close to the walls) is isentropic, i. e. reversibly adiabatic. Therefore, the gas properties are determined by their initial values (at the inlet) and one further parameter, which can be the Mach number [248].

For a nozzle cross section $F(z)$, the following holds for the density n, the temperature T, and the static pressure p [60, 249]:

$$\frac{F_0}{F} = M \left(1 + \frac{\kappa - 1}{\kappa + 1}(M^2 - 1)\right)^{\frac{-1}{2}\frac{\kappa+1}{\kappa-1}} , \tag{3.1}$$

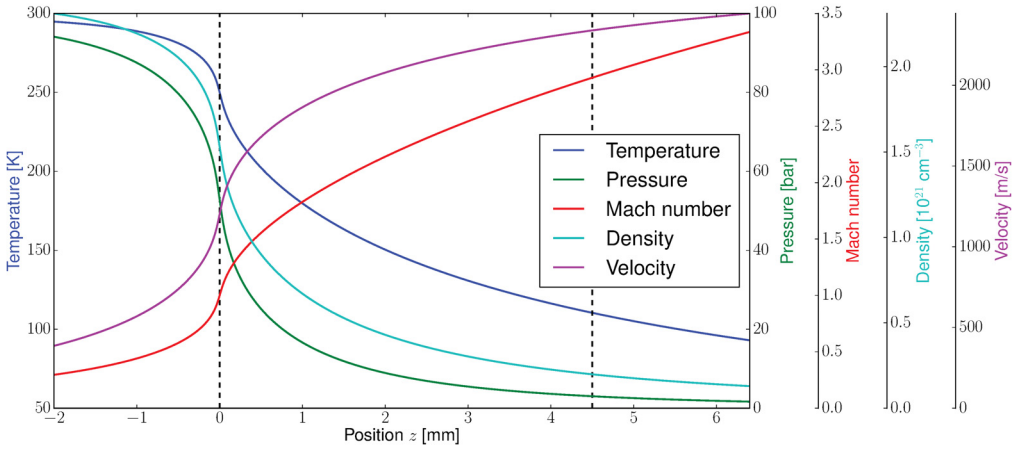

FIG. 3.6.: Flow variables in a nozzle, calculated with Eqs. (3.1) to (3.4) for a Hydrogen jet with 100 bar backing pressure, 300 K initial gas temperature, and a nozzle with 0.25 mm throat and 0.5 mm exit diameter. The throat is at 0 mm. The exit is at 4.5 mm.

$$\frac{T}{T_0} = \left(1 + \frac{\kappa - 1}{2} M^2\right)^{-1}, \tag{3.2}$$

$$\frac{p}{p_0} = \left(1 + \frac{\kappa - 1}{2} M^2\right)^{\frac{-\kappa}{\kappa - 1}}, \tag{3.3}$$

$$\frac{n}{n_0} = \left(1 + \frac{\kappa - 1}{2} M^2\right)^{\frac{-1}{\kappa - 1}}. \tag{3.4}$$

For a given nozzle geometry, the cross section $F(z)$ is known. Then, the Mach number can be calculated using Eq. (3.1). This equation has a subsonic ($M < 1$) and a supersonic ($M > 1$) solution for the Mach number. For $M < 1$, a convergent duct accelerates and a divergent duct decelerates the flow. For $M > 1$ it is the opposite. Since for a flow emanating into vacuum, the pressure ratio is sufficient for the flow to become supersonic, the duct really acts as a nozzle, i. e. it accelerates the flow. The flow values along the nozzle axis are shown in Fig. 3.6 that correspond to the jet generated by a 0.25 mm throat diameter, 0.5 mm exit diameter, and 4.5 mm length nozzle when Hydrogen at room temperature with a backing pressure of 100 bar is applied. The flow becomes supersonic at the throat ($z = 0$ mm) and is further accelerated to Mach 2.9 or 2340 m/s. The temperature decreases to 110 K, the pressure to 3 bar, and the density to 1.9×10^{20} cm^{-3}. Figure 3.6 shows also the values for a position beyond the nozzle exit ($z > 4.5$ mm), i. e. in the free jet. They were calculated with the same formulae, i. e. as if the nozzle walls were continued as represented by the dashed lines in Fig. 3.7. The validity of this assumption is discussed below.

The parameter upon which the flow variables depend in 1-dimensional theory, can be either the Mach number, or, using Eq. (3.1), the nozzle cross-section relative to the inlet

cross-section. There is, however, no dependence on the absolute cross-section. Thus, two nozzles with the same shape but scaled to different sizes create the same exit pressure, temperature, and density, as long the continuum approximation holds. The same holds for two nozzles with the same throat and exit cross-section but a different length (i. e. different nozzle divergence angles), as long as the flow is confined by the nozzle walls. Only if the nozzle divergence angle is larger than the maximum turn angle [Eq. (3.5) below], the flow becomes separated from the nozzle walls and Eqs. (3.1) to (3.4) do not correctly predict the outlet variables. It should, however, be noted that in both cases (very small and very divergent nozzles), the existence of boundary layers makes the 1D theory predictions inaccurate even when both the continuum approximation holds and the flow is not separated from the nozzle wall yet.

It is also instructive to compare the flow of two different gas species with otherwise identical parameters. In this case, the particle (atomic or molecular) mass and possibly the adiabatic exponent κ are different. Of these two parameters, the former plays no role for Mach number, temperature, pressure, and number density, but only for the absolute velocity, which is of less interest for practical applications. A different adiabatic exponent, however, changes all of the flow variables. Therefore, the density is identical for different monoatomic (or diatomic) gases but different when comparing a monoatomic to a diatomic gas: In Eq. (3.1), different κ with the same nozzle geometry ($F(z)$) leads to a different Mach number. With a different Mach number and adiabatic exponent, Eq. (3.4) yields a different density. For instance, if in the example in Fig. 3.6, the target gas is changed from Hydrogen (monoatomic) to Argon (diatomic), the Mach number changes from 2.9 to 3.5, and the number density changes from $1.9 \times 10^{20}\,\mathrm{cm}^{-3}$ to $2.2 \times 10^{20}\,\mathrm{cm}^{-3}$. This difference (16 %) is so low that one can use a Hydrogen or Helium gas jet in an experiment and characterize (Sec. 3.2.2) the nozzle using Argon, which is more suitable for characterization because of its high polarizability and low prize (compared to Helium) and for workplace safety considerations (when compared to Hydrogen).

Free jet After leaving the nozzle, the gas expands because the pressure in the jet is higher than the ambient (background) pressure in the chamber. This is referred to as an underexpanded jet [58]. Two flow zones can be distinguished in the jet (Fig. 3.7): Since the transversal expansion cannot travel into the jet any faster than with the speed of sound, there is an (unaffected) core flow zone (I), where Eqs. (3.1) to (3.4) still hold. The angle of this cone is simply the Mach angle $\zeta = \arcsin(1/M)$. The flow is expanding here as if it were still confined by nozzle walls. In the expansion zone (II), however, the flow turns outwards (Prandtl-Meyer expansion), up to a maximum angle given by

$$\theta = \frac{\pi}{2}\left(\sqrt{\frac{\kappa+1}{\kappa-1}} - 1\right) - \nu_{PM}(M,\kappa)\,, \tag{3.5}$$

where

$$\nu_{PM}(M,\kappa) := \sqrt{\frac{\kappa+1}{\kappa-1}}\arctan\sqrt{\frac{\kappa-1}{\kappa+1}(M^2-1)} - \arctan\sqrt{M^2-1} \tag{3.6}$$

is the Prandtl-Meyer function [250]. The angle strongly varies with the gas species and the Mach number. For the parameters used in Fig. 3.6 (with Hydrogen), the maximum turn angle can be as high as 85°, for the same nozzle and the same pressure but for Argon gas the angle is only 35°. Since it gives only the maximum angle, rather than an information about the form of the density profile, this is not the most relevant parameter. Beyond a distance $z_I = Md_E/2$ from the nozzle, the expansion has reached the main flow axis. From here on, the peak density decreases more strongly than in zone I. Also, the jet is less confined transversally, the further away one moves from the jet. The distance z_I can be calculated from the nozzle exit diameter and the Mach number, given in Eq. (3.1). In the literature, sometimes just the orifice diameter itself is used as a scaling parameter for the free jet. This is justified as long as nozzles with similar cross-section ratios $\frac{A_0}{A}$ are compared [60]. As in the nozzle, the flow is quite turbulent at the boundary (see below). Thus, strictly speaking, the expansion is not a pure Prandtl-Meyer expansion. However, the maximum dimensions of the flow can be described with the angle θ [60].

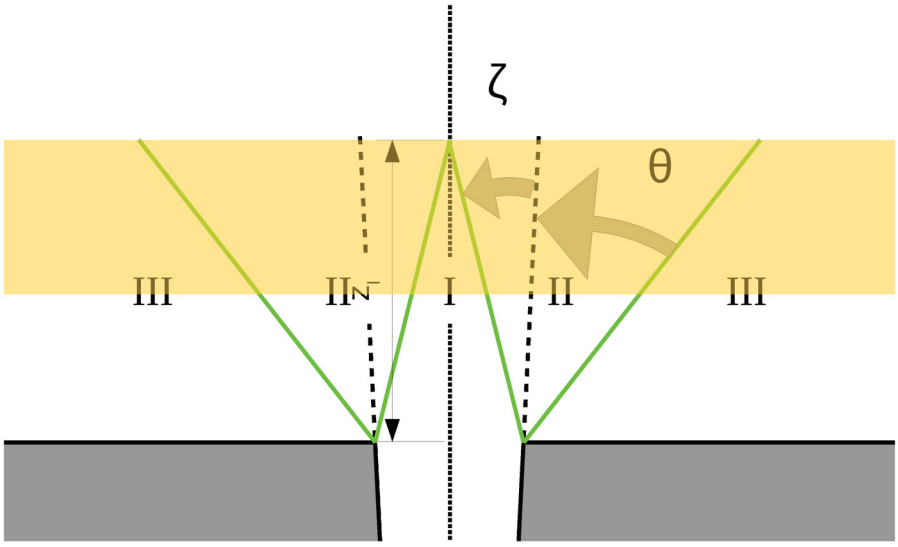

FIG. 3.7.: Sketch of the free jet emanating from a nozzle, with core flow zone (I), Prandtl-Meyer expansion zone (II), and vacuum (III). The boundaries between the zones (green lines), fictitious extension of the nozzle walls (dashed lines), and main flow axis (dotted line) are given. The Mach angle is $\zeta = \arcsin(1/M)$, the Prandtl-Meyer maximum turn angle is θ, and the maximum distance for the core flow is z_I. The typical range for the interaction axis in a laser-plasma experiment is shown in yellow.

Validity of the simple 1D model At positions further away from the nozzle than z_I the form changes qualitatively, and the on-axis density decreases more strongly [58, 59]. Therefore, Eq. (3.4) is not a correct estimate for the peak density beyond that point.

Furthermore, the model neglects the formation of boundary layers close to the nozzle walls where the flow velocity is lower. This boundary layer stems from the fact that a flow confined in a nozzle is inherently turbulent, and that the flow velocity is zero directly at the wall. Therefore, in the boundary, the velocity rises from zero to a highly supersonic value [251]. Therefore, much more energy is dissipated in this zone than in central isentropic flow [252]. The width of the free jet gradient layer at and close to the nozzle exit is determined by these boundary layers. The width of the boundary layer, in turn, cannot be derived from 1D theory and has to be modeled by computational fluid dynamics (CFD) simulations. It has been shown by Schmid and Veisz [60] that the thickness of the boundary layers depends on the length of the nozzle, i. e. longer nozzles with the same inlet and exit diameters have larger boundary layer. The resulting validity range between d_E and z_I (yellow shade in Fig. 3.7) is the usual range where the interaction in a laser-plasma experiment takes place [250], as was also the case in the experiments described here. At such a distance, the gradient layer is wider (i. e. a smoother transition from vacuum to gas) and governed by the expansion outside the nozzle. A typical value for a Mach number is $M = 3 \ldots 4$, so for a 500 μm diameter exit nozzle, $z_I = 750\,\mu\text{m} \ldots 1000\,\mu\text{m}$. This distance is, in an experiment, far enough to avoid damage to the nozzle caused by the plasma. Experience shows that one can even go as close as 300 μm.

Also, the boundary layer displaces the streamlines of the core flow from the nozzle wall by a distance δ_G, so that the zone in which the flow is governed by Eqs. (3.1) to (3.4) is reduced in size as if the nozzle was less divergent. The displacement thickness is defined by

$$\delta_G = \int_0^{\delta_{99}} dy \left(1 - \frac{u(y)n(y)}{u_\infty n_\infty}\right) , \tag{3.7}$$

where y is the coordinate normal to the wall, u is the velocity, n is the density u_∞ and n_∞ are velocity and density in the nozzle center, respectively, and δ_{99} is the distance from the wall where the flow velocity is 99 % of u_∞. This effect is stronger for smaller and longer nozzles [60]. For the geometry shown in Fig. 3.6, the displacement thickness was determined to $\delta_G = 0.05 d_E$ using the empirical formula in Ref. [245], which is low enough to neglect its influence on the on-axis density.

Furthermore, this essentially 1-dimensional treatment does not take into account the transversal shape of the nozzle. Since the flow variable relations depend only on the cross-section, they can be used to approximate an asymmetric nozzle with an axisymmetric one that has the same cross-section profile along the main flow axis.

3.2.2. Characterization

In order to know the gas jet density profile in an experiment, the neutral gas density was measured in an ex-situ characterization. Since gases have a comparably weak absorption

coefficient, the refractive index was measured by interferometry. The setup used is a Mach-Zehnder interferometer (Fig. 3.8). The gas jets in general being asymmetric, the density was calculated using a tomographic approach detailed below.

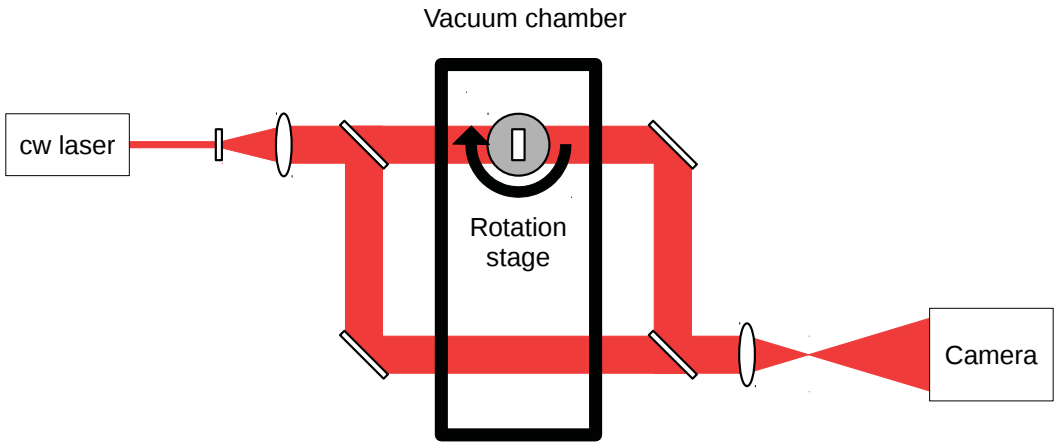

FIG. 3.8.: Mach-Zehnder interferometer.

For the nozzles used for the experiments in Chap. 5, the same gas species as in the experiments (i. e. Hydrogen) was used for characterization. For the nozzles used in the other experiments (Chap. 4 and 6), Argon was used since the use of Hydrogen was limited due to safety regulations. In this case, the densities measured with Argon were scaled using Eq. (3.1) and Eq. (3.4) to obtain the corresponding neutral gas density for Hydrogen.

Mach-Zehnder interferometer The setup used for the offline gas target characterization is shown in Fig. 3.8. The beam of a Helium-Neon laser (continuous wave, at a wavelength of $\lambda = 632.8\,\mathrm{nm}$) was expanded using an afocal telescope and split into main and reference beam by the first beam splitter. Both beams were then recombined in the second beam splitter, and the interference pattern was recorded onto a charge-coupled device (CCD) camera. The gas jet was imaged onto the camera with a lens. To realize a tomographic measurement, the gas jet itself was rotated about an vertical axis (the z axis), i. e. perpendicular to the main interferometry beam. For a number of N angles, an interferogram $I(x_l, \theta_l, z)$ was recorded. The index $l = 1 \ldots N$ identifies the projection with the angle θ_l. The N different angles span equidistantly over a range of 180°. In our case, following the approach given by Landgraf et al. [59], 4°, i. e. 45 projections have been done. This corresponds to a spatial resolution of $35\,\mu\mathrm{m}$, comparable to the point spread function of $1.22\,\lambda_0\,F = 9\,\mu\mathrm{m}$ (for $\lambda_0 = 633\,\mathrm{nm}$ and an f number of $F = 12$) of the imaging system.

In addition to the interferograms from the gas jet, an interferogram without it (ref-

erence) was recorded. For the following derivations, the coordinate system (x, y, z) is rotated (so that the jet is invariant) against the laboratory frame (x_l, y_l, z). From the interference patterns $I_G(x_l, \theta_l, z)$ (gas jet interferogram) and $I_{\mathrm{R}}(x_l, \theta_l, z)$ (reference interferogram), the phase shift patterns $\phi_{\mathrm{G}}(x_l, \theta_l, z)$ and $\phi_R(x_l, \theta_l, z)$ were determined using a Fourier transform [59].

Phase shift determination for the individual interferograms Rather than using the interferometer in its zero configuration (i. e. parallel beams after recombination) the beam splitters were rotated so that an additional shift ϕ' in phase difference was generated, which depends on the z position as follows:

$$\phi'(z) = 2\pi \frac{z \sin \theta_{BS}}{\lambda} , \tag{3.8}$$

where θ_{BS} is the angle by which the second beam splitter is turned. This way, an interference pattern with many horizontal stripes is created. The phase difference between the top and the bottom of the image is now larger than the phase difference induced by the gas jet. Therefore, it is possible to extract the phase using a Fast Fourier transform (FFT) algorithm.

The interferogram is a stripe pattern that can be described as

$$I(x_l, z) = I_0 + 2\, I_1 \cos\left(\frac{2\pi z}{d} + \phi(z)\right) = I_0 + I_1 \left(e^{i\,[2\pi z/d + \phi(z)]} + c.\,c.\right) . \tag{3.9}$$

where d is the distance between two unperturbed fringes, and $c.\,c.$ denotes the conjugate complex. Performing a FFT, filtering in the Fourier space, and backtransforming allows to remove noise and the background (zeroth order). This filtered interferogram in then a pattern

$$I_{\mathrm{G,\ filt.}}(x_l, \theta_l, z) \propto e^{i\,[2\pi z/d + \phi(z)]} \tag{3.10}$$

for the gas jet interferogram, and

$$I_{\mathrm{R,\ filt.}}(x_l, \theta_l, z) \propto e^{i\,2\pi z/d} \tag{3.11}$$

for the reference interferogram.

The phase is then

$$\phi(x_l, \theta_l, z) = \Im\left[\log\left(\frac{I_{\mathrm{G,\ filt.}}(x_l, \theta_l, z)}{I_{\mathrm{R,\ filt.}}(x_l, \theta_l, z)}\right)\right] \tag{3.12}$$

where $\Im$ denotes the imaginary part [253].

These steps (measurement and determination of the phase) were done for a total of N angles, spanning equidistantly over a range of 180°, as mentioned above.

Tomographic refractive index and density determination From the set of projections, the density is retrieved by tomography. Since the coordinate along the rotation axis z is common to laboratory and jet coordinate system (i. e. the same transformation is applied at every height above the nozzle), the task is to reconstruct a 2-dimensional refractive index profile $\eta(x_l, y_l, z) - \eta_0$ from a 1-dimensional projection

$$\phi(x_l, \theta_l, z) = \int_{-\infty}^{+\infty} k(\eta(x_l, y_l, z) - \eta_0) dy_l \,. \tag{3.13}$$

Here, $k := 2\pi\eta/\lambda$, and η_0 is the refractive index of the reference path, i. e. typically equal to one. Equation (3.13) is a Radon transform [254] that can be inversed using the Filtered Backprojection (FBP) algorithm [255], or by iterative algorithms. The precision of the reconstruction depends essentially on the number of projections (i. e. angles). The FBP algorithm is exact for infinitely many projections, and it is more precise than an iterative reconstruction for more than 20 projections [59]. Since for the offline characterization, it was possible to do many quite small steps with a motorized rotation stage, 45 projections were made and reconstructed using FBP. Numerically, the FBP was implemented by filtering the phase profiles $\phi(x_l, \theta_l, z)$ in the Fourier domain using a ramp (Ram-Lak) filter function $|k_l|$ and then projecting them onto a 2D grid:

$$\Delta\phi(x, y, z) = \underbrace{\sum_{l=1}^{N} \Delta\theta}_{\text{backprojection}} \underbrace{\int_{-\infty}^{+\infty} dk_l e^{2\pi i k_l x_l}}_{\text{inverse Fourier transform}} \underbrace{|k_l|}_{\text{filter}} \underbrace{\int_{-\infty}^{+\infty} dx_l e^{-2\pi i k_l x_l}}_{\text{Fourier transform}} \phi(x_l, \theta_l, z) \,. \tag{3.14}$$

This yields a phase shift for each infinitesimal volume [59, 256]. Calculating the refractive index from this backprojected phase shift is straightforward because

$$\frac{\Delta\phi}{2\pi} = (\eta - 1)\frac{L}{\lambda_0} \tag{3.15}$$

where L is the edge length of the probe volume, and λ_0 is the vacuum wavelength of the laser used for the characterization. For an isotropic gas, frequencies in the optical range, and refractive indices close to unity,

$$\eta^2 - 1 = \frac{\alpha n}{\epsilon_0} \,, \tag{3.16}$$

where n is the density, α is the polarizability of the gas and ϵ_0 is the vacuum permittivity [257]. Therefore,

$$n = \frac{2\epsilon_0}{\alpha}\frac{\lambda_0}{L}\frac{\Delta\phi}{2\pi} \,. \tag{3.17}$$

Some values for the polarizabilities of gases are given in Table 3.1.

TABLE 3.1.: Polarizabilities of relevant gases.

Species	Polarizability $\alpha[\mathrm{Cm}^2/\mathrm{V}]$	Ref.
Argon	1.658×10^{-40}	Asher et al. [258]
Hydrogen (molecular)	8.901×10^{-41}	Gough et al. [259]
Nitrogen (molecular)	1.958×10^{-40}	Gough et al. [259]

3.3. Target specifications for the experiments

For the experiments in Chap. 4 to 6, gas targets have been used. The gas jets have been characterized before the experiments. In some experiments (see below), the gas was ionized and heated with a pre-pulse. This section summarizes the neutral density profiles for each target and (in case of the preformed plasmas) the expected density after interaction with the prepulse.

3.3.1. Target for the proton acceleration experiment

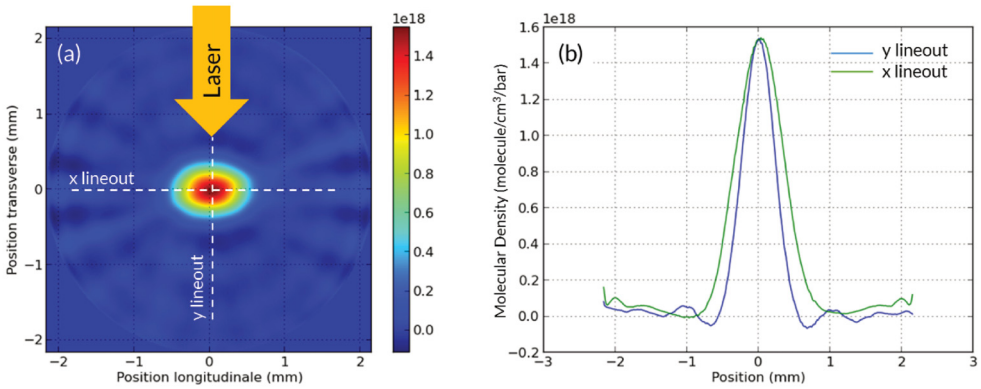

FIG. 3.9.: Density profile of the target for the CSA experiment.

For the CSA experiment (Chap. 4), a near-critical target (1 . . . 3 times the critical density) was needed. In order to have a sufficiently collimated jet, a supersonic gas jet had to be used. Given that the laser operates in the near-infrared 1054 nm, the critical density is $1.0 \times 10^{21}\,\mathrm{cm}^{-3}$ [Eq. (1.3)]. As mentioned in Sec. 3.2.1, the free jet density is related linearly to the backing pressure and on the order of $10^{18}\,\mathrm{cm}^{-3}$/bar, that is, the backing pressure must be on the order of 1000 bar to reach that density.

The target was a Hydrogen gas jet, generated with a Laval nozzle with a 0.3 mm × 0.3 mm throat, a 1 mm × 0.3 mm rectangular exit, and a length of 3 mm.

The backing pressures of up to 1000 bar were generated with a pneumatic gas compressor (Haskel, Burbank/CA, USA). The gas jet was pulsed with an EX-40 electro-valve (Clark Cooper, Roebling/NJ, USA).

For this nozzle, an offline gas jet density characterization (Sec. 3.2) had been done before the experiment.

The density varies linearly with the backing pressure. A backing pressure of 900 bar leads to a density of $2.71 \times 10^{21}\,\mathrm{cm}^{-3} = 2.7\,n_c$ for a 1054 nm laser.

3.3.2. Target for the first ARCTURUS SBS experiment

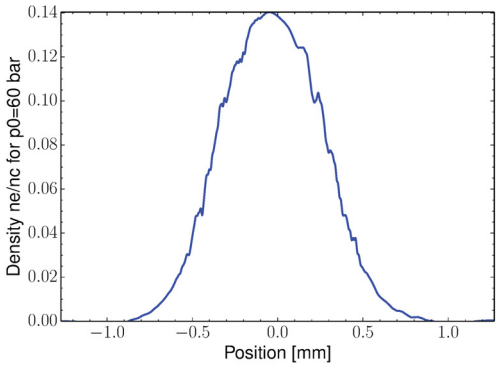

FIG. 3.10.: Nozzle I (cylindrical). Density for 60 bar, 600 μm above nozzle.

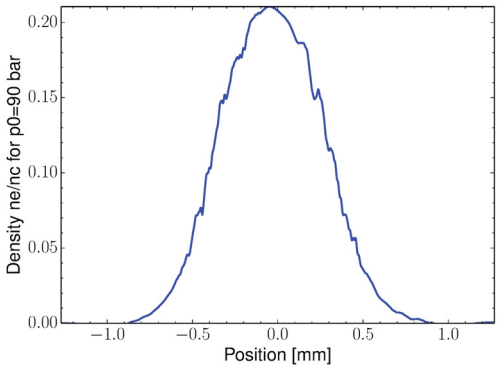

FIG. 3.11.: Nozzle I (cylindrical). Density for 90 bar, 600 μm above nozzle.

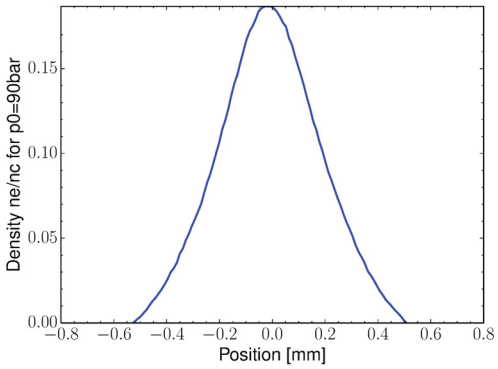

FIG. 3.12.: Nozzle II (rectangular). Density for 90 bar, 300 μm above nozzle.

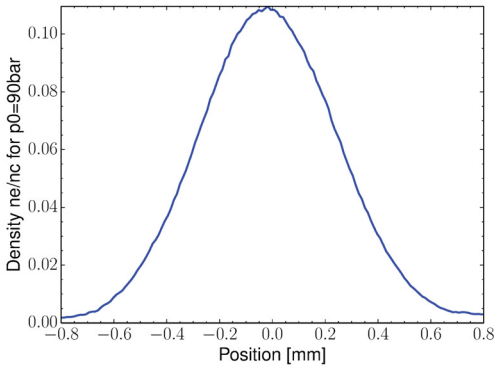

FIG. 3.13.: Nozzle II (rectangular). Density for 90 bar, 600 μm above nozzle.

The target gas was Hydrogen. Figures 3.10 to 3.13 show the plasma electron density profiles for the four different target configurations: The density and shape of the gas jet (and therefore, interaction length) were varied using two different nozzles and by varying the distance of the interaction region to the orifice. The density was regulated

by changing the gas pressure. Densities are specified in terms of the critical density for 800 nm, i. e. $n_c = 1.74 \times 10^{21}\,\mathrm{W/cm^2}$. The off-line target characterization had been done with Argon. Therefore, it was taken into account that a diatomic gas, (i. e. Hydrogen) gives a different molecular density, that the backing pressure was different, and that one Hydrogen molecule liberates 2 electrons (i. e. for fully ionized Hydrogen).

3.3.3. Target for the second ARCTURUS SBS experiment

In this experiment, a plasma was created by a short prepulse whose parameters (focusing, delay, and intensity) were chosen to obtain a plasma as homogeneous and hot as possible. In order to limit the amplifier length, a nozzle with a 0.5 mm exit diameter was used. The gas density profile was approximately Gaussian with 0.5 mm amplifier length (Fig. 3.14).

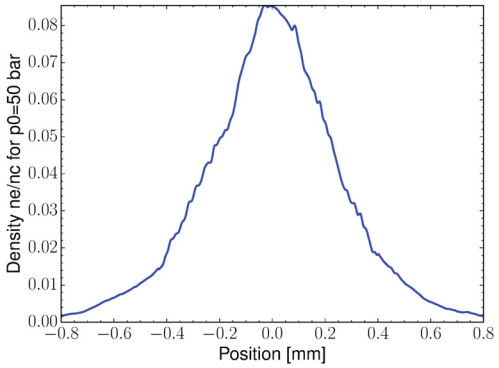

FIG. 3.14.: Gas jet for the second ARCTURUS SBS experiment: Density profile, 600 μm above the nozzle.

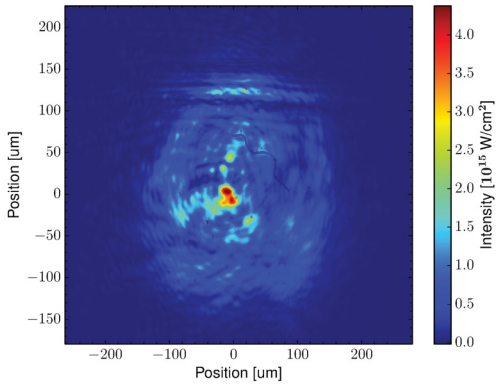

FIG. 3.15.: Focal spot of the ionization prepulse in the second ARCTURUS SBS experiment. Image taken in low-energy 10 Hz alignment mode.

The ionization prepulse was generated from one of the main beamlines of the facility. It was stretched by changing the distance of the compressor gratings to a duration of 0.26 ps. The pulse energy was 400 mJ on target. The beam was focused with an $f/8$ off-axis parabolic mirror ($f = 0.5$ m) that had a 10 mm diameter hole to let the seed beam through. A defocus was necessary to obtain a pulse intensity of $4 \times 10^{15}\,\mathrm{W/cm^2}$ (Fig. 3.15). The form of the pattern is mostly due to the hole in the OAP. The chirp was so that the red part of the spectrum went through the target first.

3.3.4. Target for the ELFIE SBS experiment

The target was a preformed plasma, generated by ionizing a supersonic Hydrogen jet with a prepulse. The nozzle was rectangular and had a length of 0.75 mm along the pump and seed beams' interaction axis and a width of 2 mm. The density was chosen by

changing the backing pressure of the nozzle. In the shot series detailed below in Sec. 6.2, the backing pressure was 55 bars, and the beams were focused 0.4 mm from the orifice. As shown in Fig. 3.16, the corresponding peak electron density in the interaction zone, inferred from ex-situ tomography with the assumption of full ionization by the prepulse, is $n_e \approx 10\,\%n_c$, and the interaction length (FWHM) is 0.5 mm.

In order to obtain a big homogeneous fully ionized plasma, the gas was preionized using the ELFIE long pulse (30 J in 450 ps) focused with a lens and a hybrid phase plate (HPP), as shown in Fig. 3.17. A HPP is a glass substrate with a coating that forms a pattern of small zones. It randomly adds a phase (between 0 and 2π) to the beam, i. e. it reduces the transversal coherence in the near field and thus in the focal plane. Focusing such a beam with a lens allows to obtain in the far field a focal spot that is much bigger than without the phase plate. Its overall shape is determined by the size of the zones on the phase plate, and contains speckles whose size is dictated by the f-number of the converging beam [260].

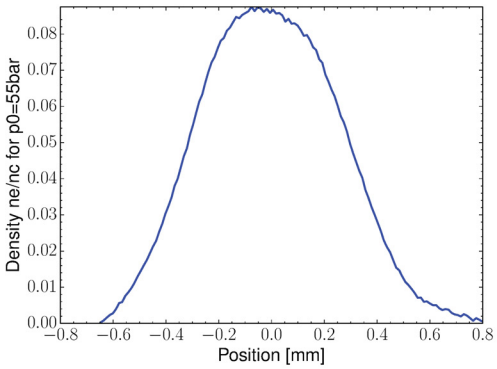

FIG. 3.16.: Gas jet density profile of the nozzle 0.4 mm above the nozzle exit. The axis of the pump and seed laser beams is horizontal.

The phase plate used in this experiment (made by Scitech, Didcot, UK) was designed to generate a 0.3 mm × 1 mm mostly homogeneous focal spot. The beam was focused with an $f/7$ lens. Figure 3.17 shows the focal spot obtained using these optics using a diode laser and scaled to an intensity corresponding to the actual ELFIE uncompressed pulse.

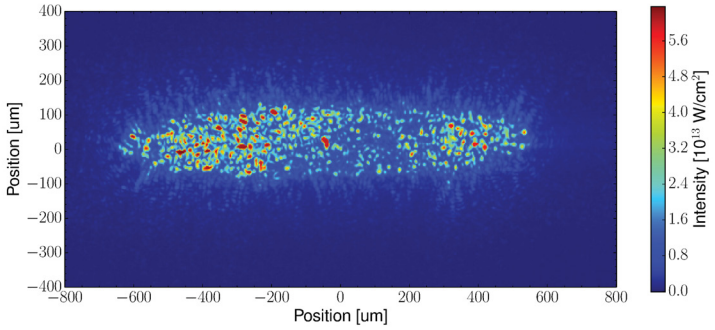

FIG. 3.17.: Focal spot of the ionization beam at the ELFIE SBS experiment.

Since the speckles inevitably generate small scale inhomogeneities in the plasma, this

pulse was made to arrive 1.5 ns before pump and seed. During this time, the plasma density and temperature inhomogeneities are likely smoothed by hydrodynamic expansion and heat conduction.

Using an analytical approach [Denavit and Phillion (1994) [261], Eq. (5) and (6)], the electron temperature can be estimated. For these parameters, one obtains an electron temperature of 280 eV right after the ionization pulse has passed. During the 1.5 ns delay, the electron temperature decreases due to expansion and heat conduction. Therefore, 280 eV is an upper limit for the electron temperature.

3.4. Diagnostics

3.4.1. Optical spectrometry

The straightforward result one obtains by using an optical spectrometer is, obviously, the spectrum of the incoming pulse. The analysis of these spectra can deliver some more interesting results.

Statistical analysis

If spectra from a campaign on a high-repetition rate system are to be analyzed, there is a huge number of shots is to be analyzed. This motivates determining some parameters numerically by an algorithmic analysis that can be easily applied onto a huge number of shots and allows to compare the results.

Starting from a recorded spectrum $S(\lambda)$, in a spectral range from λ_{min} to λ_{max}, one can calculate the center of mass,

$$\lambda_{com} = \frac{\int_{\lambda_{min}}^{\lambda_{max}} S(\lambda)\,\lambda\,d\lambda}{\int_{\lambda_{min}}^{\lambda_{max}} S(\lambda)\,d\lambda}\,. \tag{3.18}$$

One can also calculate a width,

$$\Delta\lambda = \sqrt{8\ln(2)}\left(\frac{\int_{\lambda_{min}}^{\lambda_{max}} S(\lambda)(\lambda-\lambda_{com})^2 d\lambda}{\int_{\lambda_{min}}^{\lambda_{max}} S(\lambda) d\lambda}\right)^{1/2}\,, \tag{3.19}$$

where the normalization factor $\sqrt{8\ln(2)}$ has been chosen so that for a Gaussian shaped spectrum, the width would correspond to the FWHM. Since realistic spectra can have an arbitrary shape, this is obviously not given all the time. However, it allows to compare spectra of a whole shot series easily.

It should be noted that these statistical techniques are useful only applied to a correctly denoised spectrum. A background from electronic noise or parasitic light would modify the results and make them useless.

Time development of short pulses

Since a chirped pulse with its electric field $\mathcal{E} \propto e^{-t^2/\tau^2 - i\alpha t^2}$ probes any target with different frequencies at different times, fast processes are encoded in its spectrum. The temporal shape of the process can be retrieved using a spectrometer. The temporal coordinate is

$$t = \frac{\omega_0 - \omega}{2\alpha}, \tag{3.20}$$

where ω_0 is the central frequency of the pulse and ω is the frequency coordinate. The smallest time that can still be resolved is τ_{min}, given by

$$\frac{\tau_{min}}{\tau_0} = \sqrt{\frac{\tau}{\tau_0}}, \tag{3.21}$$

where τ is the pulse duration of the chirped pulse and τ_0 is the duration of the bandwidth-limited pulse with the same spectrum [262].

Detection of infrared light: Raman spectra

As mentioned in Sec. 2.1.2, a laser beam propagating in a less-than-quarter-critical plasma always undergoes sizable Raman scattering. For backward or sideward scattering, the wavelength of the scattered electromagnetic wave is related to the density by Eq. (2.44). Therefore, measuring the scattered light's spectrum allows to obtain information on the plasma electron density.

For example, for a plasma with a density ranging from 0 to 10 % n_c, the Raman scattered radiation is to be found between λ_0 and 1.46 λ_0. For a Ti:sapphire laser ($\lambda_0 = 800\,\text{nm}$), the diagnostic has to be sensitive between 800 nm and 1170 nm. For an Nd:glass laser at $\lambda_0 = 1057\,\text{nm}$, the diagnostic has to record a spectrum between 1057 nm and 1550 nm.

This light can be detected with a spectrometer, configured to have a high spectral range, forcibly at the expense of the resolution. The detector attached to it has to be sensitive in the near infrared. Indium Gallium Arsenide (InGaAs) cameras are useful in this range [263]. A commercially available camera (Xeva 152, Xenics, Leuven, Belgium) is sensitive between 900 nm and 1700 nm (Fig. 3.18) [264]. In order to prevent the laser beams or scattered light at the laser frequency from saturating the camera, an appropriate filter is used, e. g. a solid Silicon filter (transparent for wavelengths above 1150 nm) or an appropriately chosen colored glass filter (RG, Schott, Jena, Germany).

Usage and limitations To avoid ambiguities in the spectrum due to chromatic aberrations, which would otherwise be sizable over a spectral range of 550 nm, imaging should be done using exclusively reflective optics.

It is possible that with such a diagnostic, the density at the center of the plasma is not visible. This is because the signal is attenuated on its way through the plasma.

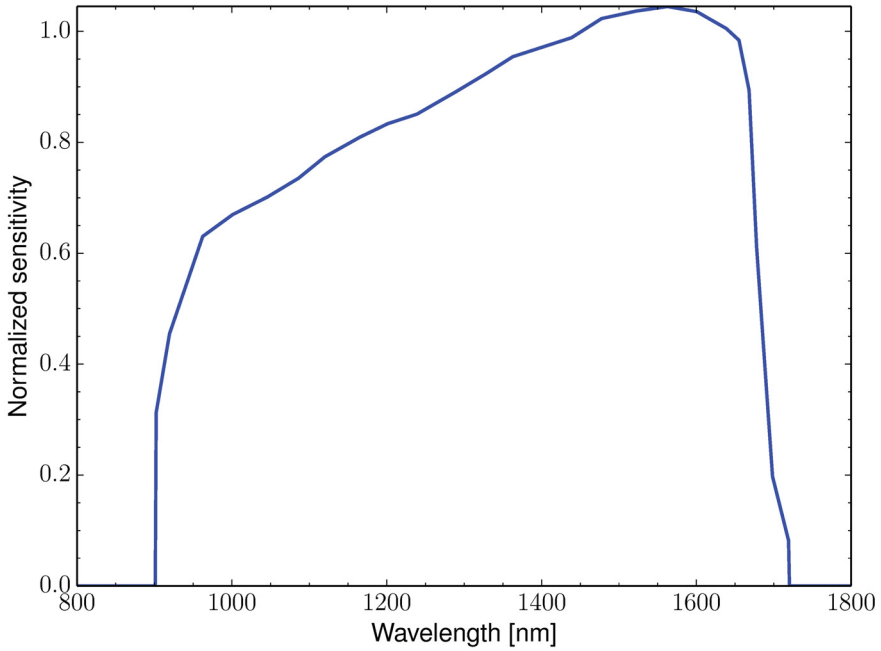

FIG. 3.18.: Response curve of an InGaAs camera.

3.4.2. Single-shot autocorrelator

For a pulse with homogeneous near-field and a known temporal (Gaussian or hyperbolic secant) shape, the duration can be determined using a second-order autocorrelator. The setup of a single-shot autocorrelator [265] is shown in Fig. 3.19.

In this setup, care has to be taken to avoid changes in the nonlinear spectral phase of the pulses up to the second harmonic crystal in order to preserve the pulse duration.

The beam is split into two replica. Since the pulse passing through the beamsplitter collects a nonlinear spectral phase, a plate of the same material as the mirror substrate is inserted into the reflected beam. This ensures that both replica acquire the same change in spectral phase. The material and thickness are chosen so that the increase of the pulse duration is not sizable for pulses longer than 50 fs. The replica are synchronized and superimposed in a nonlinear crystal, typically a potassium dihydrogen phosphate (KDP) crystal. It generates an output signal at the second harmonic by sum-frequency generation. The signal at the laser frequency is blocked by an iris and a filter. A lens images the crystal onto a camera. Since the signal intensity is proportional to the square of the incoming pulse intensity, a high-dynamic camera is used.

At zero delay, the autocorrelator trace is in the center of the crystal. At the center, the signal is created from the peak of the two pulses. Since apart from the center, the signal is created from the leading flank of one pulse and the trailing flank of the other, the spatial width of the signal corresponds to the pulse duration.

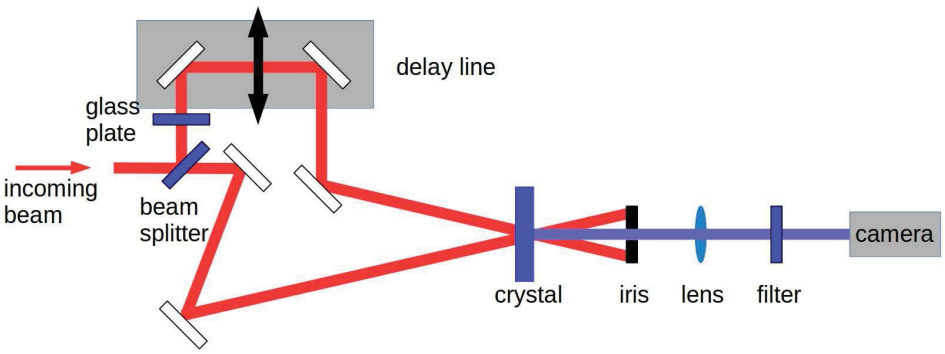

FIG. 3.19.: Schematic setup of a single-shot autocorrelator.

In order to calibrate the temporal scale, some delay known Δt delay is added to one of the replica by moving the delay line. This results in a change of the position Δx of the signal on the crystal. They are linearly related to each other,

$$\frac{\Delta t}{\Delta x} = \frac{2n \sin(\phi/2)}{c}\,, \tag{3.22}$$

where n is the linear refractive index of the crystal, c is the speed of light in vacuum and ϕ is the angle between the beams [266].

The FWHM pulse duration τ then depends linearly on the FWHM of the signal ξ,

$$\frac{\tau}{\xi} = K \frac{\Delta t}{\Delta x}\,, \tag{3.23}$$

where K is a factor depending on the pulse shape. It is $K = 1/1.414$ for a Gaussian pulse, $K = 1/1.55$ for a hyperbolic secant shaped pulse, and $K = 1$ for a square pulse [265].

To set up the autocorrelator, a suitable $\Delta t/\Delta x$ is chosen and the necessary angle ϕ between the beams is deduced from Eq. (3.22).

To calibrate the autocorrelator, the ratio $\Delta t/\Delta x$ is determined by recording the signal position for several delays. As can be seen in Eq. (3.22), the only sources of error for this ratio are a change in the refractive index n and a change in the angle ϕ. As long as the instrument is used in single shot mode, with a low repetition rate, heating of the crystal by the laser is negligible, and a change in the refractive index can therefore be excluded. Misalignment of the incoming beams, however, is inevitable because a pulse transmitted by a plasma always changes its path slightly due to refraction. A rigid shift in the beam position is not an issue per se since this only moves the position of the signal on the crystal but does not change the angle ϕ between the beams. A change in the angle can also occur. Since the chosen angles ϕ are typically small, this leads to a relative error that is proportional to the relative error in the angle. If, for instance, two irises at the autocorrelator entrance of diameter 5 mm at a distance of 500 mm fix the axis to an error

of 0.6° degrees, and $\phi = 12°$, then the maximum error of the conversion factor will be at 5%. Another source of error is the fact that pulse duration can be compared only if it can be assumed that the temporal pulse form does not change. This error, however, cannot be quantified without any knowledge about the pulse shape of a pulse after transmission by a plasma. This can be measured, in principle using more sophisticated techniques, such as a frequency-resolved optical gating (FROG) or by spectral phase interferometry for direct electrical field reconstruction (SPIDER), but these techniques are much more difficult to use, rely much more on low shot-to-shot fluctuations, and need more energy at the input.

In order to determine the duration of an unknown signal, the signal is fitted with a Gaussian curve, the FWHM is determined, and the pulse duration is calculated from Eq. (3.23). From shot to shot, intensities can be compared since $I \propto \sqrt{A}$, and the energies can be compared since $E \propto \tau I$.

3.4.3. Measurement of the amplified spontaneous emission (ASE) at a high-intensity laser facility

Unlike in the ideal case, the amplifiers in a real laser system do not only amplify the laser pulse, but also spontaneous emission growing from noise. This noise is in part emitted in the laser propagation direction and therefore amplified in the laser amplifier rods as long as there is a population inversion, i. e. during the time when the pump lasers or flash lamps are irradiating the crystal. This time is typically on the order of the nanosecond. Therefore, the amplified noise, called amplified spontaneous emission (ASE), is creating a nanosecond pedestal whose intensity is several orders of magnitude lower than the actual laser pulse intensity. Therefore, it does not harm the laser amplification nor the optics. However, as it has a low temporal coherence, it is not compressed with the main pulse and remains long when sent onto the target. The ASE contrast on target is typically 10^7 in intensity for realistic lasers, thus if the main pulse was focused to $10^{21}\,\mathrm{W/cm^2}$, the ASE intensity in the focal spot would be $10^{14}\,\mathrm{W/cm^2}$, one order of magnitude more than necessary to ionize, e. g. Hydrogen [267, 268].

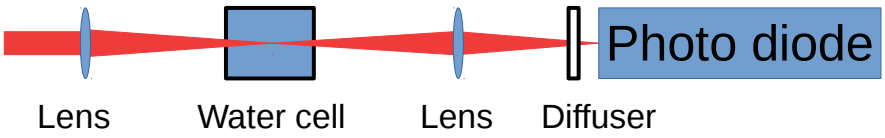

FIG. 3.20.: Water switch technique to measure the ASE energy.

Since the ASE is on a nanosecond timescale, it can in principle be measured by a fast

photodiode (with a rise time of hundreds of picoseconds). To do that, a water switch ASE monitor is used (Fig. 3.20): The leakage of the pulse is taken from behind a dielectric mirror and focused with a lens to reach an intensity high enough for the ASE to create a sizable photo-current in the diode. Since in this case, the much higher main pulse would damage the diode, a so-called water switch is employed as a saturable absorber: It is positioned so that the beam focus is in water, where the ASE is transmitted, but the more intense main pulse produces a small plasma in water, from where the laser radiation is strongly absorbed, refracted and scattered. The transmitted radiation is then weak enough so that the photodiode is not damaged, albeit still saturated. A diffuser in front of the photodiode ensures that small far-field movements do not influence the signal. In the signal, observed on an oscilloscope, the position of the main pulse is easily identified (as it is saturated). The ASE then is the slowly varying signal beginning some nanoseconds earlier, on which some prepulse traces can also be seen. Electronically integrating this signal gives a value proportional to the energy in the ASE. The factor of proportionality, i. e. the energy calibration, can be done by sending a low-energy nanosecond-scale laser pulse through the amplifier chain and measuring its energy with a calorimeter in the target chamber right before the target. The integrated signal observed on the ASE monitor then corresponds to this energy.

An ASE monitor of this kind is part of the TITAN laser facility's standard beam diagnostics [269].

3.4.4. Timing of ultrashort pulses

Multi-beam laser facilities allow to overlap different laser pulses at one point and ensure that they arrive at precisely the same time. The precision of mechanical motorized delay lines is on the order of several micrometers, corresponding to tens of femtoseconds. This allows to create relative delays at high precision. The much more challenging task is to diagnose if beams are synchronized in time, which allows to subsequently generate known absolute delays. For a coarse timing, it is always possible to superimpose both beams, or scattering of them, onto a fast photodiode and observe the pulses using an oscilloscope. The precision of this method is on the order of hundreds of picoseconds. For a more precise timing, different techniques exist.

Laser-target interaction Known effects can be used, such as creating a plasma in the target with one beam and probing the plasma with the other beam. The beams are synchronized when the plasma creation starts. They are most practical in the case of a gas target because the repetition rate is not an issue. It is limited, in that it needs an imaging system that allows to observe the plasma, and one of the beams should illuminate the plasma. With two focused beams, it is more difficult to see the change in the imaging.

Optical techniques These techniques are based on interference of synchronized beams. In this thesis, two techniques have been used: If a prism with a metallic coating is put

into TCC, both beams are reflected into the same direction. Imaging the TCC then allows to send both beams onto a diagnostic table. Observing them with a camera slightly out of focus allows to see both beams overlapped. The beams show interference fringes only if they are synchronized (Fig. 3.21).

Another possibility is to replace the prism by a piece of tracing paper. The signal of both beams is scattered on the paper, which means that overlapped speckle patterns are observed on the camera. There is a visible change in the pattern when both beams are timed. This is simpler to put into place and to align, but the interference is more difficult to see in the speckle pattern.

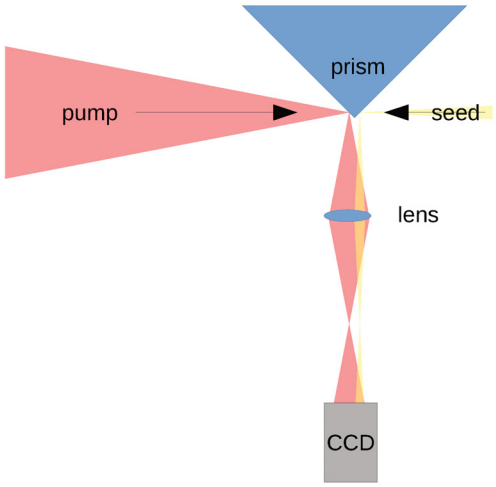

FIG. 3.21.: Timing of pump and seed beams by observing the interference pattern on a camera.

3.4.5. Magnetic ion spectrometers

Working principle of a magnetic spectrometer

A characteristic property of a proton beam is its energy spectrum. It can be measured using a simple magnetic spectrometer (Fig. 3.22). Permanent magnets in a yoke generate a magnetic field that deflects charged particles. Particles from the source enter the yoke by a slit, are deflected by the magnetic field, and are then recorded on a detector (see below). The detector and the magnetic field strength determine the spectral resolution and the lower energy limit: A weak magnet separates the energies less strongly, thus resulting in a lower resolution. A strong magnet deflects low energy particles so much that they are not visible on the detector.

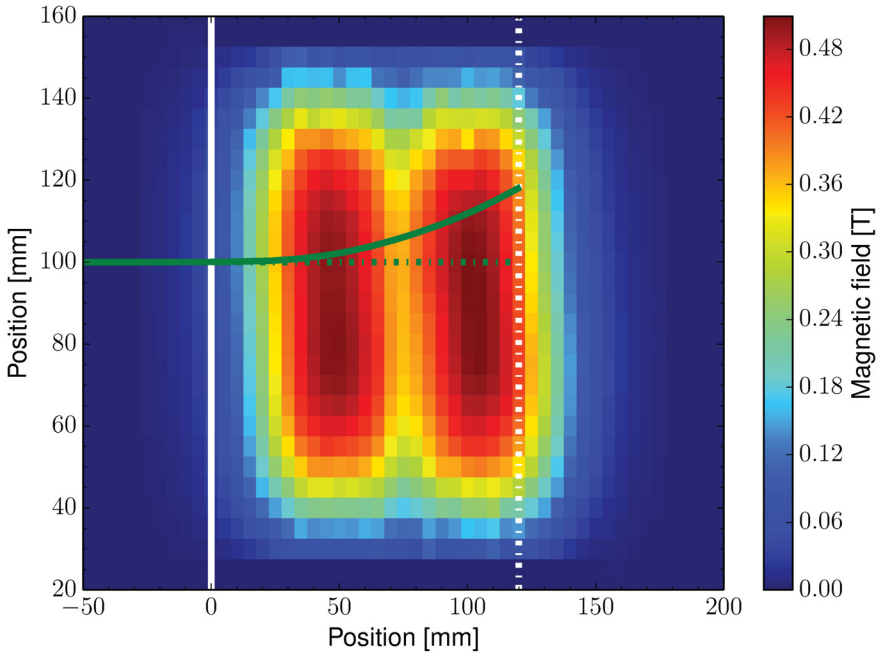

FIG. 3.22.: Magnetic field in a magnetic spectrometer with a double magnet pair. A typical particle trajectory (3 MeV proton) is shown as a continuous green line. Particle and undeflected x-rays (dash-dotted green line) enter from the left. The continuous white line on the left marks the beginning of the yoke. The dash-dotted white line on the right marks the position of the detector.

Particle and x-ray detectors

In order to detect charged particles, several kinds of devices can be used: Solid state nuclear track detectors, e. g. CR39 [270], radiochromic films (RCF) [145], scintillators [271], Cherenkov detectors, micro-channel plates (MCP), Faraday cups, and imaging plates (also referred to as image plates or IPs).

In the experiments described in the thesis, we only used IPs [272]. These detectors are based on the phenomenon of photostimulated luminescence (PSL) observed in certain materials [273]. They are ≈ 2 mm thick, film-like flexible plates. They contain specifically designed phosphor compounds that, once exposed to high-energy radiation, are excited to and trapped in a metastable state by absorbing a fraction of the radiation. The radiation can be electromagnetic, or particles (electrons, protons, ions). Upon illumination with light, e. g. in a commercial scanner, they decay into the ground state, emitting light by PSL. This process is visible on a scanned image. The digital image generated by a commercial scanner, such as the BAS 2500 (Fujifilm, Tokyo, Japan) [274], is stored using a file format that contains the signal from the detector (the so-called quantum level, QL). This is proportional to the logarithm of the actual photostimulated luminescence signal (referred to as the PSL signal). To calculate the PSL signal, the QL

signal is divided by the bit depth b, corrected for by the detector gain setting (referred to as "latitude" l), and the PSL emitted from one pixel is then $\mathrm{PSL} = Ase^{\mathrm{QL}\, l/b}$, where s is the sensitivity (another scanner setting), and A is the area of a pixel. For protons, this signal is proportional to the number of particles impinging on the detector. The factor of proportionality depends on the particle energy [275]. The image plate is deleted by exposure to light (both in the scanner and by ambient light).

Therefore, unlike RCF, it can be reused after sufficient exposure to visible light. Other advantages are its insensitivity to electromagnetic fields (as opposed to cameras coupled to MCPs), its high sensitivity, the possibility to calibrate them absolutely in energy (the flourescence emission is proportional to the radiation dose), and the high spatial resolution (limited by the scanning system). As opposed to track detectors, they do not allow to discern between different radiation types [272]. This means that CR39 are necessary in order to ascertain whether the radiation is, e. g. protons rather than x-rays. This is no major drawback in a magnetic spectrometers if the source is a Hydrogen jet, because such a target only emits electromagnetic radiation, electrons, and protons, which are easily discerned from the deflection direction.

A calibration of the image plate response was done by Mančić et al. in 2008 [275]: A broadband proton beam generated by TNSA (Sec. 2.4.1) was sent into a magnetic spectrometer. In the magnetic spectrometer, the signal was recorded both with CR39 and with an IP, mounted side by side. Counting the traces on the CR39 allows to determine the proton flux on the detector.

Additionally, a part of the proton beam was intercepted by stack of radiochromic films. This stack itself allows to determine the spectrum of the protons. This is because the protons loose energy in every layer and finally depose most of their energy at the Bragg peak (i. e. the layer where they are eventually stopped). Since the RCF are calibrated by the manufacturer for a certain energy dose, an absolutely calibrated proton spectrum can be determined.

Both spectra (RCF for the high energies, and CR39 for the low energies) then allowed to determine the IP calibration factor (PSL / proton number) for every energy.

4. Shock acceleration of protons from gaseous targets at near-critical densities

Proton acceleration by collisionless shock acceleration (CSA) has already been demonstrated at a laser wavelength of 10.6 μm. Since lasers in the near infrared, especially Nd:glass lasers at 1054 nm, deliver the highest powers, and will arguably continue to do so, it was of interest to do a proof-of-principle experiment at that wavelength. As a target, a high-density Hydrogen gas jet was chosen, which allows to reach near-critical densities. We irradiated a high density gas jet target with high intensity (1×10^{18} W/cm^2) short-pulse (5 ps) laser pulses at a wavelength of 1053 nm. Under these conditions, it is investigated whether the laser drives a shock into the target, whether protons are accelerated by TNSA or MVA (broadband) or by CSA or HBA (monoenergetically).

4.1. Acceleration experiment

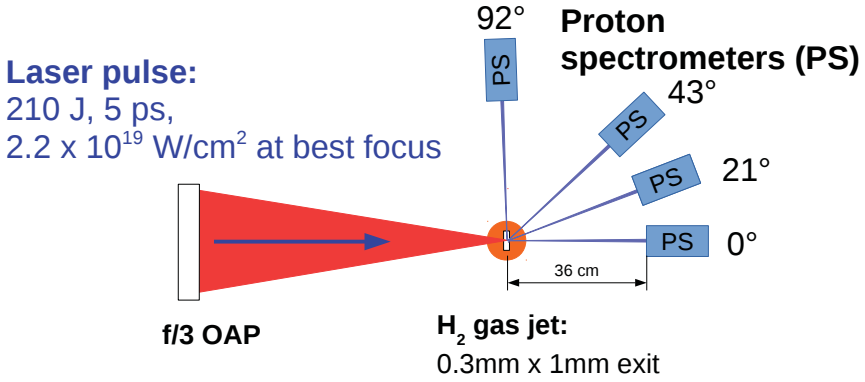

FIG. 4.1.: Schematic setup of the experiment, seen from the top.

At the Titan laser (Sec. 3.1.1, an experiment was set up with a driver laser beam, a Hydrogen gas jet target (Sec. 3.3.1) and four Thomson parabola spectrometers as diagnostics (Sec. 3.4.5). The setup is shown schematically in Fig. 4.1.

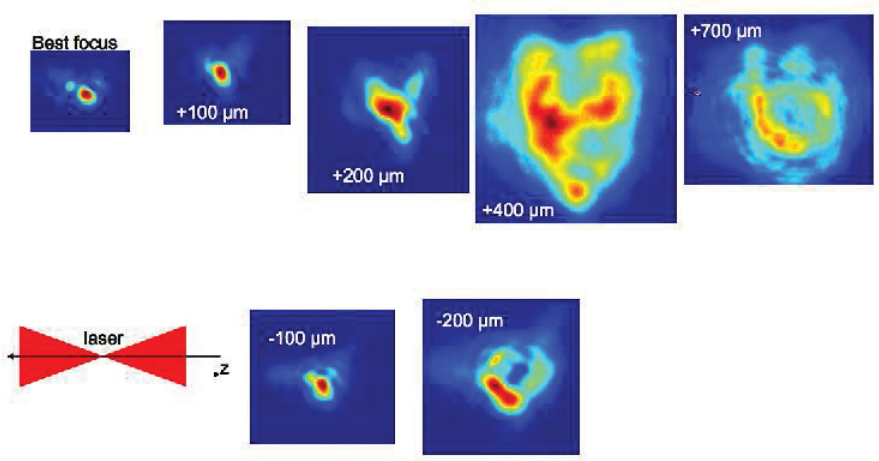

FIG. 4.2.: TITAN focal spots. Each image has its own colorscale to highlight the focal spot form. The spatial scales of the beams are all identical. The defocus (shift along the beam axis z) is negative for positions behind the best focus.

4.1.1. Laser beam

The driver laser was the TITAN short pulse at 1054 nm, with an energy of 210 J and a duration of 5 ps. Using an $f/3$ off-axis parabola (OAP), it had a best focus of 10 μm FWHM focal spot containing 30 % of the laser energy. Its peak intensity at best focus was therefore $2.2 \times 10^{19}\,\mathrm{W/cm^2}$. This corresponds to an $a_0 = 4.2$ at best focus and a relativistic critical density of $\gamma n_c = 4.6 \times 10^{21}\,\mathrm{cm^{-3}}$. In order to accelerate ions by CSA, the target density had to be slightly higher than this value. This was mitigated by reducing the laser intensity on target by a defocus, which was caused by intentionally focusing in front of the target, and / or by hydrodynamic target shaping caused by the laser ASE (see below).

A sequence of focal spots, obtained with the unamplified beam at 5 Hz, is shown in Fig. 4.2. Determining the focal spot size, depending on the position on axis, yields the longitudinal beam profile shown in Fig. 4.3. Fitting a Gaussian function to the values allows to interpolate the focus size also for intermediate defocus values. For instance, at the defocus of 150 μm, the beam FWHM increases from 10 μm to 45 μm. Therefore, the intensity is only $10^{18}\,\mathrm{W/cm^2}$ there, i. e. $a_0 = 0.93$.

The pulse did, however, not have a high contrast. As was measured with a photodiode protected by a water cell (Sec. 3.4.3), there was an ASE pedestal arriving before the main pulse (Fig. 4.4). It began with a 300 ps ramp, followed by a 1 ns pedestal before the main pulse. The ASE contained 20 mJ of energy on target, giving rise to a pedestal intensity of $10^{13}\,\mathrm{W/cm^2}$. This is already able to ionize Hydrogen, for which the ionization minimum intensity is $6 \times 10^{12}\,\mathrm{W/cm^2}$ [267, 268].

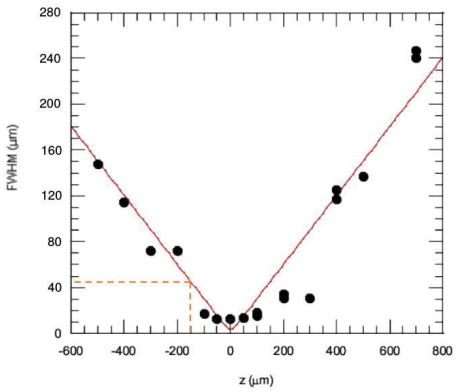

FIG. 4.3.: TITAN focus FWHM depending on defocus, with a Gaussian fit. Dashed line: beam size for 150 μm defocus as in the experiment.

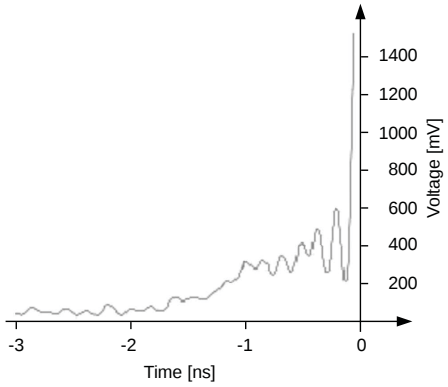

FIG. 4.4.: Measured ASE level. It is sizable from −1 ns on. The main pulse arrives at 0 ns and saturates the diode.

4.1.2. Target

In this experiment, a rectangular Laval nozzle with 1 mm × 300 μm orifice was used (Sec. 3.3.1). The laser was focused 500 μm above the orifice, onto the leading edge of the jet. The FWHM jet propagation length was 0.4 mm.

4.1.3. Diagnostics

The diagnostics were four proton spectrometers (Sec. 3.4.5), placed at the target height in a quarter-circle around the target (Fig. 4.1). Since the target gas was pure Hydrogen (H_2), all spectrometers were used as simple magnetic spectrometers, rather than Thomson parabolas [276], i. e. none of the spectrometers was equipped with electrodes to separate different ion species. The advantage of this is that the protons are deflected by the magnet in one direction only, giving the energy axis. Because the spectrometer has a known distance from the target (360 mm in the case of the 0° spectrometer), the other direction then allows to determine the solid angle into which the protons are emitted. This would not be possible with a Thomson parabola, where a pinhole ensures that only a pencil proton beam enters the spectrometer, so that only a very small spatial angle is covered. The 0° and the 21° spectrometers had a 20 mm horizontal entrance slit. Therefore, they covered an angle of ±20 mrad along the horizontal plane. The magnets were oriented so that the dispersion direction was vertical.

For all four spectrometers, Image plate BAS-TR 2025 (Fujifilm, Tokyo, Japan) detectors were used (Sec. 3.4.5). For this detector type, the absolute calibration done by MANČIĆ et al. could be used to relate the particle flow to the signal (Sec. 3.4.5).

4.2. Results

With its intensity of $10^{13}\,\mathrm{W/cm^2}$, the laser ASE was sufficiently strong to ionize the gas [267, 268], and modify its profile. The resulting shape of the target was calculated by a 2D hydrodynamic simulation (Sec. 4.2.1). Protons were accelerated by the main pulse from this preshaped target. The spectra, depending on the laser and target parameters, show features that can be attributed to different acceleration processes, which points at acceleration by CSA for shots with highest target densities (Sec. 4.2.2). In order to attribute these proton spectra to CSA, 2D PIC simulations were done which demonstrate the formation of a collisionless shock and proton acceleration by this shock for these target parameters (Sec. 4.2.3).

4.2.1. Interaction of the ASE with the target

The 1 ns duration, $10^{13}\,\mathrm{W/cm^2}$ pedestal pre-ionized the plasma and shaped its density profile. Its effect was not straightforward to analyze: Interferometry was not possible as the plasma was overcritical. Therefore, its effect had to be assessed using a hydrodynamic simulation. This allows to predict the plasma hydrodynamics reliably for plasma conditions within the parameter range of the given code. This way, plasma conditions of earlier experiments have as well been evaluated [55, 277–280].

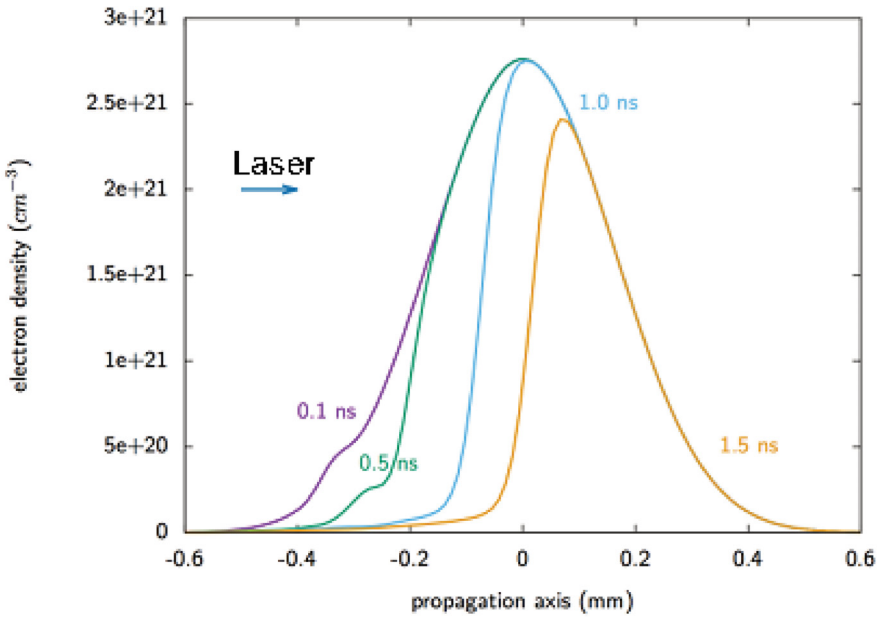

FIG. 4.5.: On-axis electron density profiles for different durations of the ASE, counted from the beginning of the pedestal. Snapshots taken right before the main pulse. FCI2 hydrodynamic simulation. The curve for 1 ns duration (blue line) corresponds to the experimental case.

This experiment is evaluated using the FCI2 (Fusion par confinement inertiel, 2 dimensions) code. FCI2 is a 2-dimensional hydrodynamic code that takes into account electron and ion heat conduction, and thermal coupling. It models laser propagation, refraction, and collisional absorption by ray tracing. Ionization, equations of state, and opacities are taken from tabulated values [281]. Starting from the correct picture of a Gaussian beam in vacuum, laser propagation is simulated by 3-dimensional ray-tracing [282]. Since ray-tracing is a geometrical optics technique, deviations from a Gaussian beam induced by diffraction cannot be modeled. However, refraction by density gradients is included in the model, as well as absorption: the power is distributed over the rays pp. Propagating in the plasma, each ray is absorbed by inverse bremsstrahlung.

In the parameter range of the TITAN ASE, the interaction of a non-relativistic laser pulse with an underdense-to-overdense target had to be modeled, which is in the parameter regime for which FCI2 has been validated [283, 284]. In contrast, FCI2 could not have been used for the interaction of the main pulse with the plasma because (1) it does not include the relativistic effects expected at this intensity and (2) as a hydrodynamic code it cannot model any effects on a timescale as short as 5 ps nor acceleration of individual particles. A minor drawback of FCI2 is that it cannot model ionization by the laser pulse, so that a fully ionized but cold target had to be assumed by the simulation.

The target was simulated on a 2-dimensional axisymmetric grid with total dimensions of 1.2 mm length and 0.4 mm diameter. The on-axis gas jet density profile was set as a Gaussian with the width of 0.4 mm and the peak density known from the offline characterization. The initial electron temperature was set to 1 eV, a low value that is realistic for a cold target without conflicting with the hypothesis of full ionization. This also avoids setting the temperature to zero, which would lead to a singularity in the inverse bremsstrahlung absorption coefficient. [Eq. (2.56)]. Not modeling the ionization can in principle lead to a minor overestimation of the available laser energy because the real laser pulse's leading flank can pass through an initially unionized or partly ionized gas. Also, the form of the blast wave created by the ASE can be different since the outer parts of the beam are ionizing the target even less. However, the differences on axis are minor.

The results of the irradiation of the jet by the prepulse are shown in Fig. 4.5. As can be seen, the plasma is pushed into the forward direction so that the density profile is steepened. This also means that the plasma is moved away from the laser focus, so that the subsequently arriving main laser pulse is effectively defocused to approximately 150 μm. The main pulse being focused with an $f/3$ parabola, this increases the focal spot size and reduces the intensity from 10 μm FWHM, 2.2×10^{19} W/cm^2, and $a_0 = 4.2$ to 45 μm FWHM, 3×10^{18} W/cm^2, and $a_0 = 1.6$ at the critical density interface position. Therefore the relativistic critical density decreased from $\gamma n_c = 4.6 \times 10^{21}$ cm^{-3} to $\gamma n_c = 1.9 \times 10^{21}$ cm^{-3}. As mentioned above, some shots were done where the focus was even more in front of the center of the gas jet, so that the defocus was even stronger. The accordingly reduced intensity was taken into account for the considerations below.

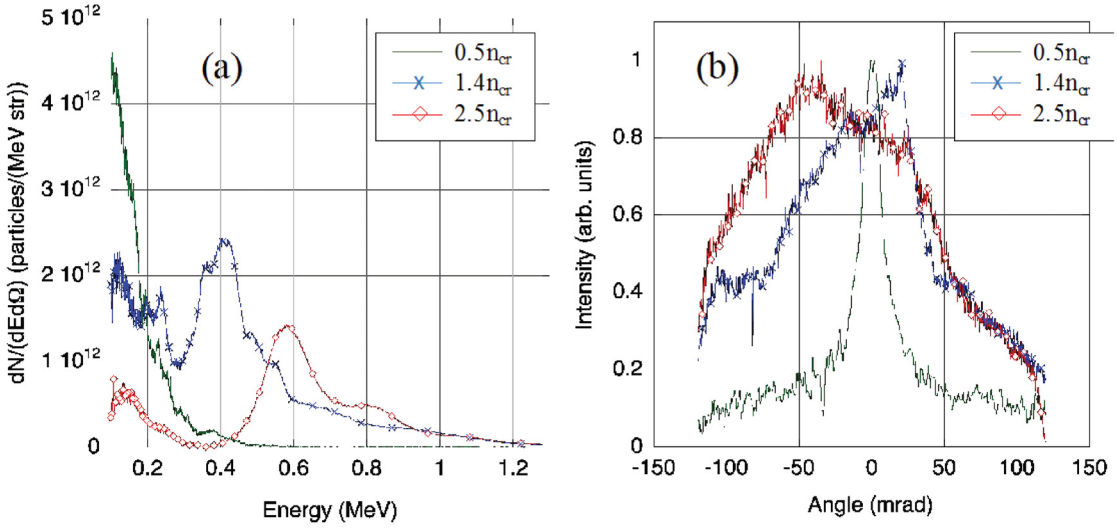

FIG. 4.6.: Experimental a) proton spectra and b) proton divergence from the forward (0 degree) proton spectrometer, measured on three shots with different backing pressures.

4.2.2. Proton beam

Varying the backing pressure to values up to 900 bar, the peak plasma electron density was tuned to values between $0.5\,n_c$ and $2.7\,n_c$, with all of the other parameters kept unchanged.

Spectrum and collimation

Accelerated protons were detected only by the spectrometer in forward direction, i. e. at 0°. Figure 4.6 shows the spectra and divergences of the beams recorded in this proton spectrometer for various backing pressures. The minimum spectral energy of 100 keV was the instrument lower detection limit. As can be seen, the spectrum has a high bandwidth and a low angular divergence for an undercritical plasma, and shows a peak and a higher angular divergence for an overcritical plasma. It should be stressed that all these spectra and divergences have been recorded with the same proton spectrometer (in forward direction) in one series of shots.

Proton spectra from undercritical plasma For the shot into underdense plasma, $(0.5\,n_c)$, the spectrum is broadband, up to 400 keV, without a peak. The angular spread of the proton beam is 13 mrad. This is much lower than for higher densities, and also lower compared to typical TNSA-generated proton beams. The high directionality in this case is not typical for TNSA per se, but rather hints at MVA, where the magnetic vortices collimate the emitted protons (Sec. 2.4.4) [285, 286].

Similarly collimated proton beams have been generated in a different experiment published by Willingale et al. in 2006 [219]. In that experiment, at the Vulcan laser

facility, a 1 ps laser pulse with an intensity of $5.5 \times 10^{20}\,\mathrm{W/cm^2}$ at 1053 nm interacted with a 2 mm diameter, $4\,n_c$ He gas jet. He^{2+} ions were accelerated in forward direction to energies up to 40 MeV, with a broadband spectrum and a divergence of < 180 mrad.

Proton spectra from overcritical plasma When passing from undercritical to overcritical density, the spectrum shows a peak that increases with the density, and is superimposed on a broadband spectrum that seems to decrease exponentially, similarly to TNSA spectra. For $n_e = 1.4\,n_c$, the energy peak is at $E = 0.4$ MeV, with a spread of $\Delta E/E \approx 0.3$, and at $n_e = 2.5\,n_c$, the peak is at $E = 0.55$ MeV, with a spread of $\Delta E/E \approx 0.16$. The angular patterns in Fig. 4.6 show that the beam is well-directed, albeit less than in the underdense case. Its spread also depends much on the density: For high densities, the protons are less directional. However, even the most divergent beam (at $2.7\,n_c$) is more directional than TNSA-accelerated proton beams, where the divergence angle is > 250 mrad [147]. Both spectral and angular change in the beam indicate a qualitative change in terms of the acceleration mechanism. For targets of this thickness, it is obvious that the light sail regime of RPA (Sec. 2.4.2) cannot be reached. However, the monoenergetic proton bunches can stem from the HBA (Sec. 2.4.2) or the CSA (Sec. 2.4.3) mechanism. The spectrally broadband contribution can originate from TNSA acceleration because the target is overdense, precluding MVA.

Scaling of the proton energy with laser intensity and target density

As discussed in Sec. 2.4.2 and 2.4.3, the accelerated ion energy depends on two important parameters: The laser intensity and the target ion density. In Eqs. (2.89), (2.109) and (2.113), relevant for HBA and CSA, this dependence is either proportional to $I^{1/4}n^{-1/2}$ or proportional to $I^{1/2}n^{-1/2}$. Figure 4.7 shows the dependence of the proton energies on the parameter $\sqrt{I/n_i}$, for several shots done under different conditions. The energies of the monoenergetic peak in the spectrum are shown as red diamonds and the areas of largest energy around the central peak are shown black error bars.

In order to compare the experimental values with the theoretical estimates for HBA and CSA, three analytical expressions were evaluated: First, the energy corresponding to the ion velocity from hole boring acceleration, as discussed in Sec. 2.4.2, was calculated with Eq. (2.89) from the article by Wilks et al. [66]. It is shown in Fig. 4.7 as blue dash-dotted line. Second, the ion energy for CSA was predicted, assuming the laser generates a planar shock. For the experimental conditions given here, an absorption coefficient for the laser of $\eta_{abs} = 0.2$ is realistic [287]. The Mach number, given by Eq. (2.109), is between 1 and 1.6 depending on the laser intensity. The velocity of the ions accelerated by the shock is then given by Eq. (2.110), which was first derived by Fiuza et al. [169]. The corresponding energy is shown in Fig. 4.7 as a green dotted line. Third, the energy corresponding to the shock velocity for a spherical shock as given by Eq. (2.113), given in the publication by Stockem-Novo et al. [114]. This energy is shown in Fig. 4.7 as a blue solid line.

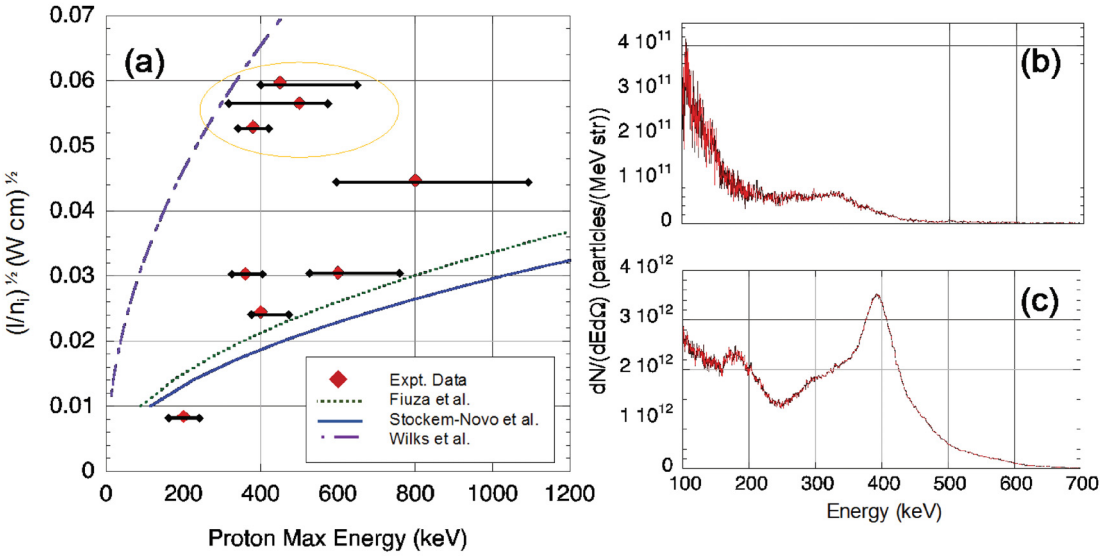

FIG. 4.7.: a) Proton energy of the depending on the parameter $\sqrt{I/n_i}$. Experimental data compared to the models by Wilks [66], Fiuza [169], and Stockem-Novo [114]. b) Typical spectrum for the low-density case (yellow encircled in a). c) Typical spectrum for a shot at higher density.

The energies were calculated using the relativistic energy-momentum relation,

$$E = A\, m_p c^2 \left(\frac{1}{\sqrt{1 - \frac{v^2}{c^2}}} - 1 \right) , \tag{4.1}$$

although the difference to the nonrelativistic energy $0.5 A m_p v^2$ is not enormous.

The experimental results for the high density shots $\sqrt{I/n_i} < 0.03\,\sqrt{\mathrm{W\,cm^2}}$ are close to the values given by Fiuza et al. and Stockem-Novo et al. They follow the same trend (higher proton energy for lower density), and their spectra all show strong peaks, as given for a typical shot in Fig. 4.7 (c). This correspondence between energy and density is a clear signature for acceleration by hole-boring or a shock. The energies range between 200 keV and 800 keV and are clearly higher than that predicted for HBA by Wilks et al. (blue dash-dotted). This leads to the conclusion that the protons have probably be accelerated by CSA. In contrast, the spectra from the low density shots with $\sqrt{I/n_i} > 0.05\,\sqrt{\mathrm{W\,cm^2}}$ (marked with a yellow ellipse) show only a weak peak on a broadband spectrum, as shown in Fig. 4.7 (b).

4.2.3. Simulations

In order to verify that the quasi-monoenergetic proton beams generated from the high density targets (Fig. 4.6 a) and Fig. 4.7 c) are created by CSA, and to obtain insight into the acceleration process, particle-in-cell (PIC) simulations were done.

Simulation setup

The simulations were done using the PIC code OSIRIS in 2D. The simulation domain is 1273 μm long and 16 μm wide. The grid had 48000 × 600 cells and 8 particles per cell. The laser main propagation axis is referred to as x, with $x = 0$ in the center of the gas jet. The total simulation time is 20 ps and the time step $\Delta t = 0.06$ fs. As an initial density profile, the result of the FCI2 hydrodynamic simulation for an ASE duration of 1 ns was used (Fig. 4.8 a), blue line) for all simulations described in this section. Additionally, some further simulations, described in Sec. 4.3, were done using a 1.9 ns prepulse. The transverse boundary conditions are periodic. The laser pulse is modeled as a plane wave with 5 ps FWHM duration, coming from the left.

The geometry being quasi-1-dimensional due to the plane wave assumption and the 80 : 1 aspect ratio of the simulation box, the proton energies will be overestimated. This effect is well-known for the TNSA case. This is a considerable disadvantage of this simulation geometry, but has to be accepted due to computing limitations: The whole target length has to be simulated, the interaction time is long, the spatial resolution must be high enough to correctly model the shock. Therefore, even in this quasi-1D approximation, a full simulation run takes 500.000 CPU hours. Another reason to use these quasi-1D simulations is that the result is so sensitive to the initial thickness that full agreement with the experiment could not even be expected from a full 3D simulation. Furthermore, the initial peak plasma density is close to critical, so that minor variations in the laser intensity lead to a change in the longitudinal position of the critical surface. Nevertheless, the simulations confirm the shock formation in these experimental conditions and reproduce the experimental results reasonably well. Table 4.1 shows an overview over the four different cases.

TABLE 4.1.: PIC simulation cases. Case I corresponds to the experimental parameters. The density was 2.7 n_c in all cases.

Case	a_0	ASE duration
I. Defocused (Exp.)	1	1 ns
II. Long ASE	1	1.9 ns
III. Best focus	4	1 ns
IV. Best focus, long ASE	4	1.9 ns

Proton acceleration under experimental conditions

In order to better understand the process as it happened in the experiment, two simulations were done with an ASE duration of 1 ns and a target density of 2.7 n_c (Cases I and III in Table 4.1. To reproduce the experimental parameters, the intensity was set to $a_0 = 1$ in case I. This is the intensity of the beam at a target 150 μm from the focal plane, as described above. To compare the process under these conditions to the

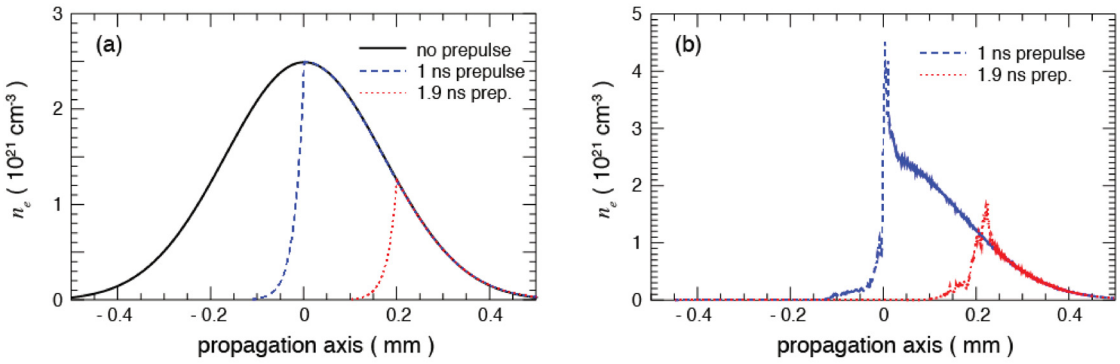

FIG. 4.8.: On-axis density profiles a) upon arrival of the main pulse (calculated from offline characterization data using FCI2) b) 5.7 ps after the main pulse (calculated with OSIRIS, using the values in (a) as input). The 1 ns prepulse case corresponds to the experiment.

acceleration with an undeformed target, another simulation run was done with $a_0 = 4$, corresponding to the experimental intensity at best focus (case III).

In both cases, the laser generates a shock at the front critical surface of the target. This can be seen in Fig. 4.8 as a peak in the density profile. The phase space for these two cases is shown in Fig. 4.9 b) and d). Protons accelerated by TNSA, HBA, and CSA can be seen in the phase space. The spectra (Fig. 4.9 b) and d) show only the CSA accelerated protons. The broadband TNSA background has been excluded from the representation to highlight only the CSA process. The peak seen in the spectrum is from the higher energy CSA accelerated protons.

These results compare favorably with the experiment: The general observation of protons accelerated by TNSA, HBA, and CSA is consistent with the experimental finding of a strong peak overlaid with a broadband spectrum. The peak energy of ≈ 1 MeV is not too far from the experimentally observed 0.6 MeV at $2.7\,n_c$ (Fig. 4.6, red curve). Since the PIC simulation results depend strongly on the input density profile (calculated with the FCI2 hydrodynamic simulation), the difference between experiment and simulation can be either an overestimation of shock acceleration in the PIC code or an inaccuracy in the hydrodynamic FCI2 simulation that influences the PIC simulation, or a combination of both. In contrast, the energy peak of ≈ 8 MeV seen in the simulation with $a_0 = 4$ (i. e. best focus and same parameters otherwise) is significantly higher than both in the more realistic simulation and in the experiment.

Proton acceleration with a shorter target

Since according to the simulations above, the acceleration by CSA took place mostly close to the front side of the target, this begged the question if the process could not be optimized with a shorter target. Therefore, two other simulations were done, with the same gas jet but an ASE duration of 1.9 ns, was more than in the experiment. As before,

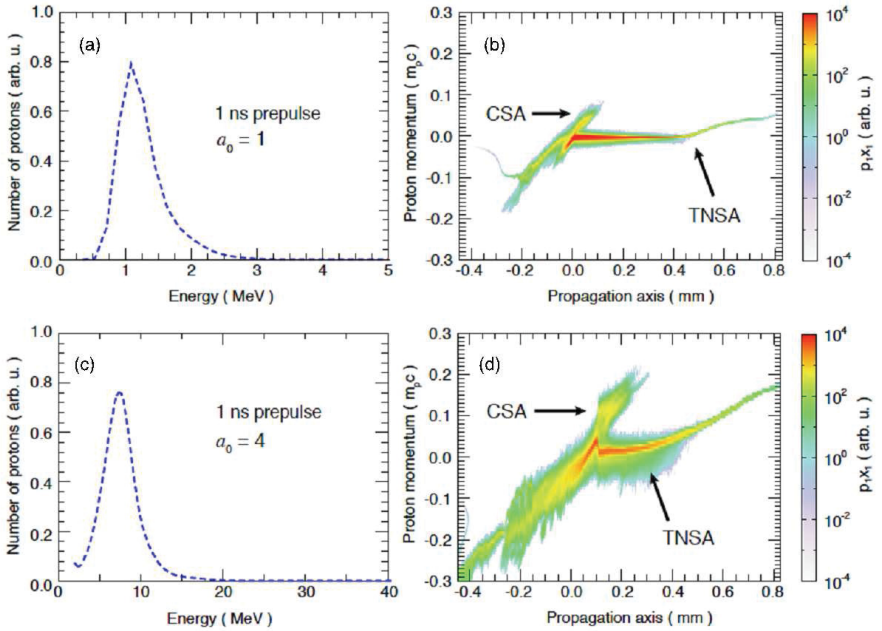

FIG. 4.9.: a), c) spectra and b), d), phase space images from the PIC simulation 11.7 ps after the main pulse for the simulation assuming a 1 ns pedestal. The amplitude of the normalized vector potential of the laser is $a_0 = 1$ (a, b) or $a_0 = 4$ (c,d).

the target deformation was calculated with FCI2 from the known gas jet density profile, resulting in a much shorter target and a lower target peak density (Fig. 4.8, red line). Although this would result in a more defocused laser under the present experimental conditions, it was chosen to compensate for that in the simulation. Therefore, two simulations were done again with $a_0 = 1$ (case II) and $a_0 = 4$ (case IV), respectively. Thus, only the effect of reducing the target length and density at constant intensity is seen here.

As can be seen in Fig. 4.10, a thinner and less dense target leads to a significantly increased proton peak energy, but also a slightly broader spectrum.

Shock formation in the simulation

In order to see directly the shock velocity, the electron density profiles from two of the PIC simulations are shown in Fig. 4.11. Since there are density gradients, there is not one single density discontinuity in Fig. 4.11 but rather several ones. They travel into the gas jet at different velocities. However, it was possible in all but one simulation case to find a dominant density discontinuity, which was responsible for most of the reflection of the ions.

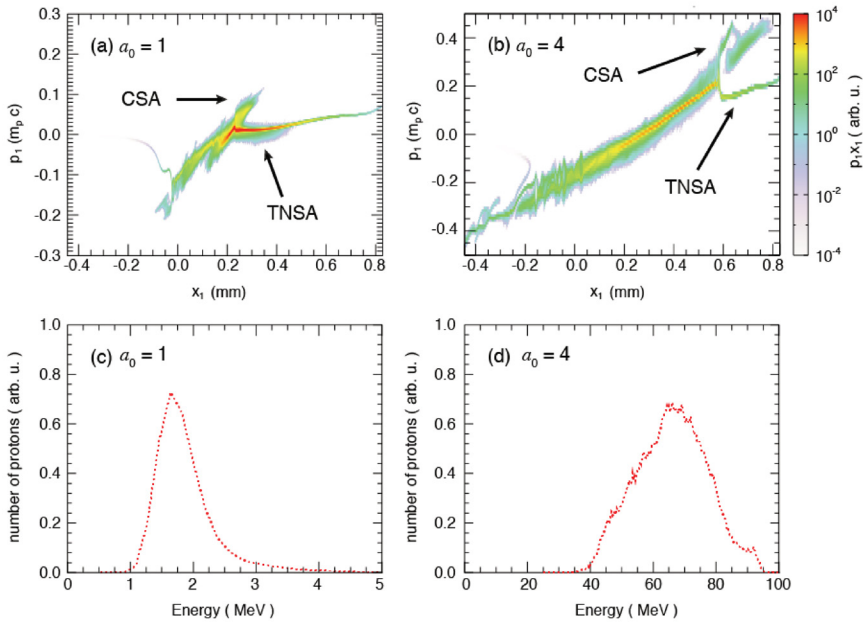

FIG. 4.10.: a), b) phase space images and c), d), spectra from the PIC simulation 11.7 ps after the main pulse for the simulation assuming a 1.9 ns pedestal. Amplitude of the normalized vector potential of the laser is $a_0 = 1$ (a, c) or $a_0 = 4$ (b,d).

In the 1 ns ASE / long target case (phase space in Fig. 4.9 b, density profile in Fig. 4.11 a), the maximum density peak velocity is $v/c = 0.017$. If ions reflected on this peak have a velocity $v_i = 2v$, then the ion energy is 0.54 MeV. This value is consistent with the spectrum of the reflected ions shown in Fig. 4.9 a) and the experimentally observed value (Fig. 4.7).

The velocity in the 1.9 ns ASE / short target case (phase space in Fig. 4.9 a, density profile in Fig. 4.11 b) is higher: $v/c = 0.024$, corresponding to 1 MeV. If ions reflected on this peak have a velocity $v_i = 2v$, then the ion energy is 1 MeV. and Fig. 4.10 c).

Additionally, the velocity of the target surface, i. e. the point where the laser is reflected, could be observed in the simulation. A summary of these values is given in Table 4.2.

In order to verify if the high density surface is a shock, it was also checked whether the upstream electron temperature T_e allowed shock formation. In cases I and II ($a_0 = 1$, for both plasma profiles), $T_e \approx 0.12$ MeV. This corresponds to a sound speed of $c_s = 0.011c$. For a shock to form, the hole boring speed must be higher than the ion sound speed, which is the case here (Table 4.2). Since the hole boring is essentially nonrelativistic ($v_{hb} \ll c$), it can be expected that $v_{sh}/v_{hb} = 4/3$ [114], which is also the case. Similarly, in cases III and IV ($a_0 = 4$), $T_e \approx 1$ MeV, so $c_s = 0.033c$. Again, $v_{hb} > c_s$, and also $v_{sh}/v_{hb} = 4/3$. This verifies the simulation result concerning the shock formation.

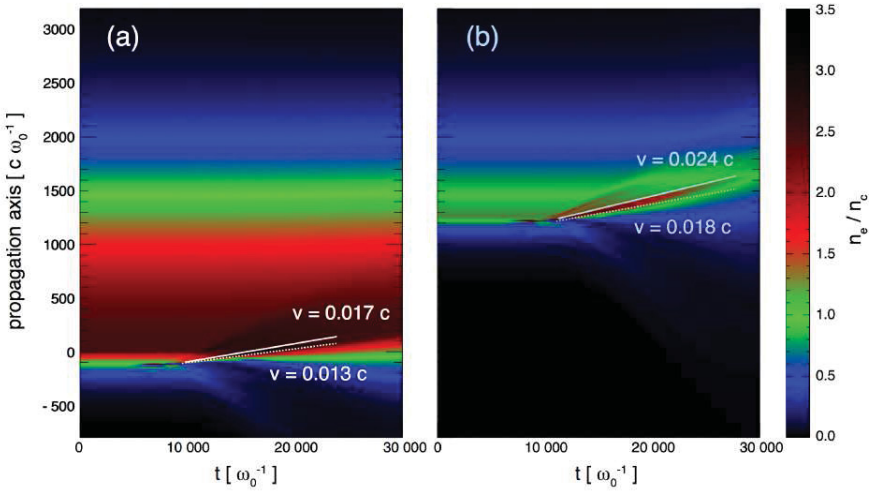

FIG. 4.11.: Electron density evolution from a PIC simulation. Time is normalized to the laser frequency ω_0, the propagation length is normalized to c/ω_0. a) corresponds to the density profile for 1 ns ASE, b) to that for 1.9 ns ASE. In both cases, $a_0 = 1$. The white dashed lines have been drawn to show the propagation of the highest density peak in time.

Therefore, several conclusions can be made from the simulations: First, under the experimental parameters, a shock forms, which propagates 4/3 times faster than the critical surface, as predicted by the analytical theory. Second, ion acceleration occurs due to HBA, CSA, and TNSA. Third, the experimentally measured proton energies are close enough to those predicted for CSA and clearly higher than those predicted for HBA.

4.3. Conclusions and prospects

With a comparably simple setup using only well-tested components that are in use for other purposes, a proton beam in the forward direction, with a small divergence and narrow spectral features, was generated. Two regimes were identified:

For an underdense plasma, the spectrum was broadband with minor peaks, and showed an extremely small angular divergence (tens of milliradians), smaller the expected divergence for TNSA. Therefore, the underlying mechanism can be MVA, similarly as observed by Willingale et al. [219, 285, 286].

For an overdense plasma, a part of the protons was accelerated monoenergetically, with peak energies up to 0.8 MeV, with a peak particle flux up to 4×10^{12} particles/MeV/sr. Simulations done with the experimental parameters, verified using analytical expressions, showed shock formation and proton acceleration due to HBA, CSA, and TNSA. TNSA explains only the broadband part of the accelerated protons. The monoenergetic part

TABLE 4.2.: PIC simulation results: The velocities are given for the critical surface (v_{hb}) and the shock (v_{sh}). The kinetic energies correspond to protons reflected on them, i. e. having twice the given velocity.

Case	a_0	ASE	v_{hb}/c	E_{HBA}	v_{sh}/c	E_{CSA}
I.	1	1 ns	0.013	0.37 MeV	0.017	0.54 MeV
II.	1	1.9 ns	0.018	0.61 MeV	0.024	1.08 MeV
III.	4	1 ns	0.049	4.54 MeV	0.065	8.03 MeV
IV.	4	1.9 ns	0.080	12.00 MeV	≥ 0.1	19.00 MeV

of the beam was attributed to CSA, because the energies predicted for CSA were close to the experimentally obtained proton energies.

Earlier experiments done with CO_2 lasers show similar proton fluxes and energies (Sec. 2.4.3): For instance, from the experiment with the ATF laser, PALMER et al. [24] report a highest flux of 3×10^{12} particles/MeV/sr at 0.6 MeV peak energy. However, their target density was $n_e/n_c = 6$ or $7 \times 10^{19}\,\mathrm{cm}^{-3}$, which is higher in terms of the critical density, but lower in absolute particle number. Experiments at lower density, e. g. $n_e/n_c = 2$ (HABERBERGER et al. [4]), have shown higher proton energies up to 18 MeV but lower fluxes (10^7 particles/MeV/sr), and the authors conclude that a higher laser intensity would be necessary.

Concerning the experiment described here, better control of the ASE can both reduce the target length (with a modified blast wave) and increase the main pulse intensity (due to the different defocus) at the TITAN laser. A PIC simulation for this case predicts a peak beyond 60 MeV, much higher than the current record for CSA protons, and comparable to the high-energy TNSA cutoff reached with similar driver lasers. These parameters are reachable with the same laser facility and a smaller gas jet or a longer laser ASE. This will be tested in an upcoming experiment done by the LULI workgroup at the PHELIX laser (GSI, Germany). Future laser facilities, allowing for shorter, more intense pulses than TITAN, offer a prospect for further optimization of CSA acceleration, as well as its exploitation at high repetition rate.

5. Experimental investigation of SBS amplification of ultrashort pulses

As mentioned in Sec. 2.1.1, the characteristic timescale $1/\gamma_{sc}$ [Eq. (2.36)] is a critical parameter for the interaction of pump and seed: In the linear phase, a seed shorter than $1/\gamma_{sc}$ is expected to develop a much longer tail before being amplified, and to grow faster in the self-similar regime [67, 73, 288] than an initially longer pulse. The chirp of the seed pulse has also an influence on the process: A spectrally wider pulse has a larger chirp factor, leading to a different phase evolution during interaction. As shown in Eqs. (2.23) to (2.26), the evolution of the phase θ, which includes the chirp phase [Eq. (2.31)], is critical for the energy transfer.

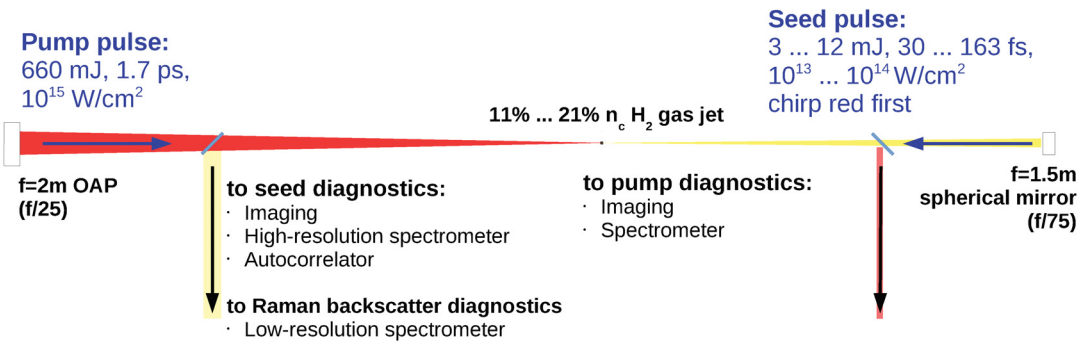

FIG. 5.1.: Schematic setup of experiment I.

In order to investigate these dependences experimentally, two experiments were set up at the ARCTURUS Ti:sapphire laser facility at ILPP (Sec. 3.1.2). In both, a $\approx 1\,\mathrm{ps}$ duration, $\approx 700\,\mathrm{mJ}$ energy, $\approx 10^{15}\,\mathrm{W/cm^2}$ intensity pump pulse was overlapped in a fully counterpropagating geometry with a $30\ldots160\,\mathrm{fs}$ duration, $1\ldots12\,\mathrm{mJ}$ energy, $\approx 10^{13}\,\mathrm{W/cm^2}$ intensity seed beam. Both beams were at 800 nm wavelength (Sec. 5.1.1).

The target was composed of Hydrogen ($Z = A = 1$) with a density of around $n_e = 10\%\, n_c$ (Sec. 5.1.2). For a pump intensity of $4 \times 10^{15}\,\mathrm{W/cm^2}$, Eq. (2.35) yields a growth rate of $\gamma_{sc} = 6 \times 10^{12} 1/s$, a timescale of $1/\gamma_{sc} = 110\,\mathrm{fs}$ and a frequency shift of 1.8 nm. Therefore, doing several runs with seed pulse durations between 30 fs and 163 fs, amplification was investigated for pulses both above and below this threshold.

After interaction, the outgoing beams were coupled out of the counterpropagating geometry using beam splitters and sent onto diagnostics for energy, pulse duration, and spectra (Sec. 5.1.3). These instruments allowed to determine whether the beams were amplified, to which extent there were losses by other processes, whether the full spectral bandwidth was amplified or only a part of the spectrum, and which duration the amplified pulses had. The use of low-resolution near infrared spectrometers allowed to investigate concurrent Raman backscattering and to compare its intensity with the Brillouin scattering, as well as measuring the target density.

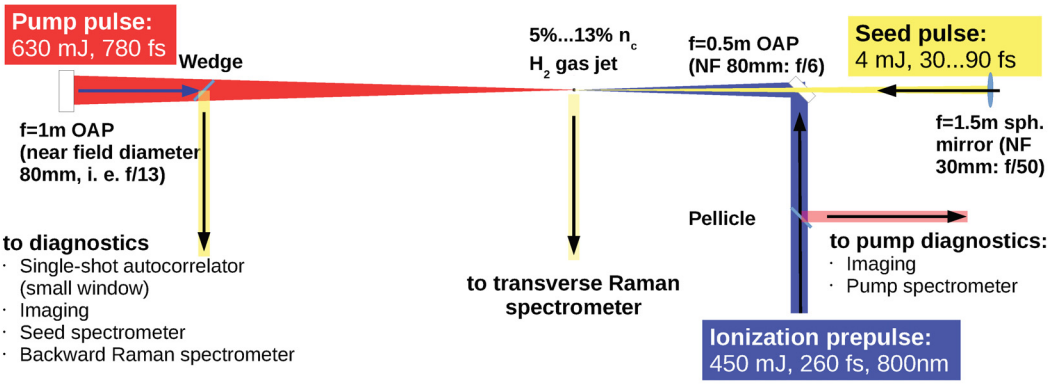

FIG. 5.2.: Schematic setup of experiment II.

The main difference between the two experiments was the target (Sec. 5.1.2): In experiment I (Fig. 5.1), pump and seed were sent into a millimeter-sized neutral gas jet (Sec. 3.3.2). Ionization was provided by the pump. These properties made the target quite absorptive.

In order to reduce the absorption of the laser beam in experiment II, the target size was reduced (from 800 μm to 450 μm) interaction length), the density was reduced (from 21 $\%n_c$ to 5, $\%n_c$), and the plasma was generated and pre-heated by a prepulse (Fig. 5.2).

5.1. Amplification experiments

In both experiments, the pump and seed pulses were fully counterpropagating (at 180°), in order to ensure that the beams overlap in the target over its full length. This is critical as the overlap has been identified as a limiting factor in an earlier experiment [289]. A fully counterpropagating setup also reduces the detrimental effect of refraction in the plasma on the beam overlap, because the beam propagation is less complex in an essentially 2D axisymmetric beam geometry.

5.1.1. Interaction beams

Pump The pump pulse was taken from one of the facility's main beamlines. The pulse energy was 650 mJ on target. The wavelength was $\lambda = (800 \pm 30)$ nm FWHM. The pulse duration was chosen by changing the distance of the compressor gratings. The chirp was positive, i. e. the red part of the spectrum came first. The duration was 1.5 ps in experiment I. Due to the shorter target (see below), the pump duration could be chosen shorter to be 0.8 ps in experiment II. The beam was focused with an off-axis parabolic mirror ($f = 2$ m, so $f/25$ in experiment I, and $f = 1$ m, so $f/13$ in experiment II). A defocus was necessary in both experiments to obtain a pulse intensity of 4×10^{15} W/cm^2 (Fig. 5.3).

Seed The seed was generated by focusing the probe beam of the facility with a $f = 1.5$ m (i. e. $f/50$) spherical mirror. The resulting focus was of 100 μm $\times$ 250 μm FWHM elliptical shape and had an intensity of up to 8×10^{13} W/cm^2 for a duration of 30 fs (Fig. Sec. 5.1.1). This is much larger than the FWHM for an ideal $f/50$ focus (27 μm FWHM). This is in part due to the imperfect focusing with a spherical mirror, and mostly due to an imperfection in the phase front that could not be corrected. Therefore, no defocus was needed to obtain a sufficient seed intensity. By regulating the compressor gratings, different durations were chosen between 30 fs and 163 fs. The seed pulse energy, at most 12 mJ on target, was reduced on some shots with the facility's attenuator setup (Sec. 3.1.2). The energy actually achieved was measured on every shot using the calorimeter in the beamline, so that the amplification could be correctly measured despite the laser shot-to-shot fluctuations. The seed chirp was chosen to be red first on all shots with $f > 30$ fs.

The focusing of pump and seed was not modified during the experiments. The seed intensity therefore depended on seed energy and duration only.

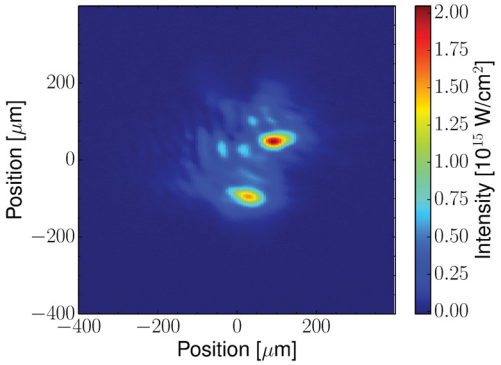

FIG. 5.3.: Focal spot of the pump pulse.

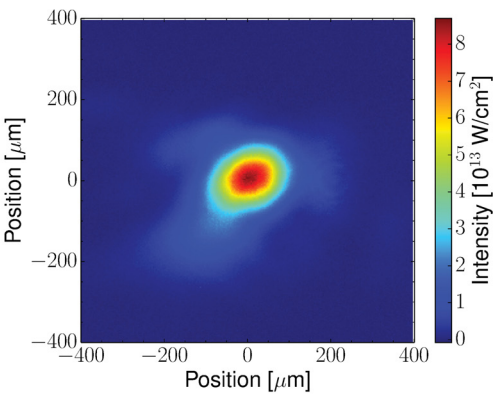

FIG. 5.4.: Focal spot of the seed pulse.

Delay The delay between pump and seed was controlled using a LIMES-150 delay stage with a stepper motor (Owis, Staufen, Germany). The maximum positioning error is 3 μm corresponding to 20 fs error on the relative delay. The zero timing (pump and seed meet in the center of the gas jet) was determined using a prism and a camera (Sec. 3.4.4) with an accuracy equal to the length of the pump beam. By convention, in both this chapter and Chap. 6 smaller delays refer to the seed coming later.

5.1.2. Target and preionization

In prior experiments (Sec. 2.3.5), both neutral gas jets [106] and preformed plasmas [6, 51] have been used as targets. In order to study the influence of the preionization, both options were chosen here:

In experiment I (Fig. 5.1), pump and seed were sent into a 12 %...21 %n_c neutral gas jet with an approximately Gaussian density profile (0.5 mm...1 mm width [interaction length]). Ionization was provided by the pump (Sec. 3.3.2). This target turned out to absorb much of the laser beam (Sec. 5.2.2), therefore diminishing the intensity and energy available for backscattering.

In experiment II, several modifications were done to avoid too much absorption. The interaction length was limited by using a nozzle with a smaller exit diameter (Gaussian density profile with 0.5 mm FWHM, Sec. 3.3.3). The density was reduced to 5 %...13 %n_c. A plasma was created and pre-heated by a short prepulse, collinear to the interaction beams and counterpropagating to the pump. The energy was fixed at 450 mJ, the highest energy available for this beam, and the pulse duration at 260 fs, the longest duration achievable by detuning the compressor. A shorter pulse duration would have lead to an intensity beyond 10^{16} W/cm^2, at which heating by inverse bremsstrahlung is less efficient. High intensities are also undesirable because the ponderomotive force, which can change the density profile, is stronger at high intensity. By choosing an appropriate focus size of 440 μm (larger than that of the 60 μm pump and 90 μm seed), the intensity was adjusted to maximize the pump transmission experimentally. The optimum ionization beam intensity turned out to be 4×10^{15} W/cm^2.

5.1.3. Diagnostics

In both experiments, the transmitted pump beam was sent onto a camera and a high-resolution spectrometer, and the seed was sent into an autocorrelator, a camera, and a high-resolution spectrometer. A part of the beam was sent into a low-resolution spectrometer in order to record the Raman backscattering of the pump pulse (see Sec. 3.4).

In experiment II, two diagnostics were different: Sideward Raman scattering was observed using another low-resolution spectrometer. Also, the autocorrelator was configured to have a higher temporal resolution at the expense of the maximum temporal range.

Outgoing pump

The transmitted pump was extracted with an uncoated glass wedge beam splitter. Afterwards, the TCC was imaged onto a camera and the entrance slit of a spectrometer using an $f = 2200\,\mathrm{mm}$ lens.

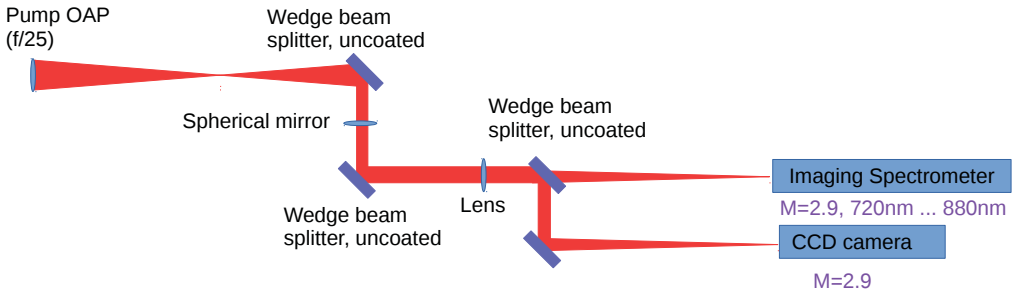

FIG. 5.5.: Pump diagnostics.

In experiment I, the solid angle collected by these diagnostics was limited to $f/21$, giving an Abbe diffraction limit of $8.4\,\mu\mathrm{m}$. In experiment II, the central part of the pump was not extracted because of the hole in the ionization beam OAP. This, however, did not prevent a spectral analysis.

Both imaging and spectrometer were using 14-bit or 16-bit CCD cameras. The spectral response was limited in both cases by an RG715 filter in front of the camera and by the camera chip response curve to $715 \ldots 1050\,\mathrm{nm}$.

The spectrometer was a high-resolution grating spectrometer, looking onto a spectral range $\geq 60\,\mathrm{nm}$ adjusted around a center wavelength of 800 nm. The slit width of typically $100\,\mu\mathrm{m}$ limited the resolution to approx. 0.5 nm. The spectrometer allowed to see the spectral transmission, which provided an encoding in time because the pump pulse was chirped.

Outgoing seed

The seed and the backscatter of the pump were extracted with an uncoated beam splitter. The beam was then split again using an uncoated pellicle beam splitter. The transmitted part, containing $\approx 90\,\%$ of the energy, was collimated by a mirror telescope and sent into a single-shot autocorrelator. To avoid pulse stretching in transmissive optics, the beam left the vacuum chamber through a 4 mm thickness, 30 mm diameter fused silica window. A detrimental effect on the pulse duration was excluded in an offline test: After the campaign, the duration of one of the facility's beams was optimized to 30 fs, as measured using a commercial SPIDER. When introducing the window into the beam, the pulse duration was not changed although the fluence was as high as in the experiment.

The pellicle beam splitter and the window were the only transmissive optics used for the beam sent into the autocorrelator.

Imaging and spectrometer The beam reflected by the pellicle beam splitter was used to image the TCC onto three other diagnostics: a camera (seed imaging) and a high-resolution spectrometer to capture the amplified seed, and a low-resolution spectrometer to measure the Raman backscattering of the pump beam. The magnification for the imaging and the spectrometer was $M = 4$ in experiment I and $M = 2$ in experiment II. The magnification of the beam on the Raman diagnostics was $M = 2$ in both experiments.

The characteristics of the imaging and high-resolution spectrometer were similar to those of the pump. The major difference was that in experiment I, the small 30 mm diameter window was used for all the seed diagnostics, therefore reducing the opening angle to $f/73$, i. e. the Abbe diffraction limit was 18 μm. An improvement was done in experiment II by extracting the seed out of the target chamber by a larger window, limiting the opening of the diagnostics to $f/55$. This allowed to monitor the form and

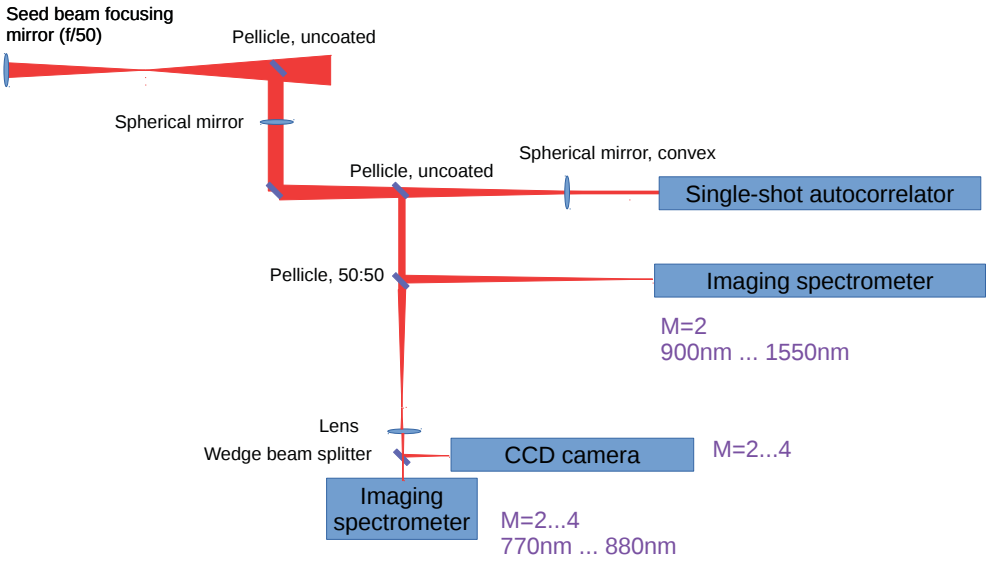

FIG. 5.6.: Seed diagnostics.

size of the focal spot and to calculate the energy (as described in Sec. 6.1.3): After calibrating the camera in each series doing a shot in vacuum, the transmission of the target was determined using the camera signal and a calibrated calorimeter positioned in the beamline. (Sec. 5.1.1).

Autocorrelator In order to measure the duration of the outgoing seed pulse, the beam was collimated by a convex spherical mirror to a diameter of 10 mm and sent into a single-shot autocorrelator (Sec. 3.4.2). There was no intermediate focus, so optical breakdown in air was avoided. The autocorrelator was the same in both experiments and equipped with a DV-420 camera (Andor, Belfast, UK). The calibration was different:

- In experiment I, the calibration was 30 fs/px, so as to give a resolution of 30 fs and total range of 15 ps. This allowed to distinguish the amplified seed from a backscattering of the pump.
- In experiment II, the calibration was changed to 7 fs/px, so as to give a resolution of 7 fs and total range of 3.5 ps. This allowed to measure the seed pulse duration precisely.

Pump Raman scattering

In order to diagnose the target density and to compare the backward Raman intensity to the seed intensity, a low-resolution spectrometer was used. It detected light in the pump backward direction (outgoing seed direction) in the range of 900 nm to 1400 nm. This corresponds to the wavelength emitted by spontaneous Raman scattering of the pump for a plasma density between 1.2 % n_c and 13 % n_c [Eq. (2.44)].

In experiment II, a second spectrometer with the same spectral range was added to measure Raman scattering in the sideward direction. Light in the 90° direction with respect to the pump and seed propagation axis was collected with an $f/4$ optics and imaged onto the entrance slit of the spectrometer. The image was turned so that the interaction axis was along the entrance slit of the spectrometer. This imaging configuration allowed to measure the Raman backscatter generated at different positions in the plasma along the interaction axis.

5.2. Single beam absorption in the target

In order to determine the energy and intensity available for backscattering, the absorption of pump and seed in the plasma are investigated.

5.2.1. Ionization

The pump beam (in both experiments) and the ionization beam (in experiment II) had similar intensities, ranging from $4 \times 10^{14}\,\mathrm{W/cm^2}$ to $8 \times 10^{15}\,\mathrm{W/cm^2}$. That means that the laser is strong enough to trigger some initial ionization by a multiphoton ionization process. Then, laser absorption by electron-neutral collision leads to full ionization.

For a Hydrogen target, the Keldysh parameter for these intensities is between $\gamma = 0.1$ and $\gamma = 0.02$. One would expect that the laser intensity is strong enough to deform the atomic potential, so that electrons leave the atom by tunneling or barrier suppression. However, it has been observed, with tens-of-femtosecond pulses, that at least at

$10^{13}\,\mathrm{W/cm^2}$ to $10^{14}\,\mathrm{W/cm^2}$ [290, 291] one can still see the distinctive peaks of perturbative above-threshold ionization (ATI). This has been ascribed to higher energy levels being involved in the ionization process, where perturbative theory applies even at higher intensities [291]. Either way, the laser energy is far above the total ionization energy needed, which for 2.4×10^{16} particles in the focal volume is about 53 mJ, less than a tenth the 630 mJ pump energy. One can conclude that the gas is ionized at the pump pulse's leading edge.

Since the plasma is cold then, it takes some time for the temperature to rise. The laser in further attenuated by collisional absorption, which converts laser energy into heat. This happens as long as the pulse is present, but calculations predict that hundreds of electronvolts are reached when the intensity reaches its peak value (see Sec. 5.2.2 below).

5.2.2. Pump transmission through the neutral gas

Transmitted energy

Table 5.1 shows the peak electron density n_e and propagation length L (full $1/e$ width from off-line gas jet characterization, assuming full ionization), as well as the experimental transmission T.

TABLE 5.1.: Gas parameters (peak density n_e and interaction length L) for different target types, and corresponding experimental pump transmitted energy T, and experimental (T_e^{exp}) and theoretical (T_e^{th}) plasma electron temperatures (see text for calculations).

Target	n_e	L	T	T_e^{exp}	T_e^{th}
Nozzle I, 90 bar, 600 μm	21 % n_c	1 mm	9 ± 2 %	134 eV	670 eV
Nozzle I, 60 bar, 600 μm	15 % n_c	1 mm	12 ± 2 %	85 eV	580 eV
Nozzle II, 90 bar, 600 μm	11 % n_c	0.8 mm	19 ± 2 %	51 eV	500 eV
Nozzle II, 90 bar, 300 μm	17 % n_c	0.5 mm	21 ± 8 %	76 eV	610 eV

Using this experimental transmission and assuming only inverse bremsstrahlung absorption, the collision frequency and thus the plasma temperature can be determined by inverting the expressions

$$T = exp\left(\frac{-\nu_{ei} L n_e / n_c}{\eta c}\right) \tag{5.1}$$

and

$$\nu_{ei} = \frac{1}{3(2\pi)^{3/2}} \frac{Z\omega_{pe}^4}{n_e v_e^3} \ln\Lambda\,, \tag{5.2}$$

from Sec. 2.2.1, giving values between ≈ 50 eV and ≈ 130 eV (Table 5.1, column T_e^{exp}). This is the temperature the plasma would have to have in order to fully explain the experimentally observed attenuation.

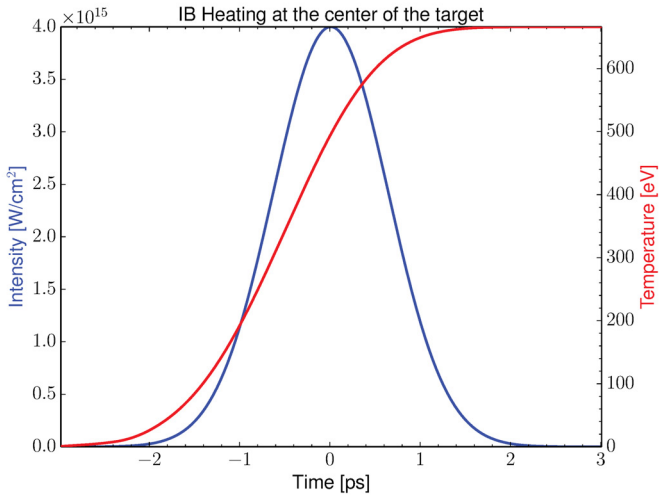

FIG. 5.7.: 1D heating calculation for case I ($n_e = 21\,\%\,n_c$). No high-intensity corrections included.

To assess if these values are realistic, the temperature was also calculated using the laser and gas parameters: A fully ionized but cold plasma was assumed, which is realistic as the laser pulse ionizes the target at the leading edge. Only the temperature and density in the center of the target (i. e. one point in space) were considered, and the laser was considered Gaussian in time with the experimental duration and peak intensity. Calculating iteratively the time integral over the heating rate [Eq. (2.57)] yields a much higher plasma temperature (column T_e^{th}). The calculated temperature for the $21\,\%\,n_c$ case is shown in Fig. 5.7. These theoretically expected temperatures correspond to transmissions around $70\,\%\ldots90\,\%$. Therefore, the low transmission is only in part due to collisional absorption. As shown below, the Brillouin backscattered energy is quite low, as should be the case for the Raman backscattering. One can suspect that small-scale density gradients refract a part of the beam out of the $f/21$ solid angle covered by the diagnostics. As this reduces the laser energy deposed into the target, the actual temperature is expected to be lower than the calculated one. For both calculations, high-intensity corrections [79, 81] have not been taken into account as the intensity is $< 10^{16}\,\mathrm{W/cm^2}$. These corrections would increase the discrepancy between theory and experiment.

Spectral transmission

The transmission of the red part of the spectrum is always higher than that of the blue part. Since the pulse has an up-chirp ("red first"), this is plausible because the (red) leading flank does not ionize the target fast enough, is transmitted, and once the density is high enough, the pump is more strongly attenuated and refracted (so that the total transmission is on the order of some percent). There is also a certain spectral broadening.

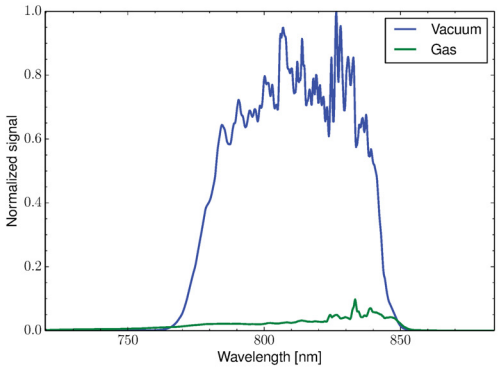

FIG. 5.8.: Pump spectra: Incoming (blue) and transmitted by the 21 $\%n_c$, 1 mm long gas target (green).

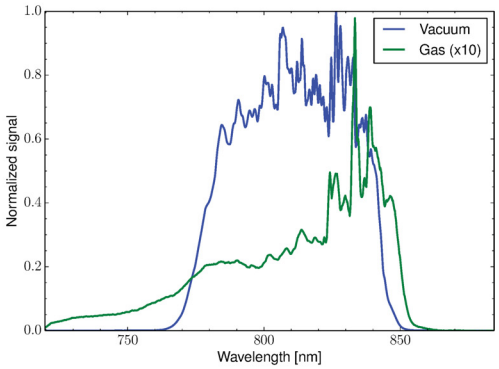

FIG. 5.9.: Same as Fig. 5.8 with transmitted pulse spectrum multiplied by a factor 10.

Absorption processes

Figures 5.10 and 5.11 show the image of the pump focal spot when shooting into vacuum or gas, respectively. As can be seen, the pump undergoes some refraction in the gas, which leads to a slightly bigger focal spot. The pulse is, however, not filamented. This is

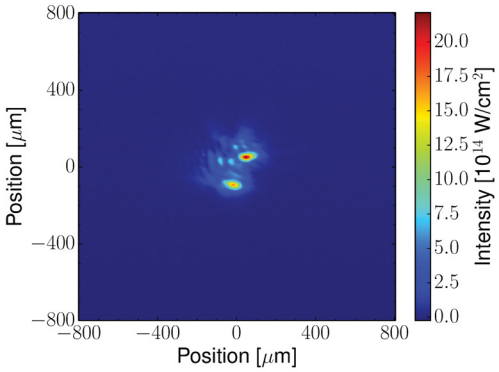

FIG. 5.10.: Pump focal spot in vacuum.

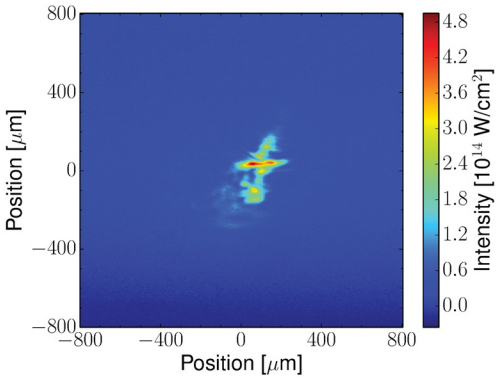

FIG. 5.11.: Pump focal spot in gas.

expected because with its 1.7 ps duration, it is too short for this instability to develop: In the case most prone to filamentation (at an intensity of 4×10^{15} W/cm^2 and a density of 21 $\%n_c$) the filamentation timescale [Eq. (2.52)] is 9 ps, five times higher than the pump duration. As the density was usually lower than that, the relevant timescales were longer on most shots during most of the interaction. The change in profile can, however, be due to refraction on small-scale inhomogeneities in the plasma.

It should be noted that also a part of the energy was reflected by the plasma via Raman and Brillouin backscattering. Due to the lack of an appropriate diagnostic for

the Raman backscattering, however, there is no indication to which amount the low transmission is caused by this effect (Sec. 5.3).

One can conclude that the transmission of the beam through the plasma was quite well behaved: The form of the beam did not change too much, there is no indication that the beam modifies the plasma profile in a highly detrimental way, and the intensity is still higher than the threshold for strong coupling, which is at $10^{13}\,\mathrm{W/cm^2}$ for these parameters. The high absorption, however, did not leave much of the energy ready for transfer to the seed. Therefore, a pre-ionized target was studied (Sec. 5.2.3).

5.2.3. Pump transmission through the preformed plasma

Two changes were made in experiment II in order to increase the transmission of the beams: First, smaller nozzles were used, which reduced the propagation length on the axis to 415 μm FWHM (or 500 μm FW1/eM). Second, a plasma was created by a prepulse arriving 1 ns before the main pulses. As expected, the pump was better transmitted through the preformed plasma.

Transmitted energy

Table 5.2 shows the peak electron density n_e (from off-line gas jet characterization, assuming full ionization) and the experimental transmissions T_{gas} and T_{plasma}.

TABLE 5.2.: Gas peak densities n_e for different target types, and corresponding experimental pump transmitted energies T_{gas} and T_{plasma}.

n_e	T_{gas}	T_{plasma}
$9\,\%\,n_c$	$15 \pm 6\,\%$	$21 \pm 4\,\%$
$11\,\%\,n_c$	$15 \pm 1\,\%$	$28 \pm 1\,\%$
$13\,\%\,n_c$	$12 \pm 5\,\%$	$35 \pm 6\,\%$

The transmission of this beam was more difficult to relate to the laser and plasma parameters because the target was ionized and heated by the ionization pulse (whose transmission was not measured), and then expanding and cooling down, before being heated again by the pump beam.

Therefore, a simulation with the hydrodynamic code FCI2 was done. The simulation starts with a perfectly ionized cold ($T_e = 300K$) plasma, which is reasonable for the prepulse intensity $> 1 \times 10^{14}\,\mathrm{W/cm^2}$. The simulation calculates the laser beam propagation with an envelope code. Heating and absorption of the laser is calculated for inverse bremsstrahlung. Ponderomotive effects are not included. The simulation includes heating by both the ionization prepulse (700 fs duration, $4 \times 10^{14}\,\mathrm{W/cm^2}$ intensity) and by the pump pulse (1 ns later, 780 fs duration, $3 \times 10^{16}\,\mathrm{W/cm^2}$).

As in the case without pre-ionization, the electron temperature predicted for these laser and plasma parameters is much higher than what to expect for this absorption,

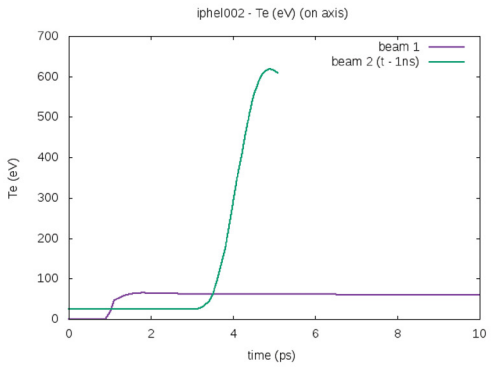

FIG. 5.12.: Plasma temperature from hydrodynamic simulation.

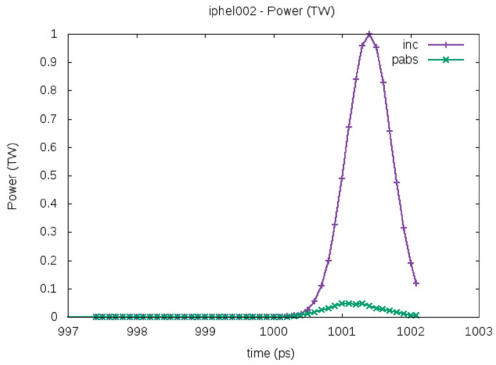

FIG. 5.13.: Incident and absorbed pump beam power in hydrodynamic simulation.

indicating that a part of the absorption is not explained by inverse bremsstrahlung. Noticeably, and on the contrary to the case without ionization, the shape of the spectrum does not change significantly by transmission through the plasma. This is expected for propagation in a preformed plasma (Fig. 5.14).

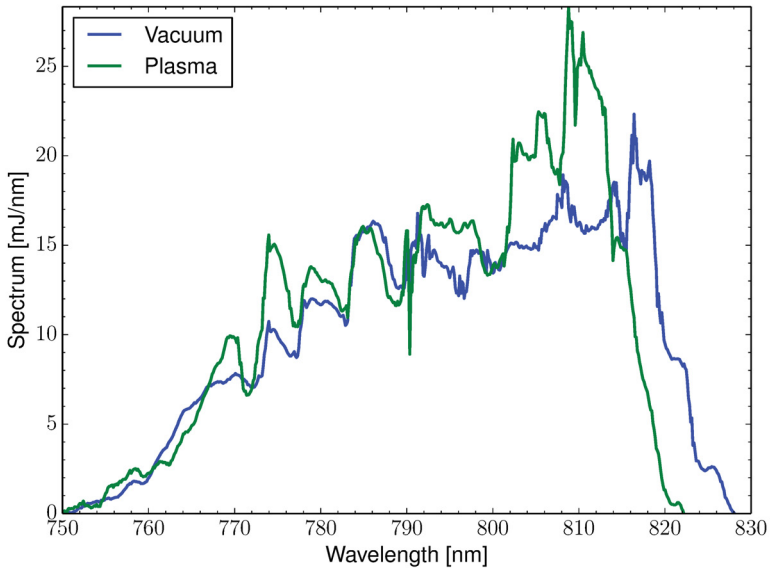

FIG. 5.14.: Incoming (Vacuum shot) and transmitted (Plasma) pump spectrum.

5.2.4. Seed transmission in gas

When the seed interacts with the neutral gas, the most intense part is attenuated whereas the outer parts of the beam are transmitted (with minor changes in the focal spot form). This leads to a much higher FWHM of the focal spot (Figs. 5.15 to 5.17). On some shot series, the focal spot size increases even more strongly (Figs. 5.18 to 5.20).

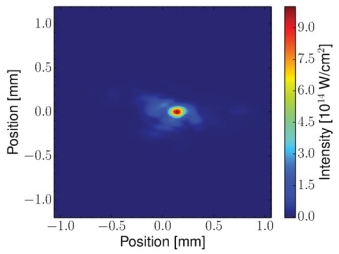

FIG. 5.15.: Focal spot of the incoming seed.

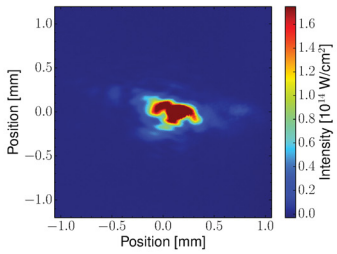

FIG. 5.16.: Fig. 5.15 with color scale of Fig. 5.17.

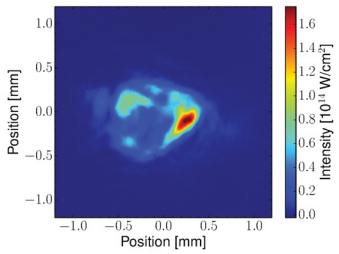

FIG. 5.17.: Focal spot of the transmitted seed.

The differences in the patterns cannot be explained by a long-term drift in the laser, as both shots were done right one after another. No systematic dependence on the gas parameters was observed.

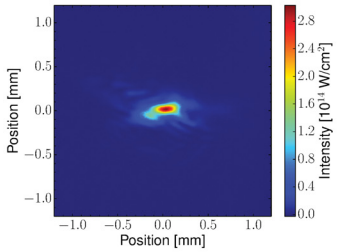

FIG. 5.18.: Focal spot of the incoming seed.

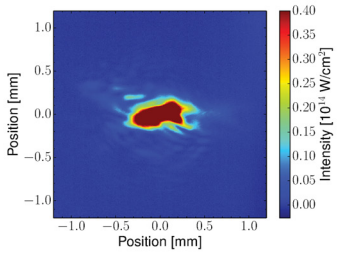

FIG. 5.19.: Fig. 5.18 with color scale of Fig. 5.20.

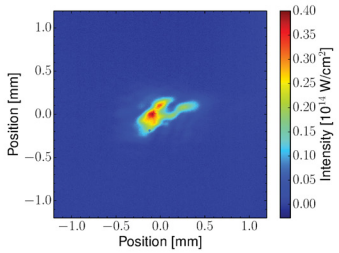

FIG. 5.20.: Focal spot of the transmitted seed.

In any case, refraction in neutral gas cannot be the reason: The diffraction limit of the imaging system is 18 μm, and a point-source with 1 mm defocus would be 2 μm in size only. The ionization energy being 13.6 eV, then for a 1 mm long and 120 μm radius focal volume, one obtains an ionization energy of 34 mJ, more than the < 12 mJ in the seed. Also, the seed intensity (6×10^{13} W/cm^2 to 4×10^{14} W/cm^2 at the peak) is at the limit for ionization by a subpicosecond pulse [290, 291]. Therefore, the attenuation can be ascribed to full or partial ionization. There are no signatures of filamentation, which is expected since the filamentation timescale [Eq. (2.52)] is even higher than for the pump (3 ns). The seed spectrum does not change much when the seed is transmitted through the plasma. On some shots, a broadening can be observed.

Figures 5.21 and 5.22 show autocorrelation traces for the incoming seed (Vacuum shot) and the amplified seed. As can be seen, the change in the form of the focal spot also lead to a change in the near field (the vertical axis of the image), but the duration remained essentially the same. This allows to conclude that the pulses were not stretched by 100 fs even when interacting with the pump. Since the measurement error on the duration of the autocorrelator trace was around 30 fs, a slight pulse broadening could not be detected, let alone compression. However, it was seen consistently throughout the experiment that no intense signal was emitted into the direction of the seed diagnostics on the order of the pump pulse duration 1.7 ps. We can conclude that the energy measured on the seed imaging was that of the seed after interaction, rather than a stimulated backscattering of the pump.

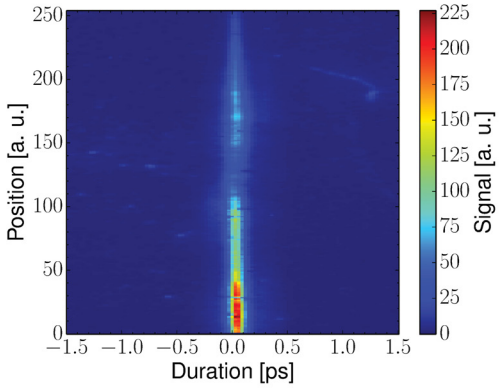

FIG. 5.21.: Autocorrelation trace of the incoming seed.

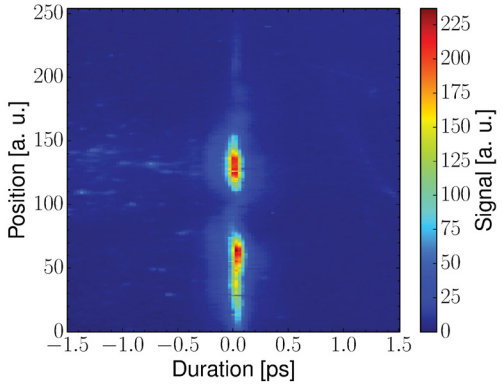

FIG. 5.22.: Autocorrelation trace of the amplified seed.

5.2.5. Seed transmission in plasma

In experiment II, the seed data analysis was complicated by the presence of the collinear ionization beam. Since both beams were collinear, they were both extracted and sent onto the seed diagnostics after interaction. Since the energy of the seed had to be determined to find out the gain, it was necessary to remove the ionization beam contribution to the diagnostic. In the experiment, this was done in two ways:

Near field Since the near field profiles of the incoming seed and ionization beams were well-separated (the seed was sent through a hole in the ionization beam OAP), this was also the case for the outgoing seed: The signal from the ionization beam was in a ring around the seed beam. Therefore, an iris was introduced into the collimated beam to remove the ionization beam. On the vacuum shots, this was sufficient to remove the ionization beam fully. On the shots involving propagation through the plasma, both beams were refracted in the plasma, so there was a residual ionization beam contribution on the camera. In order to avoid blocking a

part of the seed, the iris diameter was chosen so large that none of the seed was blocked, therefore accepting to have a part of the ionization beam on the camera.

Polarization The polarization of the ionization beam was chosen perpendicular to that of the seed beam on all shots. The ionization beam was then strongly attenuated by inserting a polarizer at the seed diagnostics entrance table. However, since the ionization beam was in part depolarized in the plasma, there was a residual component with the polarization as the seed on the seed diagnostics.

Although the iris and the polarizer reduced the ionization beam energy arriving on the seed imaging camera by a factor 100, even this signal was still on the order of the seed. Therefore, the ionization signal had to be taken into account when analyzing the data. This was possible because on the camera, both beams were visibly separated: The seed was on the same position when shots were done in a row. The ionization beam, however, formed a half-circle-like (or quarter-circle-like) structure whose position fluctuated from shot to shot. This is hardly surprising as this is the part of the beam that was affected by refraction in the plasma. To treat the camera images, two options were considered:

- If one can identify the seed on the image, then it is possible to apply a mask to the image so that the image is set to zero at the ionization beam's position.
- Similarly, in that case one can also apply a mask that sets the whole image to zero except for the seed signal.

Comparing the two different masking options gave only slightly different results. Both methods agree on which shot is strongest. Figures 5.23 to 5.25 show the seed beam in plasma with and without a mask.

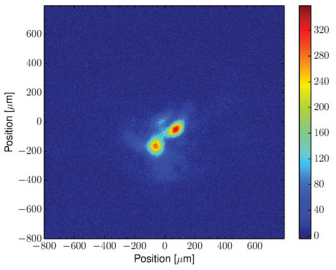

FIG. 5.23.: Seed and ionization pulse in plasma. Both foci visible.

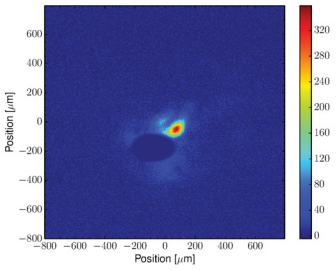

FIG. 5.24.: Same image as Fig. 5.23. Ionization pulse removed.

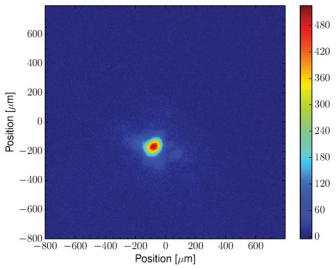

FIG. 5.25.: A shot with only the ionization beam in plasma.

Masking allowed to reduce the influence of the ionization signal on the amplification result, but there was always a residual difference. Therefore, the relative gain was computed as

$$G_{rel} = \frac{S_{interaction} - \langle S_{ionization} \rangle}{\langle S_{seed-plasma} \rangle} \,. \tag{5.3}$$

The absolute gain was computed as

$$G_{abs} = \frac{S_{interaction} - \langle S_{ionization} \rangle}{\langle S_{seed-vacuum} \rangle} . \tag{5.4}$$

Here, all quantities S refer to the camera signal obtained after removing the ionization beam and calculating the sum over the image. $S_{interaction}$ is the signal measured on the interaction shot for which to calculate the gain. $\langle S_{ionization} \rangle$ is the average of the signals from the shots where the ionization beam was sent into the plasma, that quantify the ionization beam's contribution. $\langle S_{seed-plasma} \rangle$ is the average of the signals from the shots where the seed was propagating in the plasma. $\langle S_{seed-vacuum} \rangle$ is the average of the signals from the shots where the seed was propagating in vacuum alone.

The seed transmission in the plasma is, depending on the target density, $20\,\% \ldots 30\,\%$.

5.3. Pump spontaneous backscattering

5.3.1. Raman backscattering

Figure 5.26 shows the spectrum measured using the low-resolution spectrometer (Sec. 3.4.1). Since the radiation at these wavelengths is spontaneous Raman backscattering of the pump, the plasma electron density corresponding to the wavelength, as calculated with Eq. (2.44), is given in the second horizontal scale on top of the image. There is a broad-

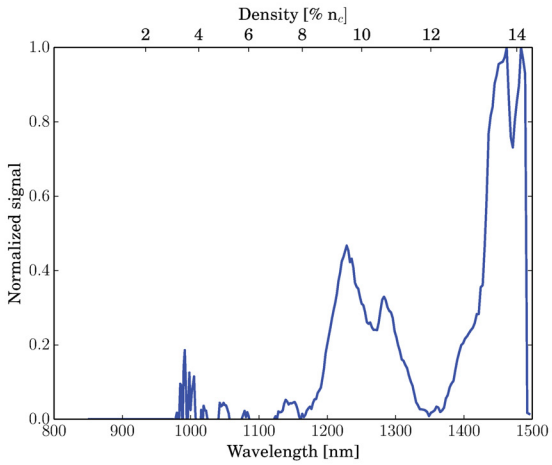

FIG. 5.26.: Pump Raman backscattering. Typical shot (Nozzle I, 90bar). The dips at 1080 nm and 1350 nm are measurement artifacts. The signal probably extends beyond the upper detection limit at ≈ 1500 nm. There is no signal detected below 1150 nm.

band pump Raman signal corresponding to densities from $4 \ldots 14\,\% n_c$, i. e. up to the end of the instrumental range. Since the gas jet peak density is $21\,\% n_c$, a signal can be expected beyond $14\,\% n_c$.

There is no Raman backscatter at lower density (except for some shots). The Raman diagnostic was also used to exclude the effect of a low-density Raman signal on the seed imaging.

The large modulation of the Raman signal (dips at 1080 nm and 1350 nm) is a measurement artifact from interference on multiple pellicle beamsplitters. The signal varies much from shot to shot. Not all spectral components are there at all times. Since the low-resolution spectrometer is not absolutely calibrated, it is not possible to account for the backscattered energy.

5.3.2. Brillouin backscattering

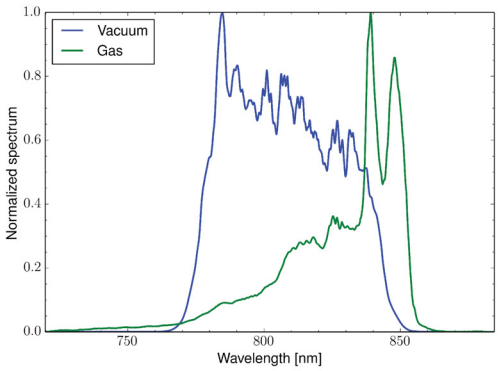

FIG. 5.27.: Pump spectrum and spectrum transmitted by the gas both from the pump spectrometer.

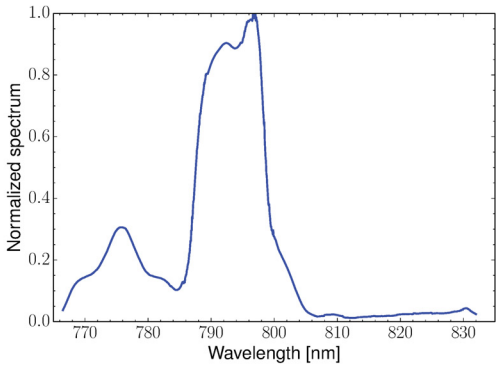

FIG. 5.28.: Pump backscatter (from the seed spectrometer) for the same shot as in Fig. 5.27.

Spontaneous Brillouin backscattering of the pump could only be detected when shooting into gas, i. e. on experiment I. In experiment II, the counterpropagating ionization beam signal on the CCD was too strong to allow detecting the pump backscattering. In experiment I, 53 shots were done with the pump beam only into gas. 26 of them showed a backscattering signal on the seed imaging CCD. Since the camera detects only radiation between 200 nm and 1150 nm, the signal can be spontaneous Brillouin backscatter or Raman backscatter at very low density. For these shots, no backscattering between 850 nm and 1150 nm was seen on any spectrometer. In contrast, there was also a spontaneous backscatter signal on the SBS spectrometer, extending not much above 800 nm (see below). Therefore, Raman backscattering is unlikely to be the reason for this: If there is no detectable Raman backscatter at higher density, then there should be none at lower density either. This backscattering, probably Brillouin backscattering, was observed for all target configurations, but for some of them more often than for others (Table 5.3). Since the objective was to see the amplified seed, the detectors were not configured for highest sensitivity and therefore it is possible that there was sizable backscattering on

TABLE 5.3.: Gas parameters (peak density n_e and interaction length L) for different target types (same as Table 5.1), and corresponding occurrence of spontaneous Brillouin backscattering when only the pump was shot into gas.

Target	n_e	L	Brillouin backscatter
Nozzle I, 90 bar	21 % n_c	1 mm	1 out of 7 shots (15%)
Nozzle I, 60 bar	15 % n_c	1 mm	19 out of 40 shots (50%)
Nozzle II, 600 μm	11 % n_c	0.8 mm	all 3 shots (100%)
Nozzle II, 300 μm	17 % n_c	0.5 mm	all 3 shots (100%)

the other shots too that remained undetected.

Spectrally, the backscattering is always between 770 nm and 810 nm, (mostly between 780 nm and 800 nm). The width varies between 15 nm and 30 nm. This shows that it is generated mostly by the trailing flank of the pump. This is not surprising for two reasons: The jet is not fully ionized at the leading flank of the pulse, as evidenced by the spectral transmission. Also, the plasma is cold in the beginning of the interaction, so that the backscattered light at this time is absorbed by collisions. During the interaction, the temperature rises. The bandwidth of > 15 nm is sufficient to have a minimum (bandwidth-limited) pulse duration of 64 fs. The energy (measured by seed imaging) is < 0.35 mJ. The sensitivity and the temporal resolution of the autocorrelator were not sufficient to determine the duration of the signal.

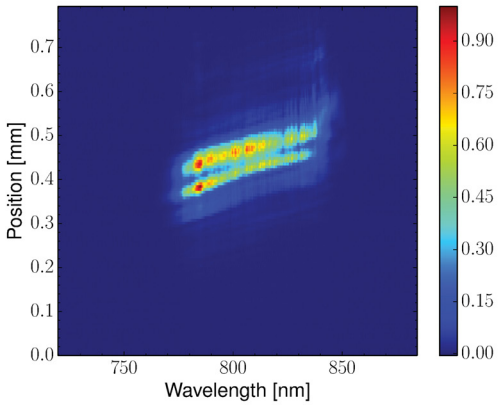

FIG. 5.29.: Pump vacuum shot (same as blue line in Fig. 5.27).

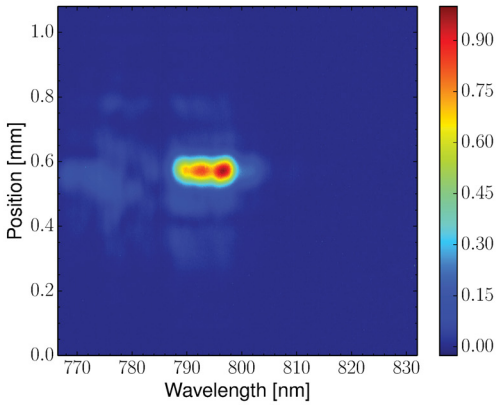

FIG. 5.30.: Spontaneous Brillouin (same as Fig. 5.28)

The backscatter is more or less flat-top with respect to the wavelength on some shots (e. g. Fig. 5.30). On most shots, there is a periodic modulation with periodicity 2 nm or more (e. g. Fig. 5.32). The backscattering seems to preserve the spectral modulation

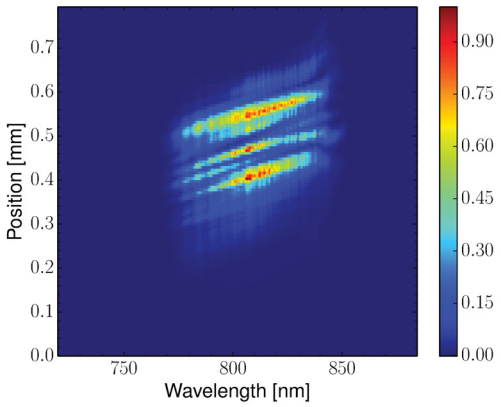

FIG. 5.31.: Pump vacuum shot No. 654

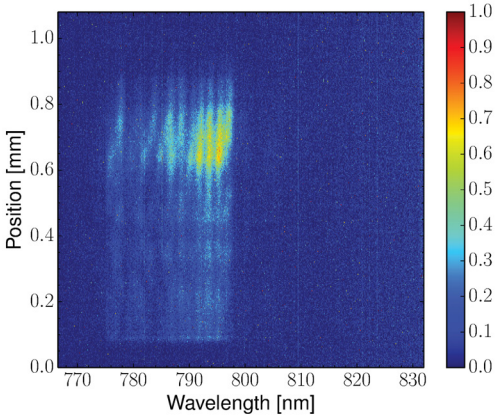

FIG. 5.32.: Spontaneous Brillouin: Shot 686

already seen on the incoming pulses at least on some shots.

The modulation in the spectra should not be confused with the rippled spectra seen in Vlasov simulations (Schluck et al. [74]). Those are due to pump depletion, whereas in our case, the spontaneous backscattering is unlikely to have a sufficiently strong effect on the pump intensity.

5.4. Interaction of pump and seed in the target

5.4.1. Shots into neutral gas

For each time scan, the temporal "zero delay" (pump and seed meet in the center of the target) was identified by the shape of the seed spot (the lowest delay $t_p - t_s$ for which the seed spot looks like it was going through the gas with no pump present). For several delays around this position, the seed energy, spectrum, and Raman backscattering were compared. In this experiment, we refer to the name "series" for sequential shots where the pump-seed delay was varied under the same conditions otherwise. The Raman backscattering diagnostic was also used to exclude the (few) shots with a sizable signal between 1000 nm and 1050 nm which would be observed on both Raman and Si detectors, and which can only be Raman at low density. Below, general observations made under all conditions will be discussed. Then, spectra for two special cases (narrow band pulses and standard [broad] band pulses) will be shown in detail.

General remarks

We compare only shots that show (at or around the zero delay) either some increase in energy or a consistent change of focal spot and spectrum, indicating that pump-seed interaction took place. These shots differ systematically in energy and spectrum from shots where no significant interaction takes place.

Energy The seed energy is slightly increased at the delay when the form of the focal spot image changes.

Reproducibility Consistent results of different diagnostics occur only if shots were done around the best timing in a row, i. e. one after another, in a couple of minutes. Apparently, the timing information changes (due to misalignment over the very long path that separates the laser room from the experiment's target chamber) during the experiment. This explains the low reproducibility, i. e. it was possible to see different results when comparing shots taken with precisely the same (supposed) parameters yet not done in close sequence. Therefore, the gain seen on individual shots was in general not reproducible, when the conditions were tested again after a long time. As the "zero" delay (pump and seed synchronized in the target center) drifts during the experiment, it is not surprising that the best shot occurs at a position that would have been identified as a delay of some picoseconds. However, the relative delay is realized much more precisely (20 fs error, see above).

Seed spectrum Shots with high delays (pump later than seed) are similar to shots into gas, because the seed traverses neutral gas before the pump arrives. Shots with low delays (seed later than pump) can have stronger blue components (770...800nm), due to stronger attenuation in the red. Shots at zero delay (pump and seed interact in the plasma) have a narrower spectrum. On some series, especially with low seed energy, there is a blue shifted narrower spectrum. This can be spontaneous Brillouin. On some series, especially with high energy, there is a red shift. This could be an indicator that the very leading edge of the pump ionizes, and (for a correctly timed seed) the leading part of the pump can amplify. It is pretty much excluded that these red-shifted spectra are from spontaneous Brillouin because that was observed only in the blue part of the spectrum. There is no systematic correlation between pump Raman backscattering and seed energy.

Narrowband case

On one shot series, the spectra of pump and seed were unusually narrow (25 nm FWHM), which has to be ascribed to laser issues. The seed had an energy of 11.9 mJ, a duration of 163 fs, and an intensity of $7 \times 10^{13}\,\mathrm{W/cm^2}$. The peak gas density was 21 %n_c. The pulse duration was the highest on that experiment and chosen by moving the compressor gratings. The seed energy increases (compared to vacuum) only by 20 % (2 mJ transferred energy) on the shot at zero delay. On this shot, the spectrum narrows and red-shifts with the peak at 820 nm (Fig. 5.34), and the Raman backscattering is weaker. The red-shift cannot stem from sc-SBS alone because it is too strong. It can be due to a stronger absorption in the blue.

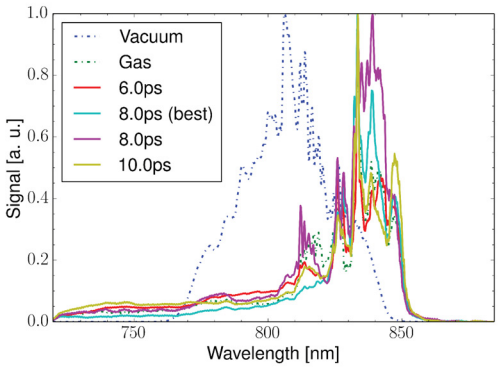

FIG. 5.33.: Narrowband case: Normalized pump spectra. Numbers in legend are delays.

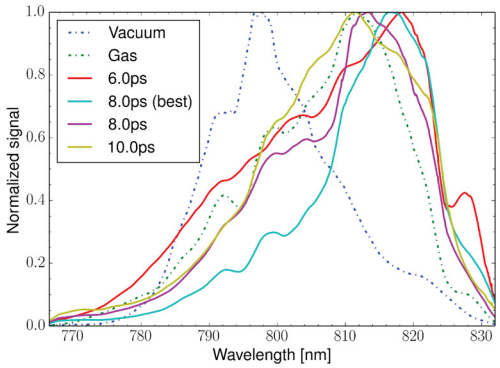

FIG. 5.34.: Narrowband case: Normalized seed spectra. Numbers in legend are delays.

Broadband case

On this shot series, the spectrum was at its nominal width. The seed had an energy of 2.3 mJ, a duration of 45 fs, and an intensity of $5 \times 10^{13}\,\mathrm{W/cm^2}$. The peak gas density was $15\,\%n_c$. The strongest shot at zero delay shows a relative gain of 1.2. The spectrum is narrower and a bit blue shifted. Raman and Brillouin scattering are not anticorrelated. The shape of the pump spectra is not modified by the presence of the seed. This is expected since the seed is much weaker.

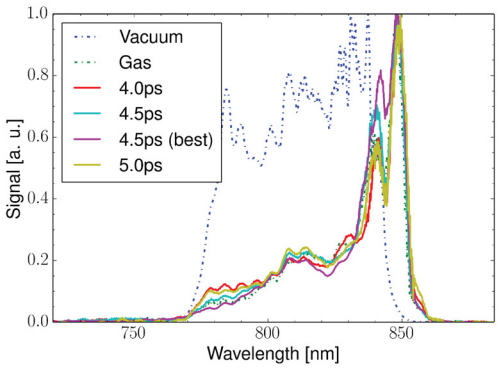

FIG. 5.35.: Broadband case: Normalized pump spectra. Numbers in legend are delays.

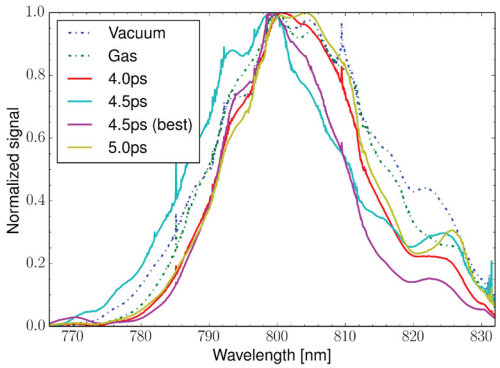

FIG. 5.36.: Broadband case: Normalized seed spectra. Numbers in legend are delays.

5.4.2. Preformed plasma target

As in experiment II, with the preformed plasma target, the transmission was higher, the interaction was easier to see. However, the results were highly dispersed, i. e. within the series, shots at the same delay could give quite different results. As mentioned above, it is justified to compare only those pump-seed interaction shots that show the highest energies on the seed imaging diagnostic, as for the other shots the overlap was insufficient. Choosing the shots around the temporal "zero" according to this criterion, one obtains comparable pulse durations and gains. For a shot series at low density ($n_e = 7.5\,\%n_c$) and with 4 mJ in the seed, these values are shown in Fig. 5.37. It should be noted that the seed transmission in the plasma (red dash-dotted) was quite high, due to the low density. The seed pulse duration increased from 51 fs to 138 fs when the beam was transmitted through the plasma. Upon interaction, gain was only observed around the 2 ps delay. The transferred energy is on the order of the millijoule. This is more than the spontaneous backscattering observed in the neutral gas (hundreds of microjoules). The reasons for the effect of the interaction on the pulse duration are not obvious. As the energy transfer is not efficient enough to deplete the pump, this is not pulse compression from self-similar seed growth. One can suspect that the leading flank and the trailing flank of the seed encounter already different conditions, and therefore, only a part of the pulse is amplified. However, simulations taking into account the real pump intensity in the plasma would be needed for a conclusive result. Unfortunately, there is no clear trend in the spectrum.

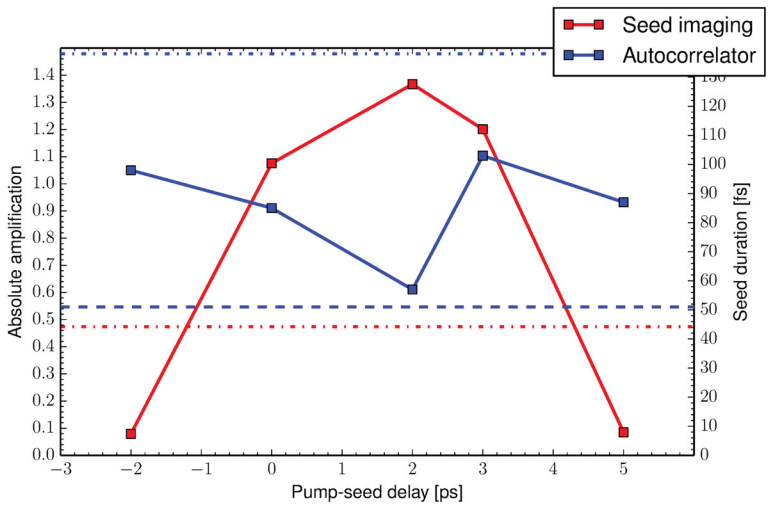

FIG. 5.37.: Shot series with preformed plasma: Absolute amplification for interaction shots (red) and transmission level in the plasma (red dash-dotted). Seed duration from the autocorrelator (blue), duration for a vacuum shot (blue dashed) and duration of the seed as transmitted by the plasma.

It is, however, instructive to compare the most energetic shots of different shot series. Figure 5.38 shows the shots at highest energy at or near zero delay, where the higher energy can be due to pump-seed interaction. There is a visible correlation between the relative gain (relative to the pulse after transmission through the plasma), and the duration. Here, the incoming seed pulses had various durations; therefore, quite different amplification attempts are compared here. After interaction, the shorter seed pulses are less energetic.

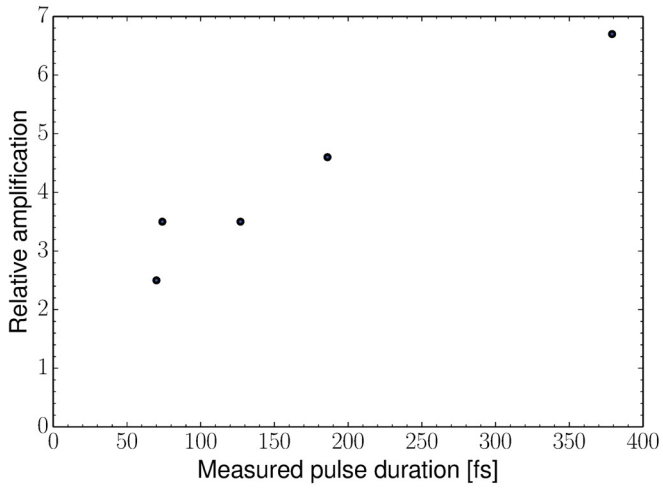

FIG. 5.38.: Durations and relative gain of the most energetic shots of five different series.

5.5. Conclusions

In these experiments, in principle the conditions for amplification by sc-SBS were met. For the experimental parameters, i. e. for Hydrogen with $n_e = 0.1 \ldots 0.2 n_c$ and $I_0 = 4 \times 10^{15}\,\mathrm{W/cm^2}$ at 800 nm, the linear theory yields a characteristic time scale of 110 . . . 90 fs and a shift of 1.8 . . . 2.2 nm in the spectrum.

However, only a low gain was observed on few shots where the conditions were most prone to amplification. Comparing these shots, a shorter seed duration after interaction was correlated with a higher relative increase in energy. This suggests that a small gain still occurred. The self-similar regime was not reached, indicating that not all the conditions were met as needed.

As stated in Sec. 2.3.3, the conditions for successful amplification are

- spatiotemporal overlap of pump and seed,
- well-behaved pump transmission to yield a sufficiently high intensity to reach the strong coupling regime within the plasma,

- conditions under which an ion acoustic wave can exist,
- a correct phase relation between pump and seed.

Concerning the seed, both its propagation and its spatiotemporal overlap with the pump could be reached. For the other parameters, this was less clear.

Pump transmission The low transmission is due to collisional absorption, Raman backscattering, and refraction. For the shots without preformed plasma (experiment I), the transmission of the pump was in the percent range. One can consider as an extreme case that at the end of the plasma only 1 % of the pump intensity is present. This intensity ($4 \times 10^{13}\,\mathrm{W/cm^2}$) is then at the lower limit of strong coupling, with a time scale of around 400 fs and a shift of around 1 nm. Therefore, the interaction was strongly coupled and the seed pulse duration was below the time scale in the linear regime, as intended. In the case of the preformed plasma (experiment II), with $20 \ldots 40\,\%$ transmission the intensity was at least $4 \times 10^{14}\,\mathrm{W/cm^2}$ in the plasma, which, for $5 \ldots 10\,\% n_c$, yields strong coupling and a time scale of $290 \ldots 230$ fs, as intended. Both pump and seed beam are too short to filament, which is predicted and evidenced by the transmission camera images.

Presence of an ion acoustic wave The buildup of an ion acoustic wave can be hampered by Landau damping and wave breaking. This is expected only for parameters far from those of this experiment (Sec. 2.3.2). In experiment I, spontaneous Brillouin backscattering was observed, which demonstrates the existence of an IAW. Although the bandwidth of the backscattered radiation was narrow, this does not forcibly mean that amplification of a seed had to be as limited to that bandwidth: The presence of a seed can change the interaction sufficiently to allow for a broader bandwidth. Therefore, it has to be concluded that the phase relation between pump and seed pulse in the plasma was not in a regime that allows to transfer energy from the pump to the seed throughout the interaction.

Pump-seed phase relation As can be seen in Eqs. (2.23) to (2.28), the pump chirp is a crucial parameter for the phase relation between pump and seed, and therefore for the directionality of the energy flow. As already pointed out by Chiaramello et al. [63], a too high chirp factor can quench amplification. A moderate chirp, with a chip parameter $\alpha = -2 \times 10^{-7}$ (the red part of the spectrum coming first), improves SBS, whereas a high chirp factor, $|\alpha| > 1 \times 10^{-6}$, is detrimental for amplification regardless of the sign.

In the ARCTURUS experiments, the 800 nm, 30 fs bandwidth-limited pulse, stretched to $0.78\,\mathrm{ps} \ldots 1.7\,\mathrm{ps}$, has a chirp factor of $|\alpha| = 2 \times 10^{-6} \ldots 5 \times 10^{-6}$. This is high enough to quench amplification.

This is in contrast to the results obtained with the ELFIE Nd:glass system, with a ten times narrower spectrum, where self-similar amplification, and SBS-SRS anticorrelation were visible (Chap. 6). In that experiment, the chirp factor (for a bandwidth-limited

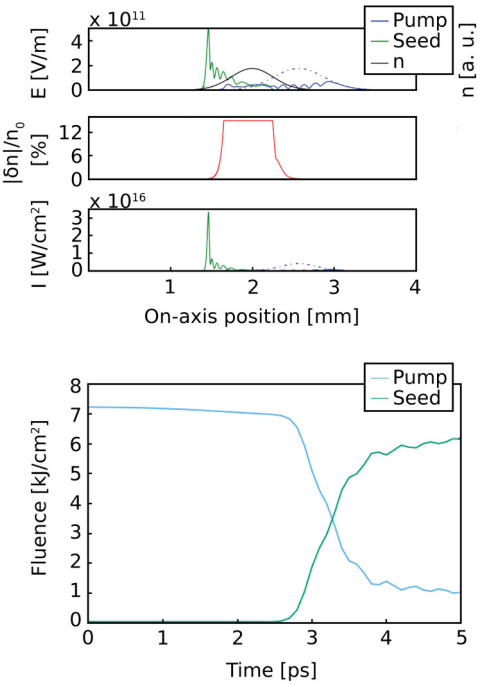

FIG. 5.39.: Envelope simulation without chirp.

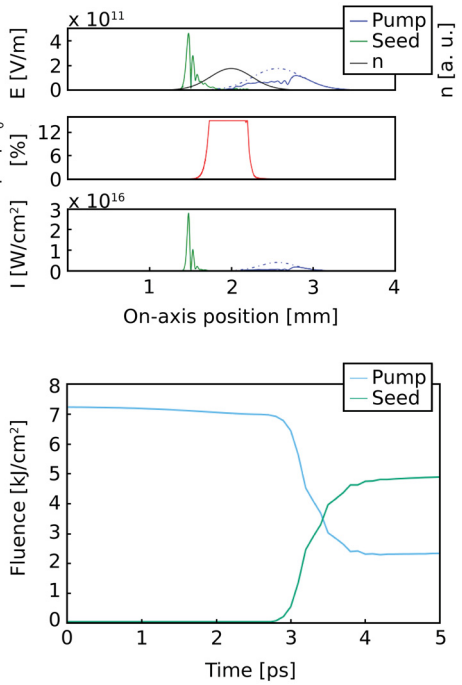

FIG. 5.40.: Envelope simulation with 5 nm spectrum.

450 fs pulse, stretched to 4 ps, with the red part of the spectrum coming first) is $\alpha = -2 \times 10^{-7}$. This happens to be just the optimal value found in the theoretical calculations. The chirp factor is lower here because the central frequency only has to traverse a ten times narrower spectrum in the same time (pulse duration).

In order to investigate the chirp influence in more detail, a 1D envelope code simulation was done [292]. The plasma was assumed fully ionized, with a Gaussian profile, a propagation length (FWHM) of 600 μm, and a peak density of $n_e = 10\,\%n_c$. A 1.7 ps, 4×10^{15} W/cm^2 pump was crossing a 160 fs, 1.7×10^{14} W/cm^2 seed. Both lasers were at 800 nm wavelength. The density perturbation in the code was limited to 15 %, which is the value observed in PIC simulations for these parameters.

Figures 5.39 to 5.43 show the simulation results. The upper graphs show, along the propagation axis, from top to bottom: The electric fields of the laser pulses (blue: pump, green: seed) together with the plasma density (black), the density perturbation, the velocity of the plasma wave oscillation, and the intensities of the laser pulses after interaction (blue: pump, green: seed). Below, the fluences of pump and seed are shown depending on the time, which shows if energy is transferred from pump to seed or vice versa.

Figure 5.39 shows the result for an idealized case where the 1.7 ps pump is bandwidth-

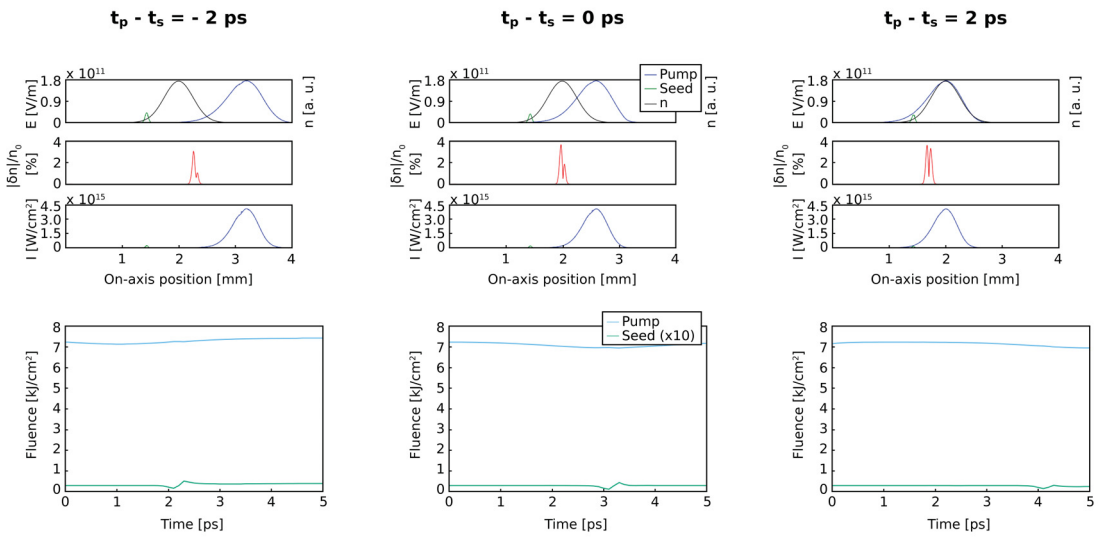

FIG. 5.41.: Envelope simulation with 30 nm spectrum, negative chirp ("red first").

limited (0.6 nm bandwidth). Here, as predicted by the analytical theory, energy is transferred from the pump to the seed. This is still the case if the pump has the same duration, but 5 nm spectral width, and the chirp is negative with a factor $\alpha = -7.8 \times 10^{-7}$. In both cases, both the temporal shape of the seed (strong first peak with post-peaks) and the depletion of the pump by sc-SBS amplification indicate amplification in the self-similar regime.

The picture changes, however, when the chirp is increased (Figs. 5.41 and 5.42). Already with a bandwidth of 30 nm, which is half the bandwidth in the experiment, the seed does not gain energy in the end because energy is transferred in both directions (pump-seed and back). The order of that depends on the sign of the chirp. In both cases and in contrast to the cases with the lower chirp, much less energy is transferred forth and back. Net gain for the seed is neither observed at zero delay (pump and seed meet at the center of the gas jet) nor at a small delay ± 2 ps, where the pulses meet on a slope, which in principle can be beneficial as spontaneous Raman backscattering is reduced there. In this case, however, Raman backscattering is strongly suppressed anyway, which is also due to the strong chirp [293]. Therefore, it is not surprising that Raman-Brillouin backscattering was not demonstrated in this experiment.

The reduced amplification is due to the higher chirp factor. This can be seen from a simulation where the pump has, again, a bandwidth of 30 nm, but it is stretched to 5 ps duration (Fig. 5.43). Then, there is some gain again, albeit weak.

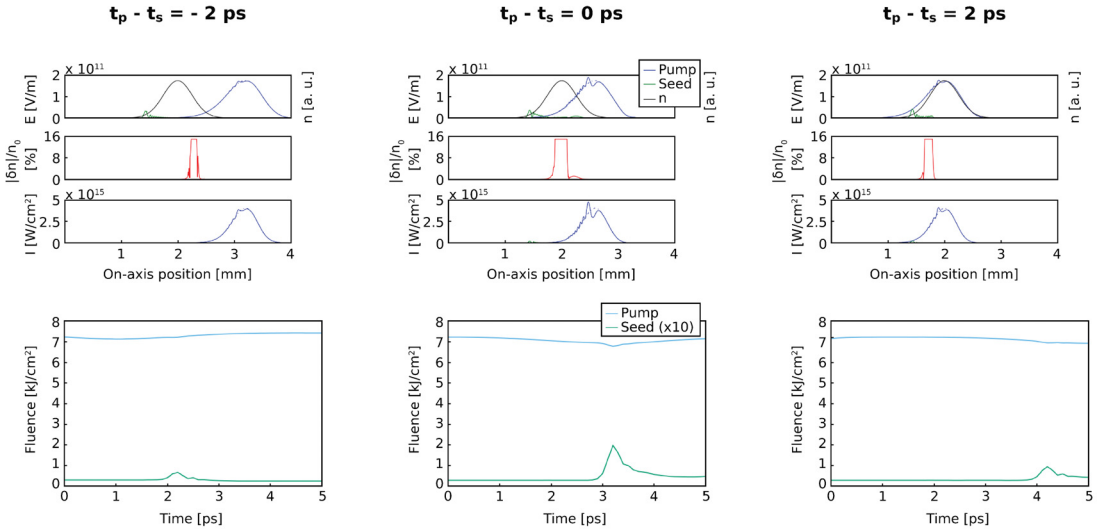

FIG. 5.42.: Envelope simulation with 30 nm spectrum, positive chirp ("blue first").

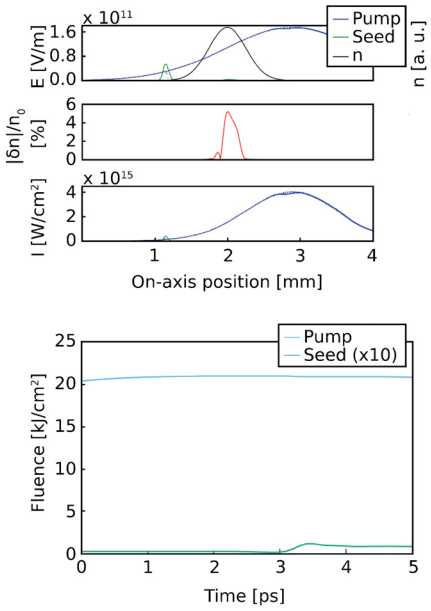

FIG. 5.43.: Envelope simulation with 30 nm spectrum, negative chirp ("red first") but pump stretched to 5 ps.

6. Experimental demonstration of SBS amplification in the self-similar regime

In order to study amplification by sc-SBS under optimized conditions, an experiment has been done at the ELFIE laser facility at LULI. This facility was chosen because it provides both a subpicosecond seed pulse and two energetic laser pulses for preionization and pump pulse (Sec. 3.1.3). The results were published in the article by LANCIA et al. [6].

This experiment is a follow-up to a previous campaign, indeed the first campaign on sc-SBS amplification in 2007 [51] (for a detailed description see Sec. 2.3.5). Then, pump and seed were under an angle of 160°. This limited the spatial extent of the overlap zone and thus the energy transfer.

In contrast to this, in this experiment, a fully counterpropagating configuration was realized for the first time. This maximizes the interaction length and the gain that can be expected. The pump energy was increased as well to have a bigger energy reservoir for amplification. Instead of Argon, in this case the gas target was chosen to be Hydrogen. This improvement allows for full ionization and, therefore, a more homogeneous plasma.

6.1. Amplification experiment

A schematic of the setup is shown in Fig. 6.1. In order to maximize the amplifier length and avoid beam deflection due to refraction, pump and seed beams were focused into a preformed plasma in a fully counterpropagating (180°) geometry. The plasma was generated by ionizing a supersonic Hydrogen gas jet using a long energetic laser pulse, the "ionization prepulse" in Fig. 6.1.

The transmitted pump beam left the counterpropagating setup by a flat mirror with a hole (the incoming seed passed through the hole). The transmitted and amplified seed left the setup via an uncoated 4" pellicle beam splitter. Spontaneous Raman backscattering was coupled out of the setup using a thin glass plate.

6.1.1. Beam parameters

Seed

The seed laser pulse was generated from the probe pulse of the facility. It was compressed to 700 fs, spatially filtered to obtain a good far field profile, and focused using an $f/40$

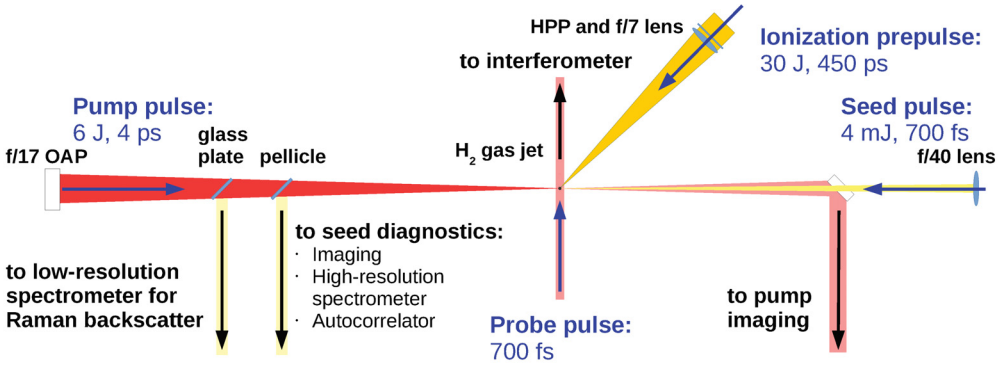

FIG. 6.1.: Schematic setup of the experiment.

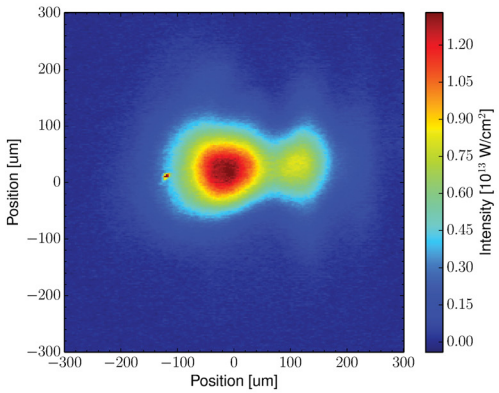

FIG. 6.2.: Focal spot of the seed pulse at 10 Hz.

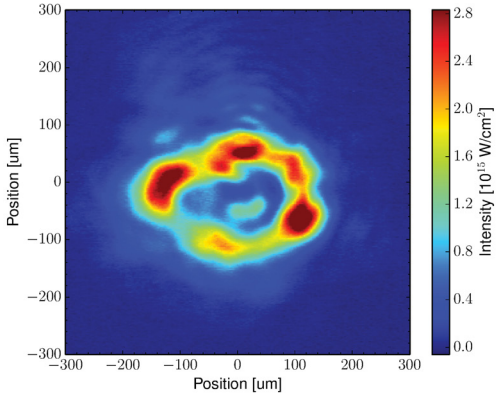

FIG. 6.3.: Focal spot of the pump pulse.

lens to a 130 μm FWHM focal spot. On target, it had an energy of 4 mJ and a peak intensity of 1.4×10^{13} W/cm^2 in the focal spot. The intensity and form of the spot could not be measured directly using the imaging camera of the seed because the seed passed over a pellicle beam splitter. This beam splitter changed the phase front in a way that made a correct imaging impossible, resulting in an artificially elongated shape (Fig. 6.6a). Therefore, before the shot series, the focal spot was recorded on a camera at low energy (10 Hz alignment mode) using a high quality imaging system that intercepted the beam after passing through focus. Figure 6.2 shows this focal spot, with the intensity scaled to full energy. In general, the focal spot is slightly smaller when shooting in full energy. In this case, however, the differences are quite low: To have a comparison, both a shot at 10 Hz (low energy) and a shot at full energy (with an ND filter as attenuator at the chamber entrance) were done on the same imaging system. The focusing conditions were the same for these two shots. Comparison yields a slightly smaller spot and a slightly higher intensity (factor 1.1). Therefore, this representation of the focus it fairly

correct.

Pump

In order to have a high-energy pump pulse, one of the main beamlines of the facilities was used. The duration of the pump was chosen slightly longer than the duration it takes the seed to pass the plasma. With a gas jet interaction length of $L = 1\,\mathrm{mm}$, this yields a time $L/c = 3.3\,\mathrm{ps}$. In the experiment, the pump pulse duration was chosen to be 4 ps. Since the bandwidth-limited beam has a duration of 700 fs, this corresponds to an up-chirp ("red first") of 1.5 nm/ps. Using an $f/17$ OAP, it was focused to a 150 μm focal spot to match the size of the seed. As in the case of the seed, there was no correct imaging for the pump focal spot at full energy. Here, the passage through the holed mirror lead to an uncorrect imaging (Fig. 6.4). Therefore, as for the seed, the profile at 10 Hz was recorded using a high quality imaging that intercepted the beam between the focus and the holed mirror. This measurement (Fig. 6.3) yielded a peak intensity of $2.8 \times 10^{15}\,\mathrm{W/cm^2}$ in the focal spot.

Pump pulse on shot Similarly to the seed, the transmitted pump was imaged onto an iKon DU 934P-BU2 16 bit CCD camera. Since the imaging system included a mirror with a hole, these camera images did not allow to fully characterize the form of the focal spot, but it was possible to make sure the overall form and position was conserved. Figure 6.4 shows a typical image of the pump camera. As can be seen, the form of the beam is not similar at all to that of Fig. 6.3.

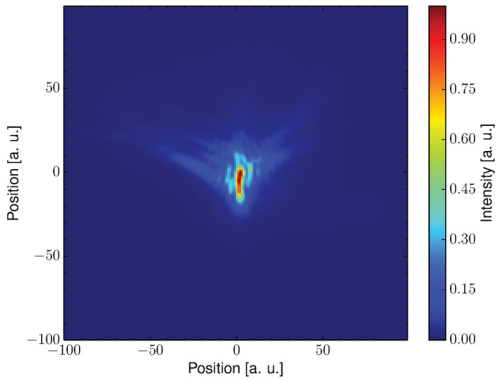

FIG. 6.4.: Transmitted pump pulse for the shot corresponding to Figs. 6.6c and 6.8c.

Delay

The delay between pump and seed was modified using a mechanical delay line, operated with a micrometer screw with a precision of 10 μm. Therefore, the uncertainty on the relative delay is 30 fs. The absolute delay, however, depends on the determination of

the zero delay (pump and seed meet in the center of the gas jet). This was done, independently from the amplification: After replacing the gas target by a piece of tracing paper, unamplified pump and seed pulses (10 Hz of the facility) were made to interfere, and the speckles were imaged onto a CCD camera. When pump and seed overlap, their interference causes a change in the speckle pattern. This allowed to determine the absolute delay with a typical error of 1.5 ps.

6.1.2. Target

The target was a preformed plasma (Sec. 3.3.4) To determine the plasma density on the shot, a part of the ELFIE probe pulse was used to probe the plasma transversally. This part of the beam was compressed to 700 fs, like the seed pulse, and frequency doubled, i. e. it was at a wavelength of 527 nm. The plasma was probed transversally at 90°, as shown in Fig. 6.1. The transmitted beam was sent into a Nomarski [294] interferometer. Figure 6.5 shows a typical interferogram. As can be seen, the probe undergoes strong

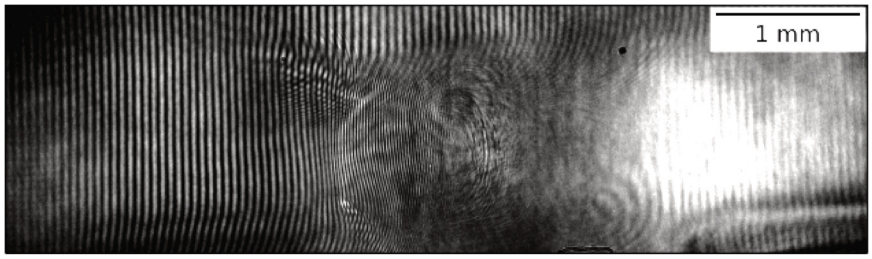

FIG. 6.5.: Typical interferogram of the plasma from the Nomarski interferometer, recorded when pump and seed laser pulses are traversing the plasma.

refraction in the plasma. This leads to both discontinuities in the plasma and reduced fringe visibility. Therefore, it is not possible to measure the plasma electron density on the whole axis. It was used to monitor the overall radial symmetry of the plasma profile.

6.1.3. Diagnostics

In order to observe the signatures of the linear and the self-similar regime of SBS, the outgoing seed was characterized in energy (imaging / calorimetry), in time (single-shot autocorrelator), and spectrally (high-resolution spectrometer).

Additionally, the transmission of the pump was measured (imaging). Concurrent Raman backward scattering was characterized with low-resolution spectrometers.

Seed pulse diagnostics

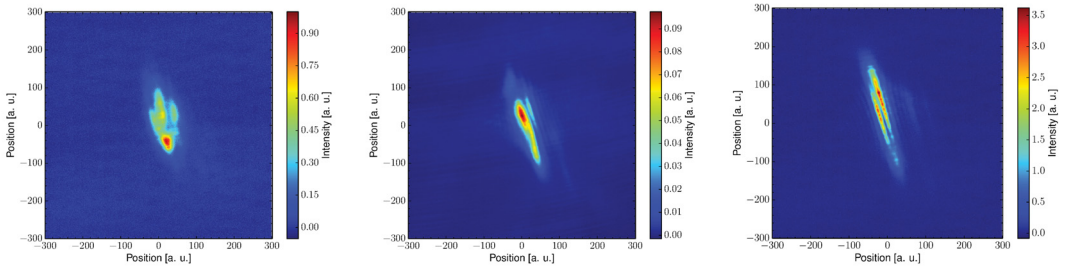

(a) Incoming seed. **(b)** Transmitted seed. **(c)** Amplified seed.

FIG. 6.6.: Images from the seed transmission diagnostic. The values given on the color scales are normalized to the maximum of the incoming seed (Fig. 6.6a).

In order to determine the transmitted energy and the shape of the focal spot, the transmitted seed beam was sent onto a camera by imaging the target chamber center (TCC) with a lens having an aperture of $f/69$, resulting in a magnification of $M = 0.78$. An iKon DU934P-BU2 (Andor, Belfast, UK) 16 bits charge-coupled device (CCD) camera was used since it is sensitive in the visible and in the near infrared and has a high dynamic range.

The transmitted pulse relative energy was determined by integrating the grayscale values of the denoised CCD camera image as shown in Fig. 6.6. The gain g_{abs} [Eq. (2.69)] was determined by dividing the value from the seed after interaction (Fig. 6.6c) by the value from a shot where only the seed was fired and the gas jet was not triggered (the seed propagates in vacuum, Fig. 6.6a). Since this is not a single-shot technique, shot-to-shot fluctuations in facility's probe beam line had to be accounted for. Do this end, the relative energy of the incoming seed was determined by focusing the leakage behind a mirror upstream to the focusing lens onto a photodiode.

Images obtained using this diagnostic are shown in Fig. 6.6. Since the beam was extracted using a pellicle, the actual focus profile (shown in Fig. 6.2) was not well depicted on the camera. Therefore, the change in the beam shape is a qualitative indication of refraction of the beam in the plasma. It does not, however, give an account on the real size of the focal spot. The intensities are scaled the same way on all three images (Fig. 6.6). They are normalized to the maximum intensity of the incoming seed, but they have their individual colorscales. Figure 6.6a shows the seed impinging on the plasma, recorded by firing the seed only but not the other beams nor the gas jet. As can be seen in Fig. 6.6b (with the gas jet being pulsed and preionized, and where the seed was fired but not the pump), the transmission level in the plasma is around 10 %.

Figure 6.6c (where the gas jet was pulsed, and all pulses were fired and synchronized) shows a case of absolute amplification.

To measure the pulse duration, the outgoing seed was collimated using a lens and sent into a single-shot second-order autocorrelator (Sec. 3.4.2), again equipped with a DV420 16-bit CCD camera. The autocorrelator trace of the incoming seed (the same shot as for Figs. 6.6a and 6.8a) is shown in Fig. 6.7. The time scale given here results from the temporal scaling for the autocorrelation trace and has to be divided by $\sqrt{2}$. The trace cannot be fully seen because the beam has shifted due to propagation in the plasma. This, however, does not prevent an extraction of the seed duration.

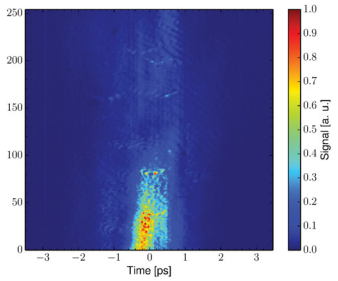

FIG. 6.7.: Autocorrelator trace of the incoming seed.

To characterize the spectrum, the amplified seed was sent onto a high-resolution spectrometer (TCC imaged with $f/69$, $M = 0.34$). The spectrometer was a Fastie-Ebert monochromator with a spherical mirror with a focal length of $f = 1\,\mathrm{m}$. The camera was a DV420 (Andor, Belfast, UK) 16 bit CCD. The spectrometer also served to determine the gain, the same way as using the imaging of the focal spot shown in Fig. 6.6. Since the image of the focal spot was centered on the spectrometer slit, this measurement (1D calorimetry) yields a gain that depends more strongly on the amplification in the center of the beam. Figure 6.8 shows the spectra recorded for the same three shots as Fig. 6.6. Again, the intensity scales are identical. It shows the low transmission in the plasma (Fig. 6.8b) as well as narrowing and a shift of the spectrum in case of amplification (Fig. 6.8c).

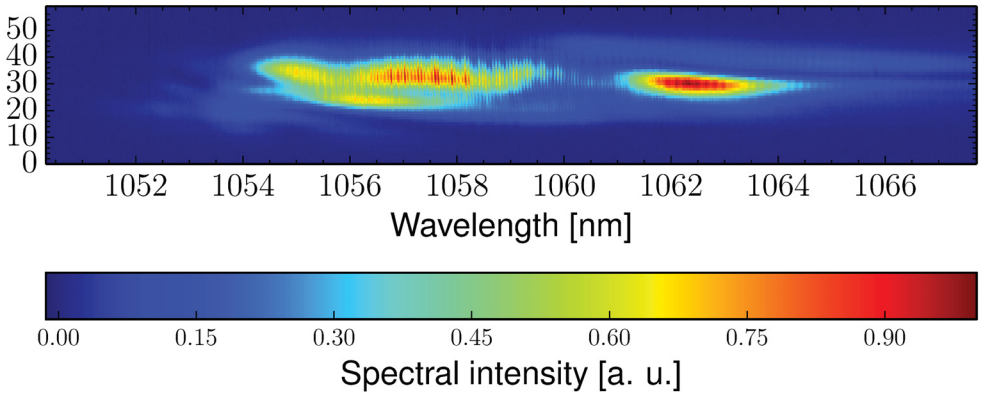

(a) Incoming seed.

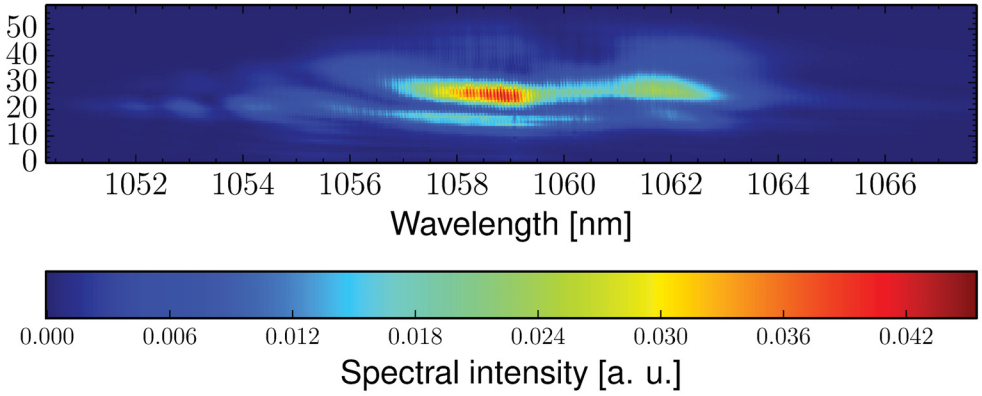

(b) Transmitted seed.

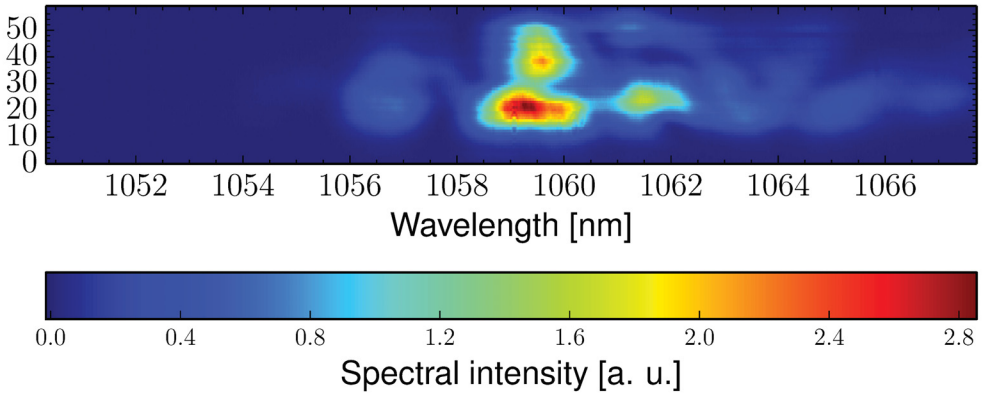

(c) Amplified seed.

FIG. 6.8.: Raw images from the seed high-resolution spectrometer for the same shots as Fig. 6.6. The images are normalized to the maximum intensity of the incoming seed (Fig. 6.8a), but they have their individual colorscales.

Concurrent Raman backscattering

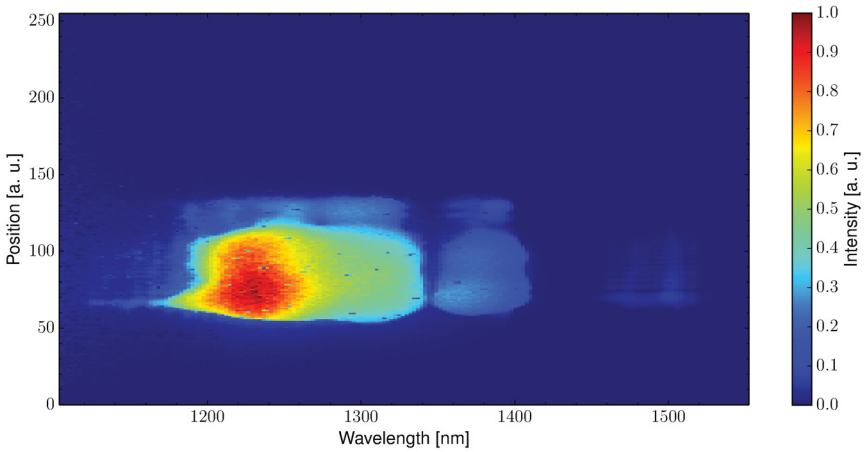

FIG. 6.9.: Raman backscattering of the pump.

To measure the Raman backscattering from the pump (Sec. 3.4.1), the TCC was imaged onto the entrance slit of a low-resolution spectrometer. To avoid ambiguities in the spectrum due to chromatic aberrations, which would otherwise be sizable over a spectral range of 550 nm, imaging was done using reflective optics only. The spectra were recorded with a commercial InGaAs 12 bit camera (Xeva 152, Xenics, Leuven, Belgium) with a 320 px × 255 px chip with 30 μm pixel size.

The spectrometer was calibrated using diode lasers at 1064 nm and 1057 nm wavelength. The spectral range (from 1150 nm to 1700 nm) was limited by the Silicon filter (used to block wavelengths below 1150 nm) and the response of the camera (see Fig. 3.18). According to Eq. (2.44), this corresponds to an electron plasma density between 0.7 % and 14.3 %.

Figure 6.9 shows the backward Raman scattering of the pump observed on a shot where no amplification took place due to an incorrect pump-seed delay. On this shot, strong Raman backscattering took place. The signal is sizable between 1200 nm wavelength (corresponding to an electron density of 1.3 %n_c) and 1400 nm wavelength (corresponding to an electron density of 7 %n_c). This means that the pump laser pulse encountered zones in the plasma of these densities. The higher density zones in the center of the plasma are not visible on this diagnostic because the signal is too much attenuated on its way through the plasma.

6.2. Results

For the pulse parameters detailed above, a scan in pump-seed delay around the temporal zero was done. The pump had an intensity of $I_0 = 2.8 \times 10^{15}\,\mathrm{W/cm^2}$ (i. e. an $a_0 =$

3.6×10^{-2}) and a duration of 4 ps. The seed had an intensity of $I_1 = 1.4 \times 10^{13}\,\mathrm{W/cm^2}$ (i. e. an $a_0 = 2.6 \times 10^{-3}$) and a duration of 700 fs. Both beams had a wavelength of 800 nm and were linearly polarized. The plasma density was $7\,\%n_c$ and its electron temperature below 280 eV.

6.2.1. Gain

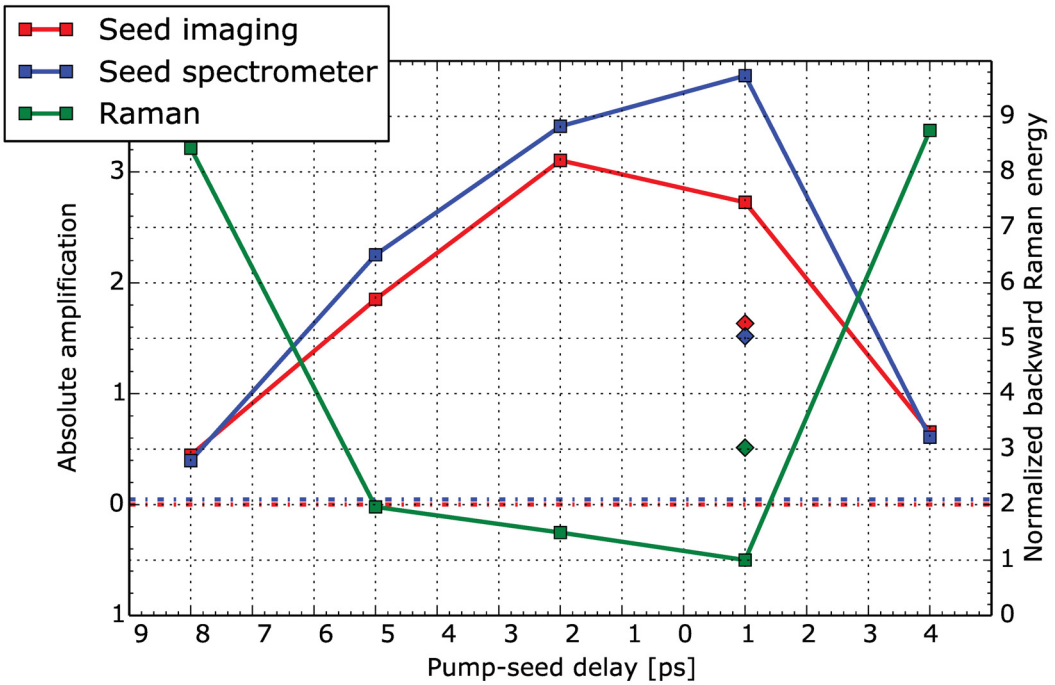

FIG. 6.10.: Integrated signals of seed imaging, seed spectrum, and Pump Raman backscatter. Diamonds represent values for the shot at $\Delta t = 1$ ps with crossed polarization. Dashed-dotted red and blue lines show transmission in plasma without amplification.

Figure 6.10 shows the gain (absolute amplification) obtained from the camera (2D calorimetry, red), the gain obtained from the spectrometer (1D calorimetry, blue), and the integrated backward Raman scattered signal. The slightly higher maximum for the 1D calorimetry shows that amplification is stronger in the center of the focal spot, because this part of the focal spot passes through the spectrometer entrance slit.

The increase of the calorimetry signals when approaching zero delay is to be attributed to amplification of the seed: The general agreement between 1D and 2D calorimetry is a clear indication that the energy transfer occurs in the spectral bandwidth of the seed, therefore proving that it is Brillouin backscattering. This quantitatively confirms that the gain occurs in a small spectral bandwidth, as is already visible in Fig. 6.8c and

will be detailed in Fig. 6.12. When the seed propagates through the preformed plasma without the pump, it is attenuated to 10 % of the vacuum level.

The gain is not symmetric with respect to the zero delay. Highest energy is observed at the optimal delay ($\Delta t = -2\,\mathrm{ps}$). This is because at positive delays, the seed propagates through the plasma and is attenuated before interacting with the maximum of the pump. Amplification starts thus with a weaker seed, the self-similar regime is reached later, and amplification ends when the seed leaves the high-intensity part of the pump. At negative delays, on the other hand, the seeds interacts with the most intense part of the pump before interaction, leading to higher gain.

6.2.2. Seed pulse spectrum

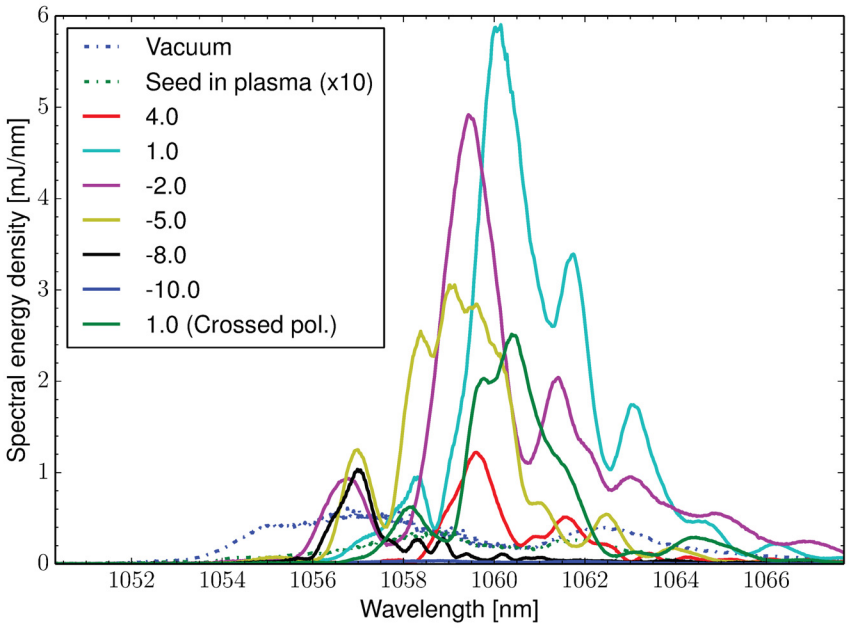

FIG. 6.11.: Seed spectra depending on the delay.

Figures 6.11 and 6.12 show lineouts of the spectra of the seed pulses for the shot series corresponding to Fig. 6.8: The incoming seed spectrum ("vacuum" case) is from Fig. 6.8a. The transmitted seed spectrum ("seed in plasma" case) is from Fig. 6.8b. The "$\Delta t = 1.0\,\mathrm{ps}$" case corresponds to Fig. 6.8c. In Figure 6.12, they were normalized to their individual maxima to show only differences in the form of the spectra. The delay indicated here is defined as $\Delta t = t_p - t_s$. This means that for $\Delta t \gg 1$, the seed passes through the unperturbed plasma before the pump arrives, which is comparable to the seed in plasma case. For $\Delta t \ll 0$, the seed arrives much later than the pump, traversing

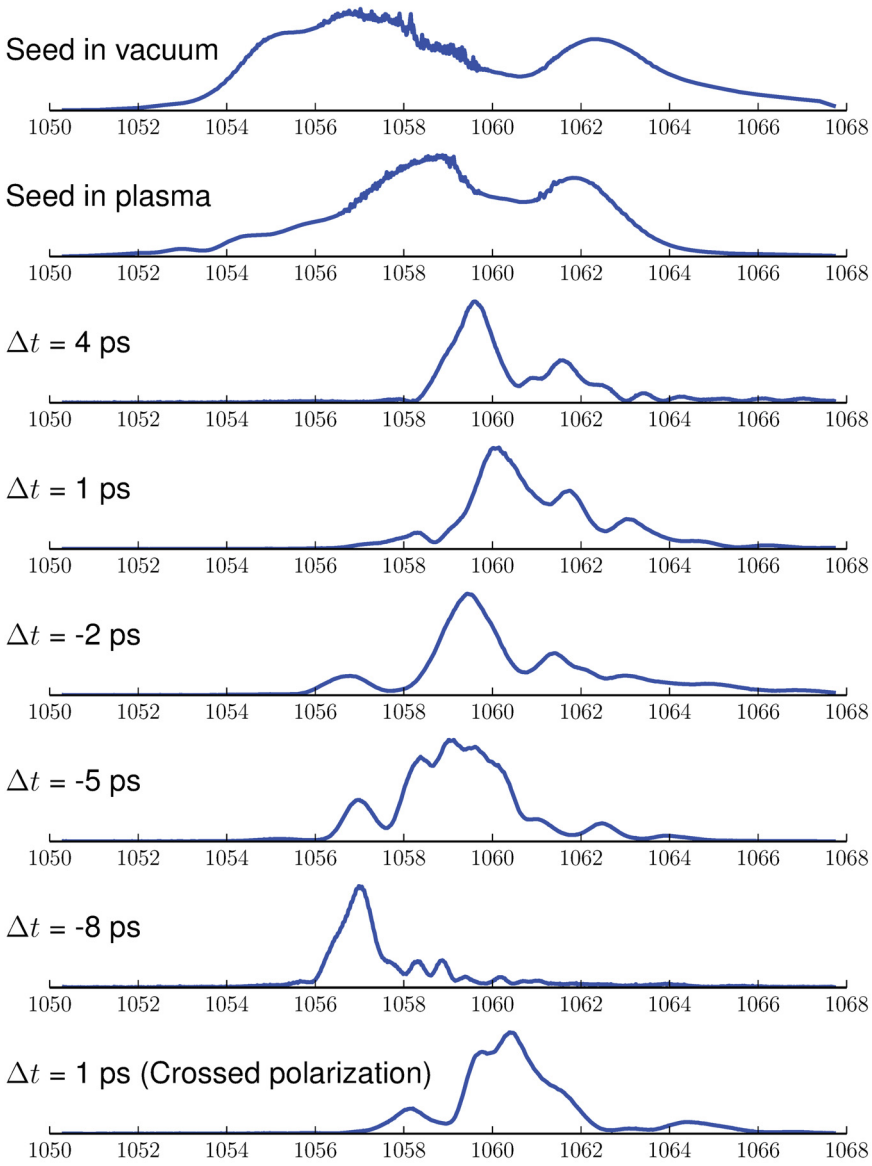

FIG. 6.12.: Normalized seed spectra depending on the delay.

a plasma that is already perturbed by the pump.

The "Seed in plasma" case shows that the spectrum narrows when transmitted by the plasma. It is also strongly attenuated.

For the interaction shots at all delays shown here, sizable amplification takes place since the signal is much stronger than in the "Seed in plasma" case. This difference is not visible in Fig. 6.12 because the plots are normalized. However, it is clearly visible that not the whole transmitted spectrum is amplified. When comparing the spectra of

the series for the different delays, one can clearly see that they have a similar overall form but a different redshift. For the spectrum $\Delta t = 1\,\mathrm{ps}$, the highest gain has been observed on the spectrometer (1D calorimetry in Fig. 6.10). Here, the spectrum is most red-shifted. It is also broadened when comparing to the cases with $\Delta t = 4\,\mathrm{ps}$ and $\Delta t = -2\,\mathrm{ps}$.

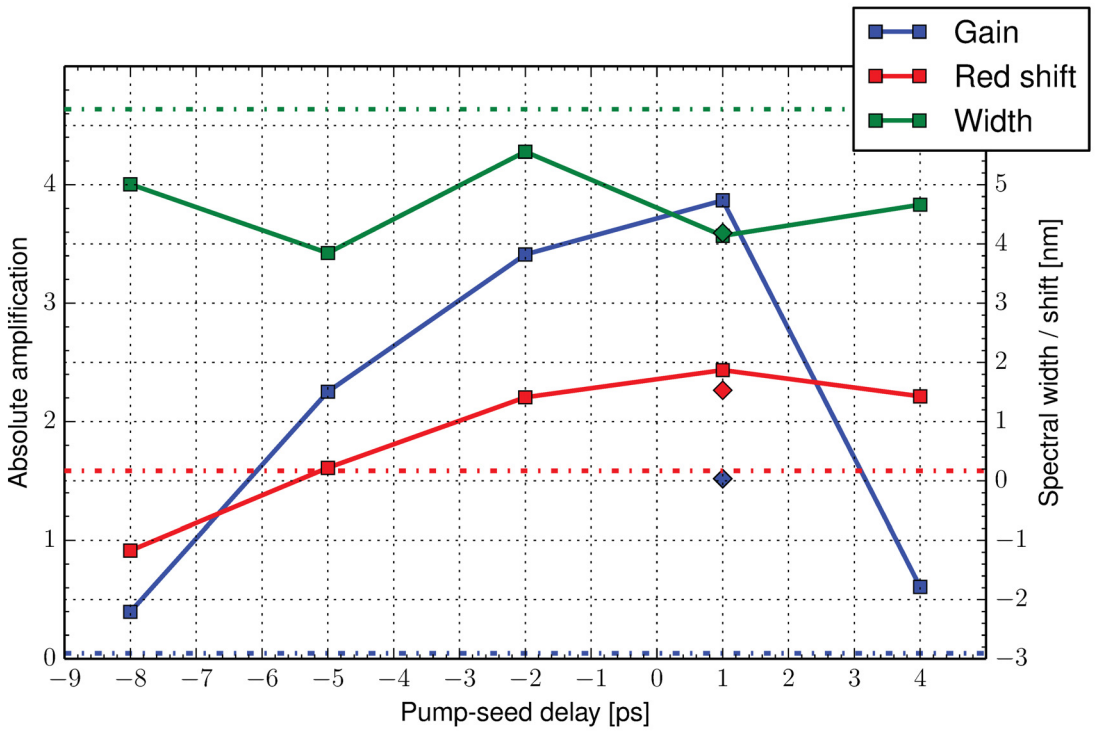

FIG. 6.13.: Integrated signal of seed spectrum (same as in Fig. 6.10; red lines, left scale), red shift of the center of mass (red line) and width (green line) of seed spectra (both right scale). Same dataset as in Fig. 6.12. Diamonds represent the values for the shot at $\Delta t = 1\,\mathrm{ps}$ with crossed polarization. Dash-dotted lines indicate the values for the seed after transmission in plasma without amplification.

This can be seen more clearly if the red shift and the spectral width are quantified using the center of mass and the width as defined in Sec. 3.4.1. Figure 6.13 shows both statistical values. To quantify the red shift of the spectrum's center of mass (calculated with Eq. (3.18)), the difference to the value for the incoming seed (vacuum shot) is shown (red line). The dash-dotted line indicates the value for the seed transmitted by the plasma. The spectral width is indicated by the green line. It has been calculated using Eq. (3.19). Again, the dash-dotted line indicates the value for the seed transmitted in the plasma.

These statistical data confirm the trend already visible on the spectra. The downshift

of the spectrum for the shot at $\Delta t = -8\,\mathrm{ps}$ is due to the fact that only the lower wavelength (blue) part of the spectrum is amplified. Starting from this value, the strongest redshift corresponds to the shot with the highest gain. The change in the spectral width is also characteristic for the transition from the linear to the self-similar regime (see Sec. 2.3.3. Linear amplification leads to spectral narrowing (delays $\Delta t = -5\,\mathrm{ps}$ and $\Delta t = 1\,\mathrm{ps}$. For self-similar amplification ($\Delta t = -2\,\mathrm{ps}$), the spectral width is in part recovered. Normally, one would expect this to happen at the delay $\Delta t = 1\,\mathrm{ps}$ because the self-similar regime is reached when the gain is highest. The fact that this happens for $\Delta t = -2\,\mathrm{ps}$ can only be attributed to shot-to shot fluctuations. This shot is also the shot for which the gain measured by 2D calorimetry was highest. This can be due to different plasma densities and thus different gains along the jet.

6.2.3. Seed pulse duration

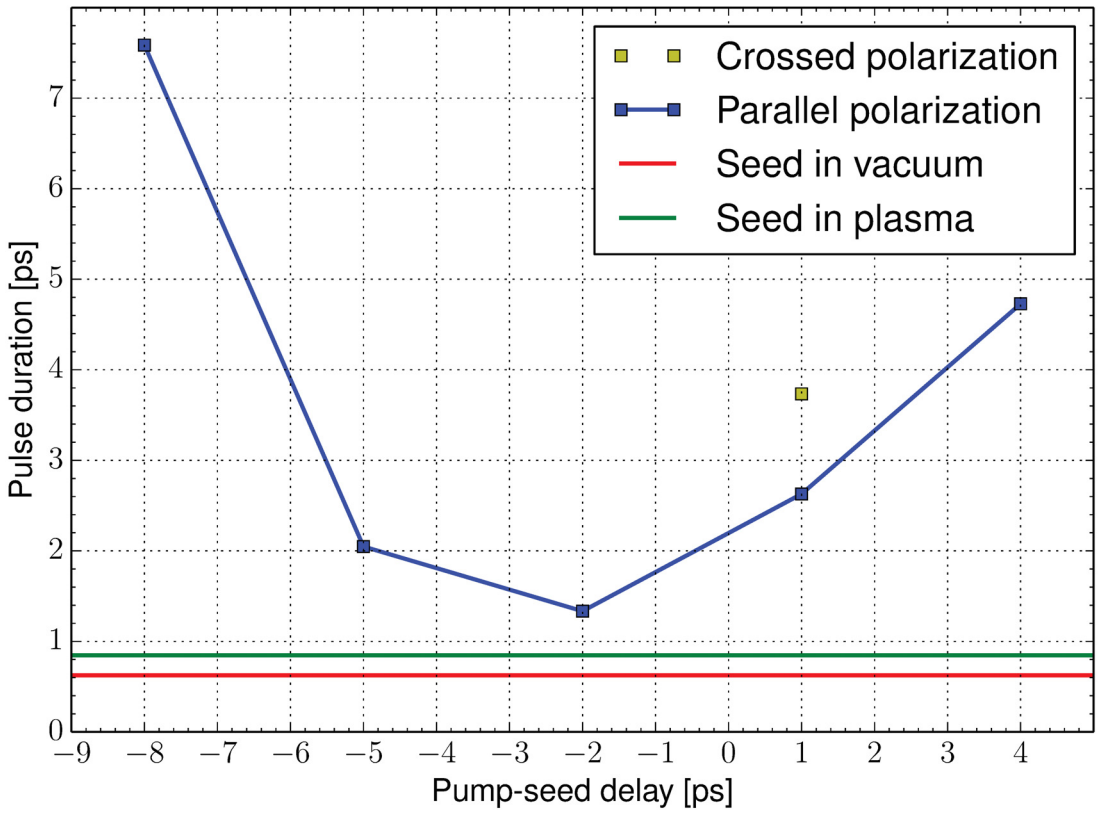

FIG. 6.14.: Autocorrelation trace width depending on the delay for the same series as Fig. 6.10.

For this shot series, the autocorrelator trace was much stronger when both pump and seed were fired and the delay was so close to the zero that interaction within the target

can be inferred. This further confirms that this signal corresponds to the duration of the seed, and not spontaneous backscattering growing from noise.

The pulse durations were retrieved by fitting Gaussian curves to the autocorrelation traces (Sec. 3.4.2), assuming the temporal profile of the seed pulse also to be Gaussian. Figure 6.14 shows the pulse durations for the same shot series as Fig. 6.10. The red line represents the duration of the incoming seed (the vacuum shot shown above, in Fig. 6.12). The blue line shows the duration of the transmitted seed from the shot where the pump was not fired (the transmission shot in Fig. 6.12). As can be seen, the pulse is only slightly stretched after transmission through the plasma. However, the amplified pulses are significantly longer. This can be explained by the fact that the seed pulses grow first in the linear regime. Here, only a part of the pulse spectrum (around 1057 nm, cf. Fig. 6.12) is amplified. Therefore, the pulses are temporally stretched at these delays, whereas they are recompressed in the self-similar regime. This is concomitant with the spectral broadening (Fig. 6.13). At optimal delay, for which the amplification is strongest, we observe that the outgoing seed is not significantly longer than the seed pulse in vacuum. This means that the seed is effectively recompressed by the amplification process.

6.3. Conclusions

Absorption Comparing the energy (determined by integrating the intensity values on the camera) of the incoming seed (Fig. 6.6a) and the transmitted seed without the pump (Fig. 6.6b), one obtains a transmission level of only 12 %. As in the ARCTURUS experiments, this is in part due to collisional absorption, in part due to refraction over small-scale inhomogeneities. The transmission is lower than in the ARCTURUS beamtimes because the plasma is longer, and because the prepulse comes under an angle, much less prone to create on-axis inhomogeneities. The form of the spectrum is preserved upon transmission, as was the case in the ARCTURUS experiment II in the preformed plasma.

Amplification In this experiment, the transition of amplification by sc-SBS from the linear to the self-similar regime could be demonstrated. This is visible from spectral broadening and shift, recompression, and SBS-SRS anticorrelation. This allows to conclude that all the conditions for efficient amplification were met, including an appropriate chirp of the pump.

Compared to the previous experiment with the same laser [51], the pump and seed intensities were lower ($3 \times 10^{15}\,\mathrm{W/cm^2}$ rather than $6 \times 10^{16}\,\mathrm{W/cm^2}$ for the pump, and $10^{13}\,\mathrm{W/cm^2}$ rather than $5 \times 10^{15}\,\mathrm{W/cm^2}$ for the seed). However, still 12 mJ of energy were transferred from the pump to the seed, leading to a conversion efficiency of 0.2 %. This shows that high intensities are not particularly the optimum for amplification by sc-SBS. This experiment also confirms the role of the pump bandwidth and chirp. For this, rather weak chirp, self-similar amplification is predicted. Also, the highest gain is observed at a pump-seed delay of −2 ps, i. e. pump and seed meet on a density slope,

rather than at highest density. This is expected because a density slope drives Raman backscattering out of the resonance, so that more energy is transferred by SBS.

7. Conclusions and future prospects

In this thesis, the feasibility of two applications of laser-plasma interaction using gas targets has been demonstrated: Collisionless shock acceleration using a high-density gas jet, and laser amplification by stimulated Brillouin backscattering.

7.1. Proton acceleration by CSA

Forward ion acceleration was observed (Chap. 4) upon interaction of single Nd:glass laser pulses (210 J, 5 ps, $a_0 \approx 1$) with a high-density gas jet ($2.5\,n_c$). The ion spectra showed a quasi-monoenergetic peak in the range of $200 \ldots 800$ keV and particle fluxes of 4×10^{12} particles/MeV/sr. The particles were accelerated in forward direction (into an angle of 150 mrad) only. The only known mechanisms for these beam properties are HBA and CSA. The acceleration was ascribed to the latter because PIC simulations show it for the experiment's parameter set, and because the energies measured in the experiment are close to predictions both from the analytic theory and the PIC simulation.

Before this experiment, CSA acceleration had been demonstrated using CO_2 lasers at a wavelength of 10 μm lasers only. At slightly higher density than in our experiment, ($n_e/n_c = 6$) [24], similar ion beam parameters had been reached. At a similar density ($n_e/n_c = 2$), higher energies up to 18 MeV density had been reached [4], albeit with a particle flux five orders of magnitude lower.

As reaching both higher energies and higher flux arguably necessitates a higher laser intensity, laser systems in the near infrared (Ti:sapphire or Nd:glass), which will reach $a_0 = 200$ in the foreseeable future, are likely to be the system of choice, combined with high-density gas jet targets. The increase in proton energy then can take advantage of the favorable CSA scaling as the peak ion energy is proportional to the laser intensity. Furthermore, established gas jet design techniques can be used to obtain a target with a shorter interaction length.

7.2. Laser-plasma interaction and laser amplification by sc-SBS

In three experiments, propagation, spontaneous, and stimulated backscattering of broadband laser pulses in underdense plasmas were studied in the context of short pulse amplification by sc-SBS, using a Ti:sapphire laser (ARCTURUS) and an Nd:glass laser (ELFIE). Pump pulses in the near-infrared range at (vacuum) intensities of $2 \ldots 4 \times 10^{15}$ W/cm^2 and durations of $0.78 \ldots 4$ ps were interacting with gas jets at $5\,\% \ldots 21\,\% n_c$ density.

Beam transmission In all experiments, the pump pulse's intensity in the plasma (1 % to 40 % of the vacuum value) was sufficiently high for SBS to be strongly coupled. The generation of an ion acoustic wave was evidenced by the observation of stimulated or spontaneous backscattering.

A seed beam of a duration of 30 . . . 700 fs and an intensity of $10^{13}\,\mathrm{W/cm^2}$ was added and overlapped with the pump in space and time. This allowed to study its interaction with and its amplification by the pump beam.

Creating a preformed plasma allowed to reduce the absorption in the target. Furthermore, it allowed to preserve the form of the spectrum after transmission, indicating that the pump absorption did not change with time during the interaction.

Amplification by sc-SBS The influence of bandwidth and duration was investigated by comparing the results from the Nd:glass system to those from the Ti:sapphire system, thus comparing a bandwidth of 6 nm to a 60 nm, and durations of 30 . . . 160 fs to 700 fs. Therefore, durations below and above the sc-SBS growth rate [Eq. (2.36)], which is the characteristic time scale of the process and typically $1/\gamma_2^{sc} = 173\,\mathrm{fs}$, were tested.

One would have expected amplification in both cases for the following reasons: In the linear regime the gain (Eq. (2.35)) depends on plasma species, density, and laser field strength, but not on the duration. The amplified seed duration is, however, limited as the sc-SBS does not amplify arbitrarily broad spectra. The analytical self-similar theory [41] suggested a seed growth $\propto t^{3/4}$ in case the initial seed duration is short compared to $1/\gamma_2^{sc}$, but a reduced growth (lower exponent than 3/4) for a longer pulse. Vlasov simulations [67] have confirmed this scenario: The initially longer seed is amplified in both linear and self-similar stage, whereas a shorter seed is stretched in time (by developing a tail), and then is more strongly amplified in the self-similar regime. This is consistent with PIC simulations [49]. These theoretical predictions did not take into account the chirp.

In an experiment, however, the pump pulse has to be chirped. This is necessary because pump and seed spectra are supposed to be equally wide, and the pump duration has to be adjusted to the desired amplifier length (which should also be the propagation length in the gas target). Therefore, in these different experiments, the chirp parameters are different and influence the phase [Eq. (2.31)], which is crucial for the amplitude and phase development of pump and seed [Eqs. (2.23) to (2.26)].

At the ELFIE Nd:glass system, pump and seed had a bandwidth of 6 nm. The pump was stretched to 4 ps, leading to a chirp factor of $|\alpha| = 2\times10^{-7}$. Here, the transition from the linear to the self-similar regime was demonstrated, confirming predictions from analytical theory and simulations [41, 73, 74]. Amplification of a factor of 5 was reached and tens of millijoules of energy were transferred from the pump to the seed. The transition to self-similar regime could be confirmed by the correlation of pulse compression, frequency broadening, and down-shifting with increasing gain. The Raman-Brillouin competition, predicted by the theory [102], has been proven by the observation of a decrease in the backward Raman signal when amplification was efficient.

In the ARCTURUS experiments, the 800 nm, 30 fs bandwidth-limited pulse, stretched

to 0.78 ps . . . 1.7 ps, has a chirp factor of $|\alpha| = 2 \times 10^{-6} \ldots 5 \times 10^{-6}$. This is higher than at ELFIE due to the higher spectral bandwidth. The amplification was quenched here.

Both results are confirmed by calculations done by CHIARAMELLO et al. [63], using an envelope code that solves the full set of wave equations [Eqs. (2.23) to (2.31)] but does not include kinetic effects: The chirp factor of $|\alpha| = 2 \times 10^{-7}$ used in the ELFIE experiments is also the optimum value for amplification, whereas a chirp factor $|\alpha| = 5 \times 10^{-6}$, which was the case for the ARCTURUS experiments, effectively quenched amplification.

Prospects In order to reach the optimum chirp for these broadband pulses, one would have to stretch them to 20 ps. For pump and seed to interact within a plasma during this time, the interaction length in the target would have to be $20\,\mathrm{ps}\, c/2 = 3\,\mathrm{mm}$. Given that the present ionization pulse was barely sufficient to make a 0.5 mm target transparent for pump and seed, amplifying the whole spectrum would necessitate an entirely different pre-ionization and pre-heating scheme, e. g. by a more energetic prepulse coming perpendicularly to the main propagation axis and focused to a line focus. Another difficulty might arise from pump filamentation, since the time scale [Eq. (2.52)] for that instability is on the order of some picoseconds for our densities and intensities. Also, a higher pump energy would be useful to maintain an intensity of $10^{15}\,\mathrm{W/cm^2}$ even for a much longer pulse. An upcoming upgrade of the ARCTURUS laser is expected to increase the available energy on target by a factor of 2. Therefore after the upgrade, the intensity on the target could be maintained by reducing the focal spot size by a factor of three, which is feasible.

Two more points merit further investigation: First, the phase matching could be optimized by using a ramp-like target [49, 295]. Second, the beam geometry used in these experiments (fully counterpropagating) is useful to investigate the process, as it is essentially 1-dimensional. As long as one-direction devices are at hand to prevent damage to the laser from the transmitted pulses, this is feasible as the transmitted pulses can be extracted using beam splitters. In a practical amplifier scenario, however, this would mean throwing away a large part of the energy. In comparison, a geometry where pump and seed are under an angle reduces the overlap zone and makes the beam propagation through an inhomogeneous plasma hard to control. Therefore, pre-ionization and beam propagation control are important challenges to come on the way towards an efficient plasma amplifier.

Appendices

A. Publications

Publications in peer-reviewed journals

5. M. Barberio, M. Scisciò, S. Vallières, F. Cardelli, S. N. Chen, G. Famulari, **T. Gangolf**, G. Revet, A. Schiavi, M. Senzaqua, and P. Antici, *Laser-Accelerated Particle Beams for Stress Testing of Materials*, Nature Commun. **9**, 372 (2018)

4. S. N. Chen, M. Vranic, **T. Gangolf**, E. Boella, P. Antici, M. Bailly-Grandvaux, P. Loiseau, H. Pépin, G. Revet, J. J. Santos, A. M. Schroer, Mikhail Starodubtsev, O. Willi, L. O. Silva, E. d'Humières and J. Fuchs, *Collimated protons accelerated from an overdense gas jet irradiated by a 1 μm wavelength high-intensity short-pulse laser*, Sci. Rep. **7**, 13505 (2017)

3. B. Landgraf, B. Aurand, G. Lehmann, **T. Gangolf**, M. Schnell, T. Kühl and C. Spielmann, *Broadband Stimulated Raman Backscattering*, New J. Phys. **18**, 073048 (2016)

2. L. Lancia, A. Giribono, L. Vassura, M. Chiaramello, C. Riconda, S. Weber, A. Castan, A. Chatelain, A. Frank, **T. Gangolf**, M. N. Quinn, J. Fuchs and J.-R. Marquès, *Signatures of the Self-Similar Regime of Strongly Coupled Stimulated Brillouin Scattering for Efficient Short Laser Pulse Amplification*, Phys. Rev. Lett. **116**, 075001 (2016)

1. A. Hage, B. Landgraf, M. Taylor, M. Wünsche, **T. Gangolf**, H. Höppner, M. J. Prandolini, R. Riedel, M. Schulz, F. Tavella, A. Willner, M. Yeung, G. G. Paulus, C. Spielmann, B. Dromey and M. Zepf, *New design of a multi-jet target for quasi phase matching*, Rev. Sci. Instrum. **85**, 103105 (2014)

Selected proceedings and conference contributions

- P. Loiseau, A. Castan, J.-R. Marquès, L. Lancia, **T. Gangolf**, J. Fuchs, P.-E. Masson-Laborde, D. Teychenné, A. Debayle, M.-C. Monteil, M. Casanova, C. Rousseaux, S. Lemaire and D. Riz, *High-power laser-plasma interaction in nanosecond regimes 'at a glance' using proton deflectometry*, J. Phys.: Conference Series **717**, 012036 (2016)

- **T. Gangolf**, M. Blecher, S. Bolanos, L. Lancia, J.-R. Marquès, M. Cerchez, R. Prasad, B. Aurand, F. Schluck, G. Lehmann, M. Chiaramello, C. Riconda, S. Weber, G. Mourou, O. Willi and J. Fuchs, *Amplification of ultrashort laser*

pulses by Stimulated Brillouin Backscattering, 43. EPS Conference on plasma physics, poster and proceedings, July 2016, Leuven (Belgium)

- **T. Gangolf**, L. Lancia, J.-R. Marquès, A. Giribono, K. Glize, M. Blecher, L. Vassura, A. Frank, M. Quinn, M. Cerchez, C. Riconda, S. Weber, M. Chiaramello, G. Mourou, O. Willi and J. Fuchs, *Amplification of short laser pulses by Stimulated Brillouin Backscattering*, 42. EPS Conference on plasma physics, poster and proceedings, June 2015, Lisbon (Portugal)

- E. d'Humières, S. Chen, M. Lobet, M. Sciscio, P. Antici, M. Bailly-Grandvaux, **T. Gangolf**, G. Revet, J. J. Santos, A. M. Schroer, O. Willi, V. Tikhonchuk, H. Pépin and J. Fuchs, *Longitudinal laser ion acceleration in low density targets: experimental optimization on the Titan laser facility and numerical investigation of the ultra-high intensity limit*, Proc. SPIE **9514**, 95140B (2015)

B. Symbols

TABLE B.1.: Fundamental constants.

Symbol	Description
e	Elementary charge
c	Speed of light in vacuum
m_e	Electron rest mass
m_p	Proton rest mass
ϵ_0	Vacuum permittivity
e^1	Euler's number
k_B	Boltzmann constant

TABLE B.2.: Neutral gas parameters.

Symbol	Description
C_p	Heat capacity at constant pressure
C_V	Heat capacity at constant volume
λ_{MF}	Mean free path
r_W	Van der Waals radius
ζ	Mach angle
T	Temperature
F	Area
p	Pressure
n	Density
M	Mach number
ν_{PM}	Prandtl-Meyer function
κ	Specific heat ratio
m_m	Molecular mass
α	Polarizability
η	Refractive index

TABLE B.3.: Laser parameters.

Symbol	Description
I	Laser intensity
λ	Laser wavelength
ω	Laser angular frequency
$\mathbf{A}$	Vector potential
a_0	Amplitude of the normalized vector potential
v^g	Group velocity
γ	Relativistic gamma factor of the laser
E_{pond}	Ponderomotive potential
F_{pond}	Ponderomotive force
P_{rad}	Radiation pressure
R	Reflection coefficient
T	Transmission coefficient
v_o	Classic electron quiver velocity
$\mathcal{E}$	Electric field
ν	Collisional absorption damping rate
R	Collisional absorption energy conversion rate
C_{Langdon}	Langdon correction factor
C_{Faehl}	Faehl correction factor
L_G	Plasma gradient scale length
$F_{\mathbf{j}\times\mathbf{B}}$	$\mathbf{j} \times \mathbf{B}$ force
Φ	Electrostatic potential
ω	Angular frequency
ϕ	Phase
λ	Wavelength
$\mathbf{k}$	Wave vector
k	Wave number
τ	Pulse duration
0 (as index to ω, λ, $\mathbf{k}$, I)	Pump
1 (as index to ω, λ, $\mathbf{k}$, I)	Seed
Δt	Pump-seed delay

TABLE B.4.: Plasma parameters.

Symbol	Description
2 (as index to ω, λ, $\mathbf{k}$)	Plasma wave
γ_2^{wc}	Plasma wave growth rate (wc-SBS)
γ_2^{sc}, γ_{sc}	Plasma wave growth rate (sc-SBS)
n_c	Critical density
n_e	Plasma electron density
η	Refractive index
T_e	Plasma electron temperature
T_i	Plasma ion temperature
c_s	Ion sound velocity
m_i	Ion mass
A	Mass number
Z	Charge number
ν_{ei}	Electron-ion collision frequency
ω_{pe}	Plasma electron frequency
ω_{pi}	Plasma ion frequency
v_e	Electron thermal velocity
$\ln \Lambda$	Coulomb logarithm for electron-ion collisions
η	Plasma refractive index
λ_D	Electron Debye length
T_h^{Brunel}	Hot electron temperature (Brunel scaling)
T_h^{Wilks}	Hot electron temperature (Wilks scaling)
T_h^{Beg}	Hot electron temperature (Beg scaling)
T_h^{Haines}	Hot electron temperature (Haines scaling)
γ_{fil}	Filamentation growth rate
τ_{fil}	Filamentation time scale
γ_{wb}	Ion acoustic wave breaking growth rate
g_{abs}	Absolute gain
g_{rel}	Relative gain
g'_{rel}	Relative gain without spontaneous backscattering
η_{amp}	Energy transfer efficiency
v_{HB}	Hole boring critical surface velocity
γ_{HB}	Hole boring critical surface gamma factor

TABLE B.5.: Ion parameters.

Symbol	Description
p	Momentum
E	Energy

Bibliography

[1] R. Betti and O. A. Hurricane, Nat. Phys. **12**, 435 (2016).

[2] B. Albertazzi, A. Ciardi, M. Nakatsutsumi, T. Vinci, J. Béard, R. Bonito, J. Billette, M. Borghesi, Z. Burkley, S. N. Chen, T. E. Cowan, T. Herrmannsdörfer, D. P. Higginson, F. Kroll, S. A. Pikuz, K. Naughton, L. Romagnani, C. Riconda, G. Revet, R. Riquier, H.-P. Schlenvoigt, I. Y. Skobelev, A. Faenov, A. Soloviev, M. Huarte-Espinosa, A. Frank, O. Portugall, H. Pépin, and J. Fuchs, Science **346**, 325 (2014).

[3] W. P. Leemans, A. J. Gonsalves, H.-S. Mao, K. Nakamura, C. Benedetti, C. B. Schroeder, C. Tóth, J. Daniels, D. E. Mittelberger, S. S. Bulanov, J.-L. Vay, C. G. R. Geddes, and E. Esarey, Phys. Rev. Lett. **113**, 245002 (2014).

[4] D. Haberberger, S. Tochitsky, F. Fiuza, C. Gong, R. A. Fonseca, L. O. Silva, W. B. Mori, and C. Joshi, Nat. Phys. **8**, 95 (2012).

[5] J. Ren, W. Cheng, S. Li, and S. Suckewer, Nat. Phys. **3**, 732 (2007).

[6] L. Lancia, A. Giribono, L. Vassura, M. Chiaramello, C. Riconda, S. Weber, A. Castan, A. Chatelain, A. Frank, T. Gangolf, M. N. Quinn, J. Fuchs, and J.-R. Marquès, Phys. Rev. Lett. **116**, 075001 (2016).

[7] M. Schnell, A. Sävert, I. Uschmann, M. Reuter, M. Nicolai, T. Kämpfer, B. Landgraf, O. Jäckel, O. Jansen, A. Pukhov, M. C. Kaluza, and C. Spielmann, Nat. Commun. **4**, (2013).

[8] H. Vincenti and F. Quéré, Phys. Rev. Lett. **108**, 113904 (2012).

[9] W. L. Kruer, *The Physics of Laser Plasma Interactions* (Westview Press, 1988).

[10] L. Obst, S. Kraft, J. Metzkes, U. Schramm, and K. Zeil, in *Proc. of International Particle Accelerator Conference (IPAC'14), Dresden, Germany, June 15-20, 2014*, International Particle Accelerator Conference No. 5 (JACoW, Geneva, Switzerland, 2014) pp. 4093–4095, https://doi.org/10.18429/JACoW-IPAC2014-TUPME033.

[11] M. Borghesi, J. Fuchs, S. V. Bulanov, A. J. MacKinnon, P. K. Patel, and M. Roth, Fusion Science and Technology **49**, 412 (2006), http://www.tandfonline.com/doi/pdf/10.13182/FST06-A1159 .

[12] H. Daido, M. Nishiuchi, and A. S. Pirozhkov, Rep. Prog. Phys. **75**, 056401 (2012).

[13] A. Macchi, M. Borghesi, and M. Passoni, Rev. Mod. Phys. **85**, 751 (2013).

[14] S. Raschke, S. Spickermann, T. Toncian, M. Swantusch, J. Boeker, U. Giesen, G. Iliakis, O. Willi, and F. Boege, Scientific Reports **6**, 32441 (2016).

[15] U. Linz and J. Alonso, Phys. Rev. ST Accel. Beams **10**, 094801 (2007).

[16] S. V. Bulanov and V. S. Khoroshkov, Plasma Physics Reports **28**, 453 (2002).

[17] M. Borghesi, D. H. Campbell, A. Schiavi, M. G. Haines, O. Willi, A. J. MacKinnon, P. Patel, L. A. Gizzi, M. Galimberti, R. J. Clarke, F. Pegoraro, H. Ruhl, and S. Bulanov, Physics of Plasmas **9**, 2214 (2002), http://dx.doi.org/10.1063/1.1459457 .

[18] A. J. Mackinnon, P. K. Patel, M. Borghesi, R. C. Clarke, R. R. Freeman, H. Habara, S. P. Hatchett, D. Hey, D. G. Hicks, S. Kar, M. H. Key, J. A. King, K. Lancaster, D. Neely, A. Nikkro, P. A. Norreys, M. M. Notley, T. W. Phillips, L. Romagnani, R. A. Snavely, R. B. Stephens, and R. P. J. Town, Phys. Rev. Lett. **97**, 045001 (2006).

[19] S. Kar, M. Borghesi, C. A. Cecchetti, L. Romagnani, F. Ceccherini, T. V. Liseykina, A. Macchi, R. Jung, J. Osterholz, O. Willi, L. A. Gizzi, A. Schiavi, M. Galimberti, and R. Heathcote, New Journal of Physics **9**, 402 (2007).

[20] A. Pelka, G. Gregori, D. O. Gericke, J. Vorberger, S. H. Glenzer, M. M. Günther, K. Harres, R. Heathcote, A. L. Kritcher, N. L. Kugland, B. Li, M. Makita, J. Mithen, D. Neely, C. Niemann, A. Otten, D. Riley, G. Schaumann, M. Schollmeier, A. Tauschwitz, and M. Roth, Phys. Rev. Lett. **105**, 265701 (2010).

[21] M. Roth, T. E. Cowan, M. H. Key, S. P. Hatchett, C. Brown, W. Fountain, J. Johnson, D. M. Pennington, R. A. Snavely, S. C. Wilks, K. Yasuike, H. Ruhl, F. Pegoraro, S. V. Bulanov, E. M. Campbell, M. D. Perry, and H. Powell, Phys. Rev. Lett. **86**, 436 (2001).

[22] K. Krushelnick, E. Clark, Z. Najmudin, M. Salvati, M. Santala, M. Tatarakis, A. Dangor, V. Malka, D. Neely, R. Allott, and C. Danson, Phys. Rev. Lett. **83**, 737 (1999).

[23] R. A. Snavely, M. H. Key, S. P. Hatchett, T. E. Cowan, M. Roth, T. W. Phillips, M. A. Stoyer, E. A. Henry, T. C. Sangster, M. S. Singh, S. C. Wilks, A. MacKinnon, A. Offenberger, D. M. Pennington, K. Yasuike, A. B. Langdon, B. F. Lasinski, J. Johnson, M. D. Perry, and E. M. Campbell, Phys. Rev. Lett. **85**, 2945 (2000).

[24] C. A. J. Palmer, N. P. Dover, I. Pogorelsky, M. Babzien, G. I. Dudnikova, M. Ispiriyan, M. N. Polyanskiy, J. Schreiber, P. Shkolnikov, V. Yakimenko, and Z. Najmudin, Phys. Rev. Lett. **106**, 014801 (2011).

[25] C. Riconda, S. Weber, L. Lancia, J.-R. Marquès, G. Mourou, and J. Fuchs, Plasma Phys. Cont. Fusion **57**, 014002 (2015).

[26] J. Fuchs, A. Gonoskov, M. Nakatsutsumi, W. Nazarov, F. Quéré, A. Sergeev, and X. Yan, Eur. Phys. J. Special Topics **223**, 1169 (2014).

[27] T. Gangolf, M. Blecher, S. Bolanos, L. Lancia, J. Marquès, M. Cerchez, R. Prasad, B. Aurand, F. Schluck, G. Lehmann, M. Chiaramello, C. Riconda, S. Weber, G. Mourou, O. Willi, and J. Fuchs, in *43rd EPS Conference on Plasma Physics 4 - 8 July 2016*, europhysics conference abstracts, Vol. 40A (2016).

[28] H. C. Kapteyn, A. Szoke, R. W. Falcone, and M. M. Murnane, Opt. Lett. **16**, 490 (1991).

[29] G. Lehmann and K. H. Spatschek, Phys. Rev. Lett. **116**, 225002 (2016).

[30] W. Cheng, Y. Avitzour, Y. Ping, S. Suckewer, N. J. Fisch, M. S. Hur, and J. S. Wurtele, Phys. Rev. Lett. **94**, 045003 (2005).

[31] N. A. Yampolsky, N. J. Fisch, V. M. Malkin, E. J. Valeo, R. Lindberg, J. Wurtele, J. Ren, S. Li, A. Morozov, and S. Suckewer, Phys. Plasmas **15**, 113104 (2008).

[32] R. D. Milroy, C. E. Capjack, and C. R. James, Phys. Fluids **22**, 1922 (1979).

[33] D. Strickland and G. Mourou, Opt. Commun. **56**, 219 (1985).

[34] A. Dubietis, G. Jonušauskas, and A. Piskarskas, Opt. Commun. **88**, 437 (1992).

[35] M. Dreher, *Experimental Demonstration of Superradiant Amplification of Ultra-Short Laser Pulses in a Plasma*, Ph.D. thesis, Ludwig-Maximilians-Universität München (2004).

[36] P. Poole, S. Trendafilov, G. Shvets, D. Smith, and E. Chowdhury, Opt. Express **21**, 26341 (2013).

[37] G. Shvets, N. J. Fisch, A. Pukhov, and J. Meyer-ter Vehn, Phys. Rev. Lett. **81**, 4879 (1998).

[38] V. M. Malkin, G. Shvets, and N. J. Fisch, Phys. Rev. Lett. **82**, 4448 (1999).

[39] G. Mourou, N. Fisch, V. Malkin, Z. Toroker, E. Khazanov, A. Sergeev, T. Tajima, and B. L. Garrec, Opt. Commun. **285**, 720 (2012).

[40] J. Zou, C. Le Blanc, D. Papadopoulos, G. Chériaux, P. Georges, G. Mennerat, F. Druon, L. Lecherbourg, A. Pellegrina, P. Ramirez, F. Giambruno, A. Fréneaux, F. Leconte, D. Badarau, J. Boudenne, D. Fournet, T. Valloton, J. Paillard, J. Veray, M. Pina, P. Monot, J. Chambaret, P. Martin, F. Mathieu, P. Audebert, and F. Amiranoff, High Power Laser Science and Engineering **3**, e2 (4 pages) (2015).

[41] A. A. Andreev, C. Riconda, V. T. Tikhonchuk, and S. Weber, Phys. Plasmas **13**, 053110 (2006).

[42] V. M. Malkin, G. Shvets, and N. J. Fisch, Phys. Rev. Lett. **84**, 1208 (2000).

[43] B. Ersfeld and D. A. Jaroszynski, Phys. Rev. Lett. **95**, 165002 (2005).

[44] R. M. G. M. Trines, F. Fiúza, R. Bingham, R. A. Fonseca, L. O. Silva, R. A. Cairns, and P. A. Norreys, Phys. Rev. Lett. **107**, 105002 (2011).

[45] Z. Toroker, V. M. Malkin, and N. J. Fisch, Phys. Rev. Lett. **109**, 085003 (2012).

[46] M. Dreher, E. Takahashi, J. Meyer-ter Vehn, and K.-J. Witte, Phys. Rev. Lett. **93**, 095001 (2004).

[47] Y. Ping, W. Cheng, S. Suckewer, D. S. Clark, and N. J. Fisch, Phys. Rev. Lett. **92**, 175007 (2004).

[48] C.-H. Pai, M.-W. Lin, L.-C. Ha, S.-T. Huang, Y.-C. Tsou, H.-H. Chu, J.-Y. Lin, J. Wang, and S.-Y. Chen, Phys. Rev. Lett. **101**, 065005 (2008).

[49] S. Weber, C. Riconda, L. Lancia, J.-R. Marquès, G. A. Mourou, and J. Fuchs, Phys. Rev. Lett. **111**, 055004 (2013).

[50] G. Lehmann and K. H. Spatschek, Phys. Plasmas **21**, 053101 (2014).

[51] L. Lancia, J.-R. Marquès, M. Nakatsutsumi, C. Riconda, S. Weber, S. Hüller, A. Mančić, P. Antici, V. T. Tikhonchuk, A. Héron, P. Audebert, and J. Fuchs, Phys. Rev. Lett. **104**, 025001 (2010).

[52] M. Schnell, A. Sävert, B. Landgraf, M. Reuter, M. Nicolai, O. Jäckel, C. Peth, T. Thiele, O. Jansen, A. Pukhov, O. Willi, M. C. Kaluza, and C. Spielmann, Phys. Rev. Lett. **108**, 075001 (2012).

[53] Y. Ping, I. Geltner, A. Morozov, N. J. Fisch, and S. Suckewer, Phys. Rev. E **66**, 046401 (2002).

[54] S. Depierreux, C. Labaune, D. T. Michel, C. Stenz, P. Nicolaï, M. Grech, G. Riazuelo, S. Weber, C. Riconda, V. T. Tikhonchuk, P. Loiseau, N. G. Borisenko, W. Nazarov, S. Hüller, D. Pesme, M. Casanova, J. Limpouch, C. Meyer, P. DiNicola, R. Wrobel, E. Alozy, P. Romary, G. Thiell, G. Soullié, C. Reverdin, and B. Villette, Phys. Rev. Lett. **102**, 195005 (2009).

[55] M. Gauthier, A. Levy, E. d'Humieres, M. Glesser, B. Albertazzi, C. Beaucourt, J. Breil, S. N. Chen, V. Dervieux, J. L. Feugeas, P. Nicolai, V. Tikhonchuk, H. Pepin, P. Antici, and J. Fuchs, Phys. Plasmas **21**, 013102 (2014).

[56] Y. Fukuda, A. Y. Faenov, M. Tampo, T. A. Pikuz, T. Nakamura, M. Kando, Y. Hayashi, A. Yogo, H. Sakaki, T. Kameshima, A. S. Pirozhkov, K. Ogura, M. Mori, T. Z. Esirkepov, J. Koga, A. S. Boldarev, V. A. Gasilov, A. I. Magunov, T. Yamauchi, R. Kodama, P. R. Bolton, Y. Kato, T. Tajima, H. Daido, and S. V. Bulanov, Phys. Rev. Lett. **103**, 165002 (2009).

[57] U. Zastrau, P. Sperling, C. Fortmann-Grote, A. Becker, T. Bornath, R. Bredow, T. Döppner, T. Fennel, L. B. Fletcher, E. Förster, S. Göde, G. Gregori, M. Harmand, V. Hilbert, T. Laarmann, H. J. Lee, T. Ma, K. H. Meiwes-Broer, J. P. Mithen, C. D. Murphy, M. Nakatsutsumi, P. Neumayer, A. Przystawik, S. Skruszewicz, J. Tiggesbäumker, S. Toleikis, T. G. White, S. H. Glenzer, R. Redmer, and T. Tschentscher, Journal of Physics B: Atomic, Molecular and Optical Physics **48**, 224004 (2015).

[58] N. Lemos, N. Lopes, J. M. Dias, and F. Viola, Rev. Sci. Instrum. **80**, 103301 (2009).

[59] B. Landgraf, M. Schnell, A. Sävert, M. C. Kaluza, and C. Spielmann, Rev. Sci. Instrum. **82**, 083106 (2011).

[60] K. Schmid and L. Veisz, Rev. Sci. Instrum. **83**, 053304 (2012).

[61] R. Campargue, The Journal of Physical Chemistry **88**, 4466 (1984), http://dx.doi.org/10.1021/j150664a004 .

[62] S. N. Chen, M. Vranic, T. Gangolf, E. Boella, P. Antici, M. Bailly-Grandvaux, P. Loiseau, H. Pépin, G. Revet, J. J. Santos, A. Schroer, M. Starodubtsev, O. Willi, L. O. Silva, E. d'Humières, and J. Fuchs, Sci. Rep. **7**, 13505 (2017).

[63] M. Chiaramello, F. Amiranoff, C. Riconda, and S. Weber, Phys. Rev. Lett. **117**, 235003 (2016).

[64] P. Gibbon, *Short pulse laser interactions with matter: an introduction* (Imperial College Press, London, 2005).

[65] E. Esarey, C. B. Schroeder, and W. P. Leemans, Rev. Mod. Phys. **81**, 1229 (2009).

[66] S. C. Wilks, W. L. Kruer, M. Tabak, and A. B. Langdon, Phys. Rev. Lett. **69**, 1383 (1992).

[67] G. Lehmann and K. H. Spatschek, Phys. Plasmas **20**, 073112 (2013).

[68] W. L. Kruer, S. C. Wilks, B. B. Afeyan, and R. K. Kirkwood, Phys. Plasmas **3**, 382 (1996).

[69] C. Neuville, C. Baccou, A. Debayle, P.-E. Masson-Laborde, S. Hüller, M. Casanova, D. Marion, P. Loiseau, K. Glize, C. Labaune, and S. Depierreux, Phys. Rev. Lett. **117**, 145001 (2016).

[70] R. K. Kirkwood, D. P. Turnbull, T. Chapman, S. C. Wilks, M. D. Rosen, R. A. London, L. Pickworth, W. H. Dunlop, J. D. Moody, D. J. Strozzi, P. A. Michel, L. Divol, O. L. Landen, B. MacGowan, B. M. Van Wonterghem, K. B. Fournier, and B. E. Blue, Nature Physics (2017), 10.1038/nphys4271.

[71] D. W. Forslund, J. M. Kindel, and E. L. Lindman, Phys. Fluids **18**, 1002 (1975).

[72] M. Chiaramello, *Laser amplification via stimulated Brillouin scattering in the strongly coupled regime : towards control and optimization*, Theses, Université Pierre et Marie Curie - Paris VI (2016).

[73] G. Lehmann and K. H. Spatschek, Phys. Plasmas **22**, 043105 (2015).

[74] F. Schluck, G. Lehmann, and K. H. Spatschek, Phys. Plasmas **22**, 093104 (2015).

[75] F. F. Chen, *Introduction to Plasma Physics and Controlled Fusion*, 3rd ed. (Springer, 2016).

[76] D. Turnbull, S. Li, A. Morozov, and S. Suckewer, Phys. Plasmas **19**, 083109 (2012).

[77] C. Goyon, *Experimental investigation of the interaction of an intense laser beam with a long and hot plasma in the context of shock ignition*, Theses, Ecole Polytechnique X (2014).

[78] C. E. Max, J. Arons, and A. B. Langdon, Phys. Rev. Lett. **33**, 209 (1974).

[79] A. B. Langdon, Phys. Rev. Lett. **44**, 575 (1980).

[80] R. D. Jones and K. Lee, Phys. Fluids **25**, 2307 (1982).

[81] R. J. Faehl and N. F. Roderick, Phys. Fluids **21**, 793 (1978).

[82] A. Pukhov, Z.-M. Sheng, and J. M. ter Vehn, Physics of Plasmas **6**, 2847 (1999), http://dx.doi.org/10.1063/1.873242 .

[83] S. P. D. Mangles, B. R. Walton, M. Tzoufras, Z. Najmudin, R. J. Clarke, A. E. Dangor, R. G. Evans, S. Fritzler, A. Gopal, C. Hernandez-Gomez, W. B. Mori, W. Rozmus, M. Tatarakis, A. G. R. Thomas, F. S. Tsung, M. S. Wei, and K. Krushelnick, Phys. Rev. Lett. **94**, 245001 (2005).

[84] C. Gahn, G. D. Tsakiris, A. Pukhov, J. Meyer-ter Vehn, G. Pretzler, P. Thirolf, D. Habs, and K. J. Witte, Phys. Rev. Lett. **83**, 4772 (1999).

[85] D. W. Forslund, J. M. Kindel, and K. Lee, Phys. Rev. Lett. **39**, 284 (1977).

[86] F. Brunel, Phys. Rev. Lett. **59**, 52 (1987).

[87] F. N. Beg, A. R. Bell, A. E. Dangor, C. N. Danson, A. P. Fews, M. E. Glinsky, B. A. Hammel, P. Lee, P. A. Norreys, and M. Tatarakis, Physics of Plasmas **4**, 447 (1997), http://dx.doi.org/10.1063/1.872103 .

[88] M. G. Haines, M. S. Wei, F. N. Beg, and R. B. Stephens, Phys. Rev. Lett. **102**, 045008 (2009).

[89] T. Feurer, W. Theobald, R. Sauerbrey, I. Uschmann, D. Altenbernd, U. Teubner, P. Gibbon, E. Förster, G. Malka, and J. L. Miquel, Phys. Rev. E **56**, 4608 (1997).

[90] I. Uschmann, P. Gibbon, D. Klöpfel, T. Feurer, E. Förster, P. Audebert, J.-P. Geindre, J.-C. Gauthier, A. Rousse, C. Rischel, and et al., Laser and Particle Beams **17**, 671–679 (1999).

[91] M. Schnürer, R. Nolte, T. Schlegel, M. P. Kalachnikov, P. V. Nickles, P. Ambrosi, and W. Sandner, Journal of Physics B: Atomic, Molecular and Optical Physics **30**, 4653 (1997).

[92] M. Schnürer, R. Nolte, A. Rousse, G. Grillon, G. Cheriaux, M. P. Kalachnikov, P. V. Nickles, and W. Sandner, Phys. Rev. E **61**, 4394 (2000).

[93] C. D. Chen, J. A. King, M. H. Key, K. U. Akli, F. N. Beg, H. Chen, R. R. Freeman, A. Link, A. J. Mackinnon, A. G. MacPhee, P. K. Patel, M. Porkolab, R. B. Stephens, and L. D. V. Woerkom, Review of Scientific Instruments **79**, 10E305 (2008), http://dx.doi.org/10.1063/1.2964231 .

[94] P. Antici, B. Albertazzi, P. Audebert, S. Buffechoux, F. Hannachi, E. d'Humières, F. Gobet, T. Grismayer, A. Mancic, M. Nakatsutsumi, C. Plaisir, L. Romagnani, M. Tarisien, H. Pépin, Y. Sentoku, and J. Fuchs, New Journal of Physics **14**, 063023 (2012).

[95] M. Gauthier, *Experimental Study of Ion Stopping Power in Warm Dense Matter: Charge-state Distribution Measurements of Ions Leaving Warm Dense Matter*, Ph.D. thesis, École polytechnique (2013).

[96] G. Vieux, A. Lyachev, X. Yang, B. Ersfeld, J. P. Farmer, E. Brunetti, R. C. Issac, G. Raj, G. H. Welsh, S. M. Wiggins, and D. A. Jaroszynski, New J. Phys. **13**, 063042 (2011).

[97] M. N. Polyanskiy, I. V. Pogorelsky, and V. Yakimenko, Opt. Express **19**, 7717 (2011).

[98] M. N. Polyanskiy, M. Babzien, and I. V. Pogorelsky, Optica **2**, 675 (2015).

[99] I. V. Pogorelsky, M. N. Polyanskiy, and W. D. Kimura, Phys. Rev. Accel. Beams **19**, 091001 (2016).

[100] M. B. Schwab, A. Sävert, O. Jäckel, J. Polz, M. Schnell, T. Rinck, L. Veisz, M. Möller, P. Hansinger, G. G. Paulus, and M. C. Kaluza, Appl. Phys. Lett. **103**, 191118 (2013).

[101] G. Lehmann, F. Schluck, and K. H. Spatschek, Phys. Plasmas **19**, 093120 (2012).

[102] C. Riconda, S. Weber, L. Lancia, J.-R. Marquès, G. A. Mourou, and J. Fuchs, Phys. Plasmas **20**, 083115 (2013).

[103] R. M. G. M. Trines, R. Bingham, P. Norreys, K. Humphrey, F. Alves, E. P.and Fiuza, R. Fonseca, L. O. Silva, and R. A. Cairns, "A robust plasma-based laser amplifier via stimulated brillouin scattering," (2013).

[104] R. Trines, E. Alves, K. Humphrey, R. Bingham, R. Cairns, F. Fiuza, R. Fonseca, L. Silva, and P. Norreys, "Optimization of interaction conditions for efficient short laser pulse amplification by stimulated brillouin scattering in the strongly coupled regime," (2014), arXiv:1406.5424v1.

[105] M. Shoucri, J.-P. Matte, and F. Vidal, Phys. Plasmas **22**, 053101 (2015).

[106] E. Guillaume, K. Humphrey, H. Nakamura, R. M. G. M. Trines, R. Heathcote, M. Galimberti, Y. Amano, D. Doria, G. Hicks, E. Higson, S. Kar, G. Sarri, M. Skramic, J. Swain, K. Tang, J. Weston, P. Zak, E. P. Alves, R. A. Fonseca, F. Fiúza, H. Habara, K. A. Tanaka, R. Bingham, M. Borghesi, Z. Najmudin, L. O. Silva, and P. A. Norreys, High Power Laser Science and Engineering **2** (2014), 10.1017/hpl.2014.35.

[107] Y. A. Bykovskii, N. Degtyarenko, V. Elesin, Y. P. Kozyrev, and S. Sil'nov, Sov. Phys. JETP **33**, 706 (1971).

[108] S. J. Gitomer, R. D. Jones, F. Begay, A. W. Ehler, J. F. Kephart, and R. Kristal, Phys. Fluids **29**, 2679 (1986).

[109] A. P. Fews, P. A. Norreys, F. N. Beg, A. R. Bell, A. E. Dangor, C. N. Danson, P. Lee, and S. J. Rose, Phys. Rev. Lett. **73**, 1801 (1994).

[110] J. Braenzel, A. A. Andreev, K. Platonov, M. Klingsporn, L. Ehrentraut, W. Sandner, and M. Schnürer, Phys. Rev. Lett. **114**, 124801 (2015).

[111] S. S. Bulanov, A. Brantov, V. Y. Bychenkov, V. Chvykov, G. Kalinchenko, T. Matsuoka, P. Rousseau, S. Reed, V. Yanovsky, D. W. Litzenberg, K. Krushelnick, and A. Maksimchuk, Phys. Rev. E **78**, 026412 (2008).

[112] S. S. Bulanov, A. Brantov, V. Y. Bychenkov, V. Chvykov, G. Kalinchenko, T. Matsuoka, P. Rousseau, S. Reed, V. Yanovsky, K. Krushelnick, D. W. Litzenberg, and A. Maksimchuk, Medical Physics **35**, 1770 (2008).

[113] S. S. Bulanov, V. Y. Bychenkov, V. Chvykov, G. Kalinchenko, D. W. Litzenberg, T. Matsuoka, A. G. R. Thomas, L. Willingale, V. Yanovsky, K. Krushelnick, and A. Maksimchuk, Physics of Plasmas **17**, 043105 (2010), http://dx.doi.org/10.1063/1.3372840 .

[114] A. Stockem Novo, M. C. Kaluza, R. A. Fonseca, and L. O. Silva, Scientific Reports **6**, 29402 (2016).

[115] T. Nakamura, S. V. Bulanov, T. Z. Esirkepov, and M. Kando, Phys. Rev. Lett. **105**, 135002 (2010).

[116] E. L. Clark, K. Krushelnick, M. Zepf, F. N. Beg, M. Tatarakis, A. Machacek, M. I. K. Santala, I. Watts, P. A. Norreys, and A. E. Dangor, Phys. Rev. Lett. **85**, 1654 (2000).

[117] E. L. Clark, K. Krushelnick, J. R. Davies, M. Zepf, M. Tatarakis, F. N. Beg, A. Machacek, P. A. Norreys, M. I. K. Santala, I. Watts, and A. E. Dangor, Phys. Rev. Lett. **84**, 670 (2000).

[118] A. Maksimchuk, S. Gu, K. Flippo, D. Umstadter, and V. Y. Bychenkov, Phys. Rev. Lett. **84**, 4108 (2000).

[119] S. P. Hatchett, C. G. Brown, T. E. Cowan, E. A. Henry, J. S. Johnson, M. H. Key, J. A. Koch, A. B. Langdon, B. F. Lasinski, R. W. Lee, A. J. Mackinnon, D. M. Pennington, M. D. Perry, T. W. Phillips, M. Roth, T. C. Sangster, M. S. Singh, R. A. Snavely, M. A. Stoyer, S. C. Wilks, and K. Yasuike, Physics of Plasmas **7**, 2076 (2000), http://dx.doi.org/10.1063/1.874030 .

[120] S. C. Wilks, A. B. Langdon, T. E. Cowan, M. Roth, M. Singh, S. Hatchett, M. H. Key, D. Pennington, A. MacKinnon, and R. A. Snavely, Phys. Plasmas **8**, 542 (2001).

[121] S. Bulanov, T. Esirkepov, V. Khoroshkov, A. Kuznetsov, and F. Pegoraro, Physics Letters A **299**, 240 (2002).

[122] A. J. Mackinnon, Y. Sentoku, P. K. Patel, D. W. Price, S. Hatchett, M. H. Key, C. Andersen, R. Snavely, and R. R. Freeman, Phys. Rev. Lett. **88**, 215006 (2002).

[123] V. T. Tikhonchuk, Physics of Plasmas **9**, 1416 (2002), http://dx.doi.org/10.1063/1.1459061 .

[124] P. Mora, Phys. Rev. Lett. **90**, 185002 (2003).

[125] Y. Sentoku, K. Mima, P. Kaw, and K. Nishikawa, Phys. Rev. Lett. **90**, 155001 (2003).

[126] M. Kaluza, J. Schreiber, M. I. K. Santala, G. D. Tsakiris, K. Eidmann, J. Meyer-ter Vehn, and K. J. Witte, Phys. Rev. Lett. **93**, 045003 (2004).

[127] M. Passoni, V. T. Tikhonchuk, M. Lontano, and V. Y. Bychenkov, Phys. Rev. E **69**, 026411 (2004).

[128] L. Romagnani, J. Fuchs, M. Borghesi, P. Antici, P. Audebert, F. Ceccherini, T. Cowan, T. Grismayer, S. Kar, A. Macchi, P. Mora, G. Pretzler, A. Schiavi, T. Toncian, and O. Willi, Phys. Rev. Lett. **95**, 195001 (2005).

[129] J. Fuchs, Y. Sentoku, S. Karsch, J. Cobble, P. Audebert, A. Kemp, A. Nikroo, P. Antici, E. Brambrink, A. Blazevic, E. M. Campbell, J. C. Fernández, J.-C. Gauthier, M. Geissel, M. Hegelich, H. Pépin, H. Popescu, N. Renard-LeGalloudec, M. Roth, J. Schreiber, R. Stephens, and T. E. Cowan, Phys. Rev. Lett. **94**, 045004 (2005).

[130] J. Fuchs, P. Antici, E. d/'Humieres, E. Lefebvre, M. Borghesi, E. Brambrink, C. A. Cecchetti, M. Kaluza, V. Malka, M. Manclossi, S. Meyroneinc, P. Mora, J. Schreiber, T. Toncian, H. Pepin, and P. Audebert, Nat. Phys. **2**, 48 (2006).

[131] T. Grismayer and P. Mora, Physics of Plasmas **13**, 032103 (2006), http://dx.doi.org/10.1063/1.2178653 .

[132] T. Grismayer, *Theoretical and numerical study hot plasma expansion as driven by high intensity lasers: high energy ions acceleration.*, Theses, Ecole Polytechnique X (2006).

[133] J. Schreiber, F. Bell, F. Grüner, U. Schramm, M. Geissler, M. Schnürer, S. Ter-Avetisyan, B. M. Hegelich, J. Cobble, E. Brambrink, J. Fuchs, P. Audebert, and D. Habs, Phys. Rev. Lett. **97**, 045005 (2006).

[134] H. Schwoerer, S. Pfotenhauer, O. Jackel, K.-U. Amthor, B. Liesfeld, W. Ziegler, R. Sauerbrey, K. W. D. Ledingham, and T. Esirkepov, Nature **439**, 445 (2006).

[135] T. Ceccotti, A. Lévy, H. Popescu, F. Réau, P. D'Oliveira, P. Monot, J. P. Geindre, E. Lefebvre, and P. Martin, Phys. Rev. Lett. **99**, 185002 (2007).

[136] P. Antici, J. Fuchs, M. Borghesi, L. Gremillet, T. Grismayer, Y. Sentoku, E. d'Humières, C. A. Cecchetti, A. Mančić, A. C. Pipahl, T. Toncian, O. Willi, P. Mora, and P. Audebert, Phys. Rev. Lett. **101**, 105004 (2008).

[137] A. Lévy, *Laser-induced ion acceleration in ultrahigh contrast regime*, Theses, Université Paris Sud - Paris XI (2008).

[138] J. Fuchs, P. Audebert, M. Borghesi, H. Pépin, and O. Willi, Comptes Rendus Physique **10**, 176 (2009), laser acceleration of particles in plasmaAccélération laser de particules dans les plasmas.

[139] O. Jäckel, *Characterization of ion acceleration with realativistic laser-plasma*, Ph.D. thesis, Universität Jena (2009).

[140] C. L. Ellison and J. Fuchs, Phys. Plasmas **17**, 113105 (2010).

[141] P. Mora, Phys. Rev. E **72**, 056401 (2005).

[142] J. Fuchs, T. E. Cowan, P. Audebert, H. Ruhl, L. Gremillet, A. Kemp, M. Allen, A. Blazevic, J.-C. Gauthier, M. Geissel, M. Hegelich, S. Karsch, P. Parks, M. Roth, Y. Sentoku, R. Stephens, and E. M. Campbell, Phys. Rev. Lett. **91**, 255002 (2003).

[143] M. Allen, P. K. Patel, A. Mackinnon, D. Price, S. Wilks, and E. Morse, Phys. Rev. Lett. **93**, 265004 (2004).

[144] J. J. Santos, F. Amiranoff, S. D. Baton, L. Gremillet, M. Koenig, E. Martinolli, M. Rabec Le Gloahec, C. Rousseaux, D. Batani, A. Bernardinello, G. Greison, and T. Hall, Phys. Rev. Lett. **89**, 025001 (2002).

[145] P. Bolton, M. Borghesi, C. Brenner, D. Carroll, C. De Martinis, F. Fiorini, A. Flacco, V. Floquet, J. Fuchs, P. Gallegos, D. Giove, J. Green, S. Green, B. Jones, D. Kirby, P. McKenna, D. Neely, F. Nuesslin, R. Prasad, S. Reinhardt, M. Roth, U. Schramm, G. Scott, S. Ter-Avetisyan, M. Tolley, G. Turchetti, and J. Wilkens, Physica Medica: European Journal of Medical Physics **30**, 255 (2014).

[146] A. Lifschitz, F. Sylla, S. Kahaly, A. Flacco, M. Veltcheva, G. Sanchez-Arriaga, E. Lefebvre, and V. Malka, New J. Phys. **16**, 033031 (2014).

[147] F. Nürnberg, M. Schollmeier, E. Brambrink, A. Blažević, D. C. Carroll, K. Flippo, D. C. Gautier, M. Geißel, K. Harres, B. M. Hegelich, O. Lundh, K. Markey, P. McKenna, D. Neely, J. Schreiber, and M. Roth, Review of Scientific Instruments **80**, 033301 (2009), http://dx.doi.org/10.1063/1.3086424 .

[148] M. Hegelich, S. Karsch, G. Pretzler, D. Habs, K. Witte, W. Guenther, M. Allen, A. Blazevic, J. Fuchs, J. C. Gauthier, M. Geissel, P. Audebert, T. Cowan, and M. Roth, Phys. Rev. Lett. **89**, 085002 (2002).

[149] B. M. Hegelich, B. Albright, P. Audebert, A. Blazevic, E. Brambrink, J. Cobble, T. Cowan, J. Fuchs, J. C. Gauthier, C. Gautier, M. Geissel, D. Habs, R. Johnson, S. Karsch, A. Kemp, S. Letzring, M. Roth, U. Schramm, J. Schreiber, K. J. Witte, and J. C. Fernández, Physics of Plasmas **12**, 056314 (2005), http://dx.doi.org/10.1063/1.1915350 .

[150] P. McKenna, K. W. D. Ledingham, J. M. Yang, L. Robson, T. McCanny, S. Shimizu, R. J. Clarke, D. Neely, K. Spohr, R. Chapman, R. P. Singhal, K. Krushelnick, M. S. Wei, and P. A. Norreys, Phys. Rev. E **70**, 036405 (2004).

[151] B. M. Hegelich, B. J. Albright, J. Cobble, K. Flippo, S. Letzring, M. Paffett, H. Ruhl, J. Schreiber, R. K. Schulze, and J. C. Fernández, Nature **439**, 441 (2006).

[152] M. Gauthier, J. B. Kim, C. B. Curry, B. Aurand, E. J. Gamboa, S. Göde, C. Goyon, A. Hazi, S. Kerr, A. Pak, A. Propp, B. Ramakrishna, J. Ruby, O. Willi, G. J. Williams, C. Rödel, and S. H. Glenzer, Review of Scientific Instruments **87**, 11D827 (2016), http://aip.scitation.org/doi/pdf/10.1063/1.4961270 .

[153] R. P. Drake, *High-Energy-Density Physics* (Springer, 2006).

[154] W. L. Kruer, E. J. Valeo, and K. G. Estabrook, Phys. Rev. Lett. **35**, 1076 (1975).

[155] Y. Sentoku, T. E. Cowan, A. Kemp, and H. Ruhl, Physics of Plasmas **10**, 2009 (2003), http://dx.doi.org/10.1063/1.1556298 .

[156] T. Schlegel, N. Naumova, V. T. Tikhonchuk, C. Labaune, I. V. Sokolov, and G. Mourou, Physics of Plasmas **16**, 083103 (2009), http://dx.doi.org/10.1063/1.3196845 .

[157] J. Schreiber, P. R. Bolton, and K. Parodi, Review of Scientific Instruments **87**, 071101 (2016), http://dx.doi.org/10.1063/1.4959198.

[158] A. Henig, S. Steinke, M. Schnürer, T. Sokollik, R. Hörlein, D. Kiefer, D. Jung, J. Schreiber, B. M. Hegelich, X. Q. Yan, J. Meyer-ter Vehn, T. Tajima, P. V. Nickles, W. Sandner, and D. Habs, Phys. Rev. Lett. **103**, 245003 (2009).

[159] A. Macchi, F. Cattani, T. V. Liseykina, and F. Cornolti, Phys. Rev. Lett. **94**, 165003 (2005).

[160] T. Esirkepov, M. Yamagiwa, and T. Tajima, Phys. Rev. Lett. **96**, 105001 (2006).

[161] T. Esirkepov, M. Borghesi, S. V. Bulanov, G. Mourou, and T. Tajima, Phys. Rev. Lett. **92**, 175003 (2004).

[162] A. Macchi, S. Veghini, T. V. Liseykina, and F. Pegoraro, New Journal of Physics **12**, 045013 (2010).

[163] F. Dollar, C. Zulick, A. G. R. Thomas, V. Chvykov, J. Davis, G. Kalinchenko, T. Matsuoka, C. McGuffey, G. M. Petrov, L. Willingale, V. Yanovsky, A. Maksimchuk, and K. Krushelnick, Phys. Rev. Lett. **108**, 175005 (2012).

[164] S. Kar, K. F. Kakolee, B. Qiao, A. Macchi, M. Cerchez, D. Doria, M. Geissler, P. McKenna, D. Neely, J. Osterholz, R. Prasad, K. Quinn, B. Ramakrishna, G. Sarri, O. Willi, X. Y. Yuan, M. Zepf, and M. Borghesi, Phys. Rev. Lett. **109**, 185006 (2012).

[165] K. V. Lezhnin, F. F. Kamenets, V. S. Beskin, M. Kando, T. Z. Esirkepov, and S. V. Bulanov, Physics of Plasmas **22**, 033112 (2015), http://dx.doi.org/10.1063/1.4915136 .

[166] L. O. Silva, M. Marti, J. R. Davies, R. A. Fonseca, C. Ren, F. S. Tsung, and W. B. Mori, Phys. Rev. Lett. **92**, 015002 (2004).

[167] D. W. Forslund and C. R. Shonk, Phys. Rev. Lett. **25**, 1699 (1970).

[168] D. W. Forslund and J. P. Freidberg, Phys. Rev. Lett. **27**, 1189 (1971).

[169] F. Fiuza, A. Stockem, E. Boella, R. A. Fonseca, L. O. Silva, D. Haberberger, S. Tochitsky, C. Gong, W. B. Mori, and C. Joshi, Phys. Rev. Lett. **109**, 215001 (2012).

[170] F. Fiuza, R. A. Fonseca, J. Tonge, W. B. Mori, and L. O. Silva, Phys. Rev. Lett. **108**, 235004 (2012).

[171] R. D. Blandford and C. F. McKee, The Physics of Fluids **19**, 1130 (1976), http://aip.scitation.org/doi/pdf/10.1063/1.861619 .

[172] E. d'Humières, P. Antici, M. Glesser, J. Boeker, F. Cardelli, S. Chen, J. L. Feugeas, F. Filippi, M. Gauthier, A. Levy, P. Nicolaï, H. Pépin, L. Romagnani, M. Scisciò, V. T. Tikhonchuk, O. Willi, J. C. Kieffer, and J. Fuchs, Plasma Physics and Controlled Fusion **55**, 124025 (2013).

[173] Y.-K. Kim, M.-H. Cho, H. S. Song, T. Kang, H. J. Park, M. Y. Jung, and M. S. Hur, Phys. Rev. E **92**, 043102 (2015).

[174] E. d'Humières, J. L. Feugeas, P. Nicolaï, S. Gaillard, T. Cowan, Y. Sentoku, and V. Tikhonchuk, Journal of Physics: Conference Series **244**, 042023 (2010).

[175] O. Tresca, N. P. Dover, N. Cook, C. Maharjan, M. N. Polyanskiy, Z. Najmudin, P. Shkolnikov, and I. Pogorelsky, Phys. Rev. Lett. **115**, 094802 (2015).

[176] D. Haberberger, S. Tochitsky, and C. Joshi, Opt. Express **18**, 17865 (2010).

[177] S. V. Bulanov, I. N. Inovenkov, V. I. Kirsanov, N. M. Naumova, and A. S. Sakharov, Physics of Fluids B: Plasma Physics **4**, 1935 (1992), http://dx.doi.org/10.1063/1.860046 .

[178] M. interaction of self-focusing channels, t. a. o. e. fluxes of electromagnetic radiation: their coalescence, and the effect of external magnetic fields on them, JETP Lett. **60**, 251 (1994).

[179] S. K. Yadav, A. Das, and P. Kaw, Physics of Plasmas **15**, 062308 (2008), http://dx.doi.org/10.1063/1.2943693 .

[180] A. Pukhov and J. Meyer-ter Vehn, Appl. Phys. B **74**, 355 (2002).

[181] J. Faure, Y. Glinec, A. Pukhov, S. Kiselev, S. Gordienko, E. Lefebvre, J.-P. Rousseau, F. Burgy, and V. Malka, Nature **431**, 541 (2004).

[182] A. Buck, M. Nicolai, K. Schmid, C. Sears, A. Savert, J. Mikhailova, F. Krausz, M. Kaluza, and L. Veisz, Nat. Phys. **7**, 543 (2011).

[183] O. Willi, M. Behmke, L. Gezici, B. Hidding, R. Jung, T. Königstein, A. Pipahl, J. Osterholz, G. Pretzler, A. Pukhov, M. Toncian, T. Toncian, M. Heyer, O. Jäckel, M. Kübel, G. Paulus, C. Rödel, H. P. Schlenvoigt, W. Ziegler, M. Büscher, A. Feyt, A. Lehrach, H. Ohm, G. Oswald, N. Raab, M. Ruzzo, M. Seltmann, and Q. Zhang, Plasma Physics and Controlled Fusion **51**, 124049 (2009).

[184] A. Ricci, A. Jullien, J.-P. Rousseau, Y. Liu, A. Houard, P. Ramirez, D. Papadopoulos, A. Pellegrina, P. Georges, F. Druon, N. Forget, and R. Lopez-Martens, Review of Scientific Instruments **84**, 043106 (2013), http://dx.doi.org/10.1063/1.4801457 .

[185] F. Verluise, V. Laude, Z. Cheng, C. Spielmann, and P. Tournois, Opt. Lett. **25**, 575 (2000).

[186] O. Lundh, J. Lim, C. Rechatin, L. Ammoura, A. Ben-Ismail, X. Davoine, G. Gallot, J.-P. Goddet, E. Lefebvre, V. Malka, and J. Faure, Nat. Phys. **7**, 219 (2011).

[187] N. A. M. Hafz, T. M. Jeong, I. W. Choi, S. K. Lee, K. H. Pae, V. V. Kulagin, J. H. Sung, T. J. Yu, K.-H. Hong, T. Hosokai, J. R. Cary, D.-K. Ko, and J. Lee, Nat. Photon. **2**, 571 (2008).

[188] C. G. R. Geddes, C. Toth, J. van Tilborg, E. Esarey, C. B. Schroeder, D. Bruhwiler, C. Nieter, J. Cary, and W. P. Leemans, Nature **431**, 538 (2004).

[189] S. P. D. Mangles, C. D. Murphy, Z. Najmudin, A. G. R. Thomas, J. L. Collier, A. E. Dangor, E. J. Divall, P. S. Foster, J. G. Gallacher, C. J. Hooker, D. A. Jaroszynski, A. J. Langley, W. B. Mori, P. A. Norreys, F. S. Tsung, R. Viskup, B. R. Walton, and K. Krushelnick, Nature **431**, 535 (2004).

[190] B. Hidding, K.-U. Amthor, B. Liesfeld, H. Schwoerer, S. Karsch, M. Geissler, L. Veisz, K. Schmid, J. G. Gallacher, S. P. Jamison, D. Jaroszynski, G. Pretzler, and R. Sauerbrey, Phys. Rev. Lett. **96**, 105004 (2006).

[191] B. Hidding, T. Königstein, J. Osterholz, S. Karsch, O. Willi, and G. Pretzler, Phys. Rev. Lett. **104**, 195002 (2010).

[192] J. Faure, C. Rechatin, A. Norlin, A. Lifschitz, Y. Glinec, and V. Malka, Nature **444**, 737 (2006).

[193] S. P. D. Mangles, G. Genoud, M. S. Bloom, M. Burza, Z. Najmudin, A. Persson, K. Svensson, A. G. R. Thomas, and C.-G. Wahlström, Phys. Rev. ST Accel. Beams **15**, 011302 (2012).

[194] V. Malka, J. Faure, Y. Glinec, A. Pukhov, and J.-P. Rousseau, Physics of Plasmas **12**, 056702 (2005), http://dx.doi.org/10.1063/1.1869498 .

[195] V. Malka, S. Fritzler, E. Lefebvre, M.-M. Aleonard, F. Burgy, J.-P. Chambaret, J.-F. Chemin, K. Krushelnick, G. Malka, S. P. D. Mangles, Z. Najmudin, M. Pittman, J.-P. Rousseau, J.-N. Scheurer, B. Walton, and A. E. Dangor, Science **298**, 1596 (2002).

[196] C. G. R. Geddes, C. Tóth, J. van Tilborg, E. Esarey, C. B. Schroeder, D. Bruhwiler, C. Nieter, J. Cary, and W. P. Leemans, Physics of Plasmas **12**, 056709 (2005), http://dx.doi.org/10.1063/1.1882352 .

[197] T. Hosokai, K. Kinoshita, T. Ueda, M. Uesaka, T. Watanabe, K. Yoshii, A. Zhidokov, M. Kando, H. Kotaki, and K. Nakajima, in *Proceedings of the Eighth European Particle Accelerator Conference* (2002) p. 981.

[198] T. Hosokai, K. Kinoshita, T. Ohkubo, A. Maekawa, M. Uesaka, A. Zhidkov, A. Yamazaki, H. Kotaki, M. Kando, K. Nakajima, S. V. Bulanov, P. Tomassini, A. Giulietti, and D. Giulietti, Phys. Rev. E **73**, 036407 (2006).

[199] A. Maksimchuk, S. Reed, S. S. Bulanov, V. Chvykov, G. Kalintchenko, T. Matsuoka, C. McGuffey, G. Mourou, N. Naumova, J. Nees, P. Rousseau, V. Yanovsky, K. Krushelnick, N. H. Matlis, S. Kalmykov, G. Shvets, M. C. Downer, C. R. Vane, J. R. Beene, D. Stracener, and D. R. Schultz, Physics of Plasmas **15**, 056703 (2008), http://dx.doi.org/10.1063/1.2856373 .

[200] A. Yamazaki, H. Kotaki, I. Daito, M. Kando, S. V. Bulanov, T. Z. Esirkepov, S. Kondo, S. Kanazawa, T. Homma, K. Nakajima, Y. Oishi, T. Nayuki, T. Fujii, and K. Nemoto, Physics of Plasmas **12**, 093101 (2005), http://dx.doi.org/10.1063/1.2017842 .

[201] S. Masuda, E. Miura, K. Koyama, S. Kato, M. Adachi, T. Watanabe, K. Torii, and M. Tanimoto, Physics of Plasmas **14**, 023103 (2007), http://dx.doi.org/10.1063/1.2434248 .

[202] E. Miura, K. Koyama, S. Kato, N. Saito, M. Adachi, Y. Kawada, T. Nakamura, and M. Tanimoto, Applied Physics Letters **86**, 251501 (2005), http://dx.doi.org/10.1063/1.1949289 .

[203] C.-T. Hsieh, C.-M. Huang, C.-L. Chang, Y.-C. Ho, Y.-S. Chen, J.-Y. Lin, J. Wang, and S.-Y. Chen, Phys. Rev. Lett. **96**, 095001 (2006).

[204] W. P. Leemans, C. G. R. Geddes, J. Faure, C. Tóth, J. van Tilborg, C. B. Schroeder, E. Esarey, G. Fubiani, D. Auerbach, B. Marcelis, M. A. Carnahan, R. A. Kaindl, J. Byrd, and M. C. Martin, Phys. Rev. Lett. **91**, 074802 (2003).

[205] C. B. Schroeder, E. Esarey, J. van Tilborg, and W. P. Leemans, Phys. Rev. E **69**, 016501 (2004).

[206] J. van Tilborg, C. B. Schroeder, C. V. Filip, C. Tóth, C. G. R. Geddes, G. Fubiani, R. Huber, R. A. Kaindl, E. Esarey, and W. P. Leemans, Phys. Rev. Lett. **96**, 014801 (2006).

[207] A. Butler, A. J. Gonsalves, C. M. McKenna, D. J. Spence, S. M. Hooker, S. Sebban, T. Mocek, I. Bettaibi, and B. Cros, Phys. Rev. Lett. **91**, 205001 (2003).

[208] A. Rousse, K. T. Phuoc, R. Shah, A. Pukhov, E. Lefebvre, V. Malka, S. Kiselev, F. Burgy, J.-P. Rousseau, D. Umstadter, and D. Hulin, Phys. Rev. Lett. **93**, 135005 (2004).

[209] K. T. Phuoc, F. Burgy, J.-P. Rousseau, V. Malka, A. Rousse, R. Shah, D. Umstadter, A. Pukhov, and S. Kiselev, Phys. Plasmas **12**, 023101 (2005).

[210] K. T. Phuoc, F. Burgy, J.-P. Rousseau, and A. Rousse, Eur. Phys. J. D **33**, 301 (2005).

[211] K. T. Phuoc, S. Corde, R. Shah, F. Albert, R. Fitour, J.-P. Rousseau, F. Burgy, B. Mercier, and A. Rousse, Phys. Rev. Lett. **97**, 225002 (2006).

[212] K. T. Phuoc, R. Fitour, A. Tafzi, T. Garl, N. Artemiev, R. Shah, F. Albert, D. Boschetto, A. Rousse, D.-E. Kim, A. Pukhov, V. Seredov, and I. Kostyukov, Phys. Plasmas **14**, 080701 (2007).

[213] K. T. Phuoc, S. Corde, C. Thaury, V. Malka, A. Tafzi, J. P. Goddet, R. C. Shah, S. Sebban, and A. Rousse, Nat. Photon. **6**, 308 (2012).

[214] C. M. Huntington, A. G. R. Thomas, C. McGuffey, T. Matsuoka, V. Chvykov, G. Kalintchenko, S. Kneip, Z. Najmudin, C. Palmer, V. Yanovsky, A. Maksimchuk, R. P. Drake, T. Katsouleas, and K. Krushelnick, Phys. Rev. Lett. **106**, 105001 (2011).

[215] S. Kneip, S. R. Nagel, C. Bellei, N. Bourgeois, A. E. Dangor, A. Gopal, R. Heathcote, S. P. D. Mangles, J. R. Marquès, A. Maksimchuk, P. M. Nilson, K. T. Phuoc, S. Reed, M. Tzoufras, F. S. Tsung, L. Willingale, W. B. Mori, A. Rousse, K. Krushelnick, and Z. Najmudin, Phys. Rev. Lett. **100**, 105006 (2008).

[216] S. Kneip, S. R. Nagel, S. F. Martins, S. P. D. Mangles, C. Bellei, O. Chekhlov, R. J. Clarke, N. Delerue, E. J. Divall, G. Doucas, K. Ertel, F. Fiuza, R. Fonseca, P. Foster, S. J. Hawkes, C. J. Hooker, K. Krushelnick, W. B. Mori, C. A. J. Palmer, K. T. Phuoc, P. P. Rajeev, J. Schreiber, M. J. V. Streeter, D. Urner, J. Vieira, L. O. Silva, and Z. Najmudin, Phys. Rev. Lett. **103**, 035002 (2009).

[217] S. Kneip, C. McGuffey, J. L. Martins, S. F. Martins, C. Bellei, V. Chvykov, F. Dollar, R. Fonseca, C. Huntington, G. Kalintchenko, A. Maksimchuk, S. P. D. Mangles, T. Matsuoka, S. R. Nagel, C. A. J. Palmer, J. Schreiber, K. T. Phuoc, A. G. R. Thomas, V. Yanovsky, L. O. Silva, K. Krushelnick, and Z. Najmudin, Nat. Phys. **6**, 980 (2010).

[218] S. Kneip, C. McGuffey, J. L. Martins, M. S. Bloom, V. Chvykov, F. Dollar, R. Fonseca, S. Jolly, G. Kalintchenko, K. Krushelnick, A. Maksimchuk, S. P. D. Mangles, Z. Najmudin, C. A. J. Palmer, K. T. Phuoc, W. Schumaker, L. O. Silva, J. Vieira, V. Yanovsky, and A. G. R. Thomas, Phys. Rev. ST Accel. Beams **15**, 021302 (2012).

[219] L. Willingale, S. P. D. Mangles, P. M. Nilson, R. J. Clarke, A. E. Dangor, M. C. Kaluza, S. Karsch, K. L. Lancaster, W. B. Mori, Z. Najmudin, J. Schreiber, A. G. R. Thomas, M. S. Wei, and K. Krushelnick, Phys. Rev. Lett. **96**, 245002 (2006).

[220] M. Kando, Y. Fukuda, A. S. Pirozhkov, J. Ma, I. Daito, L.-M. Chen, T. Z. Esirkepov, K. Ogura, T. Homma, Y. Hayashi, H. Kotaki, A. Sagisaka, M. Mori, J. K. Koga, H. Daido, S. V. Bulanov, T. Kimura, Y. Kato, and T. Tajima, Phys. Rev. Lett. **99**, 135001 (2007).

[221] S. S. Bulanov, T. Z. Esirkepov, F. F. Kamenets, and F. Pegoraro, Phys. Rev. E **73**, 036408 (2006).

[222] F. Albert, R. Shah, K. T. Phuoc, R. Fitour, F. Burgy, J.-P. Rousseau, A. Tafzi, D. Douillet, T. Lefrou, and A. Rousse, Phys. Rev. E **77**, 056402 (2008).

[223] A. Buck, J. Wenz, J. Xu, K. Khrennikov, K. Schmid, M. Heigoldt, J. M. Mikhailova, M. Geissler, B. Shen, F. Krausz, S. Karsch, and L. Veisz, Phys. Rev. Lett. **110**, 185006 (2013).

[224] S. Corde, K. T. Phuoc, R. Fitour, J. Faure, A. Tafzi, J. P. Goddet, V. Malka, and A. Rousse, Phys. Rev. Lett. **107**, 255003 (2011).

[225] S. Fourmaux, S. Corde, K. T. Phuoc, P. M. Leguay, S. Payeur, P. Lassonde, S. Gnedyuk, G. Lebrun, C. Fourment, V. Malka, S. Sebban, A. Rousse, and J. C. Kieffer, New J. Phys. **13**, 033017 (2011).

[226] M. C. Kaluza, H.-P. Schlenvoigt, S. P. D. Mangles, A. G. R. Thomas, A. E. Dangor, H. Schwoerer, W. B. Mori, Z. Najmudin, and K. M. Krushelnick, Phys. Rev. Lett. **105**, 115002 (2010).

[227] N. H. Matlis, S. Reed, S. S. Bulanov, V. Chvykov, G. Kalintchenko, T. Matsuoka, P. Rousseau, V. Yanovsky, A. Maksimchuk, S. Kalmykov, G. Shvets, and M. C. Downer, Nat. Phys. **2**, 749 (2006).

[228] J. E. Ralph, K. A. Marsh, A. E. Pak, W. Lu, C. E. Clayton, F. Fang, W. B. Mori, and C. Joshi, Phys. Rev. Lett. **102**, 175003 (2009).

[229] K. Schmid, L. Veisz, F. Tavella, S. Benavides, R. Tautz, D. Herrmann, A. Buck, B. Hidding, A. Marcinkevicius, U. Schramm, M. Geissler, J. Meyer-ter Vehn, D. Habs, and F. Krausz, Phys. Rev. Lett. **102**, 124801 (2009).

[230] K. Schmid, A. Buck, C. M. S. Sears, J. M. Mikhailova, R. Tautz, D. Herrmann, M. Geissler, F. Krausz, and L. Veisz, Phys. Rev. ST Accel. Beams **13**, 091301 (2010).

[231] W. T. Wang, W. T. Li, J. S. Liu, Z. J. Zhang, R. Qi, C. H. Yu, J. Q. Liu, M. Fang, Z. Y. Qin, C. Wang, Y. Xu, F. X. Wu, Y. X. Leng, R. X. Li, and Z. Z. Xu, Phys. Rev. Lett. **117**, 124801 (2016).

[232] S. Chou, J. Xu, K. Khrennikov, D. E. Cardenas, J. Wenz, M. Heigoldt, L. Hofmann, L. Veisz, and S. Karsch, Phys. Rev. Lett. **117**, 144801 (2016).

[233] N. Nakanii, T. Hosokai, N. C. Pathak, S. Masuda, A. G. Zhidkov, H. Nakahara, K. Iwasa, Y. Mizuta, N. Takeguchi, T. P. Otsuka, K. Sueda, J. Ogino, H. Nakamura, M. Mori, M. Kando, and R. Kodama, Phys. Rev. E **94**, 063205 (2016).

[234] S. Kuschel, D. Hollatz, T. Heinemann, O. Karger, M. B. Schwab, D. Ullmann, A. Knetsch, A. Seidel, C. Rödel, M. Yeung, M. Leier, A. Blinne, H. Ding, T. Kurz, D. J. Corvan, A. Sävert, S. Karsch, M. C. Kaluza, B. Hidding, and M. Zepf, Phys. Rev. Accel. Beams **19**, 071301 (2016).

[235] B. Beaurepaire, A. Vernier, M. Bocoum, F. Böhle, A. Jullien, J.-P. Rousseau, T. Lefrou, D. Douillet, G. Iaquaniello, R. Lopez-Martens, A. Lifschitz, and J. Faure, Phys. Rev. X **5**, 031012 (2015).

[236] C. E. Clayton, J. E. Ralph, F. Albert, R. A. Fonseca, S. H. Glenzer, C. Joshi, W. Lu, K. A. Marsh, S. F. Martins, W. B. Mori, A. Pak, F. S. Tsung, B. B. Pollock, J. S. Ross, L. O. Silva, and D. H. Froula, Phys. Rev. Lett. **105**, 105003 (2010).

[237] M. Fuchs, R. Weingartner, A. Popp, Z. Major, S. Becker, J. Osterhoff, I. Cortrie, B. Zeitler, R. Horlein, G. D. Tsakiris, U. Schramm, T. P. Rowlands-Rees, S. M. Hooker, D. Habs, F. Krausz, S. Karsch, and F. Gruner, Nat. Phys. **5**, 826 (2009).

[238] J. Osterhoff, A. Popp, Z. Major, B. Marx, T. P. Rowlands-Rees, M. Fuchs, M. Geissler, R. Horlein, B. Hidding, S. Becker, E. A. Peralta, U. Schramm, F. Gruner, D. Habs, F. Krausz, S. M. Hooker, and S. Karsch, Phys. Rev. Lett. **101**, 085002 (2008).

[239] B. B. Pollock, C. E. Clayton, J. E. Ralph, F. Albert, A. Davidson, L. Divol, C. Filip, S. H. Glenzer, K. Herpoldt, W. Lu, K. A. Marsh, J. Meinecke, W. B. Mori, A. Pak, T. C. Rensink, J. S. Ross, J. Shaw, G. R. Tynan, C. Joshi, and D. H. Froula, Phys. Rev. Lett. **107**, 045001 (2011).

[240] B. B. Pollock, F. S. Tsung, F. Albert, J. L. Shaw, C. E. Clayton, A. Davidson, N. Lemos, K. A. Marsh, A. Pak, J. E. Ralph, W. B. Mori, and C. Joshi, Phys. Rev. Lett. **115**, 055004 (2015).

[241] X. Wang, R. Zgadzaj, N. Fazel, Z. Li, S. A. Yi, X. Zhang, W. Henderson, Y.-Y. Chang, R. Korzekwa, H.-E. Tsai, C.-H. Pai, H. Quevedo, G. Dyer, E. Gaul, M. Martinez, A. C. Bernstein, T. Borger, M. Spinks, M. Donovan, V. Khudik, G. Shvets, T. Ditmire, and M. C. Downer, Nat. Commun. **4**, 1988 (2013).

[242] R. Weingartner, M. Fuchs, A. Popp, S. Raith, S. Becker, S. Chou, M. Heigoldt, K. Khrennikov, J. Wenz, T. Seggebrock, B. Zeitler, Z. Major, J. Osterhoff, F. Krausz, S. Karsch, and F. Grüner, Phys. Rev. ST Accel. Beams **14**, 052801 (2011).

[243] F. Durst, *Grundlagen der Strömungsmechanik* (Springer, 2006).

[244] S. Semushin and V. Malka, Rev. Sci. Instrum. **72**, 2961 (2001).

[245] K. Schmid, *Supersonic Micro-Jets And Their Application to Few-Cycle Laser-Driven Electron Acceleration*, Ph.D. thesis, Ludwig–Maximilians–Universität München (2009).

[246] L. D. Landau and E. M. Lifschitz, *Hydrodynamik*, 5th ed., Lehrbuch der theoretischen Physik (Akademie Verlag, 1991).

[247] R. K. Agarwal, K.-Y. Yun, and R. Balakrishnan, Phys. Fluids **13**, 3061 (2001).

[248] D. B. Atkinson and M. A. Smith, Rev. Sci. Instrum. **66**, 4434 (1995).

[249] Ames Research Staff, *NACA TR 1135: Equations, tables, and charts for compressible flow*, Tech. Rep. (Ames Aeronautical Laboratory, Moffett Field, CA, 1953).

[250] F. Sylla, M. Veltcheva, S. Kahaly, A. Flacco, and V. Malka, Rev. Sci. Instrum. **83**, 033507 (2012).

[251] D. C. Wilcox, *Turbulence modeling for CFD* (DCW Industries, 2006).

[252] T. Gangolf, *Supersonic Gas Jet Targets for Laser-Plasma Experiments*, Master's thesis, U Jena (2013).

[253] V. Malka, C. Coulaud, J. P. Geindre, V. Lopez, Z. Najmudin, *et al.*, Rev. Sci. Instrum. **71**, 2329 (2000).

[254] R. N. Bracewell, Science **248**, 697 (1990), http://science.sciencemag.org/content/248/4956/697.full.pdf .

[255] R. N. Bracewell, Aust. J. Phys. **9**, 198 (1956).

[256] "SciKit package," .

[257] J. D. Jackson, *Classical electrodynamics*, 3rd ed. (Wiley, 2009).

[258] R. L. Asher, D. Bellert, T. Buthelezi, V. Lewis, and P. J. Brucat, Chem. Phys. Lett. **234**, 113 (1995).

[259] K. M. Gough, M. M. Yacowar, R. H. Cleve, and J. R. Dwyer, Canadian Journal of Chemistry **74**, 1139 (1996), http://dx.doi.org/10.1139/v96-128 .

[260] Y. Kato, K. Mima, N. Miyanaga, S. Arinaga, Y. Kitagawa, M. Nakatsuka, and C. Yamanaka, Phys. Rev. Lett. **53**, 1057 (1984).

[261] J. Denavit and D. W. Phillion, Phys. Plasmas **1**, 1971 (1994).

[262] F. G. Sun, Z. Jiang, and X.-C. Zhang, Appl. Phys. Lett. **73**, 2233 (1998).

[263] P. W. Sullivan, B. Croll, and R. A. Simcoe, Pub. Astronom. Soc. Pac. **125**, 1021 (2013).

[264] "Xeva-1.7-640 - Shortwave infrared (SWIR) camera | Xenics - Infrared Solutions," .

[265] A. Brun, P. Georges, G. L. Saux, and F. Salin, J. Phys. D: Appl. Phys. **24**, 1225 (1991).

[266] J. Janszky, G. Corradi, and R. Gyuzalian, Optics Communications **23**, 293 (1977).

[267] M. L. Van, G. Mainfray, C. Manus, and I. Tugov, Phys. Rev. Lett. **29**, 1134 (1972).

[268] M. L. Van, G. Mainfray, C. Manus, and I. Tugov, Phys. Rev. A **7**, 91 (1973).

[269] A. G. MacPhee, K. U. Akli, F. N. Beg, C. D. Chen, H. Chen, R. Clarke, D. S. Hey, R. R. Freeman, A. J. Kemp, M. H. Key, J. A. King, S. L. Pape, A. Link, T. Y. Ma, H. Nakamura, D. T. Offermann, V. M. Ovchinnikov, P. K. Patel, T. W. Phillips, R. B. Stephens, R. Town, Y. Y. Tsui, M. S. Wei, L. D. V. Woerkom, and A. J. Mackinnon, Review of Scientific Instruments **79**, 10F302 (2008), http://dx.doi.org/10.1063/1.2978199 .

[270] R. L. Fleischer, P. B. Price, and R. M. Walker, Journal of Applied Physics **36**, 3645 (1965), http://dx.doi.org/10.1063/1.1703059 .

[271] A. Pellegrino, M. van Beuzekom, E. van den Born, D. Groep, W. Hesselink, E. Jans, N. Kalantar-Nayestanaki, W.-J. Kasdorp, J. Kos, M. Kruszynska, E. Kwakkel, J. van Leeuwe, F. Mul, C. Onderwater, H. Peek, T. Ploegmakers, A. Poelman, R. Starink, J. Steijger, H. Sturris, J. Templon, J. Visschers, R. van Wijk, and A. Zwart, Nuclear Instruments and Methods in Physics Research Section A: Accelerators, Spectrometers, Detectors and Associated Equipment **437**, 188 (1999).

[272] J. Miyahara, K. Takahashi, Y. Amemiya, N. Kamiya, and Y. Satow, Nuclear Instruments and Methods in Physics Research Section A: Accelerators, Spectrometers, Detectors and Associated Equipment **246**, 572 (1986).

[273] K. Takahashi, K. Kohda, J. Miyahara, Y. Kanemitsu, K. Amitani, and S. Shionoya, Journal of Luminescence **31**, 266 (1984).

[274] *Image format description BAS2500 system.*

[275] A. Mančić, J. Fuchs, P. Antici, S. A. Gaillard, and P. Audebert, Rev. Sci. Instrum. **79**, 073301 (2008).

[276] J. N. Olsen, G. W. Kuswa, and E. D. Jones, Journal of Applied Physics **44**, 2275 (1973), http://dx.doi.org/10.1063/1.1662550 .

[277] M. Borghesi, A. Giulietti, D. Giulietti, L. A. Gizzi, A. Macchi, and O. Willi, Phys. Rev. E **54**, 6769 (1996).

[278] O. Willi, R. G. Evans, and A. Raven, The Physics of Fluids **23**, 2061 (1980), http://aip.scitation.org/doi/pdf/10.1063/1.862893 .

[279] M. Börner, J. Fils, A. Frank, A. Blažević, T. Hessling, A. Pelka, G. Schaumann, A. Schökel, D. Schumacher, M. M. Basko, J. Maruhn, A. Tauschwitz, and M. Roth, Review of Scientific Instruments **83**, 043501 (2012), http://dx.doi.org/10.1063/1.3701366 .

[280] A. Aliverdiev, D. Batani, R. Dezulian, T. Vinci, A. Benuzzi-Mounaix, M. Koenig, and V. Malka, Plasma Physics and Controlled Fusion **50**, 105013 (2008).

[281] G. P. Schurtz, P. D. Nicolaï, and M. Busquet, Phys. Plasmas **7**, 4238 (2000).

[282] T. B. Kaiser, Phys. Rev. E **61**, 895 (2000).

[283] D. J. Y. Marion, A. Debayle, P.-E. Masson-Laborde, P. Loiseau, and M. Casanova, Physics of Plasmas **23**, 052705 (2016), http://dx.doi.org/10.1063/1.4948489 .

[284] P. E. Masson-Laborde, M. C. Monteil, V. Tassin, F. Philippe, P. Gauthier, A. Casner, S. Depierreux, C. Neuville, B. Villette, S. Laffite, P. Seytor, P. Fremerye, W. Seka, D. Teychenné, A. Debayle, D. Marion, P. Loiseau, and M. Casanova, Phys. Plasmas **23**, 022703 (2016).

[285] S. V. Bulanov and T. Z. Esirkepov, Phys. Rev. Lett. **98**, 049503 (2007).

[286] L. Willingale, S. P. D. Mangles, P. M. Nilson, R. J. Clarke, A. E. Dangor, M. C. Kaluza, S. Karsch, K. L. Lancaster, W. B. Mori, Z. Najmudin, J. Schreiber, A. G. R. Thomas, M. S. Wei, and K. Krushelnick, Phys. Rev. Lett. **98**, 049504 (2007).

[287] Y. Ping, R. Shepherd, B. F. Lasinski, M. Tabak, H. Chen, H. K. Chung, K. B. Fournier, S. B. Hansen, A. Kemp, D. A. Liedahl, K. Widmann, S. C. Wilks, W. Rozmus, and M. Sherlock, Phys. Rev. Lett. **100**, 085004 (2008).

[288] F. Schluck, *Amplification of ultra-short relativistic laser pulses by stimulated Brillouin scattering*, Ph.D. thesis, Heinrich-Heine-Universität Düsseldorf (2016).

[289] L. Lancia, *Study of non-linear effects on laser propagation and electron transport in plasmas*, Ph.D. thesis, Università di Roma, Ecole Polytechnique (2010).

[290] H. Rottke, D. Feldmann, B. Wolff-Rottke, and K. H. Welge, Journal of Physics B: Atomic, Molecular and Optical Physics **26**, L15 (1993).

[291] G. G. Paulus, W. Nicklich, F. Zacher, P. Lambropoulos, and H. Walther, Journal of Physics B: Atomic, Molecular and Optical Physics **29**, L249 (1996).

[292] J. R. Marquès and M. Chiaramello, "1d simulations with envelope equations," (2017), private communication.

[293] R. Nuter and V. Tikhonchuk, Phys. Rev. E **87**, 043109 (2013).

[294] R. Benattar, C. Popovics, and R. Sigel, Rev. Sci. Instrum. **50**, 1583 (1979).

[295] M. Chiaramello, C. Riconda, F. Amiranoff, J. Fuchs, M. Grech, L. Lancia, J.-R. Marquès, T. Vinci, and S. Weber, Physics of Plasmas **23**, 072103 (2016), http://dx.doi.org/10.1063/1.4955322.

List of Figures

List of Tables